Design and Test of a High Capacity Pulse-Tube

by

Seth Potratz

A thesis submitted in partial fulfillment of

the requirements for the degree of

Master of Science

(Mechanical Engineering)

at the

UNIVERSITY OF WISCONSIN-MADISON

2005

Approved by

_____ _____

Professor Gregory F. Nellis Date

Abstract

The objective of this project has been the development of a high capacity, single-stage Stirling-type pulse-tube refrigerator. The specific design target was 300 W of cooling at 65 K. A thermodynamic design model of the pulse tube refrigeration cycle was developed and used, in conjunction with the regenerator design code REGEN, to specify the thermal-fluid design of a pulse-tube apparatus. The pulse-tube was fabricated, assembled, and tested. The results of the tests indicated that a large and previously unconsidered loss was present and resulted in performance that was far short of our design target or the model predictions. Based on this outcome, the flow distribution within the pulse tube was investigated using computational fluid dynamic (CFD) modeling. The results of the CFD analysis suggested a series of hardware design changes which were sequentially implemented into the pulse-tube; each hardware modification yielded incrementally better understanding of the performance and ultimately substantially improved performance. Although the original design target was not ultimately achieved, the current configuration is capable of providing substantial refrigeration at temperatures below 100 K. Furthermore, the experimental data has verified many of the physical insights and performance trends predicted by the thermodynamic design model, the regenerator model REGEN, and the CFD models. Consequently, these results provide a clear path towards further optimization.

Acknowledgements

I would like to recognize and thank the following people for their support and direction during my time as a graduate student here at the University of Wisconsin-Madison. First and foremost I would like to thank my advisors, Professor Greg Nellis and Professor John Pfotenhauer. Greg for your tireless effort, constant encouragement, and deep knowledge base was instrumental in my development not only as an engineer, but also as a person. John for your steady support and the security of knowing that I had so much experience in cryogenics and the rest of my subject area to fall back on whenever I needed it. Thank you both for helping me accomplish more than I thought would be possible in the two years I spent with you.

I would also like to express my deep gratitude to Dr. Jim Maddocks for his constant support and assistance. Jim your ability to teach, your patience, and your ability to keep my work from consuming me were all assets. Your willingness to give yourself to me and this project was greatly appreciated. You taught me how to hold my work to the highest standard and what it takes to be a successful, professional researcher. Most importantly you taught me this while showing me how to completely enjoy my work.

I would like to thank Dr. Barrett Flake at the Air Force Research Labs in Albuquerque, New Mexico for his assistance in my project and his mentoring on how to develop my career. I would also like to recognize Dan Hoch for always being a selfless resource and teacher to ensure the success of my project.

On the social aspect of life I would like to thank Kurt Engelbrecht for being a solid friend and at times being the only sane opinion that I had left. To Cory Hughes thanks for Anaheim and the not well-advised great times we had. To Ryan Taylor thanks for pushing me to work as hard as I could. To Cheadle, Schuetter, Brandon, Michael, Widalys, Holly, and Gayathri thanks for relieving the stress on a regular basis.

Last, but not least, I would like to say thank you to my family. Mom and Dad thank you for being great examples. To my sisters Angi and Jacki thank you for being great counselors and a constant fixture of support. To my little sister Bethany thanks for being my hero.

Table of Contents

List of Figures

List of Tables

Nomenclature

A	*area (m^2), outside flange diameter (in), constant*
B	*inside flange diameter (in)*
C	*bolt circle diameter (in), inertial resistance*
c_P	*specific heat capacity at constant pressure (J/kg-K)*
D	*diameter (m)*
E	*modulus of elasticity (psi)*
f	*frequency (Hz), friction factor*
f_s	*screen geometry factor*
ffs	*fraction of full-stroke*
G	*gasket diameter (in)*
H	*total hydrostatic end force (lbf)*
H_D	*hydrostatic end force on area inside of flange (lbf)*
h_D	*radial distance from the bolt circle, to the circle on which H_D acts (in)*
H_G	*gasket load (lbf)*
h_G	*radial distance from gasket load reaction to the bolt circle (in)*
H_P	*total joint-contact surface compression load (lbf)*
H_T	*difference between total hydrostatic end force and the hydrostatic end force on area inside of flange (lbf)*
h_T	*radial distance from the bolt circle to the circle on which H_T acts (in)*
htc	*heat transfer coefficient (W/m^2-K)*
K	*ratio of outside diameter of flange to inside diameter of flange*
k	*thermal conductivity (W/m-K)*
L	*fluid inertance ($Pa\text{-}s^2/kg$), length (m)*
$\dot{m}$	*mass flow rate (kg/s)*
m	*gasket factor*
M	*mass (kg)*
M_o	*total moment acting upon the flange (in-lbf)*
M_D	*component of moment due to H_D (in-lbf)*
M_G	*component of moment due to H_G (in-lbf)*
M_T	*component of moment due to H_T (in-lbf)*
Nu	*Nusselt number*
p	*pressure (Pa)*
$\tilde{p}$	*amplitude of oscillating pressure (Pa)*
pitch	*distance between wires in screen*
Pr	*Prandtl number*
PR	*pressure ratio*
$\dot{q}$	*heat transfer rate (W)*
R	*flow resistance, thermal resistance (K/W)*
r	*fluid resistance (Pa-s/kg), radius (m)*
Re	*Reynolds number*
Rg	*gas constant (N-m/kg-K)*
$\dot{S}_{gen}$	*entropy generation rate (W/K)*

S *pressure gradient (Pa/m)*
t *time (s), thickness (in)*
T *temperature (K)*
u *velocity (m/s)*
V *volume (m^3), voltage (V)*
v *velocity (m/s)*
$\dot{w}$ *work transfer rate (W)*
W_{m1} *bolt load (lbf)*
x *position (m)*
Y *geometric factor involving K*

Greek

α *permeability*
β *hydraulic diameter (m)*
Δn *depth (m)*
ΔP *pressure drop (kPa)*
ΔT *change in fluid temperature (K)*
Δx *fluid motion (m)*
δ *deflection (in)*
ε *strain (in/in), emissivity*
γ *ratio of specific heat capacities*
ϕ *time*
Γ *inertance*
λ *volume*
η *efficiency*
θ *temperature*
μ *viscosity (Pa-s)*
ρ *density (kg/m^3)*
σ *stress (psi), Stefan-Boltzmann constant (W/m^2-K^4)*
τ *compressor period (s)*
ω *angular frequency (rad/s)*

Subscripts

ac *acoustic*
ad *adiabatic*
b *bolt*
by *bypass*
c *cold end*
C *compressor*
can *vacuum can*
ch *charge*
char *characteristic*
cond *conduction*
conv *convection*
d *dead*
h *hot end*

hyd	*hydraulic*
i	*inner*
load	*refrigeration load*
loss	*loss*
long	*longitudinal*
mag	*magnitude*
max	*maximum*
mix	*related to mixing*
p	*physical, piston*
ps	*phase-shifter*
pt	*pulse tube*
r	*regenerator*
rad	*radial*
rej	*rejection*
rms	*root mean square*
Rsv	*reservoir*
s	*surface, superficial*
surr	*surroundings*
shuttle	*shuttle*
sw	*swept*
vac	*vacuum space*
wall	*wall*

Chapter 1 – Introduction

1.1 Objective

The objective of this thesis is to develop the technology required for high capacity, Stirling-type pulse-tubes capable of operating at temperatures that are consistent with high-temperature superconductors; more specifically the goal has been to design and test a single-stage pulse-tube capable of providing 300 Watts of cooling at 65 K. This technology will have potential applications that are related to high-temperature superconductors operating in power applications such as motors, generators, power lines. The technology will have broader application anyplace that large amounts of cooling are required in an efficient, cost effective, and extremely reliable package.

The organization of this thesis is related to the path that was followed during the development of the pulse-tube. The introduction describes the concepts and governing principles of the Stirling cryocooler cycle and how they can be used to understand the Stirling-type pulse-tube. Chapter 2 introduces the thermodynamic model and describes how it is used to optimize the pulse-tube. Chapter 3 explores the mechanical design of the components and discusses the instrumentation and data acquisition system used for testing. Chapter 4 presents the initial test results and compares them to the predictions of the thermal-fluid model. Chapter 5 discusses a computational fluid dynamic model of the initial pulse-tube design that was used to explore optimal geometries for best flow distribution. Chapter 6 describes the testing of a 2nd generation pulse-tube that was re-designed based on the results predicted by the computational fluid dynamic model. The

final chapter, Chapter 7, summarizes the conclusions associated with the experiment and design process.

1.2 The Stirling Cryocooler Cycle

A Stirling-type pulse-tube's operation is governed by essentially the same principles that govern the behavior of the Stirling cryocooler cycle. The Stirling cycle is implemented by a system that consists of a linear compressor and a cold piston, a regenerator, cold heat exchanger, and aftercooler; as shown in Figure 1.1.

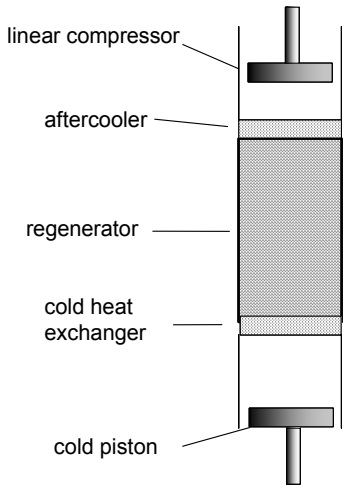

Figure 1.1. Schematic of the components in a Stirling cryocooler cycle.

The linear compressor pushes gas through an aftercooler that is thermally connected to some heat rejection medium. The cold piston pushes gas through the cold heat exchanger which is connected to the refrigeration load. The aftercooler and the cold heat exchanger are separated by a regenerator matrix, which is a solid material with a high heat capacity that contains many small passages for flow. The regenerator matrix alternatively accepts energy from the gas flow during the hot-to-cold flow and gives it back to the gas during the cold-to-hot flow. Note that, because the compression process occurs at the upper end

and the expansion process occurs at the lower end, the gas coming from the upper end tends to a higher temperature while the gas returning from the lower end tends to a cold temperature. As a result, the net energy flow at any location in the regenerator must be towards the cold end. At best, for a perfect regenerator, the energy flow will be zero indicating that the hot and cold ends are perfectly isolated from one another.

In order for the Stirling cycle to operate correctly, the pistons must move independently of each other and out of phase with one another; this causes the pressure and volume variation in the cold space to be out of phase which causes the cold piston to receive a net amount of work during each cycle. The cold piston sees larger pressure when it is retracted as compared to when it is moved towards the cold heat exchanger and so a pressure-volume diagram for the cold space will sweep out a net positive area.

To further clarify the Stirling cycle, Figure 1.2 illustrates the working process.

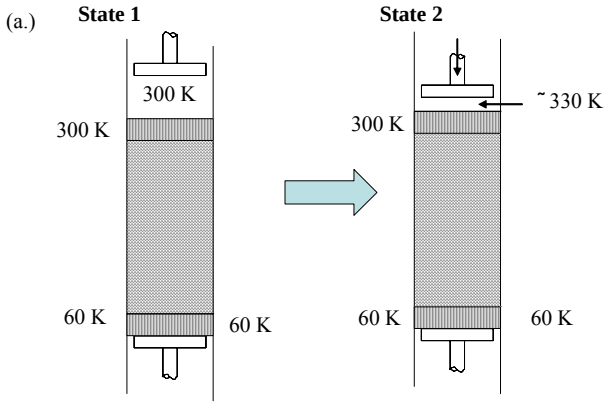

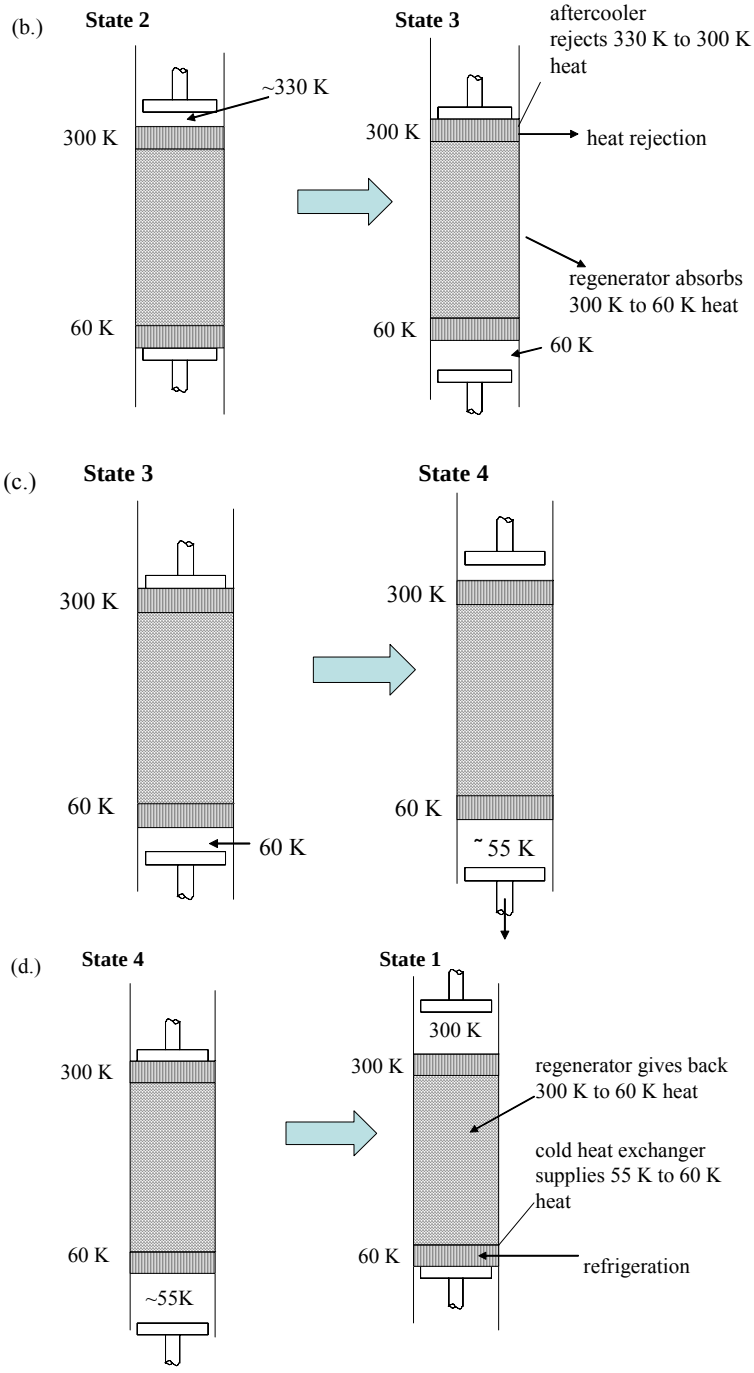

Figure 1.2. Summary of the Stirling cryocooler cycle: (a) compression, (b) hot to cold flow, (c) expansion, (d) cold to hot flow

Figure 1.3 shows the pressure, expansion space volume and the volumetric flow rate at the cold end of the regenerator during the Stirling cycle. Note that a positive flow rate is toward the cold end.

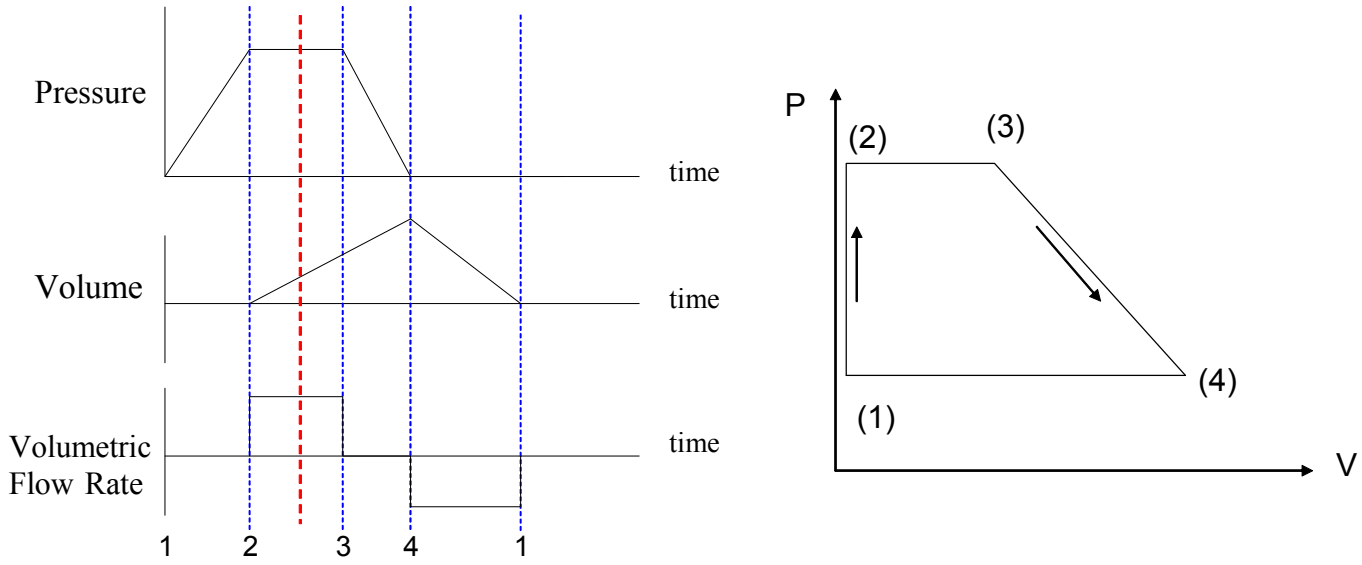

Figure 1.3. The volume and pressure relations in the cold space during the Stirling Cycle (left) and a pressure-volume diagram of the cycle (right).

During the compression process (state 1 to 2), the pressure increases as the cold piston is locked against the cold heat exchanger and so the expansion space volume is essentially zero. During the hot-to-cold flow process (state 2 to 3), the flow is pushed from the compression to the expansion space through the regenerator matrix; a constant velocity motion of the piston would result in a constant flow rate into the cold end. The expansion process (state 3 to 4) results in an increase in the expansion space volume and a decrease in pressure. Finally, during the cold-to-hot flow process (state 4 to 1), the gas is pushed from the expansion space back to the compression space. The P-V diagram associated

with this set of processes is shown in Figure 1.3 and indicates that the cycle has a positive area or a net work from the gas to the cold piston; in the ideal cycle, this work is equal to the refrigeration load accepted per cycle.

Figure 1.4 shows a summary of the energy flows that characterize a Stirling cryocooler.

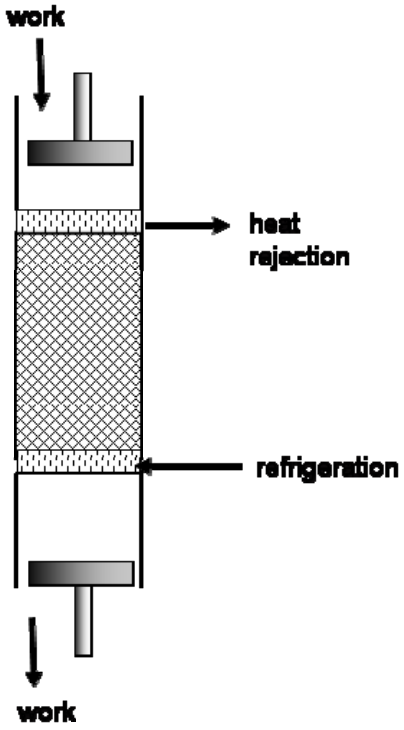

Figure 1.4. Summary of energy flows in a Stirling cryocooler cycle.

Work enters the system through the compressor and the heat of compression is removed through the aftercooler. The refrigeration load enters the system through the cold heat exchanger and is transferred to the hot end as work through the cold piston. The key disadvantage of the Stirling cycle is that the mechanical cold piston is prone to failure as is any moving, mechanical part at the cold end of a cryogenic system.

1.3 Stirling-Type Pulse-Tubes

The Stirling-type pulse-tube operates using essentially the same principle as the Stirling cycle, except that the cold piston is removed and replaced by an empty tube, which is called a pulse-tube. The pulse-tube serves the same purpose as the cold piston, it transfers work from the cold end to the hot end of the pulse-tube. However, the work is transferred through a compliant piston formed by the "stagnant" gas that is trapped in the pulse-tube. A hot heat exchanger is placed at the warm end of the pulse-tube in order to transform the work that is transferred through the tube into heat which is rejected to the ambient environment. The phase between the motion of the compliant "piston" that is associated with the gas in the pulse-tube and the compressor cannot be mechanically and precisely controlled as it can in the Stirling cryocooler. Instead, an acoustic network consisting of an inertance tube and a reservoir is placed on the warm end of the pulse-tube; the acoustic network can be tuned to provide the correct phase between the flow and the pressure. Figure 1.5 shows a schematic of a Stirling-type pulse-tube.

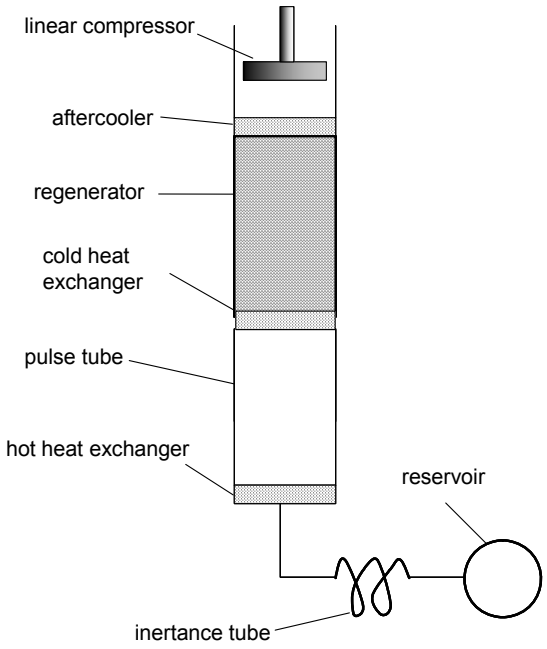

Figure 1.5. Schematic of components in a Stirling-type pulse-tube.

The energy flows in the pulse-tube are shown in Figure 1.6. As with the Stirling cryocooler, work is input to the system through the linear compressor and the heat of compression is removed with the aftercooler. The refrigeration load into the cold heat exchanger is transferred to the warm end as work through the compliant piston that is the pulse-tube. Finally the work is rejected as heat at the hot heat exchanger.

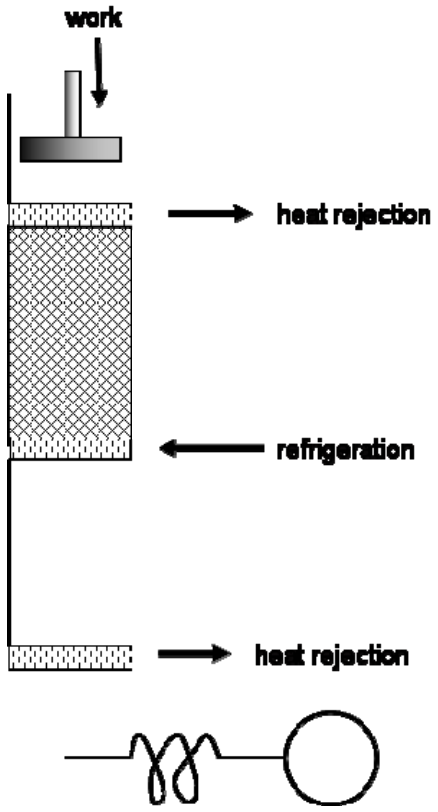

Figure 1.6. Summary of energy flows in a Stirling-type pulse-tube.

In the Stirling-type pulse-tube the cold piston is removed. This causes a loss of efficiency because the work that was recovered by the cold piston is now lost. However this work is a small fraction of the compressor power, particularly as the load temperature is reduced. The advantage of pulse-tube is that all cold moving parts are eliminated which provides a very large increase in reliability.

Chapter 2 – Thermodynamic Design of High-Capacity Pulse-Tube

2.1 Introduction

This chapter investigates the thermodynamic design and analysis of the pulse-tube. The model is very idealized but the objective is to accurately represent the pressure-flow behavior in the pulse-tube and predict the associated losses. The thermodynamic design of the pulse-tube was a two step operation; the regenerator was optimized first in order to provide a reasonable starting point for the balance of the pulse-tube which was subsequently modeled.

The regenerator, which many consider the most vital component in the pulse-tube, was optimized using the regenerator simulation program REGEN v3.2. REGEN v3.2 is a simulation program implemented in FORTRAN and developed at NIST, as described by Gary et al (1985, 1990, 2001). REGEN v3.2 is a powerful tool for investigating the influence of geometry, material selection, frequency, temperature, pressure ratio, and the phase between flow and pressure on regenerator performance. The pulse-tube system model was subsequently developed using a first-order model that calculates the pressure-flow characteristics of the system in the absence of thermal losses that is coupled with models of the various internal loss mechanisms

2.2 Regenerator Optimization

The losses in a regenerative refrigeration cycle such as the Stirling-type pulse-tube considered here are primarily associated with the regenerator itself; therefore, a logical

first step in an optimization process is to consider the performance of the regenerator without the details associated with the other components that make up the system. This can be accomplished using phasors to describe the relationship between the mass flow rates and pressure within the regenerator at various locations. The phasor diagram can be used to predict the flow conditions that will be experienced by the regenerator within an optimally designed pulse-tube, given arbitrary regenerator geometry. This approach allows the regenerator simulation program, REGEN v3.2, to be used to investigate the performance of various regenerator designs in the context of this application.

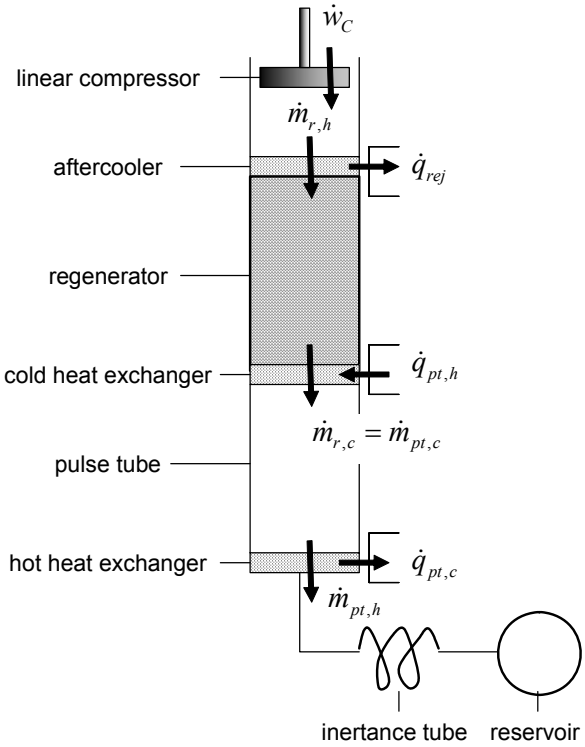

Figure 2.1. Schematic of a single-stage pulse-tube.

The phasor diagram for the pulse-tube shown in Figure 2.1 is illustrated qualitatively in Figure 2.2. The magnitudes of the mass flow phasors shown in Figure 2.2 represent the

amplitude of the mass flow variations at the different locations in the pulse-tube. The angle between the phasor and the real axis represents the phase between the mass flow rate and the pressure variation (which is assumed to be spatially uniform in this representation). A mass flow rate phasor that lies on the real axis is in phase with the pressure variation. Mass flow rates that lie in the first quadrant lead the pressure in time and those in the second quadrant lag the pressure variation.

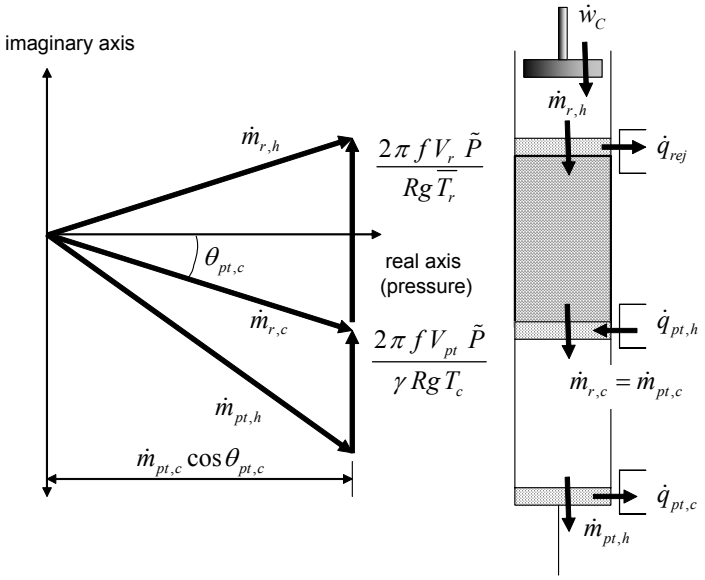

Figure 2.2. Phasor representation of mass flow and pressure within a single stage pulse-tube.

Note that the phasors that lie perpendicular to the real axis represent the storage of mass in the various volumes in the pulse-tube. The $\frac{2\pi f V_r \tilde{p}}{Rg\ \overline{T}_r}$ term represents the amount of mass in the regenerator, while the $\frac{2\pi f V_{pt} \tilde{p}}{\gamma Rg\ T_c}$ term represents the amount of mass stored in the pulse-tube; where Rg is the gas constant, V_r is the dead volume in the regenerator, V_{pt} is the volume of the pulse-tube, f is the frequency, γ is the ratio of specific heat

capacities, T_c is the cold end temperature, and $\tilde{p}$ is the amplitude of the pressure variation, which is defined by:

$$\tilde{p} = p_{ch}\left(\frac{PR-1}{PR+1}\right) \tag{2.1}$$

where p_{ch} is the charge pressure and PR is the pressure ratio. The mass average temperature in the dead volume of the regenerator, $\overline{T}_r$, is defined by:

$$\overline{T}_r = \frac{T_{rej} - T_c}{\ln\left(\frac{T_{rej}}{T_c}\right)} \tag{2.2}$$

where T_{rej} is the heat rejection temperature. The acoustic power ($\dot{w}_{ac}$) delivered to the pulse-tube represents the maximum possible refrigeration that could be provided and can be determined approximately from the following expression:

$$\dot{w}_{ac} = \frac{Rg\ T_c \tilde{p}\ \dot{m}_{pt,c} \cos\theta_{pt,c}}{2\ p_{ch}} \tag{2.3}$$

where $\dot{m}_{pt,c}$ is the mass flow rate at the cold end of the pulse-tube and $\theta_{pt,c}$ is the phase between the pressure variation and the mass flow rate at the same location (see Figure 2.2). The mass flow rate leaving the cold end of the regenerator ($\dot{m}_{r,c}$) can be expressed as:

$$\dot{m}_{r,c} = \left(\left|\dot{m}_{pt,c}\right|\cos\theta_{pt,c}\right) + \left(\left|\dot{m}_{pt,c}\right|\sin\theta_{pt,c}\right)i \tag{2.4}$$

The first term in the above equation represents the projection of the phasor onto the pressure (real) axis, while the second part of the equation represents the projection of the phasor onto the imaginary axis. The mass flow rate at the warm end of the regenerator

($\dot{m}_{r,h}$) leads the mass flow rate at the cold end of the regenerator due to mass storage in the dead volume of the regenerator:

$$\dot{m}_{r,h} = \left(\left|\dot{m}_{pt,c}\right|\cos\theta_{pt,c}\right) + \left(\left|\dot{m}_{pt,c}\right|\sin\theta_{pt,c} + \frac{2\pi f V_r \tilde{p}}{Rg\,\bar{T}_r}\right) i \tag{2.5}$$

The net heat transferred to the regenerator is approximately:

$$\dot{q}_r = \bar{\dot{m}}_r c_p (T_{rej} - T_c) \tag{2.6}$$

where $\bar{\dot{m}}_r$ is the average amplitude of the mass flow rate in the regenerator which can be expressed approximately as:

$$\bar{\dot{m}}_r = \frac{\left|\dot{m}_{r,c}\right| + \left|\dot{m}_{r,h}\right|}{2} \tag{2.7}$$

The dominant losses within the pulse-tube are related to the regenerator and the important regenerator losses (e.g., pressure drop and ineffectiveness) all scale with the mass flow rate through the regenerator. Therefore, the optimal phase angle between the mass flow rate at the cold end of the pulse-tube and the pressure, $\theta_{pt,c}$, will minimize the average amplitude of the mass flow rate in the regenerator, Eq. (2.7), and therefore the amount of heat that must be transferred in the regenerator, Eq. (2.6). This optimum is consistently found when the phasors that represent the mass flow rates at the hot and cold ends of the regenerator are centered over the real axis; this represents putting the mass flow rate at the center of the regenerator in phase with the pressure variation and results in minimizing the average regenerator mass flow rates required. The optimal phase angle for the mass flow rate entering the cold end of the regenerator is therefore given by the following relation:

$$\theta_{r,c} = -\arctan\left[\frac{f\,2\pi\,V_r\tilde{p}}{2Rg\,\overline{T}_r\,\dot{m}_{pt,c}\cos\theta_{pt,c}}\right] \tag{2.8}$$

Equations (2.1), (2.3), and (2.8) taken together allow the specification of the mass flow rates and their phase with respect to pressure at either end of the regenerator, given a desired value of acoustic power, charge pressure, and pressure ratio together with a value of the regenerator dead volume that is based on a candidate regenerator geometry. These parameters are sufficient to set the boundary conditions required by REGENv3.2, as described by Pfotenhauer et al. (2004), and therefore allow a complete optimization of the regenerator geometry for a particular application. Figures 3 and 4 show the adjusted cooling power (the acoustic power less the regenerator losses related to ineffectiveness, conduction, and pressurization of the void volume) and the average pressure drop, respectively, predicted by REGENv3.2 as a function of the regenerator length for several diameters. For each case, the pressure ratio was assumed to be 1.2, the charge pressure was 2.5 MPa, the acoustic power 700 W, the hot and cold end temperatures were 300 K and 60 K, respectively, and 400 mesh stainless steel screen was assumed to be the packing material.

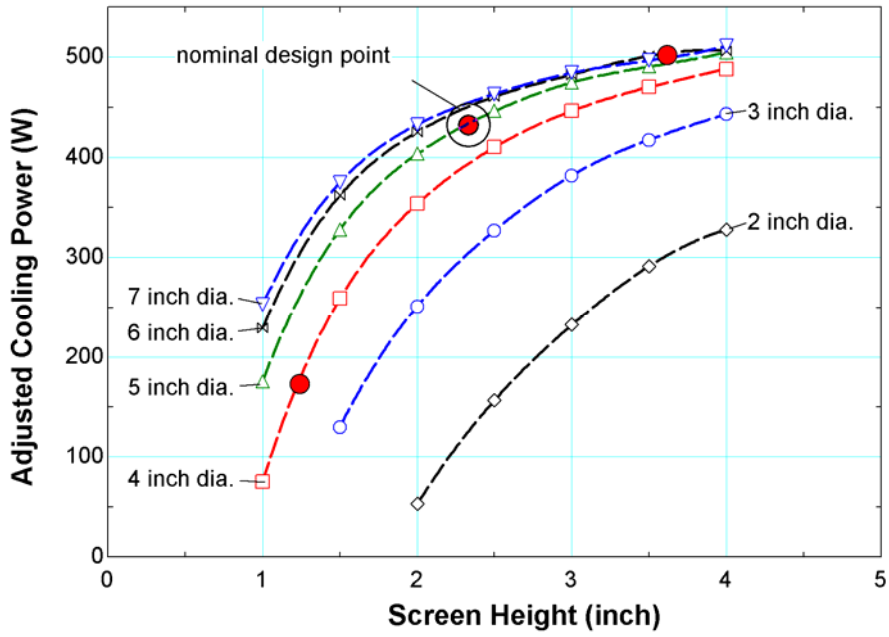

Figure 2.3. Adjusted cooling capacity as a function of the regenerator length for various diameters (PR = 1.2, P_{ch} = 2.5 MPa, $\dot{w}_{ac}$ = 700 W).

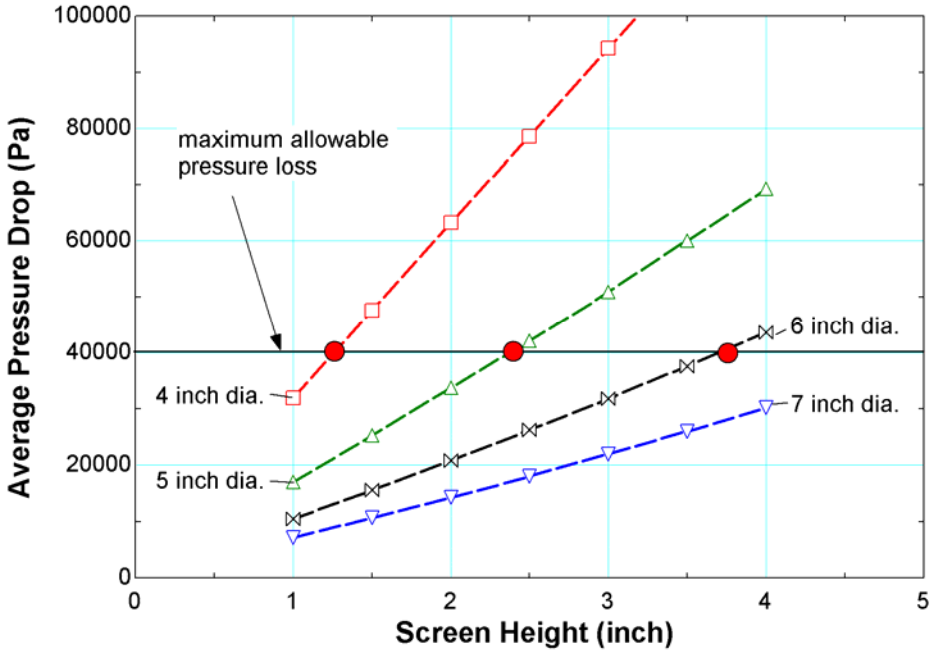

Figure 2.4. Regenerator average pressure drop as a function of regenerator length for various diameters (PR = 1.2, P_{ch} = 2.5 MPa, $\dot{w}_{ac}$ = 700 W).

The optimization process proceeds by setting a certain, maximum allowable regenerator pressure drop; in this case, 40 kPa or roughly 15% of the pressure amplitude was selected. This maximum pressure drop is overlaid on Figure 2.4 and allows an appropriate length to be selected for each diameter, indicated by the solid circles. These solid circles are transferred to Figure 2.3 to study the effect of regenerator diameter on cooling capacity when the pressure drop is constrained. Notice that the cooling capacity increases dramatically with regenerator diameter up to approximately 5 inch, after which it levels out and would eventually fall at very large diameters due to the impact of axial conduction. Practical difficulties were anticipated relative to transitioning from a very large diameter regenerator (greater than 5 inch) to the considerably smaller diameter pulse-tube; therefore, a 5 inch diameter regenerator with a 2.2 inch height was selected as the nominal design point, as shown in Figure 2.3. This nominal design point provided the starting point for the more detailed design process accomplished using the pulse-tube detailed design model.

2.3 Pulse-tube Detailed Model

The previous section describes the procedure used to optimize the regenerator; however, the results of the optimization process are not predictive and therefore cannot be directly compared with the experimental results. This motivated the development of a detailed model which predicts the pressure-flow behavior and the losses in excess of the regenerator loss. The detailed design model can therefore be used to confirm our physical understanding of the pulse-tube system through comparison of the measured pressure behavior as well as the overall system performance (i.e., the measured load

curve). The detailed model is developed as two separate, but interfaced models: the first order model captures the essential fluid-mechanical processes that are responsible for the refrigeration mechanism. These include the pressures and flow rates that result from the compressor piston motion, including pressure loss and inertance tube effects that were ignored during the optimization procedure. These quantities are predicted using mass conservation together with constitutive equations for the various components. The first order model is highly idealized in that most of the important loss mechanisms in the system are not considered and several idealizations are employed, including ideal gas behavior, isothermal volumes, and perfect heat transfer. The pressure loss and dead volume characteristics of the regenerator are concentrated and modeled using a single fluid resistance and capacitance. Therefore, while the results of the first order model are useful for establishing a nominal set of flow conditions, these results are only predictive when coupled with the subsequent, post-calculation of the important losses.

2.3.1 First Order Model

Figure 2.5 depicts the pulse-tube system used to develop the first order model

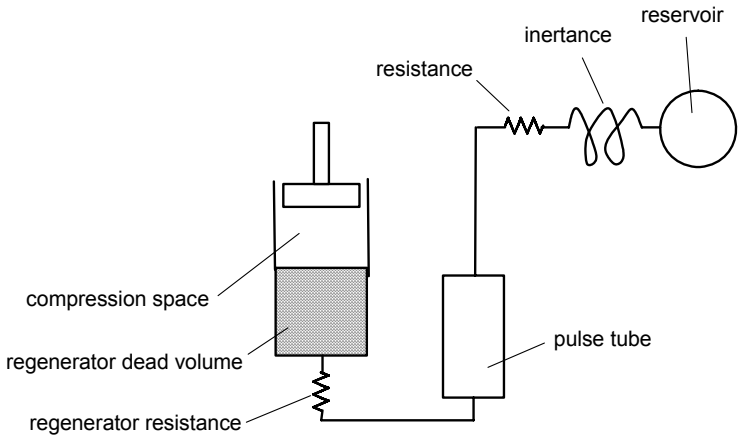

Figure 2.5 Schematic of the pulse-tube system used for the first order model.

An inertance tube is placed at the warm end of the pulse-tube in order to establish the proper phase relationship. The inertance tube is modeled as a fluid resistor (r_{ps}) in series with an inductive element (L_{ps}), as suggested by Roach and Kashani (1997).The mass flow rate through the inertance tube ($\dot{m}_{ps}$) is therefore given by:

$$p_{pt} - p_{Rsv} = \dot{m}_{ps}\, r_{ps} + \frac{d\,\dot{m}_{ps}}{dt} L_{ps} \tag{2.9}$$

where p_{pt} and p_{Rsv} are the instantaneous pressures in the pulse-tube and reservoir. A mass balance on the reservoir leads to:

$$\frac{V_{Rsv}}{Rg\,T_{rej}} \frac{dp_{Rsv}}{dt} = \dot{m}_{ps} \tag{2.10}$$

where V_{Rsv} is the reservoir volume. A mass balance on the dead volume in the regenerator leads to:

$$\frac{V_r}{Rg\,\overline{T}_r} \frac{dp_r}{dt} = \dot{m}_{r,h} - \dot{m}_{r,c} \tag{2.11}$$

where p_r is the pressure in the regenerator dead volume. Energy conservation on the pulse-tube together with the assumption of isothermal compression and expansion volumes leads to:

$$\dot{m}_{r,c} = \frac{T_{rej}}{T_c} \dot{m}_{ps} + \frac{V_{pt}}{\gamma\, Rg\, T_c} \frac{dp_{pt}}{dt} \tag{2.12}$$

The volume in the compression space (V_C) is assumed to vary sinusoidally with frequency *f,* according to:

$$V_C = V_{C,d} + \frac{V_{C,sw}}{2}\left[1 + ffs \sin\left(2\pi f\, t\right)\right] \tag{2.13}$$

where $V_{C,sw}$ is the swept volume of the compressor at full-stroke, $V_{C,d}$ is the unswept (or dead) volume of the compressor, and *ffs* is the fraction of full-stroke at which the compressor is operating. The rate of change of the compression space volume is then:

$$\frac{dV_C}{dt} = -ffs\, f\, \pi V_{C,sw} \cos\left(2\pi f\, t\right) \tag{2.14}$$

Mass conservation applied to the compression space (assuming that it is isothermal) leads to:

$$\dot{m}_{r,h} + \frac{1}{Rg\, T_{rej}}\left[p_r \frac{dV_C}{dt} + V_C \frac{dp_r}{dt} \right] = 0 \tag{2.15}$$

The mass flow rate through the regenerator is governed by the regenerator fluid resistance (r_r) according to:

$$\dot{m}_{r,c} = \frac{p_r - p_{pt}}{r_r} \tag{2.16}$$

The 8 equations, Eq. (2.9) through Eq.(2.16), are sufficient to determine the derivative of the state variables that define the system (p_r, p_{pt}, p_{Rsv}, and $\dot{m}_{ps}$) given their instantaneous values. These state equations are integrated forward in time until cyclic steady-state is achieved using a 4th order Runga-Kutta technique. The result of the first order model is therefore the prediction of the variation of the state variables mentioned above and all of the mass flow rates in the system over a steady state cycle.

We have non-dimensionalized equations (2.9) through (2.16) in order to reduce the number of variables that are required to specify the system and therefore facilitate the eventual design process, obtain a better understanding of the underlying governing dimensionless parameters, and carry out numerical modeling using variables that are all of the same order. In order to

accomplish this, we have defined a non-dimensional mass flow rate ($\dot{M}$), pressure (P), time (ϕ), flow resistance (R), inertance (Γ), temperature (θ), and volume (λ) according to:

$$\dot{M} \equiv \frac{\dot{m} \cdot \tau \cdot Rg \cdot T_C}{p_{charge} \cdot V_{swept}} \tag{2.17}$$

$$P \equiv \frac{p}{p_{charge}} \tag{2.18}$$

$$\phi \equiv \frac{2 \cdot \pi \cdot t}{\tau} \tag{2.19}$$

$$R \equiv \frac{r \cdot V_{swept}}{\tau \cdot Rg \cdot T_C} \tag{2.20}$$

$$\Gamma \equiv \frac{L \cdot V_{swept}}{\tau^2 \cdot Rg \cdot T_C} \tag{2.21}$$

$$\theta \equiv \frac{T}{T_C} \tag{2.22}$$

$$\lambda \equiv \frac{V}{V_{swept}} \tag{2.23}$$

The non-dimensional forms of equations (2.9) through (2.16) are given by equations (2.24) through (2.31):

$$P_{pt} - P_{Rsv} = \dot{M}_{ps} \cdot R_{ps} + 2 \cdot \pi \cdot \frac{d\dot{M}_{ps}}{d\phi} \cdot \Gamma_{ps} \tag{2.24}$$

$$2 \cdot \pi \cdot \lambda_{Rsv} \cdot \frac{dP_{Rsv}}{d\phi} = \dot{M}_{ps} \tag{2.25}$$

$$2 \cdot \pi \frac{\lambda_r}{\theta_r} \cdot \frac{dP_r}{d\phi} = \dot{M}_C - \dot{M}_{r,c} \tag{2.26}$$

$$\theta_E \cdot \dot{M}_{r,c} = \dot{M}_{ps} + 2 \cdot \pi \frac{\lambda_{pt}}{\gamma} \cdot \frac{dP_{pt}}{d\phi} \tag{2.27}$$

`

$$\lambda_c = \lambda_{cd} + \frac{1}{2} \cdot \left[1 + f \cdot \sin(\phi)\right] \tag{2.28}$$

$$\frac{d\lambda_c}{d\phi} = -\frac{f}{2} \cdot \cos(\phi) \tag{2.29}$$

$$\dot{M}_C + 2 \cdot \pi \cdot \left[P_r \cdot \frac{d\lambda_c}{d\phi} + \lambda_c \cdot \frac{dP_r}{d\phi} \right] = 0 \tag{2.30}$$

$$\dot{M}_{r,c} = \frac{P_r - P_{pt}}{R_r} \tag{2.31}$$

These 8 non-dimensional equations can be solved to yield the derivatives of the state variables together with the relevant mass flow rates throughout the system given the non-dimensional parameters shown in Table 2.1. The solution of the state equations is accomplished by the MATLAB subroutine dXdphi_PTSS.m as shown in Figure 2.6. This MATLAB code is contained in Appendix B.

Table 2.1: Non-dimensional parameters that characterize system

Symbol	Physical Significance
R_{ps}	phase shifter resistance
Γ_{ps}	phase shifter inertance
λ_{Rsv}	reservoir volume
θ_E	load temperature
λ_r	regenerator dead volume
R_r	regenerator resistance
θ_r	regenerator dead volume temp.
λ_{pt}	pulse-tube volume
γ	ratio of specific heat capacities
λ_{cd}	dead-volume in compression space
f	fraction of compressor stroke

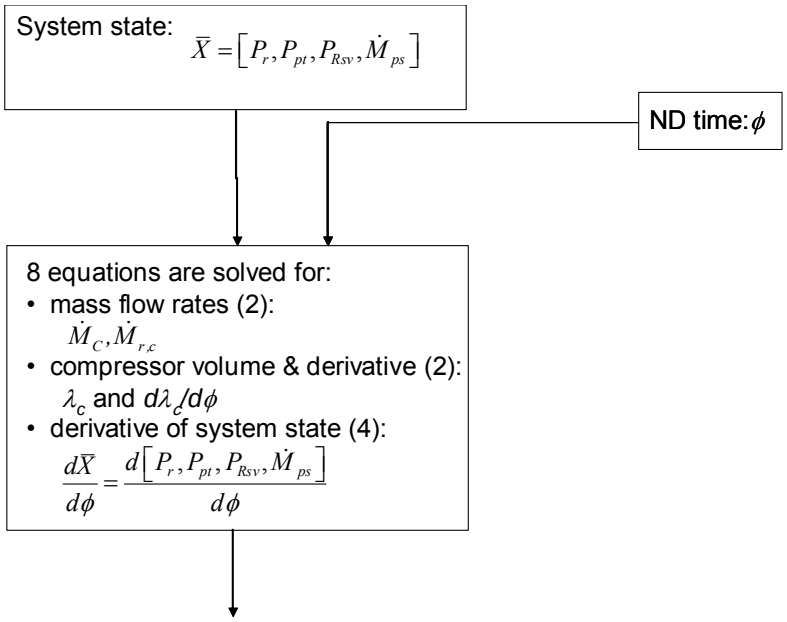

Figure 2.6. State equation formulation of hybrid system.

The state equation derivatives are integrated in time using a Runga-Kutta 4th order technique using the MATLAB routine PTSS.m, also contained in Appendix B. The integration is continued until a steady state cycle is achieved, as shown in Figure 2.7.

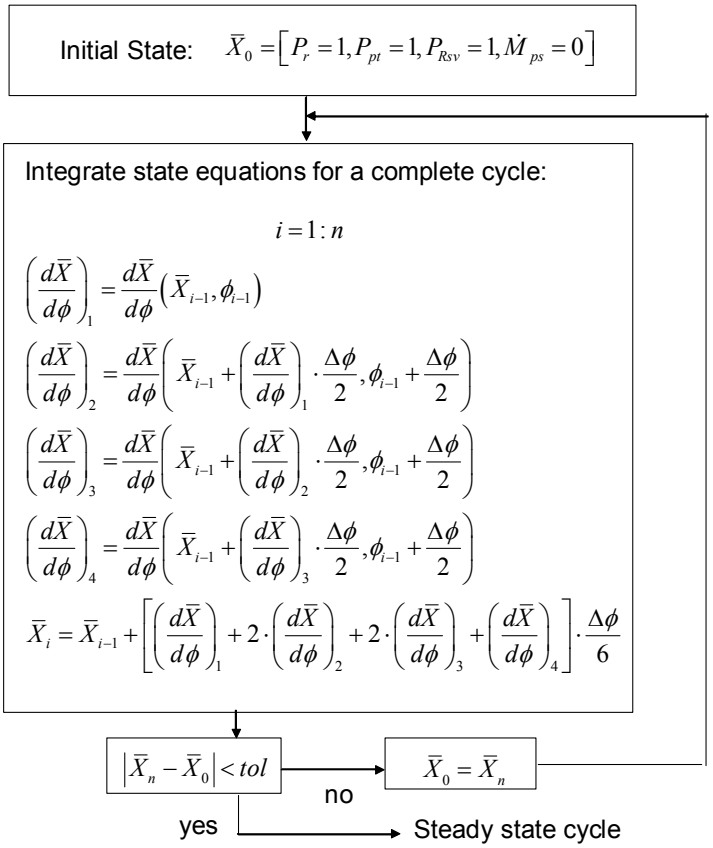

Figure 2.7. Integration of state equations to steady state cycle

The average *P-V* power delivered to the compression space ($\dot{w}_C$) over the cycle is equal to:

$$\dot{w}_C = -f \int_{V_C(t=0)}^{V_C(t=\tau)} p_r \, dV_C \tag{2.32}$$

The instantaneous volume of the expansion and compression spaces within the pulse-tube ($V_{pt,c}$ and $V_{pt,h}$) are defined by:

$$V_{pt,c}(t) = \frac{Rg\, T_c}{p_{pt}} \int_0^t \dot{m}_{r,c} \, dt \tag{2.33}$$

$$V_{pt,h}(t) = -\frac{Rg\,T_{rej}}{p_{pt}} \int_0^t \dot{m}_{ps}\,dt \tag{2.34}$$

The average rate of work transfer from the pulse-tube expansion and to the pulse-tube compression spaces ($\dot{w}_{pt,c}$ and $\dot{w}_{pt,h}$) are therefore given by:

$$\dot{w}_{pt,c} = f \int_{V_{pt,c}(0)}^{V_{pt,c}(\tau)} p_{pt}\,dV_{pt,c} \tag{2.35}$$

$$\dot{w}_{pt,h} = -f \int_{V_{pt,h}(0)}^{V_{pt,h}(\tau)} p_{pt}\,dV_{pt,h} \tag{2.36}$$

Because the regenerator is assumed to be perfect (for the first order model only), the refrigeration load and hot heat exchanger load are equal to these work transfer rates ($\dot{q}_{pt,c} = \dot{w}_{pt,c}$ and $\dot{q}_{pt,h} = \dot{w}_{pt,h}$).

2.3.2 Second Order Model

The first order model is capable of predicting the performance of the pulse-tube in the absence of any thermal losses, although it does capture the fluid loss related to pressure drop in the regenerator. The thermal losses must be post-calculated and applied to the first order model results. These thermal losses include the shuttle heat transfer loss, conduction losses, regenerator losses, losses related to the non-isothermal expansion and compression of the gas in the pulse-tube and compression space, and losses related to mixing and jetting within the pulse-tube. This section describes how these losses are computed in order to obtain an accurate prediction of the refrigeration capacity of the system.

The results of the first order allow the computer model REGEN 3.2 to be applied to the regenerator in order to obtain a more realistic estimate of its performance, as previously described in the context of the optimization procedure. The pressure loss predicted by REGEN 3.2 is also used to determine the resistance of the regenerator, required by the first order model.

The shuttle heat transfer loss within a pulse-tube is computed using an approximate technique described by Diab (2003). The nominal motion of a fluid particle contained in the pulse-tube (Δx_{pt}) is obtained using the results of the 1st order model:

$$\Delta x_{pt} = \frac{4}{\pi D_{pt}^2}\left[max\left(V_{pt,c}\right) - min\left(V_{pt,c}\right)\right] \tag{2.37}$$

where D_{pt} is the pulse-tube diameter. The change in the temperature of the wall seen by the gas particle during this motion ($\Delta T_{wall,pt}$) is approximately:

$$\Delta T_{wall,pt} = \frac{\left(T_{rej} - T_c\right)\Delta x_{pt}}{L_{pt}} \tag{2.38}$$

where L_{pt} is the pulse-tube length. The characteristic velocity of the gas particle ($u_{char,pt}$) is calculated according to:

$$u_{char,pt} = 2\, f\, \Delta x_{pt} \tag{2.39}$$

The appropriate Reynolds number (Re_{pt}) is therefore:

$$Re_{pt} = \frac{\overline{\rho}_{pt}\, u_{char,pt} \Delta x_{pt}}{\overline{\mu}_{pt}} \tag{2.40}$$

where $\bar{\mu}_{pt}$ and $\bar{\rho}_{pt}$ are the average viscosity and density of the gas in the pulse-tube. Assuming that the pulse-tube is designed such that the Reynolds number is less than the critical Reynolds number related to transition to turbulent flow, the Nusselt number (Nu_{pt}) can be computed approximately according to:

$$Nu_{pt} = 0.664\, Re_{pt}^{1/2}\, Pr^{1/3} \tag{2.41}$$

where Pr is the Prandtl number of the gas in the pulse-tube. The heat transfer coefficient between the wall and the gas (htc_{pt}) is computed according to:

$$htc_{pt} = \frac{Nu_{pt}\,\bar{k}_{pt}}{D_{pt}} \tag{2.42}$$

where $\bar{k}_{pt}$ is the average thermal conductivity of the gas in the pulse-tube. The heat transfer rate due to shuttle heat loss ($\dot{q}_{shuttle}$) can be approximately calculated by:

$$\dot{q}_{shuttle} = \frac{htc_{pt}\,\pi\, D_{pt}\,\Delta x_{pt}\,\Delta T_{wall,pt}}{8} \tag{2.43}$$

The conduction heat loss through the regenerator and pulse-tube tube walls ($\dot{q}_{cond,tube,r}$ and $\dot{q}_{cond,tube,pt}$) are calculated using the integrated average thermal conductivity of the tube materials and the geometry of these components.

The first order model assumes isothermal compression and expansion processes. Within the actual pulse-tube, the gas is compressed or expanded nearly adiabatically, resulting in a temperature change, and then this hot/cold is pushed through the aftercooler/cold heat exchanger. This results in an entropy generation as heat is transferred from the constant temperature metal to the gas during this process. These losses are significant and must be accounted for. An approximate technique is used here in place of the more rigorous but

computationally intensive option of tracking this adiabatic process throughout the cycle, as was described by Diab (2003).

The mass of gas that enters the compression space (M_C) and the pulse-tube expansion space ($M_{pt,c}$) during a cycle are computed according to:

$$M_C = \frac{ffs\, V_{C,sw}\, p_{ch}}{Rg\, T_{rej}} \tag{2.44}$$

$$M_{pt,c} = \frac{\left[max\left(V_{pt,c}\right) - min\left(V_{pt,c}\right)\right] p_{ch}}{Rg\, T_c} \tag{2.45}$$

The temperature change due to the expansion and compression of the gas in these spaces (ΔT_C and $\Delta T_{pt,c}$) can be approximated by:

$$\Delta T_C = \frac{\dot{w}_C}{f\, c_P\, M_C} \tag{2.46}$$

$$\Delta T_{pt,c} = \frac{\dot{q}_{pt,c}}{f\, c_P\, M_{pt,c}} \tag{2.47}$$

The entropy generated by the passage of the gas through the aftercooler ($\dot{S}_{gen,C,ad}$) and the cold heat exchanger ($\dot{S}_{gen,ptc,ad}$) can be approximated by:

$$\dot{S}_{gen,C,ad} = \frac{\dot{w}_C}{T_{rej}} - f\, M_C\, c_P \ln\left(\frac{T_{rej} + \Delta T_C}{T_{rej}}\right) \tag{2.48}$$

$$\dot{S}_{gen,pt,ad} = f\, M_{pt,c}\, c_P \ln\left(\frac{T_c}{T_c + \Delta T_{pt,c}}\right) - \frac{\dot{q}_{pt,c}}{T_c} \tag{2.49}$$

The resulting power penalty and loss of refrigeration ($\dot{w}_{ad,C}$ and $\dot{q}_{loss,ad}$) are estimated according to:

$$\dot{w}_{ad,C} = T_{rej}\,\dot{S}_{gen,C,ad} \tag{2.50}$$

$$\dot{q}_{loss,ad} = T_c\,\dot{S}_{gen,pt,ad} \tag{2.51}$$

Finally, a loss is assumed for the mixing and jetting processes that occur as cold gas enters the pulse-tube from the cold heat exchanger ($\dot{q}_{loss,mix}$). This loss is assumed to be some fraction of the acoustic power entering the pulse-tube and is computed according to:

$$\dot{q}_{loss,mix} = \left(1-\eta_{pt}\right)\dot{q}_{pt,c} \tag{2.52}$$

where η_{pt} is a pulse-tube efficiency, taken to be 90%. The compressor electrical input power ($\dot{w}_{C,elec}$) is predicted assuming a compressor efficiency (η_C) of 85% according to:

$$\dot{w}_{C,elec} = \frac{1}{\eta_C}\left(\dot{w}_C + \dot{w}_{ad,C}\right) \tag{2.53}$$

The net refrigeration load ($\dot{q}_{load}$) is computed by debiting the ideal load predicted by the first order model by the various losses computed above. The second order model can be used to predict the performance of a specific pulse-tube design subject to given operating conditions.

2.4 Predicted Results

The optimization procedure together with the detailed model was used to compile the optimal dimensions for the pulse-tube, given constraints associated with the characteristics of commercially available linear compressors. Table 2.2 presents the key dimensions of the fabricated pulse-tube.

Table 2.2. Thermal design of 300 W pulse-tube

Characteristic	Value
Regenerator diameter	5.14 inch (13.0 cm)
Regenerator length	2.00 inch (5.1 cm)
Regenerator matrix	400 mesh SS
Regenerator wall thickness	0.062 inch (1.575 mm)
Pulse-tube diameter	2.35 inch (6.00 cm)
Pulse-tube length	3.00 inch (7.62 cm)
Pulse-tube wall thickness	0.035 inch (0.81 mm)

The pulse-tube assembly is mounted in a vacuum chamber and integrated with a compressor and aftercooler. The compressor is a linear compressor rated to 10.0 kW of input power manufactured by CFIC. The predicted performance of the experimental system is summarized in Table 2.3.

Table 2.3. Predicted performance of experimental pulse-tube

Characteristic	Value
Acoustic power	**721.4 W**
PV power required by compressor	**3.83 kW**
Average mass flow rate through regenerator	75.7 g/s
Average pressure drop through regenerator	35.7 kPa
Void volume pressurization loss	36.0 W
Regenerator ineffectiveness loss	195 W
Conduction through regenerator matrix	5.9 W
Conduction through regenerator tube	37.1 W
Conduction through pulse-tube tube	5.8 W
Shuttle heat loss	13.8 W
Net refrigeration load	**319.2W**
Net electrical power input	**5.89 kW**

The final dimensions of the regenerator are slightly varied from the original design point described in Section 2.1 due to manufacturing and cost constraints. However, the design changes are small and the performance remains consistent with the desired 300 W at 65 K for an electrical input power of 5.89 kW, as seen in Table 2.3.

Chapter 3. Mechanical Design of High-Capacity Pulse-Tube

3.1 Introduction

The objective of the mechanical design of the 300W, 65K pulse-tube was to develop a practical implementation of the thermodynamic design that was presented in chapter 2. The design must compatible with conventional manufacturing techniques, able to withstand the anticipated pressure loads, and also be modular so that components could be removed and replaced easily. This chapter includes the thermal design of the cold heat exchanger and detailed mechanical design of the regenerator, pulse-tube, cold and hot heat exchangers, and the vacuum can with the pass-thrus required to support testing. The chapter will also discuss the data acquisition setup.

3.2 Mechanical Design of Pulse-tube

Figures 3.1 and 3.2 show exploded and solid model views of the pulse-tube. Design details of each component are contained in the following sections; the part numbers referenced in this chapter correspond to detailed drawings which are contained in Appendix A of the thesis.

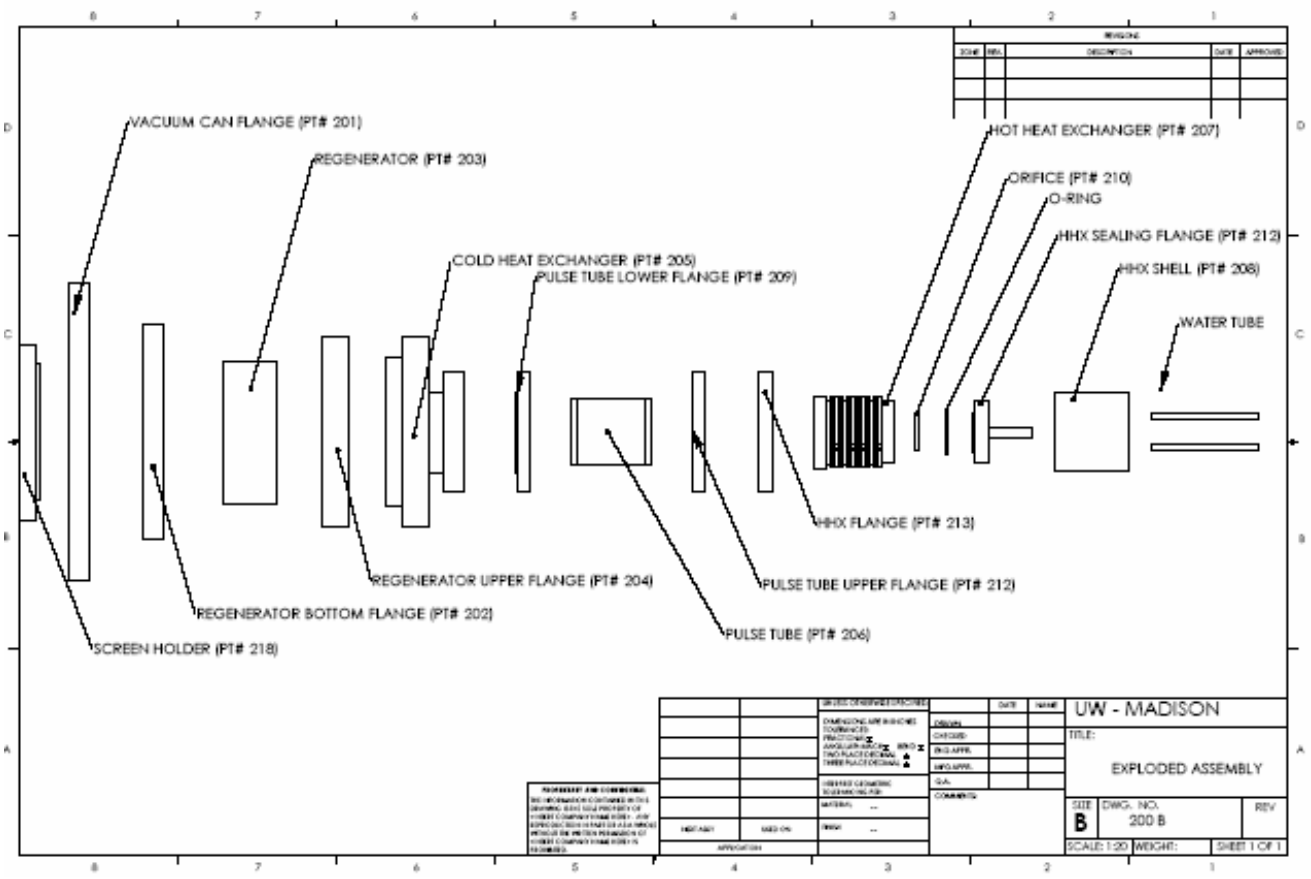

Figure 3.1. Exploded view of the high-capacity pulse-tube.

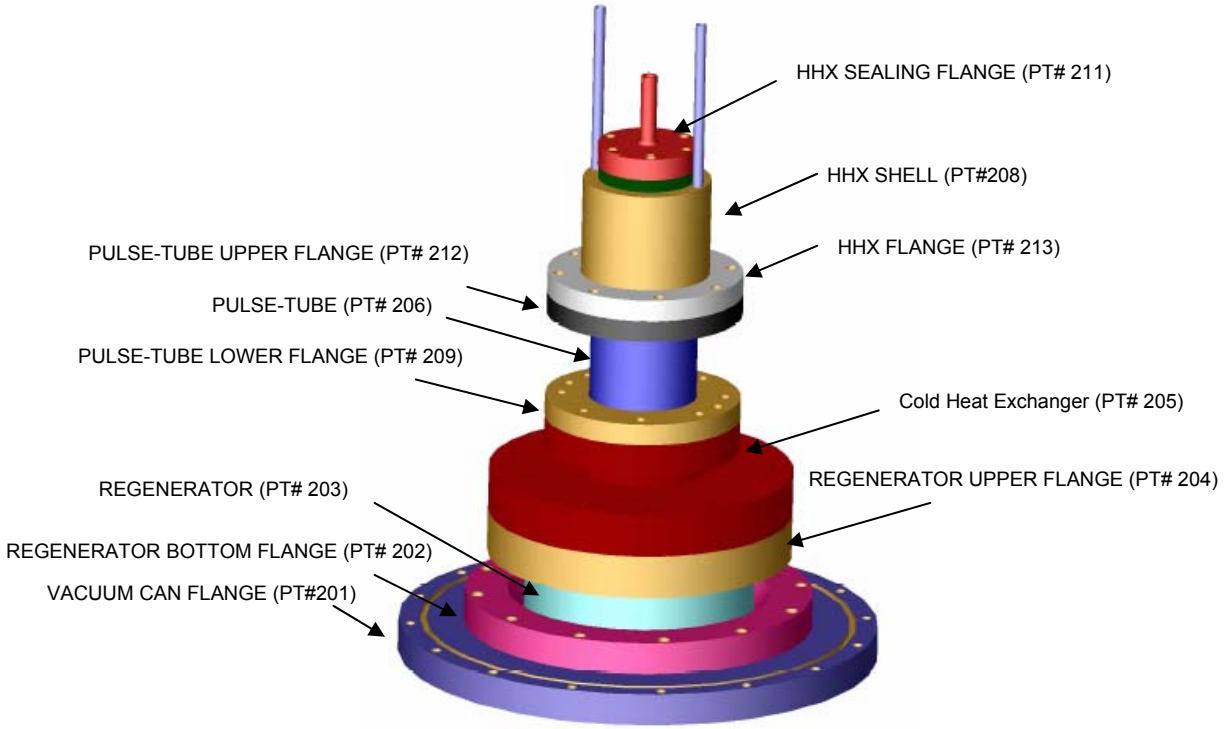

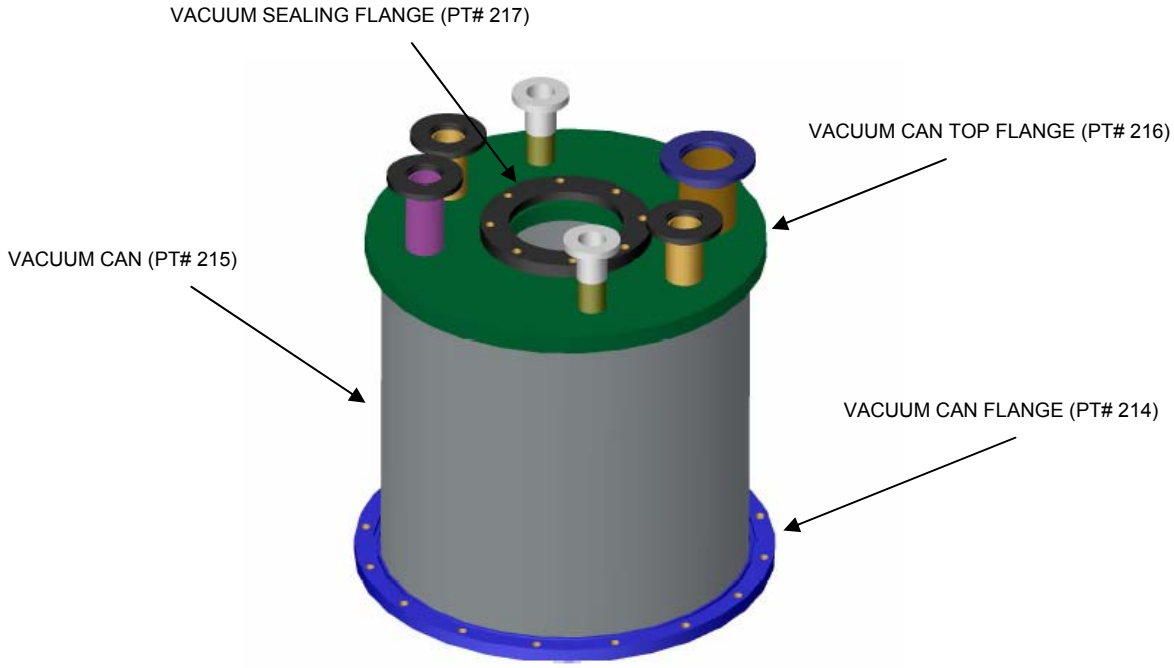

Figure 3.2. Solid model view of both the pulse-tube (top) and the vacuum can (bottom).

3.2.1 Regenerator Design

3.2.1.1 Regenerator Tube – Part # 203

The nominal pulse-tube dimensions were determined based on the system level model presented in the previous chapter. The modeling indicated that the optimal pulse-tube would consist of a regenerator with a nominal diameter of 5.0 inch and length of 2.0 inch coupled to a pulse-tube with a nominal diameter of 2.5 inch and a length of 3.0 inch.

The regenerator consists of four main parts, the regenerator tube, the lower regenerator flange, the upper regenerator flange, and the matrix. The regenerator tube is designed

using 304-stainless steel, due to its thermal low conductivity. The minimum wall thickness of the tube was determined using the ASME Boiler and Pressure Vessel Code (Section VIII, Division I, Paragraph UG27) which suggests the following equation for thin-walled vessels.

$$t = \frac{\left(P_{\max}\, r_i\right)}{\sigma_{allowable} - 0.6\, P_{\max}} \tag{3.54}$$

where t is the wall thickness, P_{max} is the maximum pressure, r_i is the inside radius of the vessel, and $\sigma_{allowable}$ is the allowable stress for the material. In the design of the regenerator and for the rest of the pulse-tube, the maximum design pressure used was 400 psig which is higher than the maximum operating pressure of 370 psig which will be experienced when the pulse-tube is charged to 300 psig. The allowable stress for 304-stainless steel is 16 ksi (Section II-D of the Pressure Vessel Code) and therefore Eq. (3.1) indicates a minimum wall thickness of 0.062 inch.

Elongation and radial deflection of the regenerator tube was also considered. The regenerator is designed to be filled with a 400 mesh stainless steel screen matrix. Since the screens will not deform under pressure in the same manner as the tube, care must be taken to ensure a large gap is not generated between the edges of the screens and the wall of the regenerator tube. Also, axial elongation of the tube must not allow the screen packing to loosen and therefore allow the screens to oscillate during pulse-tube operation. The maximum radial and longitudinal deflections were estimated using the following stress-strain relations as suggested by Beer and Johnston (1992):

Radial Deflection:

$$\varepsilon_{r,rad} = \frac{\delta_{rad}}{2r_i} \tag{3.55}$$

$$\sigma_{r,rad} = E\ \varepsilon_{r,rad} \tag{3.56}$$

$$\sigma_{r,rad} = P_{max}\left(\frac{r_i}{t}\right) \tag{3.57}$$

Longitudinal Deflection:

$$\varepsilon_{r,long} = \frac{\delta_{long}}{L_r} \tag{3.58}$$

$$\sigma_{r,long} = E\ \varepsilon_{r,long} \tag{3.59}$$

$$\sigma_{r,long} = P_{max}\left(\frac{r_i}{2t}\right) \tag{3.60}$$

where $\varepsilon_{r,rad}$ and $\varepsilon_{r,long}$ is the strain in the radial and longitudinal directions, respectively; δ_{rad} and δ_{long} is the deflection in the radial and longitudinal directions; L_r is the length of the regenerator; E is the modulus of elasticity, $\sigma_{r,rad}$ is the associated radial stress, and $\sigma_{regen,long}$ is the longitudinal stress. The length of the regenerator is 2 inches resulting in a maximum longitudinal deflection, δ_{long}, of 0.0005 inch. The modulus of elasticity for 304-stainless steel was estimated at 29 x10^6 psi by Beer and Johnston (1992). The radial stress is more critical to the performance; using equations (3.55) through (3.57), with the final machined diameter of the regenerator being 5.136 inch the resulting radial deflection was found to be 0.0026 inch. This calculation of radial deflection is conservative because the ends of the regenerator will be fixed by welding to the upper and lower flanges which will stiffen the tube and result in a smaller radial deflection.

The longitudinal deflection is approximately equal to ¼ the thickness of a single screen. To prevent any potential oscillation of the regenerator matrix, a flange (PT # 218) was designed to bolt to the regenerator bottom flange (PT# 202) for the purpose of pre-stressing the matrix, the lip on the screen holder (PT# 218) is designed to do this. Figure 3.3 shows an exploded solid model of the flange assembly. While Figure 3.4 shows a cross-sectional view of the solid model.

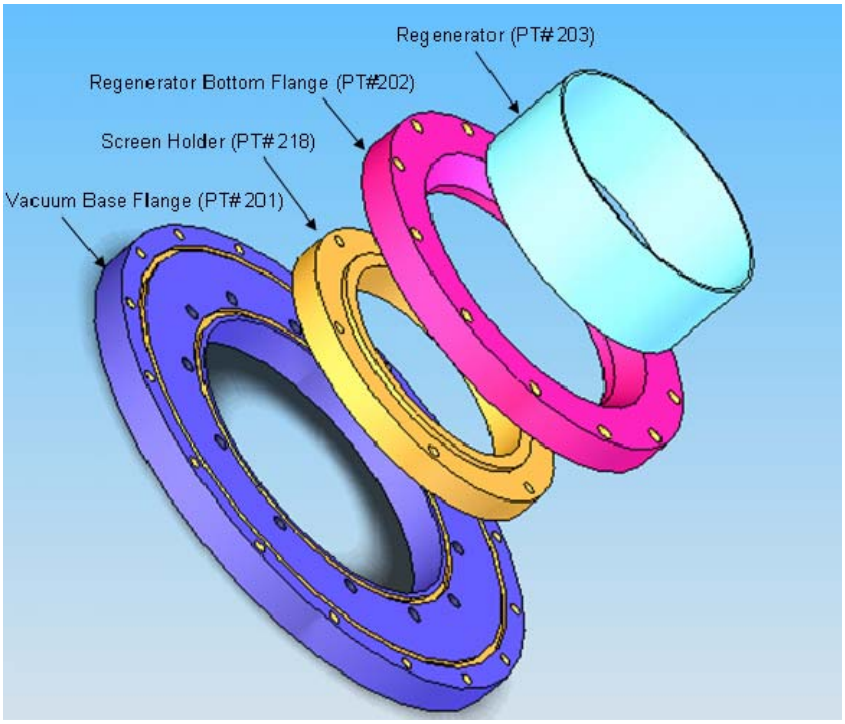

Figure 3.3. The screen holder (PT# 218) is designed to minimize the room for screens to flex inside the regenerator. The screen holder is bolted to the regenerator bottom flange (PT# 202) and tucks inside the vacuum base flange (PT# 201).

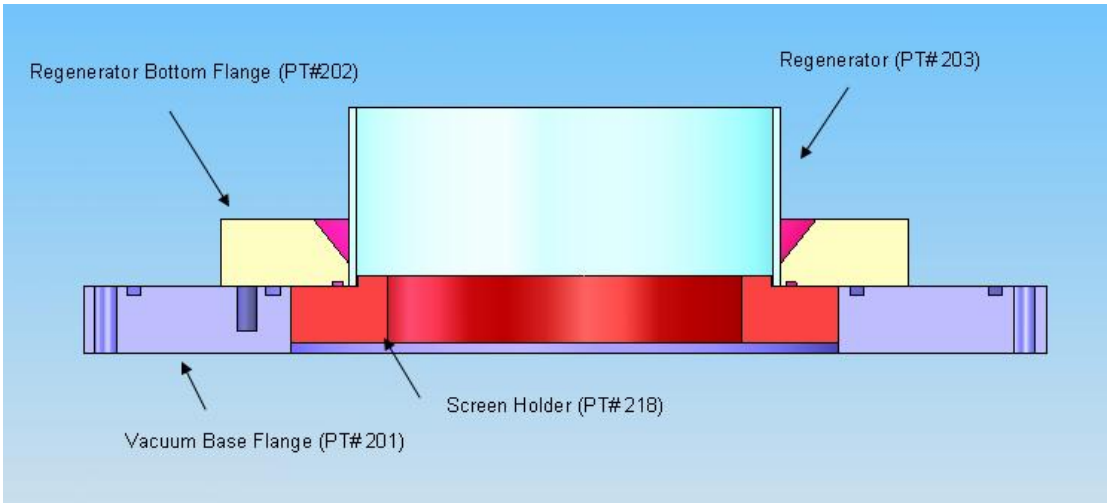

Figure 3.4. Cross-sectional view of the regenerator assembly, with the screen holder (PT# 218) pressing into the regenerator to hold the screens tight and in place during operation.

3.2.1.2 Regenerator Bottom Flange – Part # 202

The regenerator bottom flange was designed using the same constraints as the regenerator tube and assuming the same maximum pressure. The following equations, from the ASME Pressure Vessel Code, Section VIII, Division I, Appendix 2, were used to determine the flange thickness required to withstand the pressure force. The original concept for the design of the flange has the outside diameter of the flange, *A*, being 8 inch with 12 x 5/16-18 UNC bolts on a 7.5 inch bolt circle. The inside diameter of the flange is taken to be the diameter of the machined regenerator tube before pressurization expansion, which is 5.136 inch; the o-ring diameter was taken to be nominally 6.0 inch. All important geometric flange dimensions are shown on Figure 3.5.

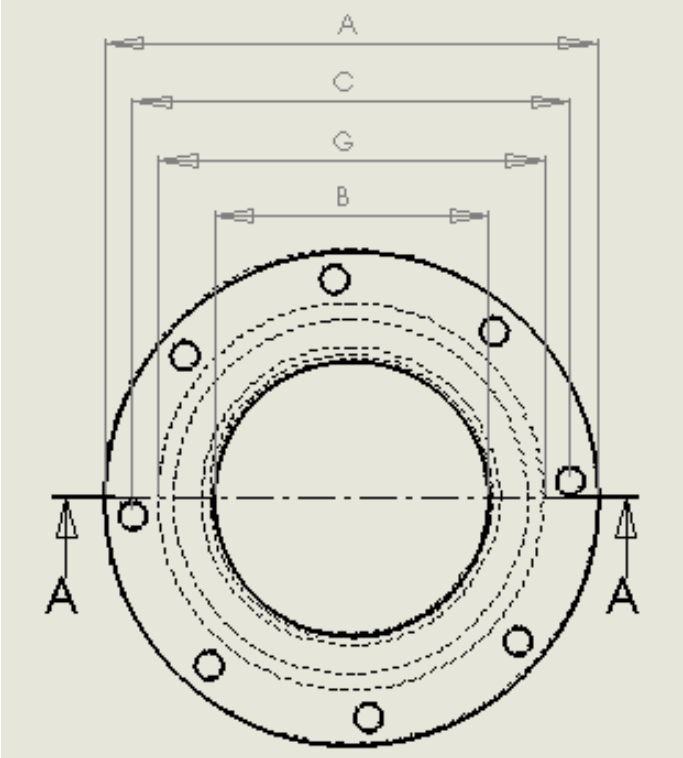

Figure 3.5. Dimensions of significant geometric items, these include (A) outside flange diameter, (B) inside flange diameter, (G) gasket diameter, and (C) bolt circle.

With these dimensions set, consideration is given first to the bolt loading according to (note that variables used in the following equations correspond to those used in the ASME Boiler and Pressure Vessel Code (PVC)):

$$H = \frac{\pi}{4} G^2 P_{\max} \tag{3.61}$$

$$H_P = 2\ b\ \pi\ G\ m\ P_{\max} \tag{3.62}$$

$$W_{m1} = H + H_P \tag{3.63}$$

Here, H is the total hydrostatic end force and G is the gasket diameter. H_p is the total joint contact surface compression load and m is a gasket factor. A gasket factor is a

number that characterizes the strength needed to compress and seal an o-ring; gasket factors vary on material. In this case H_p is zero because the gasket factor for a self energizing o-ring is zero, which is dictated by the ASME Pressure Vessel Code (Section VIII, Division I, Appendix 2, Table 2-5.1). Throughout this design only two types of gaskets are used, indium and butyl rubber. The gasket factor, m, for both types of gaskets are zero; thus H_p is always zero and the bolt load (W_{m1}) is always equal to the hydrostatic end force:

$$W_{m1} = A_b \sigma_b \tag{3.64}$$

The area, A_b, is the bolt cross-sectional area multiplied by the number of bolts used. The cross-sectional area of a standard bolt is obtained from the Machinery's Handbook. The equation then yields the total bolt stress, σ_b, which is equal to the stress per bolt. The total bolt stress dictates the grade of bolt that must be used, in this case the bolt stress was found to be 24.5 ksi. Grade 8 bolts, with a yield strength of 130 ksi according to Juvinall and Marshek (2000), were used because of availability and are more than adequate to provide the needed strength.

The flange loads for the worst-case operating condition are evaluated as follows:

$$H_D = \frac{\pi}{4} B^2 P_{\max} \tag{3.65}$$

$$H_T = H - H_D \tag{3.66}$$

H_D refers to the hydrostatic end force on the area inside the flange, and B is the inside diameter of the flange. The load, H_T, is the difference between total hydrostatic end force and the hydrostatic force on the inside area of the flange. The gasket load, H_G, is just

equal to the load H_P which has already been noted is zero because of the self-energizing o-ring.

The lever arms associated with each load about the center of the flange are then calculated using the following relationships taken from Table 2-6 of Section VIII, Division I, Appendix 2, Table 2-5.1 in the ASME Pressure Vessel Code:

$$h_D = \frac{1}{2}(C - B) \tag{3.67}$$

$$h_G = \frac{1}{2}(C - G) \tag{3.68}$$

$$h_T = \frac{1}{2}(h_D + h_G) \tag{3.69}$$

where C is the bolt circle diameter. Each of the individual lever arms are denoted as follows: h_D is the distance from the bolt circle to the circle on which H_D acts, h_G is the radial distance from the gasket to the bolt circle, and h_T is the radial distance from the bolt circle to the circle on which H_T acts. A summary of these moment arms and pertinent forces can be viewed on the Figure 3.6.

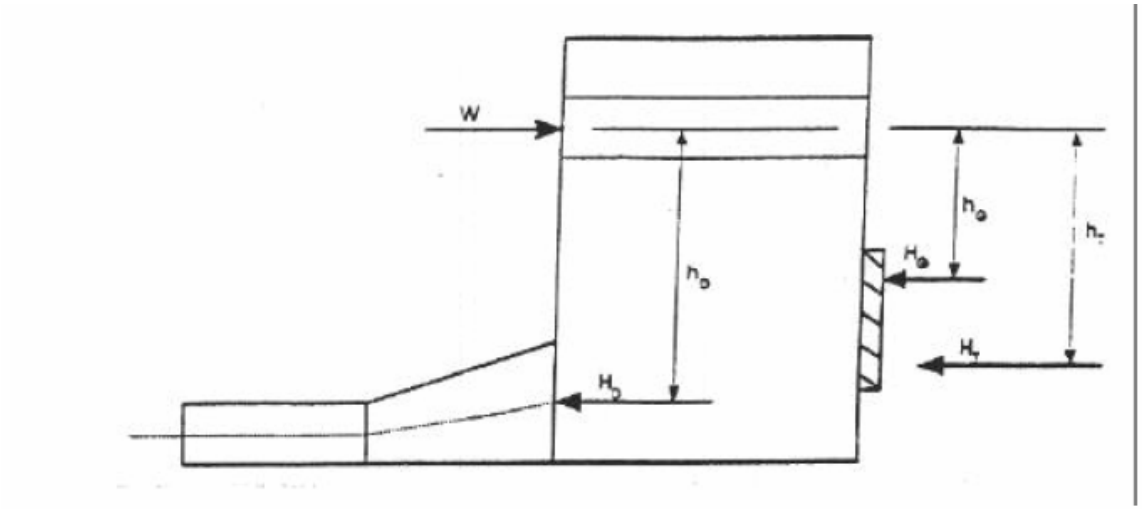

Figure 3.6. Summary of moment arms and forces applied to a bolted, gasket-sealed flange.

These lever arms are then multiplied by the corresponding loads to obtain the following moments:

$$M_D = H_D h_D \tag{3.70}$$

$$M_G = H_G h_G \tag{3.71}$$

$$M_T = H_T h_T \tag{3.72}$$

$$M_O = M_D + M_G + M_T \tag{3.73}$$

The resulting overall moment, M_o, is then used to determine the flange thickness in the following equation:

$$t_{flange} = \sqrt{\frac{M_O Y}{\sigma_{allowable} B}} \tag{3.74}$$

The Y value in equation (3.74) refers to a shape factor dictated by the ASME code in appendix 2. The following relationship and curve fit is used to determine the Y value:

$$K = \frac{A}{B} \tag{3.75}$$

$$Y = \left[0.66845 + 5.7169 \left(\frac{K^2 \log(K)}{K^2 - 1} \right) \right] \frac{1}{K - 1} \tag{3.76}$$

The calculated flange thickness is 0.81 inch when a maximum pressure of 400 psig is considered. After careful consideration of the safety factor, price, and availability of 304-stainless steel, a thickness of 0.75 inch was specified. This corresponds to a safety factor of 1.44 as opposed to 1.5, and is deemed reasonable.

The physical design of the flange included one addition constraint; the contact length between the regenerator and the lower regenerator flange must be limited. Since the regenerator is operating in a vacuum, radiation is the only mode of heat transfer. The regenerator bottom flange will be at room temperature, because of the contact with the vacuum can flange (PT# 201), while the regenerator wall will reach cryogenic temperatures. The following calculation was used to determine the significance of the heat leak between the flange and the regenerator:

$$\dot{Q} = \varepsilon A_s \sigma \left(T_s^4 - T_{surr}^4 \right) \tag{3.77}$$

Figure 3.7 represents the situation:

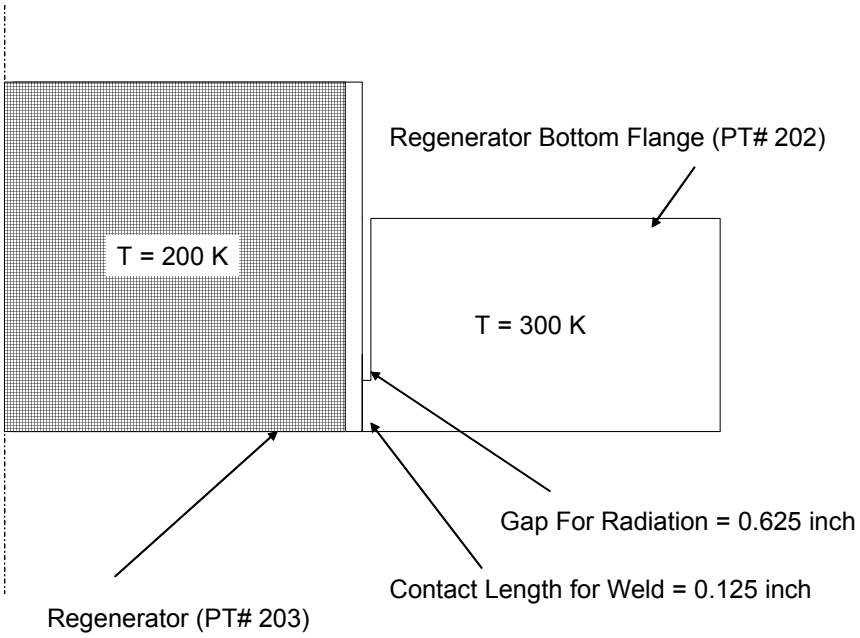

Figure 3.7. Schematic of the radiative heat loss between the regenerator and the regenerator bottom flange during operation.

The worst case scenario was considered by using an emissivity, ε, of unity. The surface area, A_s, is the surface area of a cylinder with a height of 0.625 inch with the same outside diameter of the regenerator, and σ refers to the Stefan-Boltzmann constant. The surrounding temperature, T_{surr}, was taken to be 300 K, while the average surface temperature of the regenerator, T_s, was taken at 200 K for the length of the gap which is a total of 0.625 inch. T_s was over-estimated to show the greatest fathomable amount of radiative losses. The 0.125 inch contact length is considered negligible on conductive losses since the lower part of the regenerator is theorectically very close to room temperature during steady-state operation. The heat transfer $\dot{Q}$ is 2.4 W, under these conditions which is negligible relative to the refrigeration load. To minimize this factor

even further a chamfer was used to provide conductive and radiative separation from the regenerator.

The following figure shows a CAD model of the regenerator bottom flange with the chamfer.

Figure 3.8. The regenerator bottom flange with chamfer.

3.2.1.3 Regenerator Upper Flange – Part # 204

Design of the upper regenerator flange follows the same principles as the lower regenerator flange. The same equations and program are used to evaluate the flange thickness. While calculations indicate this flange can be thinner than the bottom flange ($\frac{5}{8}$ inch); however, other considerations dictated that the final thickness of this flange be 1.0 inch. The 1.0 inch dimension allows the cold heat exchanger to be inset into the upper regenerator flange. This allows more room for instrumentation on the regenerator since the weld is made at the bottom of the flange instead of the top of the flange. This can be viewed in Figure 3.9.

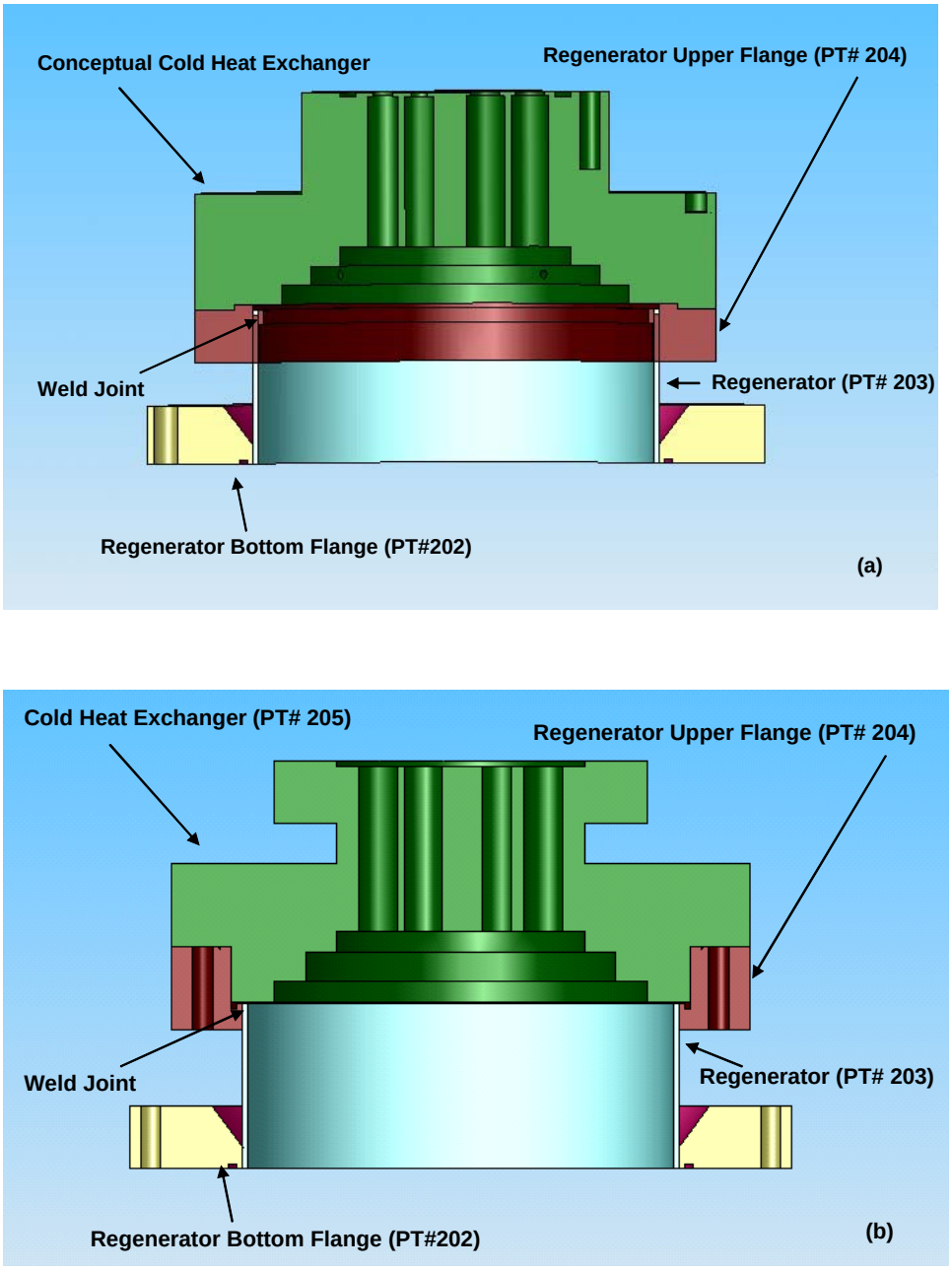

Figure 3.9. The regenerator upper flange (PT# 204) with the regenerator welded to the top lip (a) showing the decreased length of exposed regenerator length compared to the weld toward the bottom of the flange (b).

The indium seal that is used on this flange tends to bond with the mating surfaces and can therefore be difficult to remove. Therefore, jacking screws were inserted to facilitate the separation of the seal with minimum damage to the copper of the flange. Figure 3.10 is a CAD model of the upper regenerator flange.

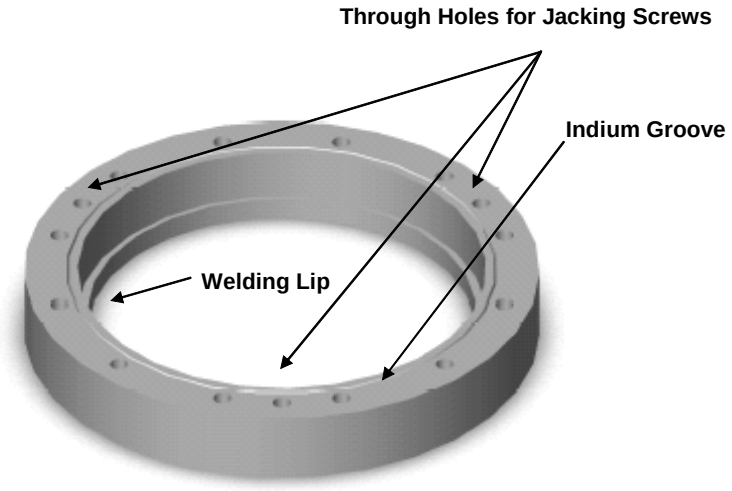

Figure 3.10. The regenerator upper flange (PT# 204) showing the locations of the main features. The twelve hole bolt circle are all threaded, blind holes used as a backing for the bolt connection of the cold heat exchanger (PT# 205)

3.2.1.4 Regenerator Matrix

The regenerator screen matrix was specified to be 400-mesh stainless steel based on the thermodynamic design. One of the main concerns in all large pulse-tubes is the possibility that helium gas will blow by the regenerator matrix along its edges and result in a large loss. To reduce the possibility of this bypass loss, the screens for the matrix were stacked, sintered, and cut to the appropriate diameter using an EDM process. This process gives the screen stack a much tighter roundness tolerance than conventional

stacking. The drawback of the sintering process is that it increases the conductive losses through the regenerator. The advantage is increased reliability because the mechanical motion of the screens is limited.

Flow maldistribution within the stack is also a possible source of loss. The resistance of the screens in the radial direction is much larger than in the axial direction; as a result, it is not easy for the flow to redistribute itself in the presence of any geometrical or flow non-uniformities. In order to guard against this potential problem, a 100 mesh stainless steel screen is inserted between every fifty 400 mesh stainless steel screens. The 100 mesh stainless screen acts much like a gap; the resistance of the screen is small in both the axial and radial directions and therefore flow redistribution is possible. The resulting mixing action will hopefully lead to a more uniform temperature distribution.

3.2.2 Cold Heat Exchanger Design

3.2.2.1 Conventional Design for Small Pulse-tubes

Conventional cold heat exchangers for small pulse-tubes (intended to lift heat loads that are on the order of 10 W to 20 W in the 60 K to 80 K range) typically consist of a copper shell that is filled with copper screens. Heat is applied along the outer diameter of the shell and is conducted into the fluid efficiently due to the high specific surface area of the screens. Such heat exchangers are easy to fabricate and generally function quite well. A heat exchanger using this design was employed in a previous generation of a large pulse-

tube manufactured by Atlas Scientific and tested at the UW-Madison; a solid model of this design is shown in Figure 3.11.

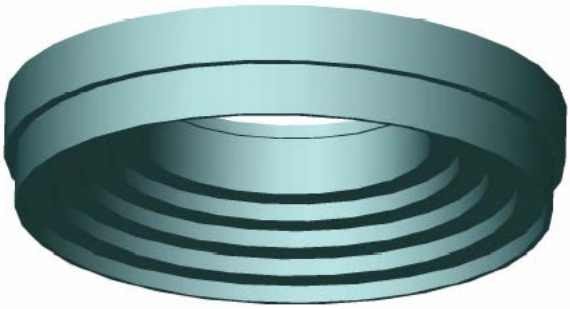

Figure 3.11. The original design of the cold heat exchanger has flow-straightening steps.

The heat exchanger is machined from copper and has four internal steps that serve to direct the flow from the regenerator to the pulse-tube; note that in this previous generation pulse-tube, the regenerator had a diameter of 2.5 inch diameter while the pulse-tube had a diameter of 1.5 inch. Each step was filled with copper screens in order to reduce the dead volume, serve as flow straighteners, and also provide a high surface area for heat transfer.

The initial approach for the design of the cold heat exchanger for this 300 W pulse-tube was to scale up the design illustrated in Fig. 3.6. In order to assess this design in the context of the 300 W pulse-tube, a thermal model of the screen-filled heat exchanger configuration was developed. The model consists of two, de-coupled sub-models. The first sub-model calculates a temperature drop associated with the thermal resistance due to the conduction of heat radially through the copper screens, ΔT_{cond}. The second sub-model calculates a temperature drop associated with the convective heat transfer from the

surface of the screen mesh to the cold gas, ΔT_{conv}. Comparison of these two temperature drops then gives an indication of which process dominates; the addition of these temperature drops provides an indication of the performance of the heat exchanger.

In order to simplify the calculation of the temperature drop due to conduction, a central area of constant temperature is assumed. The radial location of this uniform temperature surface is arbitrarily taken to be at half the radius of the cold heat exchanger. Figure 3.12 shows the simplified geometry, with the blue area representing the assumed isothermal core.

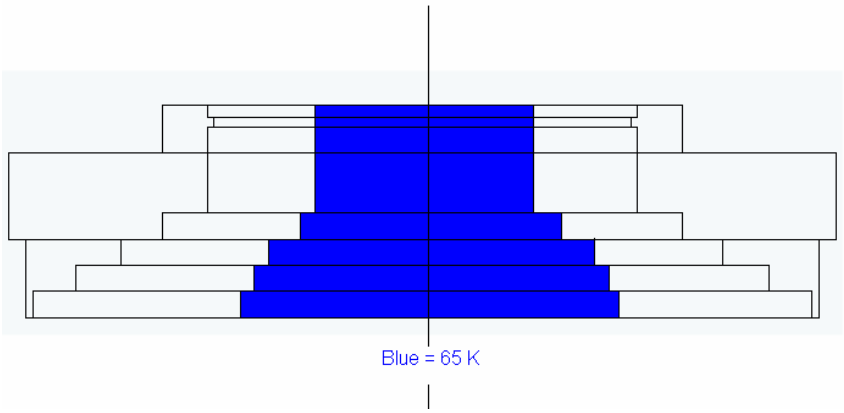

Figure 3.12. The blue region of the cold heat exchanger represents a uniform temperature zone.

The thermal resistance of the screen mesh is given by

$$R_{cond} = \frac{\ln\left(\frac{1}{r_{fraction}}\right)}{2\pi k(height) f_s} \tag{3.78}$$

where $r_{fraction}$ is the ratio of the radius of uniform temperature surface to the radius of the heat exchanger. The thermal resistance may also be expressed as:

$$R_{cond} = \frac{\Delta T_{cond}}{\dot{Q}_{cooling}} \tag{3.79}$$

where f_s is the fraction of heat exchanger wall that is in contact with the perimeter of the copper screens which functions as a porosity for the screens, *height* is the length of the screens, k is the thermal conductivity, $\dot{Q}_{cooling}$ is the cooling load. The following relation shows how f_s is obtained:

$$f_s = \frac{A_{solid}}{A_{total}} \tag{3.80}$$

$$A_{solid} = \frac{\pi}{4} D_{wire}^2 \tag{3.81}$$

$$A_{total} = 2\left(pitch\right) D_{wire} \tag{3.82}$$

where A_{solid} is the cross-sectional area of the copper, A_{total} is the total cross-sectional area, D_{wire} is the diameter of the copper wire, and *pitch* is the distance between the centers of two adjacent wires. Since the cold helium gas is expected to be at 65 K, the resulting thermal conductivity, k, of the copper will be approximately 500 W/m-K according to Timmerhaus and Flynn (1989). The height of the screen bed is initially taken to be 1.0 inch, which allows for ten screens in each of the four flow-straightening steps and 60 screens in the top heat-exchange region. Given the design requirement that the refrigeration load ($\dot{Q}_{cooling}$) is 300 W, ΔT_{cond} was found to be 16.4 K.

To calculate the convective temperature drop, the Reynolds number (Re) and physical velocity (V_p) are calculated using the following formulas:

$$\mathrm{Re} = \frac{\rho V_p D_{hyd}}{\mu} \tag{3.83}$$

$$V_p = \frac{\dot{m}_{rms}}{\rho A_{screen}} \tag{3.84}$$

where A_{screen} is the area of the screen, and $\dot{m}_{rms}$ is the root mean square value of the mass flow rate, since the compressor operates in an AC fashion. The properties of helium, density (ρ) and viscosity (μ), are evaluated using the computer program EES at a pressure of 335 psia and a temperature of 65 K. The hydraulic diameter, D_{hyd}, is evaluated as follows:

$$D_{hyd} = pitch - D_{wire} \tag{3.85}$$

The resulting Reynolds numbers indicated that the flow would be laminar so that the heat transfer coefficient (*htc*) correlation from Kays and London (1998) could be used.

$$htc = 0.47\,\dot{m}_{rms}\,C_p\left(\frac{\mathrm{Re}^{-0.388}}{\mathrm{Pr}^{0.67}\,A_{screen}}\right) \tag{3.86}$$

where C_p is the specific heat and Pr is the Prandtl number. The heat transfer coefficient was then multiplied by the surface area of the screen. This process was repeated for each of the levels of the cold heat exchanger.

Finally, the following relations were used to find ΔT_{conv}

$$R_{conv} = \frac{1}{htcA_s} \tag{3.87}$$

$$R_{conv} = \frac{\Delta T_{conv}}{\dot{Q}_{cooling}} \tag{3.88}$$

where A_s is the surface area of the screens. The value of ΔT_{conv} was found to be 0.034 K for the same conditions under which the conductive temperature drop is calculated. This result indicates that the resistance associated with conduction through the screens dominates the performance of the cold heat exchanger. The conduction resistance through the screens is directly related to the diameter of the screens and the analysis above indicates that screens with a diameter that is greater than approximately 0.5 inch will result in an unacceptably large temperature gradient.

In addition to the thermal performance of the cold heat exchanger, the pressure drop associated with flow through the screens is also of concern as it reduces the pressure amplitude experienced by the pulse-tube and therefore the acoustic power delivered to the pulse-tube. The friction factor, *f*, can be determined for laminar flow using equation (3.89) from Miyabe (1982).

$$f = \frac{33.6}{\mathrm{Re}} + .337 \tag{3.89}$$

The pressure drop for each step in the cold heat exchanger is computed using the associated friction factor according to:

$$\Delta P = 2 f \rho (height) \left(\frac{V_p^{\,2}}{D_{hyd}} \right) \tag{3.90}$$

3.2.2.2 New Cold Heat Exchanger Design

The analysis carried out in the previous section suggested that a conventional cold heat exchanger design is not appropriate for this very large pulse-tube. Therefore, a new

design is considered, shown in Figure 3.13. The entry region of the cold heat exchanger is again equipped with flow straightening steps; however, the heat exchange region has ten 0.50 inch holes that are filled with screens. This design is much more massive than the design considered in the previous section. However, much of the additional mass is related to the inclusion of a bolted flange for purposes of facilitating removal and replacement of this component.

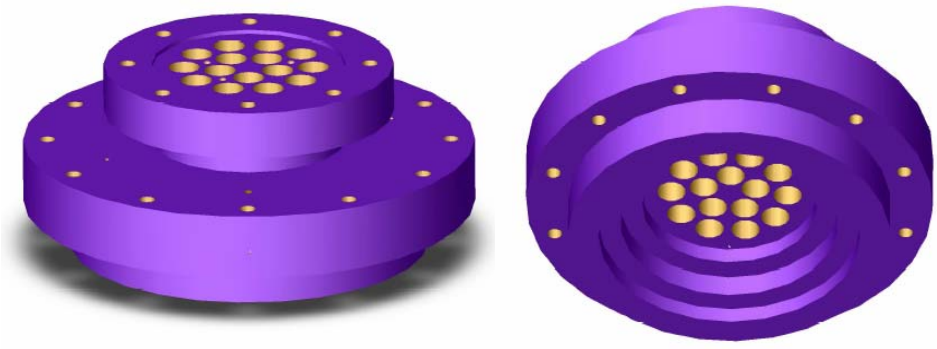

Figure 3.13. Solid model of the cold heat exchange

The conductive heat transfer analysis is more complicated for this design. The inner five holes are assumed to be isothermal for the analysis, as shown in Figure 3.9:

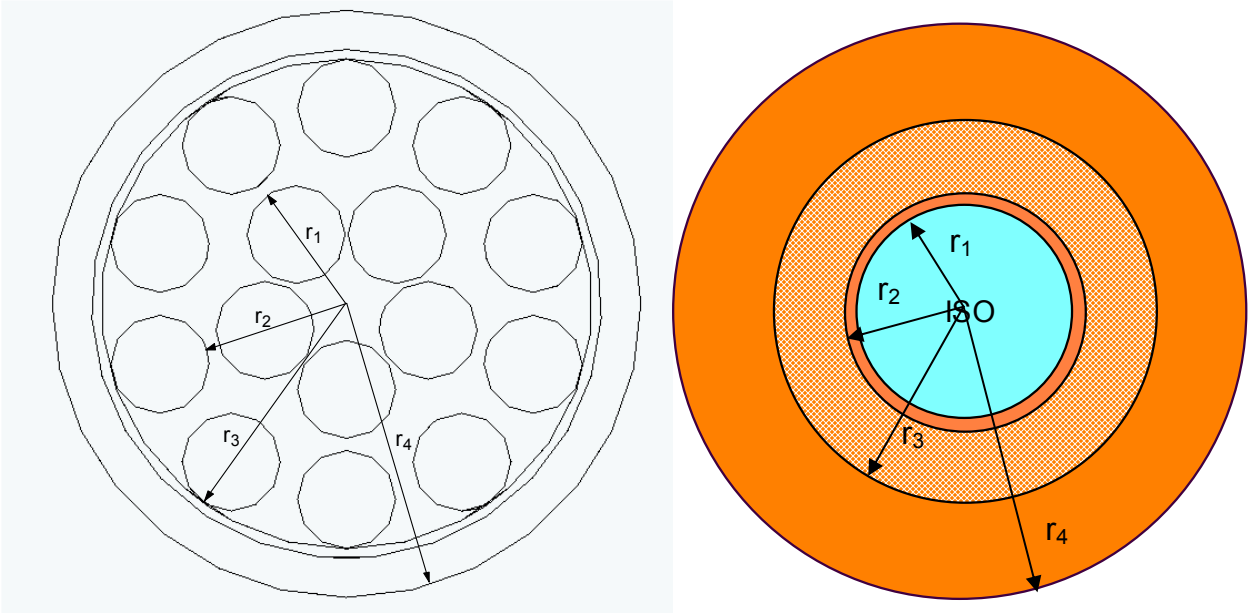

Figure 3.14. The cold heat exchanger indicating the radii that are used for detailed analysis. The isothermal region is represented by the blue on the right-hand figure

The conductive heat transfer problem is solved by setting up a series of thermal resistances. The first resistance ($R_{cond,1}$) is associated with the thin copper ring between the first set of holes, referred to as the isothermal region, and the second ring of holes.

$$R_{cond,1} = \frac{\ln\left(\frac{r_2}{r_1}\right)}{2\pi k\left(height\right)} \tag{3.91}$$

where r_1 refers to the outside radius of the isothermal region which is equal to 0.6875 inch and r_2 is equal to the radius of the inner edge of the ring of ten holes, which is 0.75 inch. The thermal conductivity, k, is again assumed to be 500 W/m-K and *height* refers to the height of the screen stack. The second conduction resistance ($R_{cond,2}$) is related to conduction through the second ring of screens.

$$R_{cond,2,screen} = \frac{\ln\left(\frac{r_3}{r_2}\right)}{2\pi k\left(height\right) f_s} \tag{3.92}$$

where r_3 is the outside radius of the outer holes, which is equal to the pulse-tube radius of 1.25 inch, and the f_s factor is used again to represent porosity of the screens. In parallel with the screen resistance is the resistance of webbing between each of the holes. The thermal resistance used to represent the heat transfer across this web (R_{web}) is

$$R_{cond,2,web} = \frac{\ln\left(\frac{r_3}{r_2}\right)}{k\left[\pi\left(r_2 + r_3\right) - \left(holes_{outer} D_{screen}\right)\right] height} \tag{3.93}$$

where D_{screen} is the diameter of the holes, which is 0.50 inch; $holes_{outer}$ is the ten holes in the outer ring of the circular pattern. Equation (3.93) takes the average circumference of the circle inscribed by r_2 and r_3 to function as the part of the effective area for heat transfer. The space occupied by the holes is accounted for by adding their diameters together and subtracting them from the circle's circumference. This way, the webs are treated as small rectangular strips between adjacent holes. Combining the two parallel components of $R_{cond,2,web}$ and $R_{cond,2,screen}$ the following expression is obtained.

$$R_{cond,2} = \frac{R_{cond,2,screen} R_{cond,2,web}}{R_{cond,2,screen} + R_{cond,2,web}} \tag{3.94}$$

The final conduction resistance ($R_{cond,3}$) represents the remainder of the copper block

$$R_{cond,3} = \frac{\ln\left(\frac{r_4}{r_3}\right)}{2\pi k\left(height\right)} \tag{3.95}$$

where r_4 is the outside radius of the copper which is 1.5 inch. The largest of these resistances is $R_{cond,2}$, the resistance associated with conduction through the second row of screens. Figure 3.15 shows the resistor diagram for this heat transfer analysis.

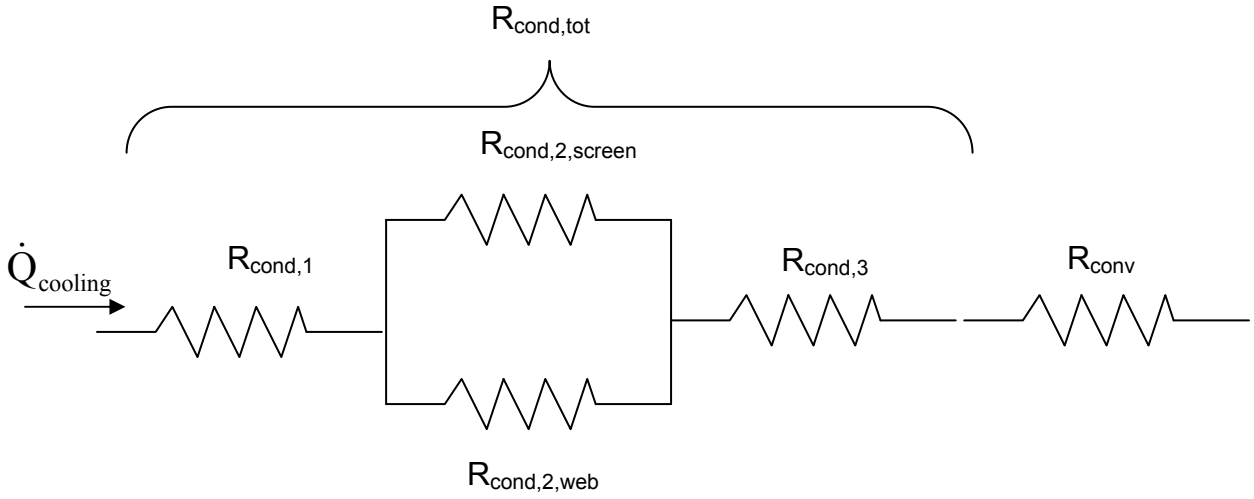

Figure 3.15. Resistor network for heat transfer in the cold heat exchanger.

The thermal resistances are then added together and the temperature differences are determined using the following equations:

$$R_{cond,tot} = R_{cond,1} + R_{cond,2} + R_{cond,3} \tag{3.96}$$

$$R_{cond,tot} = \frac{\Delta T_{cond}}{\dot{Q}_{cooling}} \tag{3.97}$$

$$R_{conv} = \frac{\Delta T_{conv}}{\dot{Q}_{cooling}} \tag{3.98}$$

Based on this model, the optimal height of the screen bed was found to be 2.00 inch and the optimal screen size is 50-mesh which has a wire diameter of 0.009 inch. This design leads to a convective temperature difference that is approximately an order of magnitude

larger than in the original design due to a reduction in total cross sectional area. The expected conductive temperature drop is approximately 6 K with a convective temperature drop of 1 K. The pressure drop across the screens also increases due to the smaller total cross section. Using equations (3.89) and (3.90), the pressure drop is found to be 24.5 kPa, which is within 5% of the total pressure swing of the system. The values for the various total temperature and pressure drops for various meshes are summarized in Table 3.1.

Table 3.1. Pressure drop and total temperature difference for various screen meshes.

Mesh [1/in]	Diameter of Wire [in]	ΔPressure [kPa]	ΔTemperature [K]
100	0.0045	50.90	6.213
80	0.0055	39.30	6.454
60	0.0075	29.56	6.545
50	0.0090	24.43	6.733
40	0.0100	17.71	7.744
30	0.0120	12.34	9.036
20	0.0160	7.678	11.31
10	0.0250	3.454	18.99

The final design of the cold heat exchanger incorporates a mechanism for mounting platinum resistance thermometers (PRTs) directly in the cold gas stream. In this way, the temperature drop between the outer heat exchanger shell (where the heat is applied) and the cold gas can be measured and compared with these model predictions. A heater wire will be attached to the cold heat exchanger between the top and bottom flanges of the cold heat exchanger and be attached before bolting the pulse-tube in place. Inside the lower flange of the cold heat exchanger are three holes that are specifically designed to accept the PRTs and therefore provide an accurate measure of the flange temperature.

Finally, the dimensions of the bolted flanges are determined in accordance with the ASME Pressure Vessel Code. Since the yield strength of copper is much lower than that for steel, the flanges must be made quite thick. The upper flange is designed to mate to the pulse-tube with an indium seal. The upper flange was designed for a thickness of 0.75 inch. The thickness of the flange is as thick as the stainless steel regenerator bottom flange. The thickness of this flange is determined by competing effects. A flange, under ASME Pressure Vessel Code, will be increasingly thinner as the outside diameter is made smaller; this is due to the reduced moment arms. The other effect is the material, in this case OFHC copper is used, which has an allowable stress of 6.25 ksi, compared to the 20 ksi for stainless. The lower flange of the cold heat exchanger mates with an indium seal to the upper regenerator flange, and the thickness of this flange is 1.00 inch.

3.2.3 Pulse-Tube Design

The pulse-tube is designed so that it may be easily removed and replaced. Therefore, the design includes two flanges, the upper pulse-tube flange and the lower pulse-tube flange, as shown in Figure 3.16.

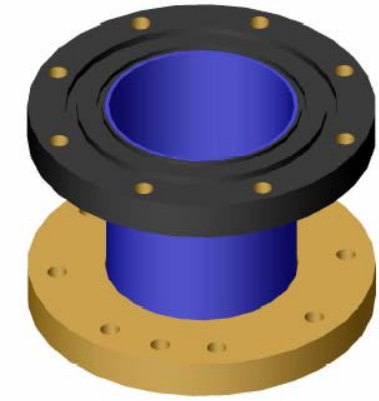

Figure 3.16. The pulse-tube assembly shown with both upper and lower flanges.

The pulse-tube design procedure is identical to the regenerator design procedure. The length of the pulse-tube is dictated by the thermodynamic model, 3.0 inch. The following equation is used to evaluate the wall thickness

$$t = \frac{\left(P_{\max} \cdot r_i\right)}{\sigma_{allowable} - 0.6P_{\max}} \tag{3.99}$$

The resulting wall thickness is 0.032 inch. The flange design for the pulse-tube uses the same calculations as the flange design for the cold heat exchanger and the regenerator flanges. The thicknesses were determined to be 0.385 inch, using the same material, 304 stainless steel, and pressure loading conditions, 400 psig. Since material of this thickness is hard to find, 0.50 inch stainless is used for the both flanges. The lower pulse-tube flange seals to the CHX with an indium seal, while the upper pulse-tube flange seals to the HHX with an o-ring.

3.2.4 Hot Heat Exchanger Design

The hot heat exchanger design was strongly influenced by the experimentally observed fact that most of the heat is rejected at the orifice valve and not the hot heat exchanger. Therefore, for this design the orifice valve was replaced with a fixed orifice which is included as an integral part of the hot heat exchanger. An exploded view of this design is shown in Figure 3.17.

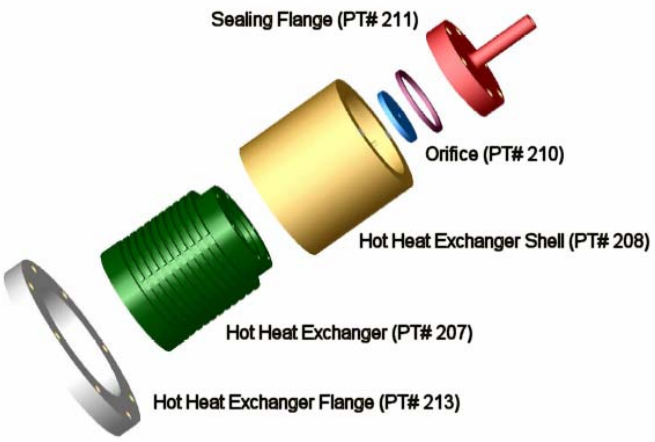

Figure 3.17. Exploded assembly of the hot heat exchanger with integral orifice.

The design incorporates a built-in orifice that is held in place by a lip on the hot heat exchanger and sealed with an o-ring against the sealing flange. The sealing flange is connected to the hot heat exchanger with 10-24 UNC bolts. During initial testing, an orifice valve is installed so that the optimal resistance can be determined. The valve is removed and an equivalent fixed orifice installed in the hot heat exchanger.

3.2.5 Vacuum Container Design

The vacuum container design was not only designed for performance but also for safety. The thickness of the vacuum can is designed to protect against the possibility that a leak in the pulse-tube might pressurize the vacuum space; if this occurs then the maximum amount of gas that can be released into the vacuum can is related to the volume of the compressor and the pulse-tube.

Approximations are used for the evaluation of the pressure released into the can. The volume of the entire system is estimated at 4.0 liter, this includes the compressor, pulse-tube, and reservoir. The vacuum space is estimated according to:

$$V_{vac} = V_{can} - V_{pt} \tag{3.100}$$

The volume of the vacuum can, V_{can}, is associated with its diameter, 9.5 inch, and height, 10 inch. The volume of the pulse-tube, V_{pt}, was estimated based on an assumed constant average diameter of 6.5 inch and height of 10.0 inch. The volumes of each were calculated by assuming both were cylinders. The resulting vacuum space volume, V_{vac}, is equal to 0.22 ft^3. The ideal gas law is used to estimate the pressure in the vacuum can that would result in the event of a leak.

$$P_{pt} \cdot V_{dead} = P_{vac} \cdot V_{vac} \tag{3.101}$$

The pulse-tube pressure was set at 400 psig and the dead volume, V_{dead}, was estimated at 4.0 liter. The final pressure in the vacuum can, P_{vac}, was found to be 260 psig. This pressure was then set as the maximum pressure in equation (3.99) and the required vacuum can wall thickness was determined to be 0.078 [in]. This is very close to the

thickness of a 14 gauge sheet of metal (0.075 inch) and therefore 14-gauge sheet metal was chosen as the material for the vacuum wall.

The vacuum container has two flanges that are welded to its top and bottom. The top flange is designed to accommodate the required feed-throughs, KF vacuum fittings, and a relief valve, as shown in Figure 3.18.

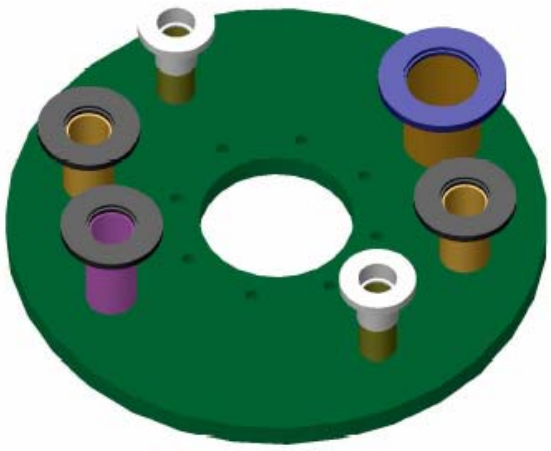

Figure 3.18. The top flange of the vacuum container

The flange includes one KF-40, used to connect the vacuum pump, three KF-25 and two KF-16's are used for miscellaneous electrical and other feed-throughs. One of the KF-16's is used to accommodate a relief valve that provides additional security against a leak. The bolt circle in the middle of the top flange is to secure a flange that compresses an o-ring seal between the vacuum can and the hot end of the pulse-tube. The o-ring is compressed using a flange that has a chamfered edge in order to compress the o-ring simultaneously against the shell of the hot heat exchanger and the sealing surface of the

top flange. The bottom flange is welded to the vacuum can and used to attach the vacuum can to the base flange which is mounted to the aftercooler. The vacuum can seals to the bottom flange with a rubber o-ring.

3.3 Fabrication of the 300W, 65K Pulse-tube

3.3.1 Regenerator

The regenerator tube and both flanges were machined in accordance to the detailed drawings in Appendix A. Figure 3.19 shows the fabricated parts.

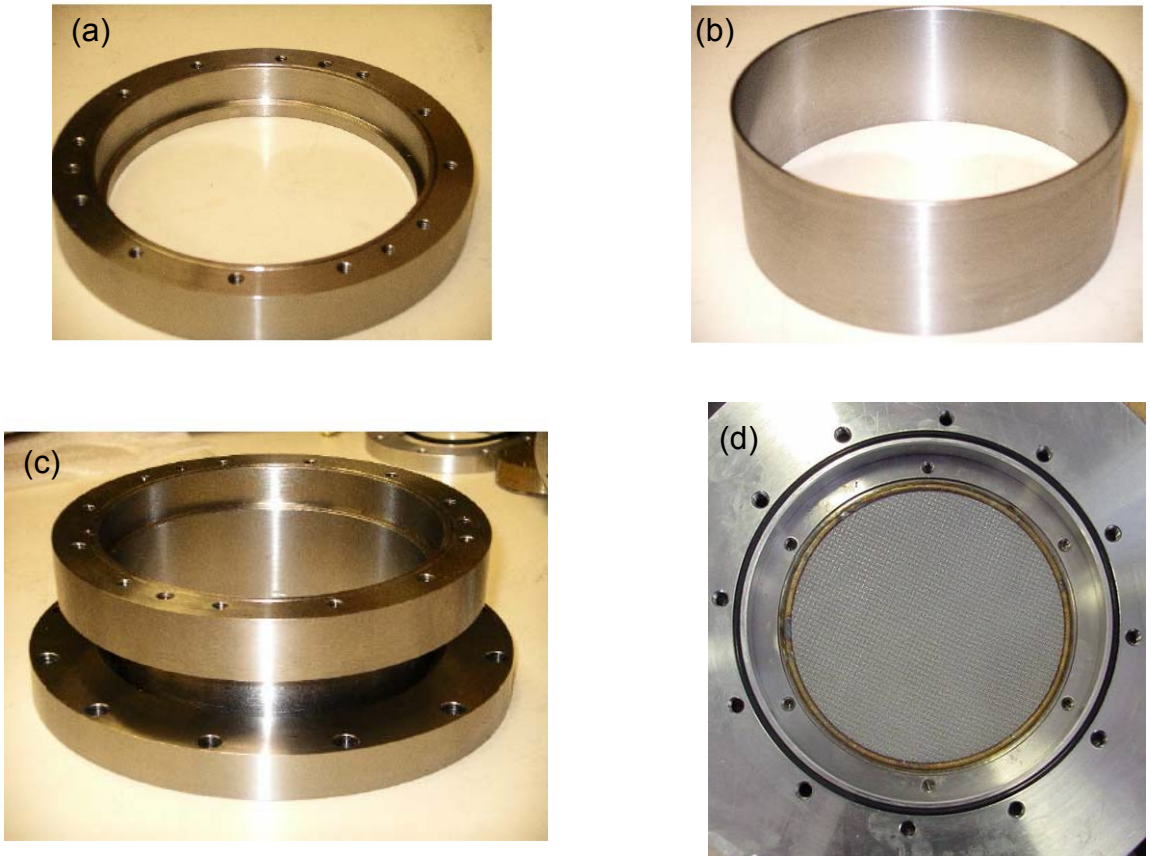

Figure 3.19. The upper regenerator flange (a), the regenerator tube (b), the assembly of flanges and regenerator tube (c), and the matrix (d) create the entire regenerator assembly.

The regenerator was welded together by the University of Wisconsin, Physical Plant and hydrostatically pressure tested to 450 psig. The screen matrix was inserted after welding the housing assembly. The sintered matrix was ordered from Martin Kurz & Co. oversized by approximately 0.002 inch in order to ensure that there would be no bypass flow even after the regenerator tube expands due to the pressure load. Oversizing individual screens is a common practice in pulse-tube design; however, when individual screens are compliant and can therefore be inserted into the regenerator tube relatively easily. However, when inserting a solid, oversized sintered block of screens there is very little compliance and therefore it was necessary to immerse the screens in liquid nitrogen (which boils at 77 K) so that it contracted and could be inserted into the regenerator tube; a disk with a diameter of 3.0 inch was used to apply some force during the insertion.

3.3.2 Cold Heat Exchanger

The cold heat exchanger was machined by the College of Engineering machine shop. The screens were inserted in each of the holes; the screens are loose in the holes and could easily be packed. The screen pack was held in place by a piece of brass that matched the 15-hole pattern. Beneath the brass piece were layers of larger screens that matched the inside diameter of the pulse-tube; these screens ensured that the screens would hold their position and also aided in flow straightening. Figure 3.20 illustrates the cold heat exchanger and brass piece after machining.

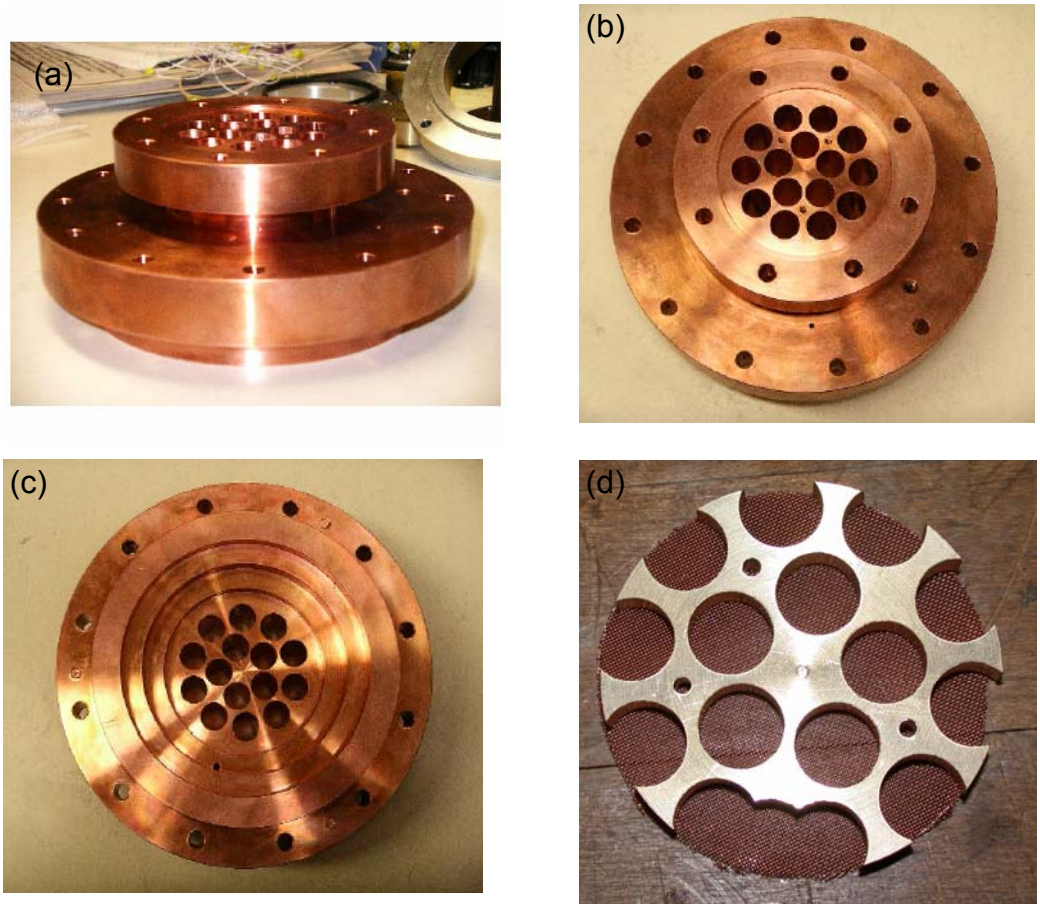

Figure 3.20. The cold heat exchanger isometric (a), top (b), bottom (c), and brass screen holder (d).

3.3.3 Pulse-tube

All the components of the pulse-tube were fabricated according to the drawings in Appendix A. Figure 3.21 are pictures of the pulse-tube and assembly:

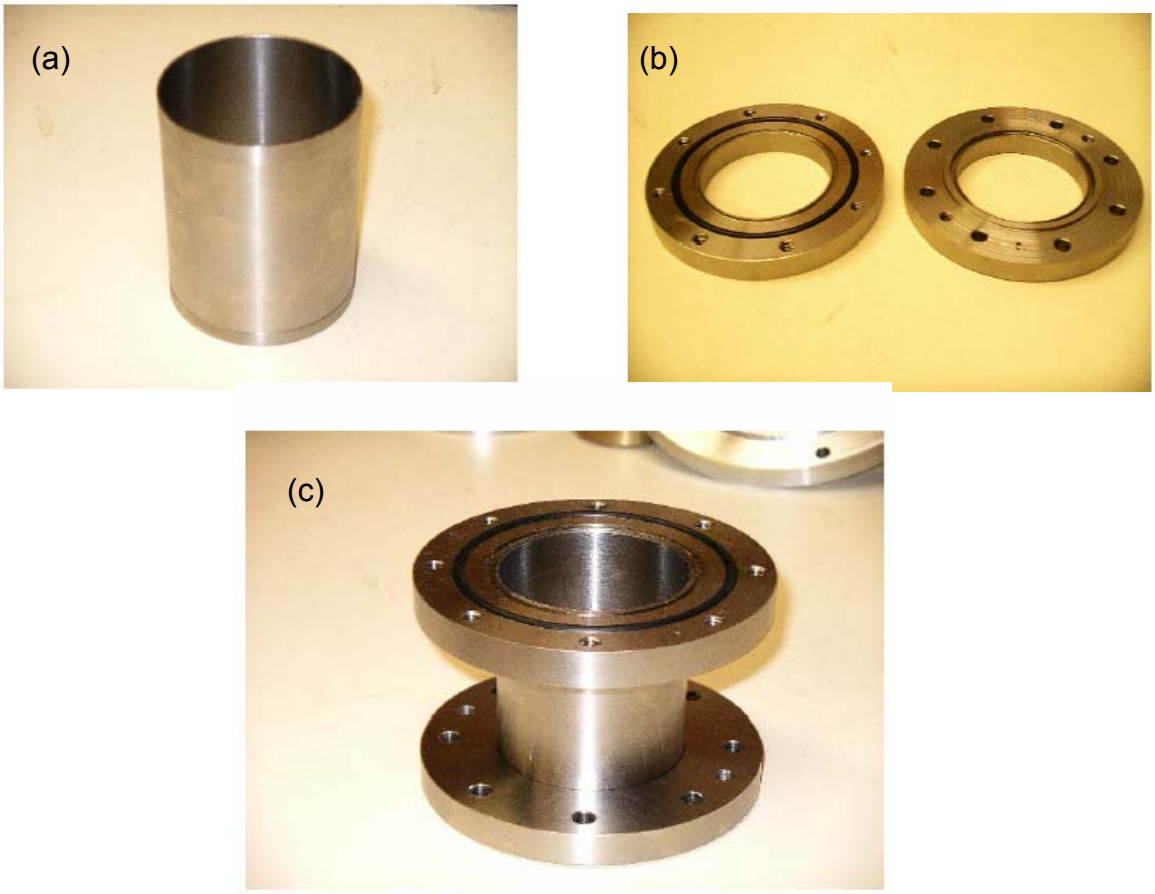

Figure 3.21. The pulse-tube (a), flanges (b), and assembly (c).

3.3.4 Hot Heat Exchanger

The hot heat exchanger was also machined in accordance to the drawings in Appendix A. Figure 3.18 shows the machined components of the hot heat exchanger (HHX).

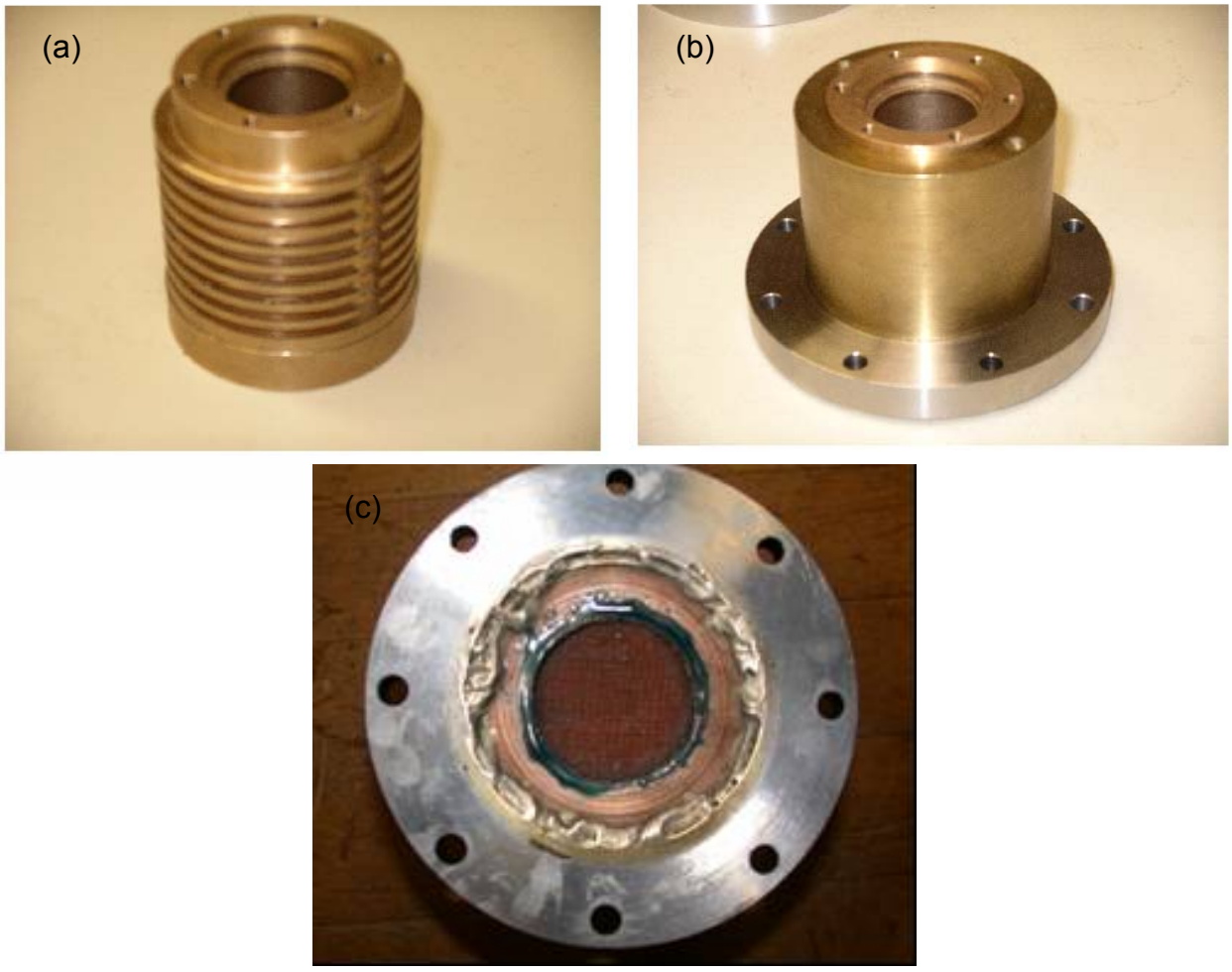

Figure 3.22. Hot heat exchanger with eight rows of fins (a), with the water shell installed (b) and bottom view of soldering and screens (c).

The assembly was created by using a high temperature silver solder for the HHX shell to the HHX flange joint. A lower temperature silver solder was then used to bond the HHX to the HHX shell. The screens were then loose packed into the hole and held in place with epoxy, which can be seen around the screens in Figure 3.22. The water lines were also bonded using epoxy.

3.3.5 Vacuum Container

The final assembly can be viewed in Figure 3.23. All of the parts were machined in accordance to the drawings presented in Appendix A.

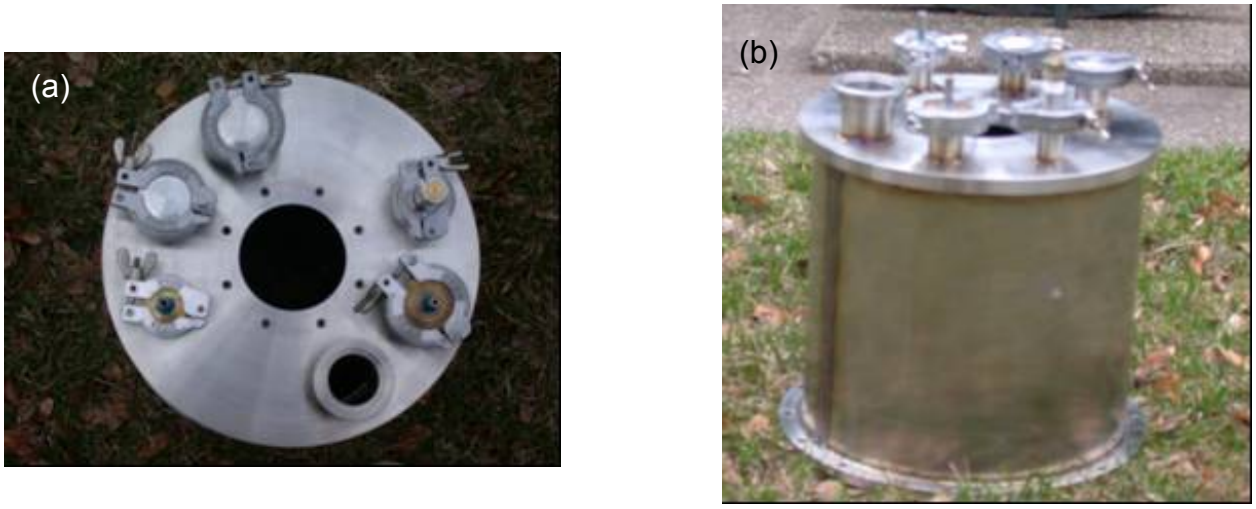

Figure 3.23. Top view of finished vacuum can (a) and isometric (b).

All the pieces for the vacuum can were machined by the University of Wisconsin, Physical Plant. The seam on the shell was welded initially and then the flanges were welded to the can.

3.3.6 Assembly

The final assembly is shown in Figure 3.24.

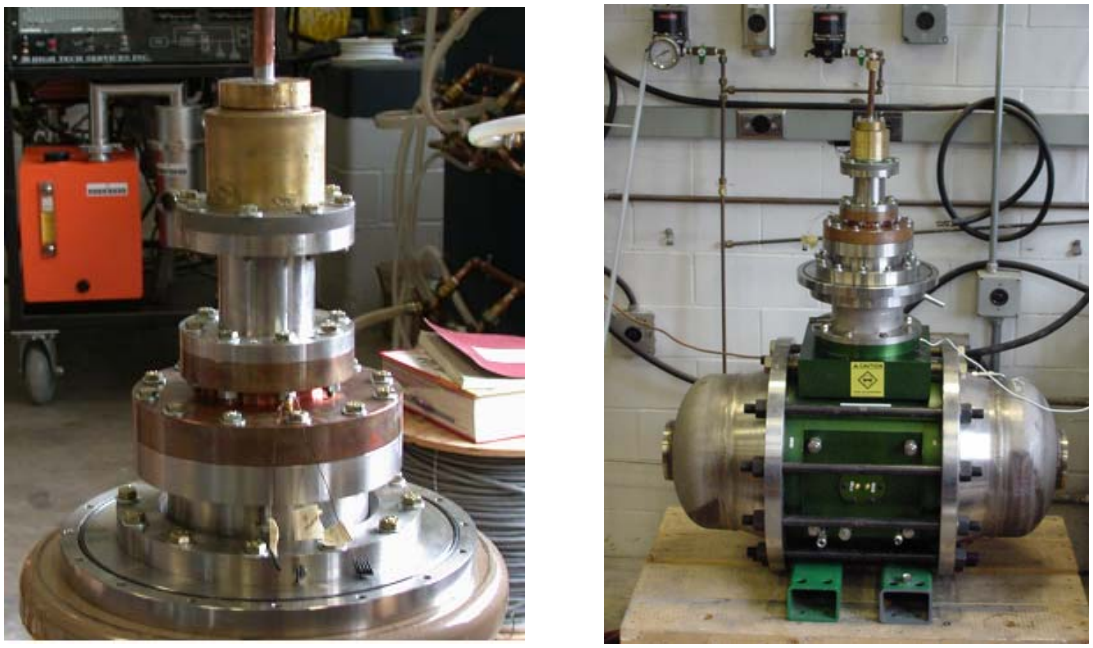

Figure 3.24. Complete assembly of 300W, 65K pulse-tube (left) and assembly mounted on aftercooler and the 10kW CFIC compressor (right).

The assembly is created by bolting the flanges together. The seal made between the aftercooler and compressor is achieved by a standard o-ring. O-rings are used for every interface except for the cold heat exchanger (CHX). Thus the regenerator-base flange, pulse-tube-HHX, HHX-inertance tube, vacuum can-base flange, and vacuum can-HHX all are made using o-rings. The CHX is sealed using indium wire on both the top and bottom. The indium wire that was used had a diameter of 0.045 inch. Indium is unlike an o-ring because it has no elasticity after it is compressed. As a result, the creep in the indium was a problem that prevented making a reliable, leak-tight test section. To counter this problem, the indium seal was torque-speced to 100 inch-pounds for each bolt four times before pressurizing the system and subsequently leak testing the apparatus.

3.4 Experimental Test Setup

The pulse-tube assembly is mounted in a vacuum chamber and integrated with a compressor and aftercooler. The compressor is a linear compressor rated to 10.0 kW of input power manufactured by CFIC. The predicted performance of the experimental system is summarized in Table 2.3. Figure 3.25 shows the pulse-tube during an experimental run.

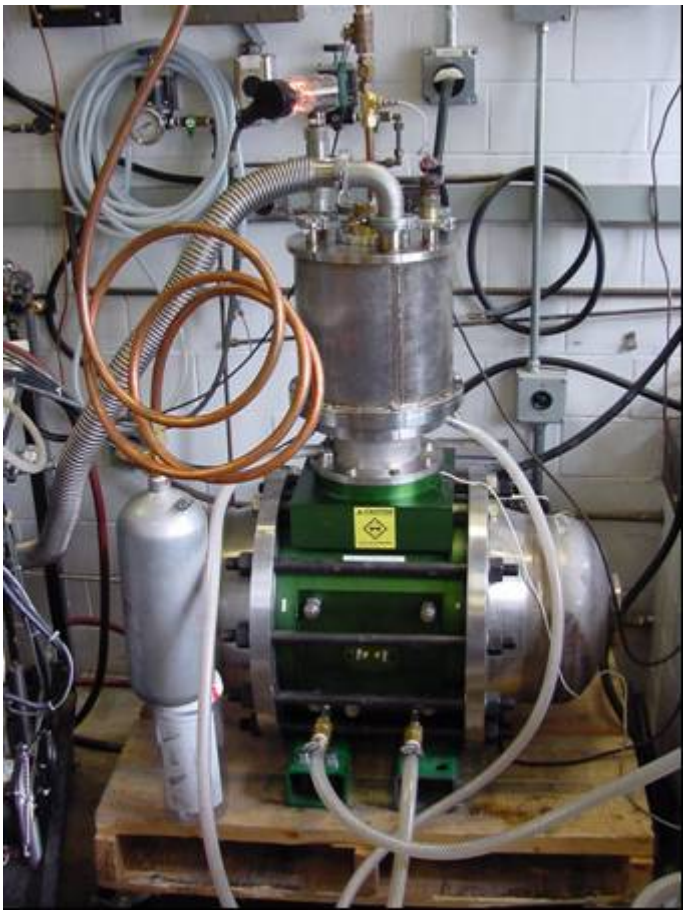

Figure 3.25. Complete test assembly, the reservoir is located to the lower right of the picture and water lines directed to the right of the apparatus to the chiller.

Figure 3.26 summarizes the locations of the instrumentation installed on the experimental pulse-tube apparatus. Three pressure transducers are placed in the system; one each at the compressor outlet, at the reservoir, and after the hot heat exchanger. Omega pressure transducers model PX302-500GV are used for accuracy (0.25% of full scale) and response time (1 msec). Platinum resistance thermometers (PRTs) are used to measure the temperature at various locations on the cold end of the system. Each PRT was individually calibrated at liquid nitrogen and ice point temperatures. Three of the PRTs, Lakeshore model PT-102, are inserted directly into the gas flow through the cold heat exchanger in order to allow an accurate measurement of the refrigeration temperature that is independent of the performance of the cold end heat exchanger. This measurement also facilitates model verification. Three additional PRTs, Lakeshore model PT-111, are inserted inside the copper flange on the outside of the cold heat exchanger. Figure 3.27 illustrates the cold heat exchanger from the regenerator side. Note the PRTs installed in the flow straightener screens which are used to measure the internal gas temperature.

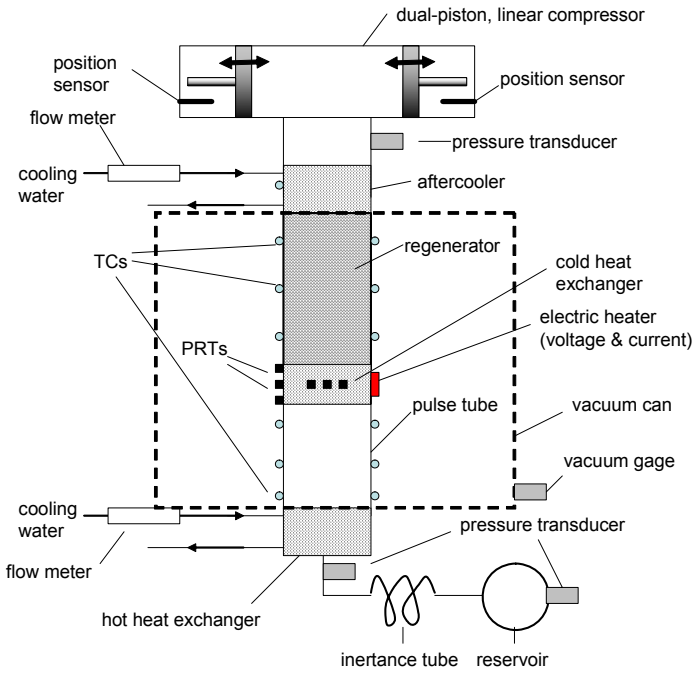

Figure 3.26: Instrumentation on experimental pulse-tube apparatus

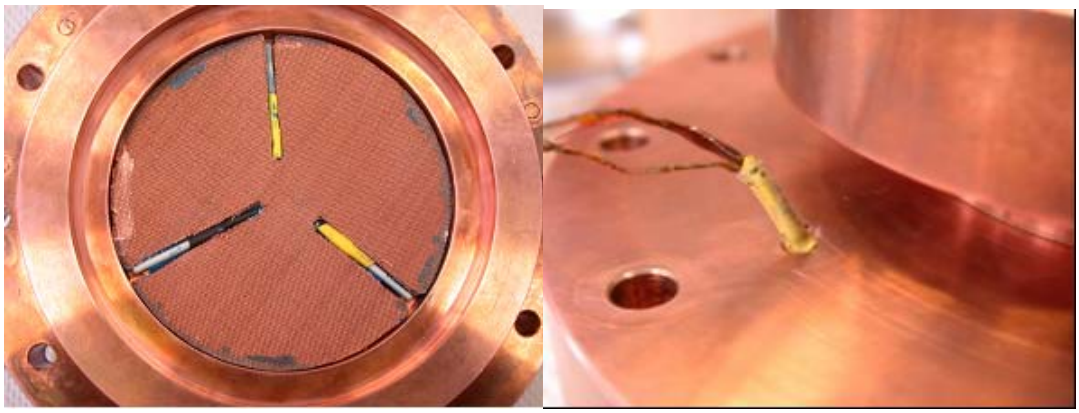

Figure 3.27: Cold heat exchanger (regenerator side) showing the location of the embedded PRTs

Type-E thermocouples are installed externally to measure the temperature at all other points of interest. This includes three thermocouples that are equally spaced along the wall of the regenerator and three more thermocouples on the opposite side in order to provide redundant measurements and verify symmetrical flow in the regenerator. Three

thermocouples are placed on the pulse-tube with replicants exactly opposing these as well. Finally thermocouples are placed on the water inlet, outlet, and exit of the hot heat exchanger.

Chapter 4 – Initial Testing of High Capacity Pulse-Tube

4.1 Introduction

An initial series of runs were accomplished using the 300 W pulse-tube in the vacuum vessel; many of these runs were accomplished with a limited set of instrumentation and no radiation shielding in order to evaluate the nominal performance before proceeding with more detailed testing. This chapter describes the analysis of this initial data which was accomplished in order to understand whether the pressure-flow behavior and thermodynamic performance agree with the predictions of the thermal fluid design model. One important conclusion associated with these initial data is that the pressure loss between the compression space and pulse-tube is larger than expected based on the regenerator geometry which may be due to a fluid resistance in the cold heat exchanger resistance that is larger than expected. However, once the fluid resistance is accounted for, the pressure-flow behavior appears to be consistent with predictions of the design model; however, the performance (as indicated by the no-load temperature) is very poor. Moreover, the performance degradation must be attributable to a loss that is only present when the pulse-tube is operating; the warmup rate indicates that the parasitic heat load on the cold head is within the expected range. These observations motivated the CFD analysis and testing presented in the subsequent chapters.

4.2 Initial Dynamic Testing

4.2.1 Operating Conditions and Instrumentation

The measurements listed in Table 4.1 were recorded by the Data Acquisition System (DAS).

Table 4.1. Measurements recorded during preliminary testing

Symbol	Instrument	Description
P_c	Endevco Pressure Transducer	Pressure between comp. and AC
P_{pt}	Endevco Pressure Transducer	Pressure at hot end of pulse-tube
P_{Rsv}	Endevco Pressure Transducer	Pressure in reservoir
x_A	position sensor	Position of piston A
x_B	position sensor	Position of piston B

The pulse-tube was operated with an inertance tube with a length of 3.6 m, with a 0.5 inch inside diameter, which was connected between the 2.5 liter reservoir and a valve. Data was recorded with the cold end near room temperature and the valve position adjusted from fully closed to fully open in increments of 1/8 turn.

4.2.2 Pressure-Volume Behavior with Valve Fully Closed

The data with the valve fully closed was considered first because the uncertainty associated with the inertance and resistance of the inertance tube and the volume of the reservoir is removed. Figure 4.1 illustrates the voltage measured from the position sensors for the 10 kW CFIC compressor for the fully closed valve condition.

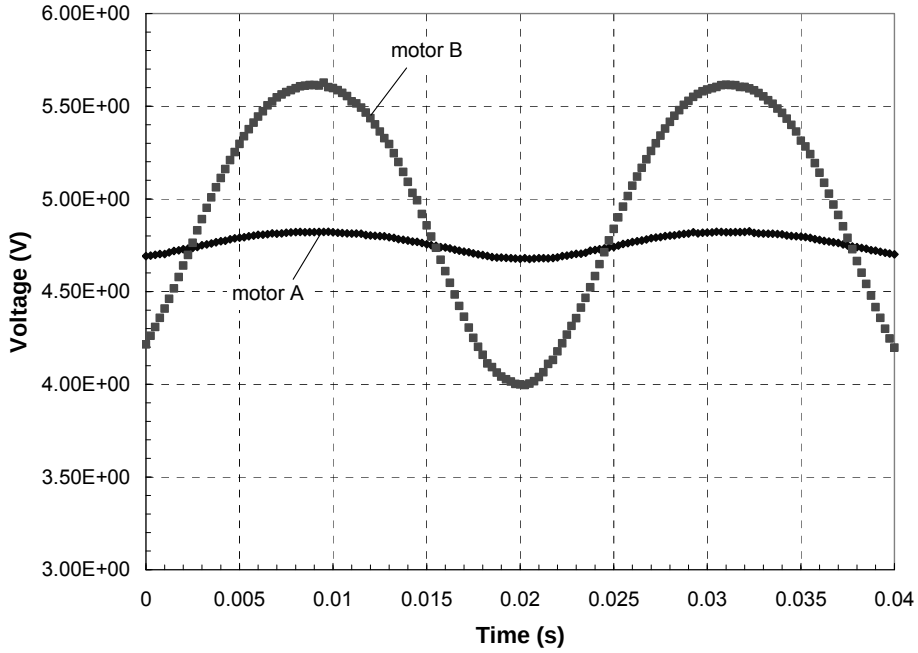

Figure 4.1. Voltages recorded from position sensors for valve fully closed condition.

The average voltage for each position sensor was computed and the deviation relative to this average (δV) was determined. The result is shown in Figure 4.2.

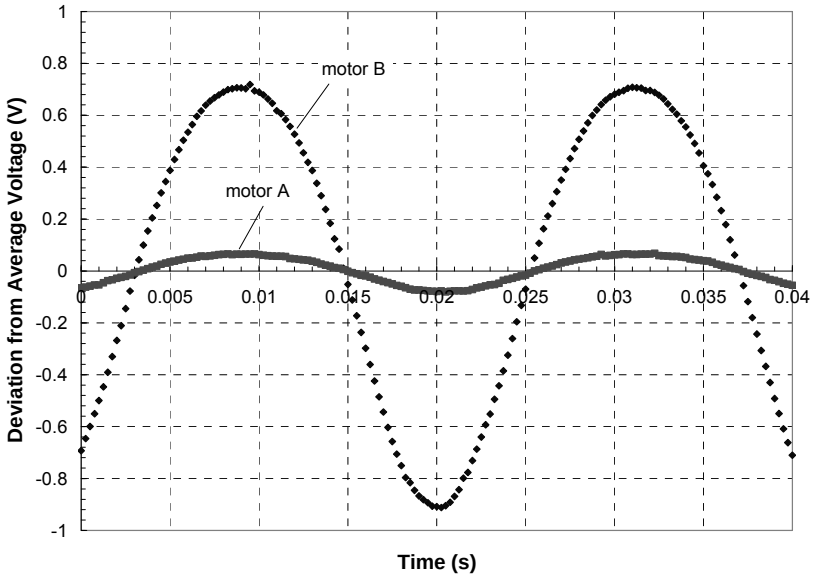

Figure 4.2. Deviation from average voltage recorded from position sensors for valve fully closed condition.

The following correlations were used to relate the voltage deviation to the position of each piston:

$$x_A = 996\,V_A^2 + 197.39\,V_A + 0.1027 \tag{4.1}$$

$$x_B = 8.4311\,V_B^2 + 16.768\,V_B + 0.0794 \tag{4.2}$$

where x_A and x_B are the instantaneous positions of pistons A and B in mm. These equations were developed through an on-site calibration process. The piston positions as a function of time are shown in Figure 4.3.

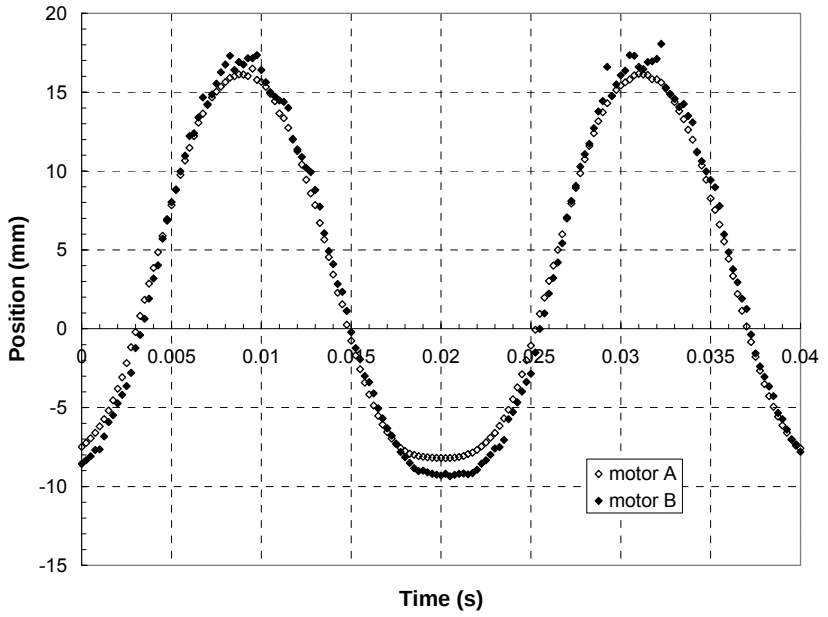

Figure 4.3. Calculated piston position measured for valve fully closed condition.

The compressor volume (V) is therefore:

$$V = \left(x_A + x_B \right) A_p \tag{4.3}$$

where A_p is the cross-sectional area of the piston (0.01423 m^2). Figure 4.4 illustrates the compressor volume:

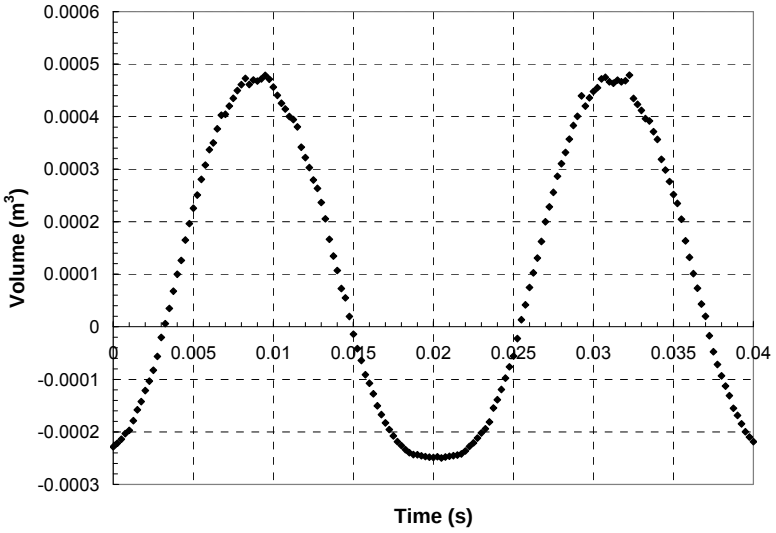

Figure 4.4. Calculated compressor volume measured for valve fully closed condition.

The swept volume (V_{sw}) is the maximum volume less the minimum volume, in Figure 4.4 the swept volume is 0.000741 m^3 (741 cm^3). The maximum swept volume that can be attained by the compressor ($V_{sw,max}$) is nominally 0.000795 m^3, which corresponds to a 28 mm peak to peak stroke. Therefore, the compressor is operating at nominally 93.3% of its full stroke. The total dead volume in the compressor and aftercooler ($V_{C,dead}$) has been estimated to be 2130 cm^3; this is the volume that is not swept even if the compressor were operating at full stroke. In other words, if the compressor were operating at full stroke, the volume in the "compression space," taken to be the aftercooler and compressor together, would oscillate between 2130 cm^3 and 2925 cm^3. The compression space volume (V_C) is therefore calculated according to:

$$V_C = V + V_{C,dead} \tag{4.4}$$

Figure 4.5 illustrates the compression space volume calculated using this technique as well as the compression space volume assumed by the model when the compressor is operating at 93.3% of its full stroke.

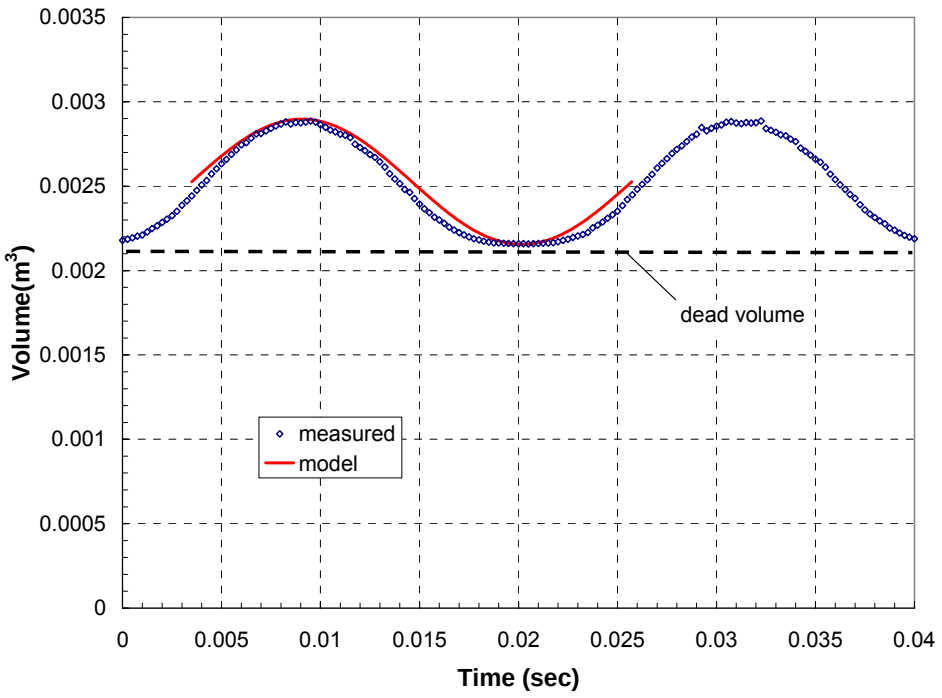

Figure 4.5. Calculated and modeled compression space volume for the valve fully closed condition.

The fully closed valve test conditions may be simulated using the thermal-fluid model of the pulse-tube by setting the resistance of the inertance tube to an essentially infinite value. The piston volume variation used to drive the model was adjusted to match the measured piston volume, as shown in Figure 4.5 Figure 4.6 illustrates the measured and predicted pressures in the compression space and the pulse-tube (note that the reservoir pressure remains essentially constant in this condition and is therefore not shown). The predicted pressures in the pulse-tube and reservoir were adjusted slightly up or down so that they oscillated about the same mean value as the pressure in the compression space.

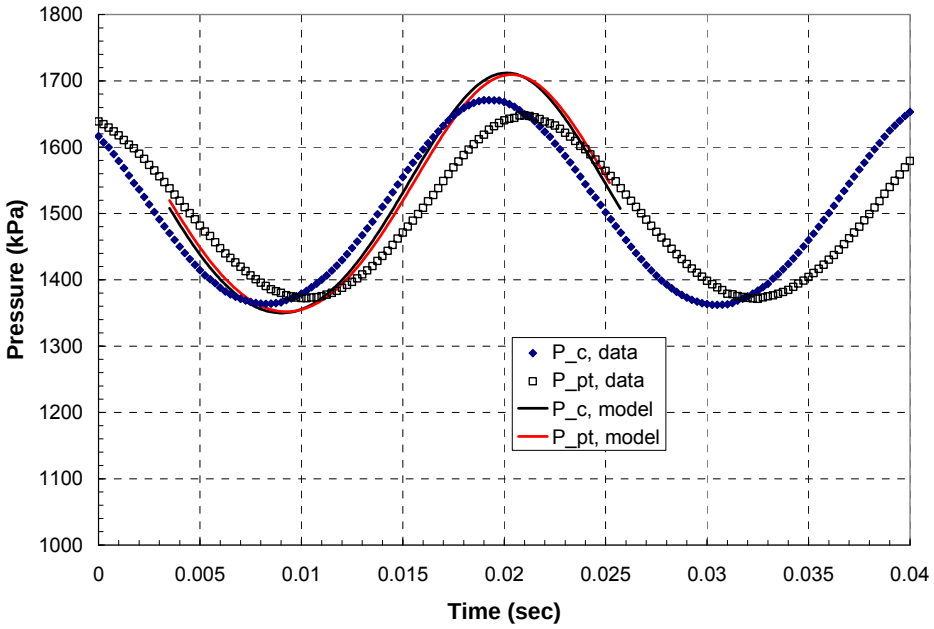

Figure 4.6. Calculated and modeled pressure in the compression space and pulse-tube for the valve fully closed condition.

There are a few things to notice in Figure 4.6. First, the predicted pressure amplitude in the compression space is larger than the actual amplitude, possibly indicating that there is more dead volume in the actual system than is considered in the model. Also, there is a phase shift and attenuation between the actual pulse-tube and compression space pressures that is not predicted by the model; this indicates that there is a resistance between the pulse-tube and compressor that is not included in the model.

The resistance of the regenerator predicted by the model is nominally 9.8e5 Pa-s/kg at the operating conditions associated with this test point. The regenerator void volume is nominally 440 cm^3. As previously mentioned, the dead volume of the compressor and aftercooler (as well as the flange connecting the aftercooler to the regenerator and the

regenerator to the compressor) was estimated to be 2130 cm^3. If an additional resistance of 2.2e6 Pa-s/kg is added to the resistance of the regenerator in the model, possibly corresponding to the cold heat exchanger, and an additional 300 cm^3 of volume is added to the pulse-tube (also possibly corresponding to the cold heat exchanger), and finally an additional 420 cm^3 of dead volume is added to the compressor dead space then very good agreement is achieved between the model and the data for this valve fully closed condition. Figure 4.7 illustrates the calculated and measured volumes under these conditions and Figure 4.8 illustrates the calculated and measured pressures.

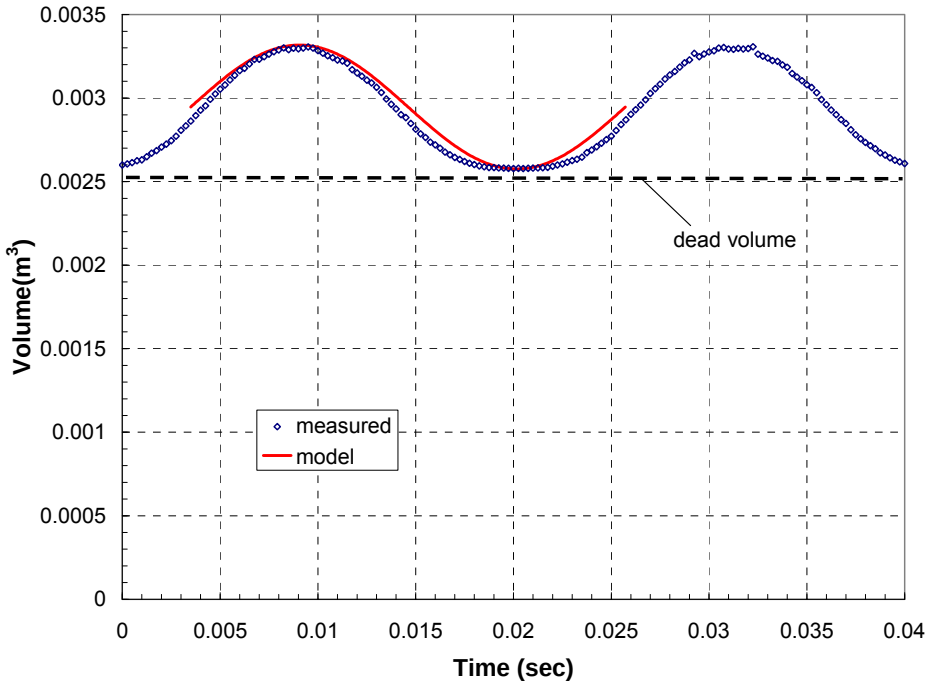

Figure 4.7. Volume of compression space measured and modeled assuming a total dead volume of 2550 cm^3 (rather than 2130 cm^3 as initially assumed) for the test with valve fully closed.

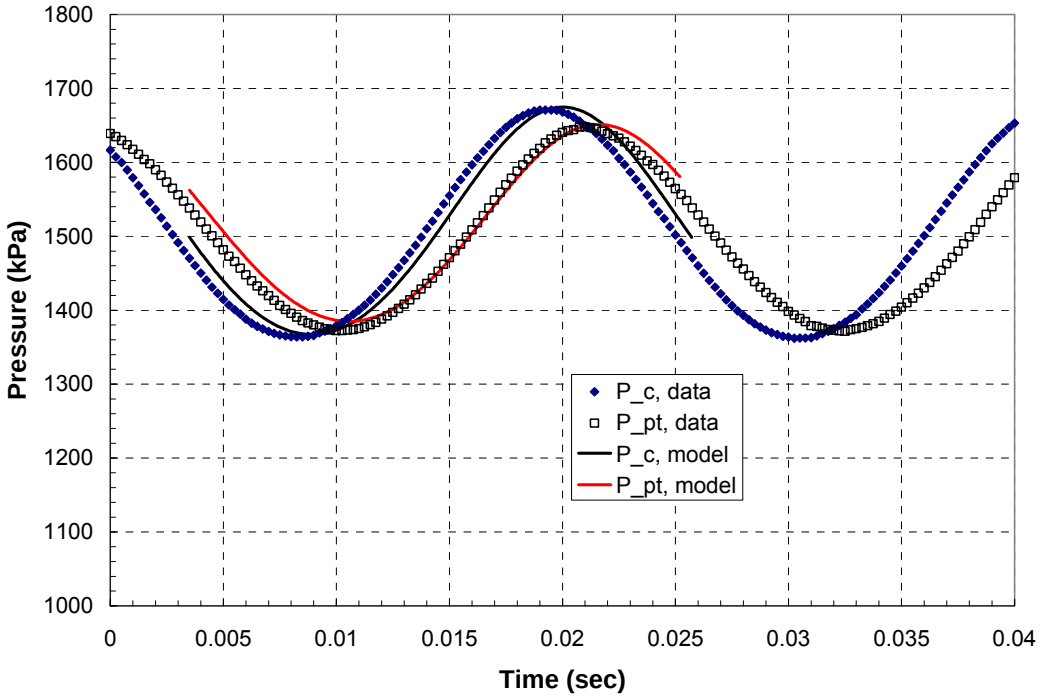

Figure 4.8. Modeled and measured pressures with a compressor dead volume of 2550 cm^3, 2.2e6 Pa-s/kg of additional cold heat exchanger resistance, and 300 cm^3 of cold heat exchanger dead volume for the test with valve fully closed.

Figure 4.9 illustrates the predicted mass flow rate at the warm and cold ends of the regenerator as well as the measured and predicted pressures. Notice that the mass flow rate at the cold end of the pulse-tube leads the pressure at that location by 90 degrees, as it should for this basic pulse-tube. Also notice that the mass flow rate is nominally in phase with the pressure difference across the regenerator. Figure 4.9 illustrates the mass flow rate at the cold end of the regenerator and the pressure difference between the compressor and the pulse-tube.

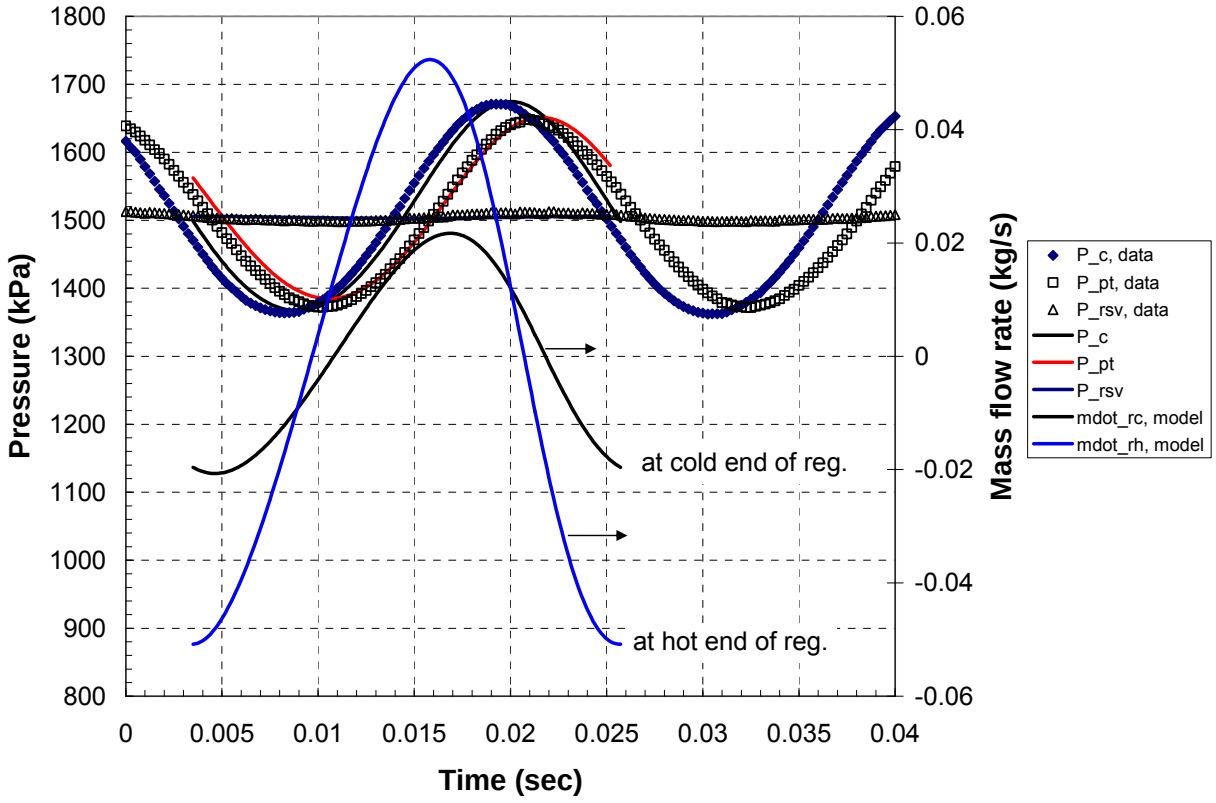

Figure 4.9. Mass flow rate at the hot and cold ends of the regenerator and the pressures for the test with valve fully closed.

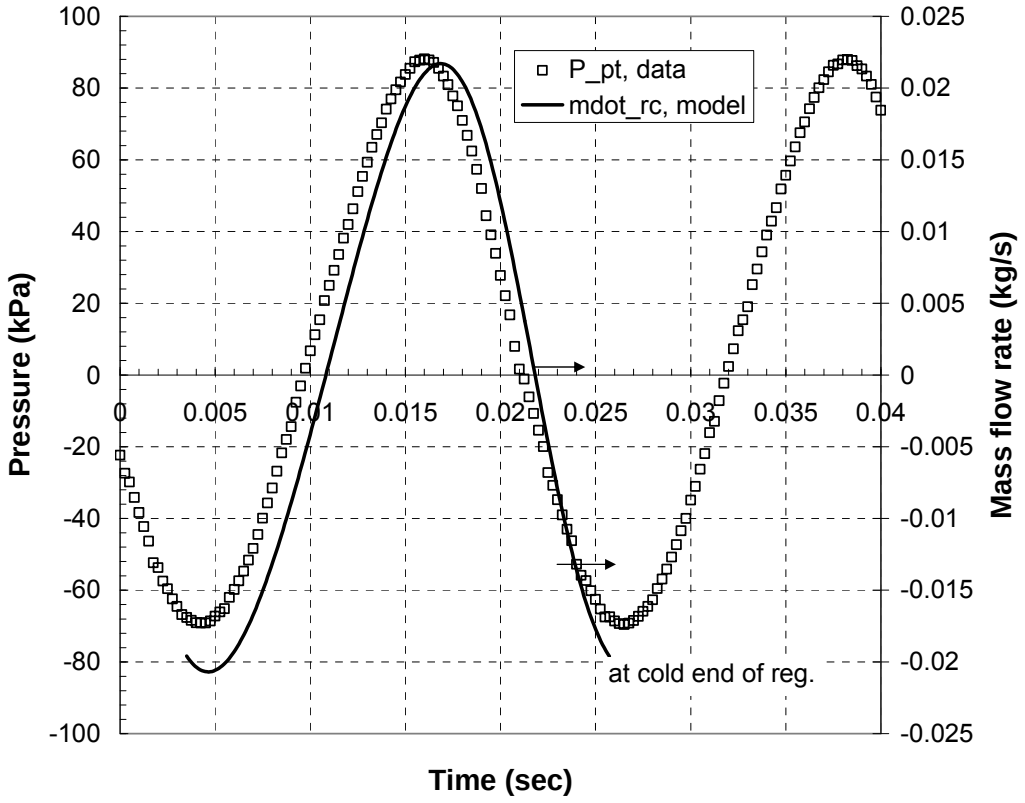

Figure 4.10. Measured pressure difference and predicted flow for 6/4/04 test with valve fully closed.

Finally, it is worth noting that the P-V work delivered to the cold end under this condition is nominally 80 W, according to equation 2.35.

4.2.3 Pressure-Volume Behavior with Valve Fully Open

The compression space volume is calculated from the piston position sensor for the data collected with the valve fully open using the same technique described previously. The compressor was found to be operating at nominally 75.4% full stroke; the compression space volume that was measured and the volume used to energize the model are shown in Figure 4.11.

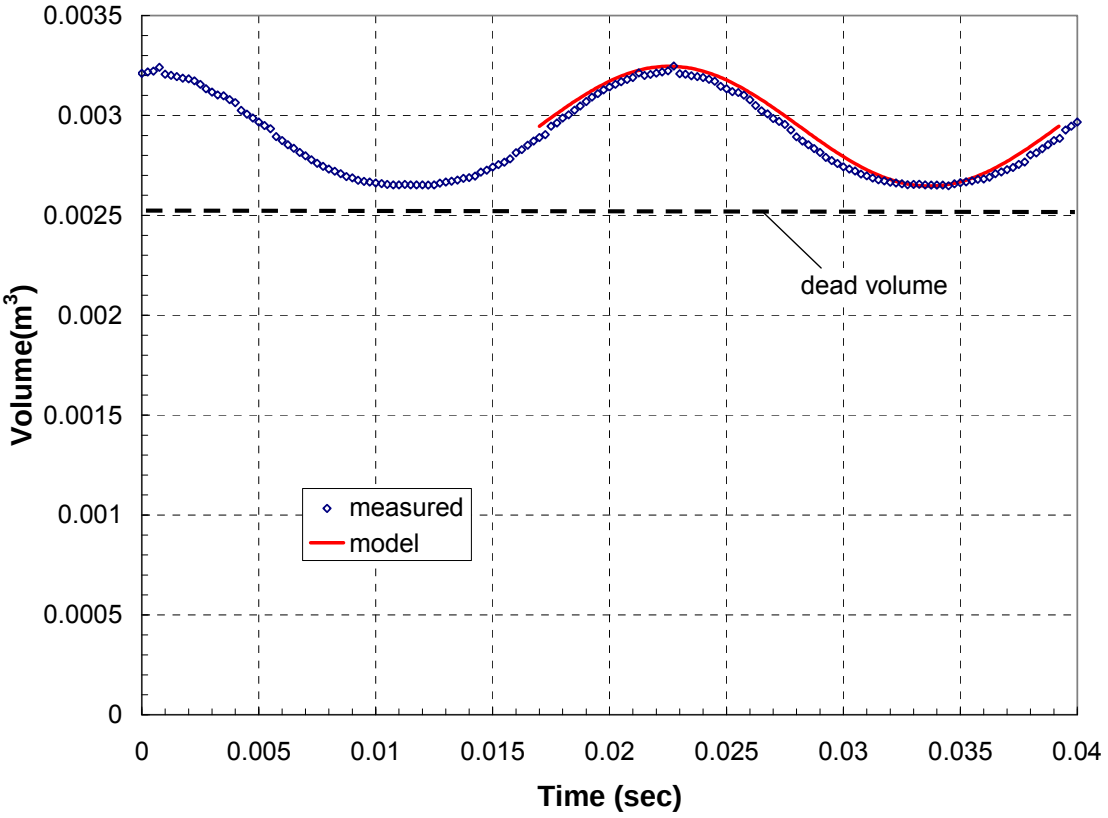

Figure 4.11. Volume measured and used by the model to simulate the fully open valve case for the data.

Figure 4.12 indicates the relatively good agreement between the predicted and measured pressures in the compression space, pulse-tube, and reservoir. Note that the same modifications to the modeling parameters were used (i.e., an additional resistance of 2.2e6 Pa-s/kg and an additional volume of 300 cm^3 associated with the cold heat exchanger as well as an additional compression space dead volume of 2550 cm^3). The resistance of the valve was assumed to be 8e5 Pa-s/kg in order to achieve this agreement.

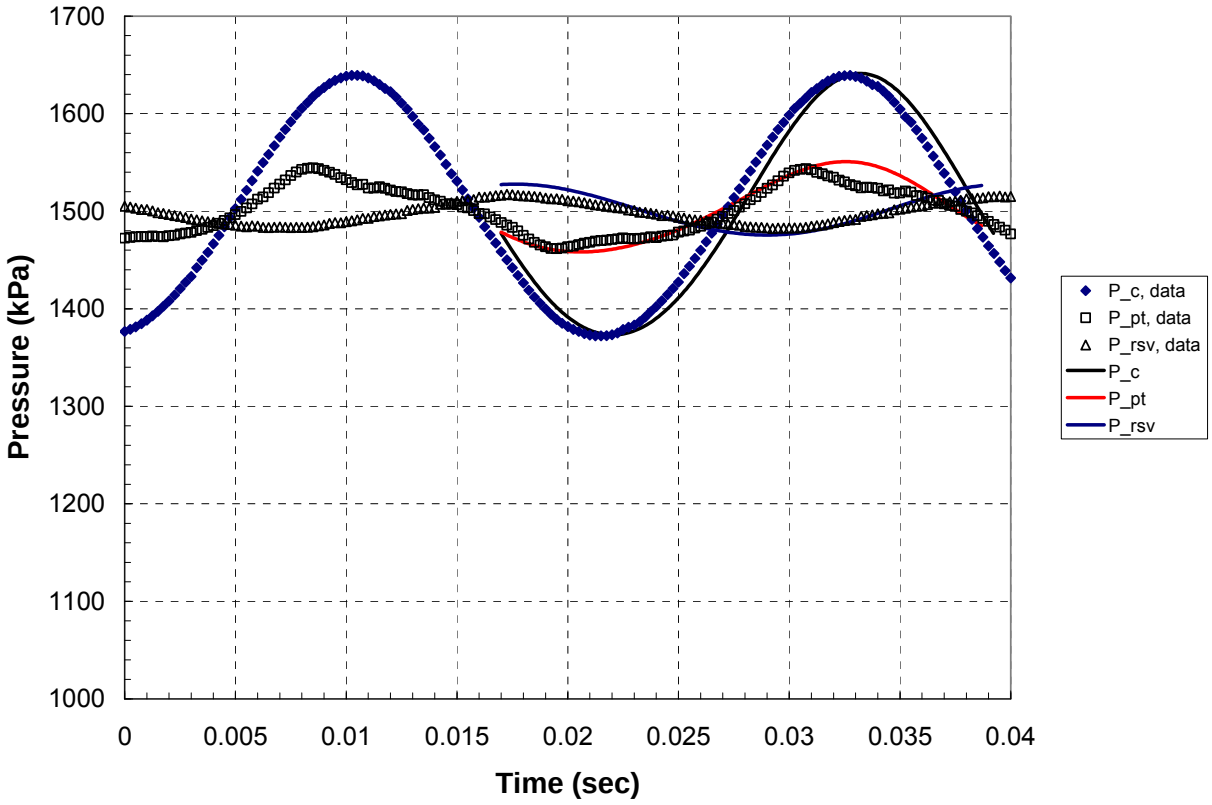

Figure 4.12. Pressure measured and predicted for the valve fully open condition.

Figure 4.13 illustrates the pressures and the mass flows for this case.

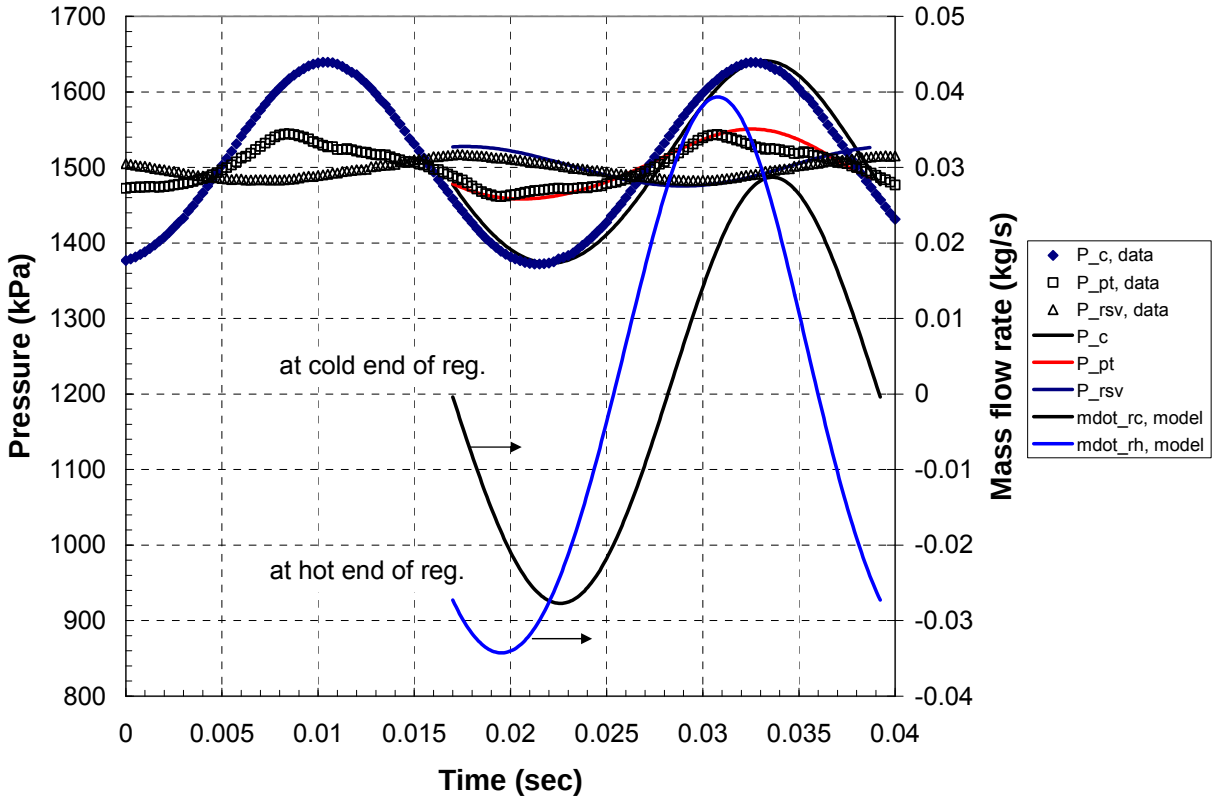

Figure 4.13. Pressure and mass flow rates for the valve fully open condition.

It is worth noting that that the mass flow rate at the cold end of the pulse-tube is larger than the fully closed valve position and more in phase with the pressure at the cold end, as is expected for an orifice-type pulse-tube. The P-V power delivered to the cold end is larger, nominally 230 W, for the valve fully open condition. Figure 4.14 illustrates the mass flow rate at the cold end and the pressure difference between the compression space and the pulse-tube and again shows that these quantities are nearly in phase with one another, as they should be. The model appears to do a good job of predicting the pressure-flow behavior of the pulse-tube both at the valve fully closed and fully open condition.

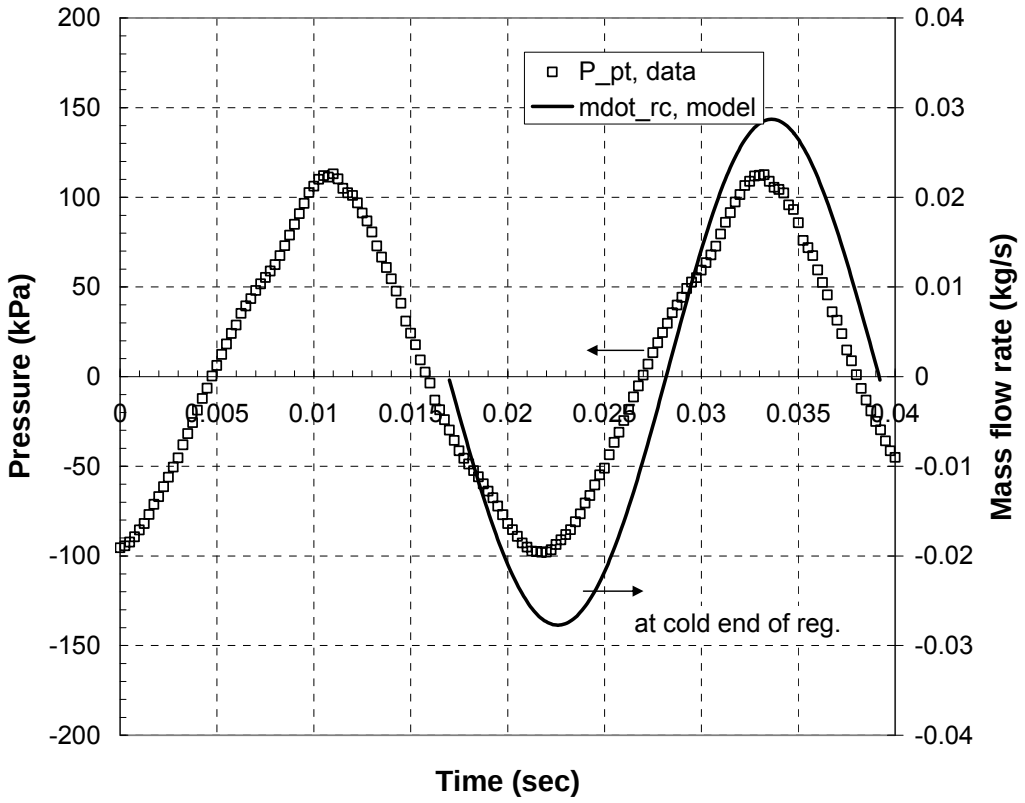

Figure 4.14. The measured compression space to pulse-tube pressure difference and the predicted regenerator cold end mass flow rate.

4.2.4 Pressure-Volume Behavior with the Valve Half Open

The compression space volume is calculated from the piston position sensor using the same technique described previously. The compressor was found to be operating at nominally 77.3% stroke. The pressures measured and predicted by the model (assuming a valve resistance of 2.0e6 Pa-s/kg) are shown in Figure 4.15. The mass flow rates are also shown.

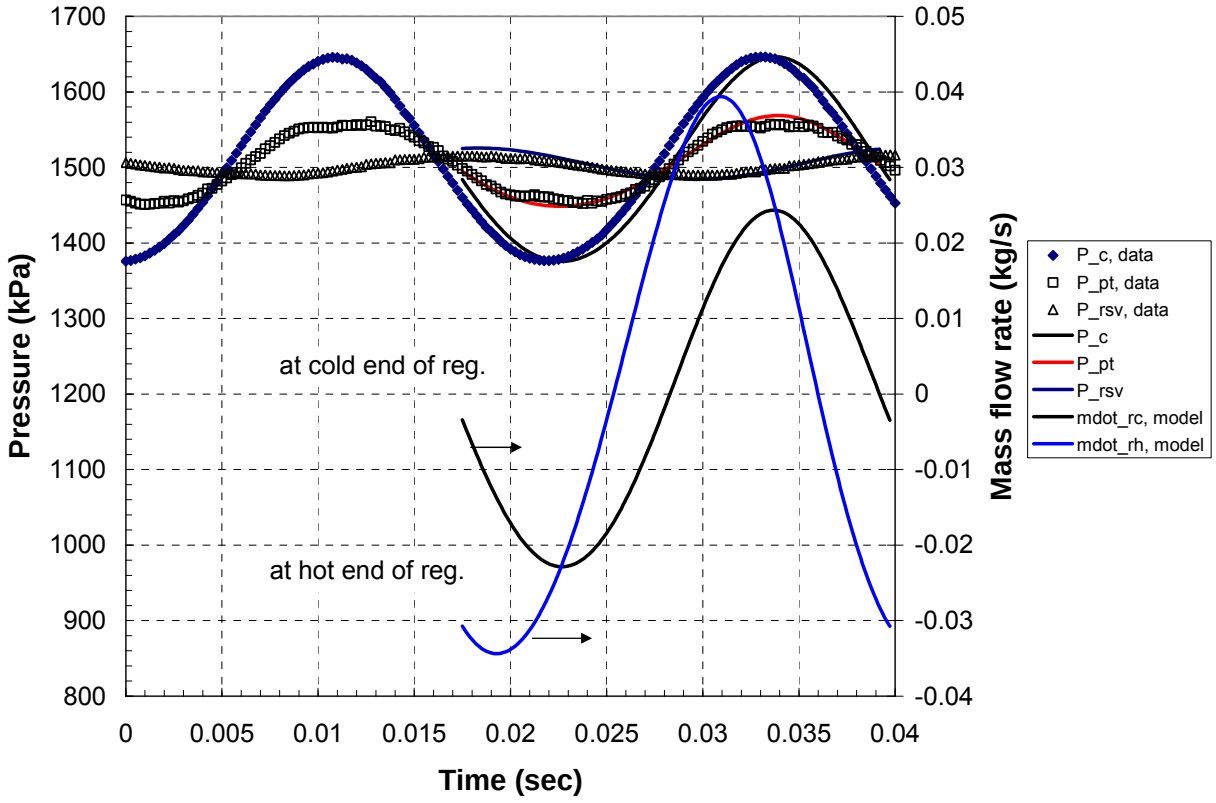

Figure 4.15. Predicted and measured pressures for the data taken with the valve half open. The predicted mass flow rates are also shown.

Note that the mass flow rate at the cold end is moving out of phase (beginning to lag) with the pressure in the pulse-tube. The P-V power delivered to the pulse-tube is nominally 280 W and the pressure difference between the compressor and pulse-tube is again in phase with the mass flow rate at the cold end.

4.3 Initial Performance Analysis

The initial test of the 300 W pulse-tube was performed in the vacuum vessel with a limited set of instrumentation and no radiation shielding; this was done in order to allow tests to be carried out rapidly so that iterations on the design could proceed more quickly.

The inertance tube connected to the pulse-tube was relatively long (4 m to 5 m) with a 0.5 inch inside diameter. The previous section analyzed the data from the pulse-tube in the same condition but with a very short inertance tube; a condition where the pressure-flow behavior is more predictable because the inertance of the fluid is small. However a longer inertance tube should produce better performance and was therefore used for this test.

The previous analysis indicated that a large fluid resistance was present somewhere between the compression space and the pulse-tube; this additional resistance may be attributable to the cold heat exchanger and certainly causes a significant reduction in the acoustic power that is delivered to the pulse-tube relative to the design. Still, the analysis indicated that depending on the valve position there should be on the order of 250 W of acoustic power available to provide cooling. This section analyzes the initial data in order to determine whether the cooldown and warmup rates are consistent with the losses predicted by the model and this level of acoustic power.

The measurements listed in Table 4.2 were recorded by the Data Acquisition System (DAS).

Table 4.2. Measurements recorded during preliminary testing

Symbol	Instrument	Description
T_{gas}	PRT Temp. Sensor	gas temp. within CHX
T_1	PRT Temp. Sensor	external CHX surface 1
T_2	PRT Temp. Sensor	external CHX surface 2
T_3	PRT Temp. Sensor	external CHX surface 3

Figure 4.16 illustrates the temperatures that were recorded as a function of time for this initial test run.

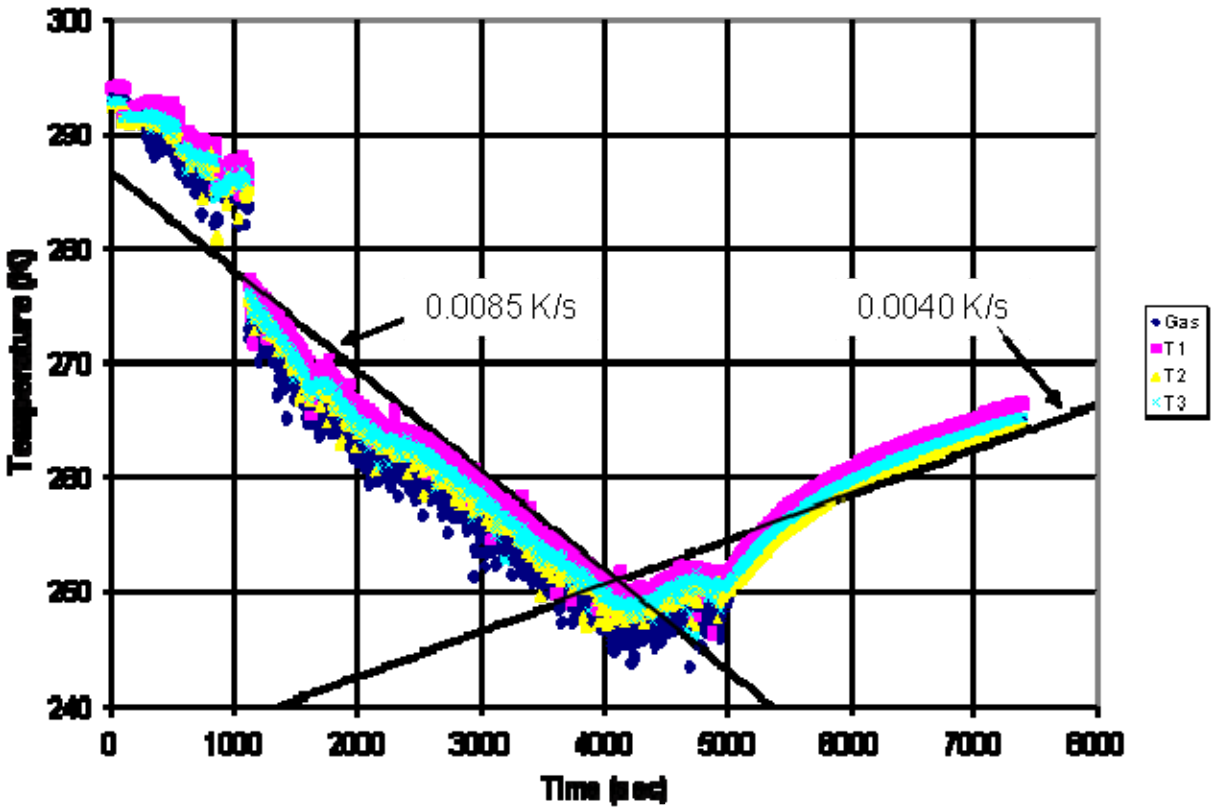

Figure 4.16. Temperature recorded on initial test run

Under these conditions, the model predicts an acoustic power of 250 W at 250 K even after modifying the model to account for the additional dead volume and resistance, as described in the previous section. Table 4.3 shows predicted losses in the system under these conditions.

Table 4.3. The predicted pulse-tube losses for the initial test condition.

Characteristic	Value
Regenerator ineffectiveness	5.0 W
Regenerator matrix conduction	5.4 W
Loss related to pressurization	2.3 W
Conduction through reg. tube	9.4 W
Conduction through pulse-tube	1.7 W
Pulse-tube loss (assumes 80% eff.)	50.2 W
Shuttle heat loss	1.5 W

Also, a radiation loss of 9.6 W is estimated assuming that the cold surface area is twice the outer area of the regenerator and an emissivity of 1.0. Finally, the REGEN code assumes stacked rather than sintered screens and therefore there may be two to three times the estimated 5.4 W (10-15 W), according to Lewis and Radebaugh (2003).

If these losses are totaled and subtracted from the predicted 250 W of acoustic power then a net cooling power of 150 W can be expected. The heat capacity of the cold end has previously been estimated at about 9000 J/K. Therefore the cooling rate should be nominally 0.017 K/s (1.04 K/min) for a 150 W cooling power. Note from Figure 4.16 that the observed cooling rate is nominally 0.0085 K/s, or half of this predicted value indicating that there is an additional, operating loss of about 70 W that cannot easily be explained.

By analyzing the warm up data we can eliminate some potential sources of this loss. The warm up is caused by a combination of conduction and radiation to the cold head (i.e., losses related to shuttle heat transfer, regenerator ineffectiveness, pulse-tube losses, etc. will not be present when the machine is shut off). The sum of regenerator tube conduction, pulse-tube conduction, regenerator matrix conduction, and radiation is

nominally 35 W. The observed rate of temperature change during the warm up is nominally 0.004 K/s (0.24 K/min) which is consistent with a 36 W parasitic. This consistency suggests that the additional loss is probably due to either some sort of pulse-tube inefficiency (jetting or some other mixing) or regenerator ineffectiveness (flow maldistribution). Both are explored in the following chapters.

Chapter 5. Computational Fluid Dynamic Evaluation of the Pulse-Tube

5.1 Introduction

The poor performance of the pulse-tube reported in the previous chapter indicated a large and unanticipated loss mechanism that becomes active only when the pulse-tube is operating (i.e., the loss is not a passive one such as conduction or radiation heat leak). The most likely sources of this loss are bypass flow in the regenerator or flow maldistribution in the pulse-tube. Therefore, it was necessary to model the flow within the pulse-tube in order to investigate the flow distribution associated with the current pulse-tube design and, if it was found to be a problem, re-design the flow path to improve the performance.

This chapter describes the flow characteristics associated with different configurations of the 300 W, 65K pulse-tube design. The computational fluid dynamic (CFD) modeling package *Fluent* version 6.1.22 is used to visualize the expected fluid flow pattern under the complex operating conditions and geometries associated with the pulse-tube. Particular emphasis is placed on the impact of the flow straighteners that are required at either end of the pulse-tube.

5.2 Porous Media Modeling

The flow path within the pulse-tube is filled in large part with flow refining media, such as screens and tube banks. Therefore, each zone of the pulse-tube is modeled in order to represent the momentum loss associated with the appropriate porous media. In the most

general situation, porous media are modeled in *Fluent* by the addition of a (negative) momentum source term to the standard fluid flow equations. The momentum loss term is composed of two parts: a viscous loss term and an inertial loss term, as shown by Eq. (5.5).

$$S_i = -\left(\sum_{j=1}^{3} D_{ij} \mu v_j + \sum_{j=1}^{3} C_{ij} \frac{1}{2} \rho v_{mag} v_j \right) \tag{5.5}$$

where S_i is the source term for the *i'*th zone of the pulse-tube in the momentum equation, D and C are prescribed matrices for the model that are related to the characteristics of the porous media that make up the pulse-tube, v_{mag} represents the magnitude of the total velocity, and the variable v_j accounts for the velocity in each direction (x, y, and z). The momentum sink contributes to the pressure gradient in the porous cell and therefore generates a pressure drop across the cell that is related to the fluid velocity in the cell, as mentioned in the *Fluent* user manual (2003).

Equation (5.5) can be simplified for a simple, homogeneous porous media

$$S_i = -\left(\frac{\mu}{\alpha} v_i + C \frac{1}{2} \rho v_{mag} v_i \right) \tag{5.6}$$

where α is the permeability, μ is the viscosity, ρ is the density, and C is the inertial resistance factor. Note that in general, C and α depend on the flow direction and are written as C_x, C_y, etc. At low flow rates, the inertial resistance factor, C, is assumed to be zero. For laminar flow through a porous media, the pressure drop is assumed to be proportional to the velocity and the inertial term is neglected so that the porous media model reduces to Darcy's Law:

$$\nabla p = -\frac{\mu}{\alpha}\vec{v} \tag{5.7}$$

The pressure drop in the *x*-direction can then be calculated according to:

$$\Delta p_x = \frac{\mu}{\alpha_x} v_x \, \Delta n_x \tag{5.8}$$

where Δn_x is depth or thickness of the media. Eq. (5.4) can be repeated for the *y*- and *z*-directions or in the axi-symmetric case the radial direction.

The inertial losses associated with porous media are included by using a non-zero *C*. The simplified form of the inertial loss component is:

$$\nabla p = -\sum_{j=1}^{3} C_j \left(\frac{1}{2} \rho v_j \, v_{mag} \right) \tag{5.9}$$

which can be written in terms of pressure drop in the *x*-direction

$$\Delta p_x \approx C_x \Delta n_x \frac{1}{2} \rho v_x v_{mag} \tag{5.10}$$

Equation (5.10) is repeated for the *y*- and *z* or radial directions. The total pressure drop in the *x*-direction is obtained by summing the viscous and inertial losses, given by Eqs. (5.8) and (5.10), respectively:

$$\Delta p_x \approx v_x \Delta n_x \left(\frac{\mu}{\alpha_x} + C_x \frac{1}{2} \rho v_{mag} \right) \tag{5.11}$$

Equation (5.11) is cast in the form of Eq. (5.6) by dividing through by the media depth in order to obtain a pressure gradient:

$$S_x \approx \frac{\Delta p_x}{\Delta n_x} \approx \left(\frac{\mu}{\alpha} v_x + C_x \frac{1}{2} \rho v_{mag} v_x \right) \tag{5.12}$$

When defining a homogeneous porous media zone into *Fluent*, the following inputs are required: viscous resistance ($\frac{1}{\alpha}$), inertial resistance (C), and porosity (γ). Since a pulse-tube consists primarily of screens, these parameters must be related to the screen geometry. It is assumed here that the screens are homogeneous and that the axial velocity component dominates the other velocity components so that $v_x \approx v_{mag}$, which simplifies Eq. (5.12):

$$\frac{\Delta p_x}{\Delta n_x} \approx \left(\frac{\mu}{\alpha} v_{mag} + C \ \frac{1}{2} \rho v_{mag}^2 \right) \tag{5.13}$$

The pressure drop related to internal flow can be expressed by

$$\Delta p_x = \frac{1}{2} f \rho \frac{\Delta n_x}{\beta} v_{mag}^2 \tag{5.14}$$

where f is the friction factor and β is the hydraulic diameter. The friction factor for laminar flow through a screen is often expressed in the following general form

$$f = \frac{A_1}{\mathrm{Re}_\beta} + A_2 \tag{5.15}$$

where A_1 and A_2 are constants and Re_β is defined by

$$\mathrm{Re}_\beta = \frac{\rho v_{mag} \beta}{\mu} \tag{5.16}$$

where β is the hydraulic diameter of the screen mesh. By substituting equations (5.15) and (5.16) into equation (5.14), an expression in the form of equation (5.13) is achieved. A summary of this manipulation can be viewed below

$$S_x = \frac{\Delta p_x}{\Delta n_x} = \frac{A_1 \mu \gamma V_s}{2\beta^2} + \frac{A_2 \rho \gamma^2 V_s^2}{2\beta} \tag{5.17}$$

where γ is the porosity of the screen and V_s is the superficial or inlet velocity. The superficial velocity represents the velocity of the flow if no porous media was present. Superficial velocity then differs from the physical velocity according to the porosity, as seen in the following equation.

$$v_{mag} = \gamma V_s \tag{5.18}$$

Fluent requires that superficial velocities are used in equation (5.17), hence the distinction between physical and superficial velocities. From equations (5.13) and (5.17), one can deduct that the required *Fluent* inputs for a screen filled zone are

$$\frac{1}{\alpha} = \frac{A_1 \gamma}{2\beta^2} \tag{5.19}$$

$$C = \frac{A_2 \gamma^2}{\beta} \tag{5.20}$$

The coefficients for A_1 and A_2 can be determined experimentally by measuring pressure drop or by using correlations from the literature; for example, the correlation developed by Miyabe et al.(1982)which is valid for laminar, oscillatory flow, where the reynolds number is between 5 and 2000, through woven screens indicates that the coefficients are $A_1 = 33.6$ and $A_2 = 0.337$.

The porous media model described above is applied to various zones of the 300 W pulse-tube. The following zones of the pulse-tube are represented with porous media: the tube bank of the aftercooler, the screens of the regenerator, the screens of the cold heat exchanger (CHX), and also the screens of the hot heat exchanger (HHX).

5.3 User Defined Boundary Conditions

The moving compressor piston is not modeled explicitly in the CFD simulation. Therefore, since a pulse-tube operates under an oscillatory flow condition, it is necessary to define an appropriate flow inlet for the model. *Fluent* will model constant flow inlets and other more common configurations, but not oscillating flow. However, *Fluent* allows the use of user-defined functions (UDFs) to simulate more complicated situations.

The pressure wave generated by the compressor is simulated using a sinusoidal pressure variation that is specified by an external subroutine written in the programming language C. *Fluent* requires the charge pressure of the pulse-tube as an initial condition and therefore the pressure variation at the compressor boundary is defined by the following formula

$$P_{comp} = A_{swing} \sin(\omega t) \tag{5.21}$$

where P_{comp} is the instantaneous compressor pressure, A_{swing} is the amplitude of the pressure variation, ω is the angular operating frequency, and t is time.

The reservoir is also not modeled explicitly; the boundary between the reservoir and the pulse-tube is simulated by another UDF. The reservoir UDF allows the specification of the appropriate reservoir size that will ensure the correct phase shift. The UDF uses the ideal gas law with helium properties to calculate the flow across the reservoir/pulse-tube boundary based on a mass balance. The mass of helium in the reservoir (m_{rsv}) is calculated according to:

$$m_{rsv} = \frac{P_{ch} V_{rsv}}{R T_{vol}} \tag{5.22}$$

where m_{rsv} is the mass in the reservoir, P_{ch} is the charge pressure, R is the gas constant, T_{vol} is the temperature of the volume. The UDF assumes an isothermal condition and determines the pressure in the reservoir at every iteration; continuity allows the calculation of the mass flow rate across the boundary of the reservoir at all times.

5.4 Design #1 - Original Pulse-tube Design

The CFD model of the original, as specified, pulse-tube design is shown in Figure 5.1. This model includes the entire pulse-tube: the compressor, aftercooler, the pulse-tube, and the reservoir (although the reservoir is controlled and modeled by a UDF). A mesh was designed specifically to capture the interaction between the fluid and the wall within the pulse-tube and is therefore concentrated in the near-wall region. The mesh created for the original design can also be viewed in Figure 5.1. Note that the model is two-dimensional due to the assumption of axi-symmetric flow.

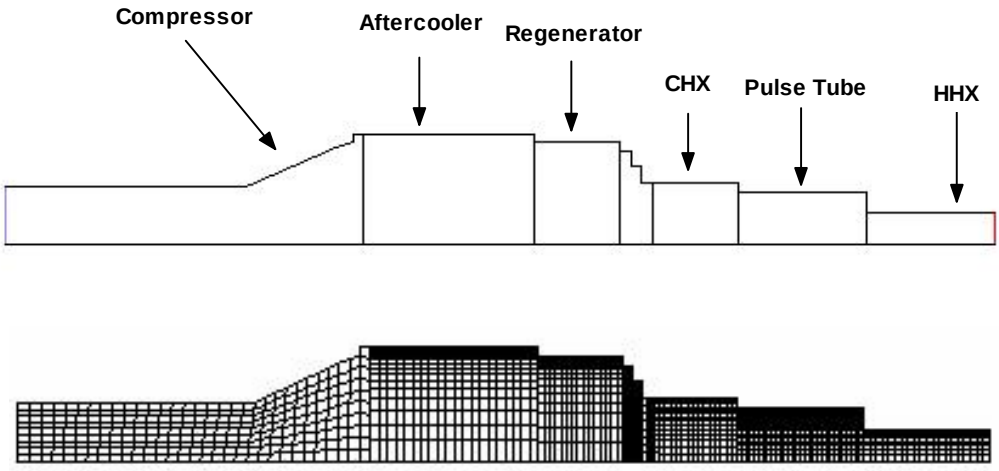

Figure 5.1. Design 1, the as-specified design of the high-capacity pulse-tube.

For straight screen mesh components, such as the HHX and regenerator, the *Fluent* inputs of $1/\alpha$ and C, see equations (5.19) and (5.20), are based upon the assumption of A_1=33.6 and A_2=.337 from Miyabe (1982).The values of porosity and hydraulic diameter are based upon the screen size.

The aftercooler and CHX were modeled as screen beds. The original geometry for the aftercooler is a tube bank which consists of 512 tubes of 0.1 inch diameter that are 4.0 inch long. The CHX consists of 15 tubes of 0.5 inch diameter that are 2 inch long; the tubes are filled with 50 mesh screens. Photographs of the aftercooler and the CHX are shown in Figure 5.2.

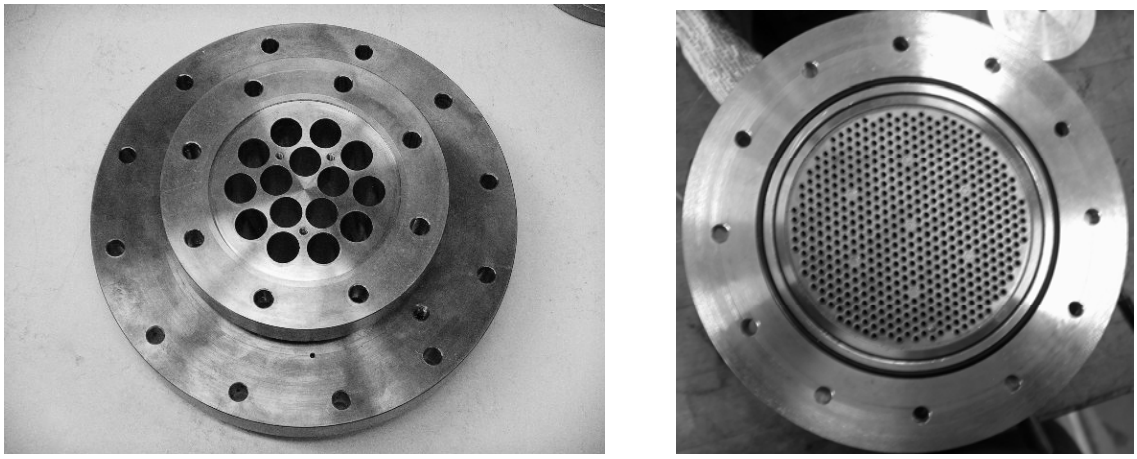

Figure 5.2. The design of the tube banks in the CHX (left) and the aftercooler (right).

To model this porous media a pressure drop across each component must be known. The pressure drop estimations allow one to determine the *S* value associated with Eq, (5.17) and back solve for the porosity, the inertial coefficient, and the viscous coefficients required for the model. For the CHX the pressure drop estimation was taken from the chapter 3 results, where each of the fifteen tubes would have a pressure drop of 15.15 [kPa]. The fifteen tubes are then treated as a continuous screen bed with the same outside diameter as an inscribed circle around the outer ring of the tubes. To solve for a representative porosity (γ) and hydraulic diameter (β) that would correspond to an equivalent bed of woven screens, one of the variables must be constrained to a reasonable value. In this case, the porosity was set to 0.60 and this resulted in the very small hydraulic diameter of .0023 inch. Knowing the porosity and hydraulic diameter allowed the *Fluent* parameters for the aftercooler to be determined using the method descrbed above for the HHX and regenerator.

The boundary conditions were specified for each zone: all components except the aftercooler and hot heat exchanger (HHX) were modeled as having adiabatic walls, consistent with the thermal vacuum environment used to carry out the testing and a no-load operating condition. The aftercooler and HHX were modeled with an isothermal wall condition of 300 K, consistent with the presence of cooling water in these components. The exit of the experimental pulse-tube is interfaced with an inertance tube in order to allow for the proper phase between the mass flow rate and oscillating pressure. However, modeling an inertance tube in *Fluent* would dramatically increase an already long computation process; as a result an orifice was placed at the exit face of the HHX. It is difficult to accurately model the flow through an orifice using *Fluent*; however, *Fluent* offers a boundary condition referred to as a porous jump which behaves at the system level as an orifice but provides an instantaneous, uniform pressure drop across a plane. *Fluent* requires a constant loss factor in order to generate the correct pressure loss across this boundary. The following equation is used to quantify the loss factor (k_L)

$$\Delta p = \frac{1}{2} k_L \rho v_{mag}{}^2 \tag{5.23}$$

where Δp was set to the value of the pressure oscillation while the physical velocity, v_{mag}, was determined using a predicted mass flow rate obtained from the thermodynamic model of the pulse-tube. The value of the mass flow rate at the HHX was predicted to be 47 g/s, resulting in a velocity of 79.8 m/s. The resulting orifice loss factor, k_L, is 26.35.

The model of the original pulse-tube design was run for a simulated time period of approximately half a second or 23 cycles. The simulations for the modified designs that are described in subsequent sections were run for various lengths of time that depended

both on the computer resources that were available as well as the initial flow distribution that was observed. The actual computational time required for the 23 cycles is approximately 5 hours. Figure 5.3 illustrates the predicted temperature contours through the system at various times during the 23rd cycle and indicates clearly that a large amount of swirling flow is present in the pulse-tube. The images labeled #1, 2, and 3 in Figure 5.3 show the instantaneous temperature distribution in the pulse-tube at various times in the 23rd cycle and show clearly that a large scale swirling flow structure is present.

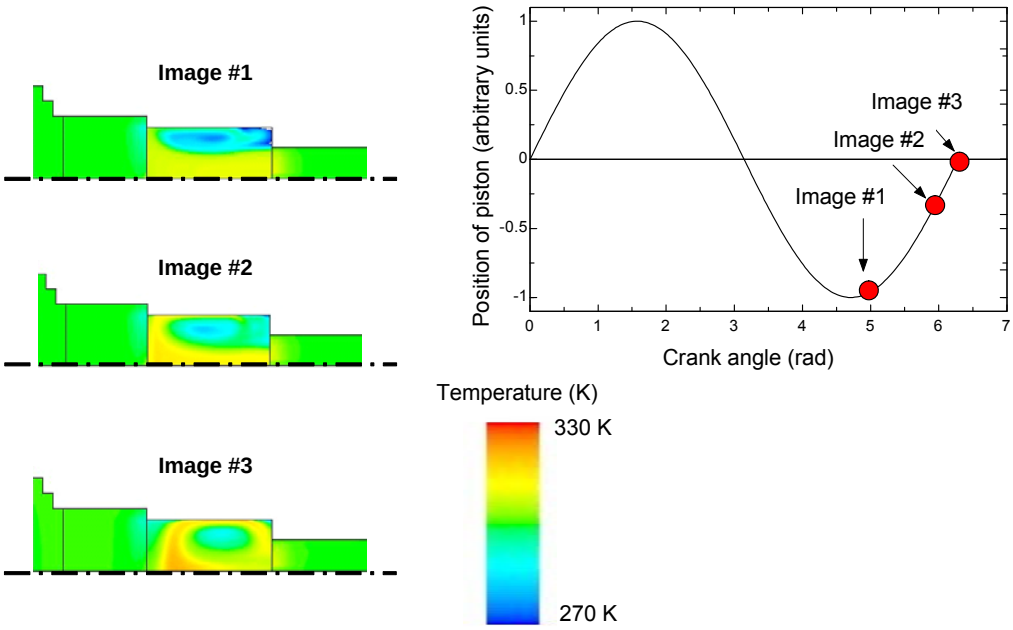

Figure 5.3. Temperature contours in the system predicted by the CFD model at various times in the 23rd cycle for the original design.

The large vortices evident in the temperature distributions indicate a large amount of mixing of the hot and cold gas, which destroys the cooling capacity of the cooler by preventing any temperature separation between the two ends of the pulse-tube and also reducing the efficiency of the expansion process experienced by the cold gas in the pulse-tube. The top left picture (image #1) in Figure 5.3 illustrates cold gas trapped in the

sharp transition between the HHX and the pulse-tube. Image #2 shows the hot gas starting to swirl and mix with the cold gas. Finally, image #3 shows the hot gas completely encompassing the cold gas. The plot shown in Figure 5.3 illustrates the location of the images in time, relative to the pressure oscillation that defines a cycle. The swirling behavior is either a consequence of the sharp transition between the HHX and the pulse-tube or the resistance of the screen mesh that is inserted inside the HHX. These observations motivated the investigation of two modified designs, one in which the screen mesh resistance is removed (Design #2) and another in which the transition geometry is altered (Design #3).

5.5 Design #2 – Removal of Porous Media from the Hot Heat Exchanger

The second design looks at a modification to the original design in which the porous media in the HHX is removed in order to reduce the resistance in the HHX and, hopefully, eliminate the swirling effect. All of the other parameters and boundary conditions are the same as was described for the original design. Figure 5.4 illustrates the temperature contours predicted by the CFD model for Design #2.

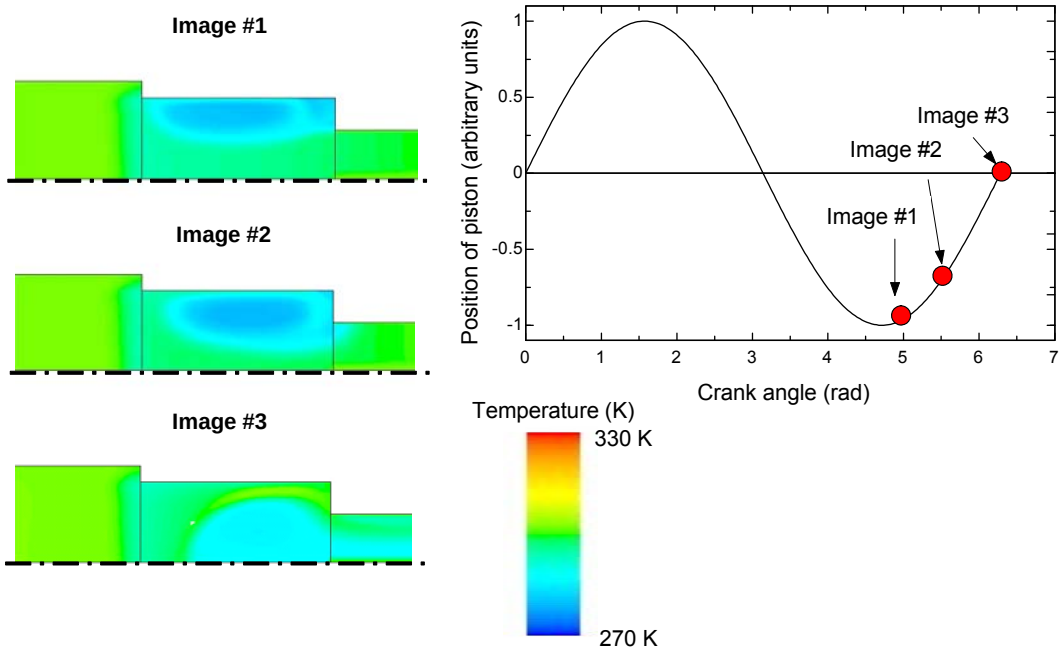

Figure 5.4. Temperature contours predicted for Design #2 during the 6th cycle.

The swirling action shown in Figure 5.4 is less severe than what was observed for the original design; however it is clearly still present. The other obstacle to high performance is the increased displacement of the cold gas. Since the porous media is removed from the HHX, the gas moves further up into the HHX. The constant wall temperature of the HHX is 300 K, which warms the cold gas and therefore reduces the cooling effect. The simulation was run for a significantly shorter time, six cycles, because of the poor visual performance that the pulse-tube was showing. The swirling is still present and thus the problem lies in the geometry of the transition and not in the screen resistance.

5.6 Design #3 – Tapered Transition in HHX without Porous Media

In the third design, the HHX was tapered and contained no screens in order to allow a smoother transition between the pulse-tube and the inertance tube. Also, in this design the CHX is changed from fifteen half inch diameter holes filled with screens to a single, 2.5 inch diameter tube in an effort to reduce the pressure drop. The porosity and other *Fluent* inputs required to simulate the upper part of the CHX were changed in order to correctly represent this modification. Figure 5.5 illustrates the design changes along with the detailed mesh used in the simulation.

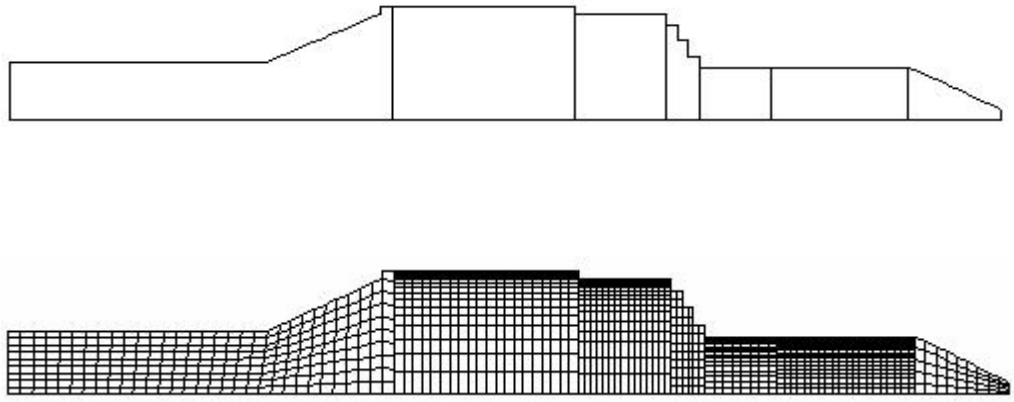

Figure 5.5. Design #3 – note the tapered transition at the HHX (which is not filled with screens) and the altered CHX geometry.

Figure 5.6 illustrates the temperature contours in the pulse-tube predicted by the CFD model for design #3.

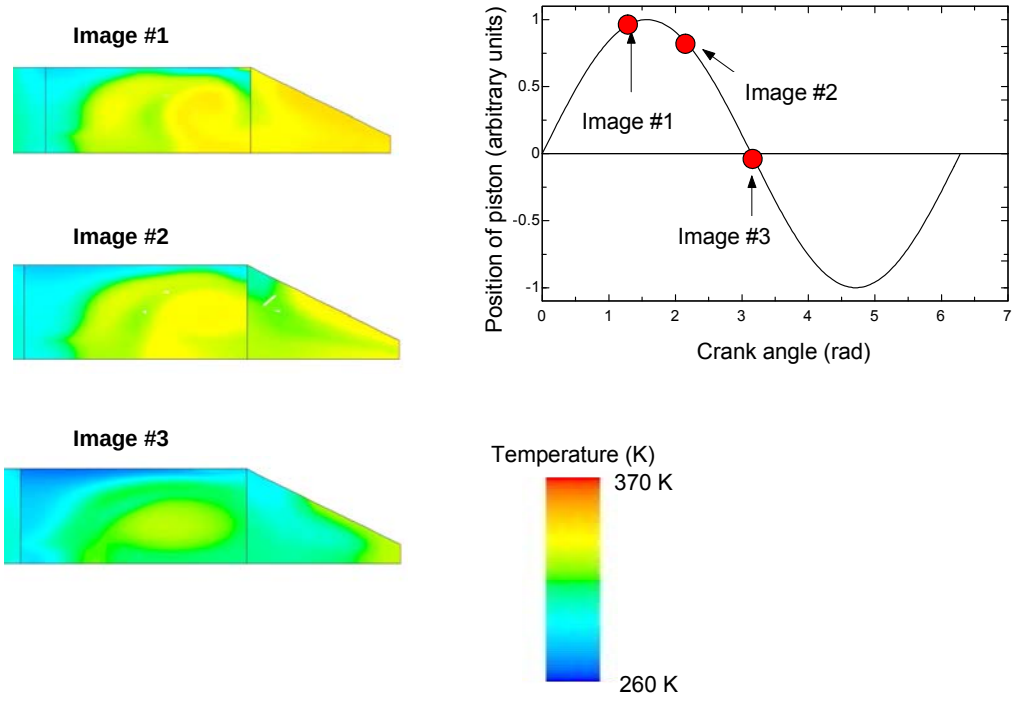

Figure 5.6. Temperature contours predicted by the CFD model for Design #3 during the 124th cycle.

The simulation of Design #3 was run for 124 cycles or 2.8 seconds of actual time (the computational time was much longer). The temperature of the cold end is not reduced significantly relative to the first two designs despite the fact that the model was run for a significantly longer time; this indicates the generally poor cooling performance of this design. The first image in Fig. 5.6 shows that mixing still exists in the pulse-tube, while the second image is a further evolution of the vortex. The third image shows the cold gas with a "pocket" of hot gas in the middle. Once again the cold gas has traveled into the HHX, which reduces the cooling capacity of the pulse-tube. As observed for Design #2 which had porous media in the HHX, the cold gas tends to travel a significant distance into the HHX. Therefore, the next design focuses on the insertion of a porous media into the HHX.

5.7 Design #4 – Tapered Transition in HHX with Porous Media

Design #4 is essentially the same as Design #3 except that a porous media, equivalent to 50 mesh copper screens, are inserted in the HHX. Figure 5.7 illustrates the temperature contours in the system predicted by the CFD model for Design #4.

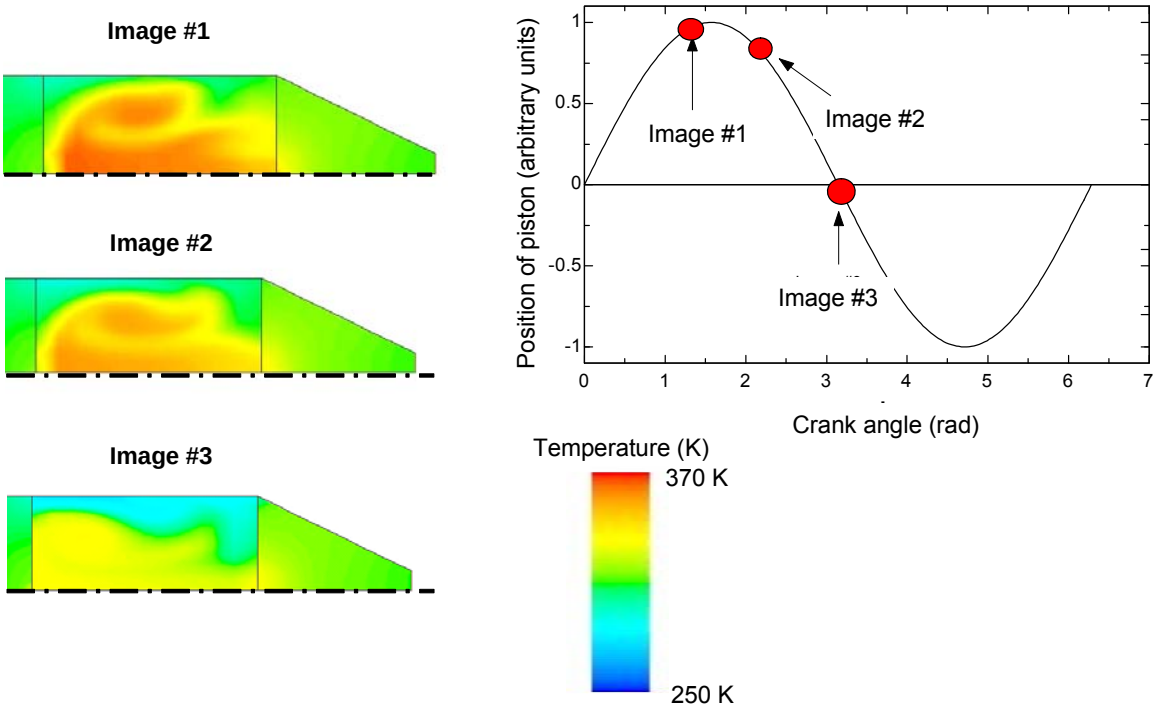

Figure 5.7. Temperature contours predicted by CFD model for Design #4 for the 186th cycle.

This simulation was run for 186 cycles or 4.1 seconds of actual time. The same general flow phenomena are observed in this design as was observed in Design #3 in which the hot gas swirls and mixes with the cold gas. The porous media in the HHX does prevent the cold gas from traveling into the HHX any significant distance; however, this design does not seem promising relative to its use as an efficient refrigeration device.

5.8 Design #5 – Hollow Tapered Transition in series with a HHX filled with Porous Media

Design #5 combines the principles used in the previous designs in hopes of developing a smoother fluid flow. The design uses a HHX filled with a porous mesh which has the same diameter as the pulse-tube in-line with an empty, tapered flow transition to the inertance tube diameter. All other components and boundary conditions are the same. Figure 5.8 illustrates the internal design of the pulse-tube.

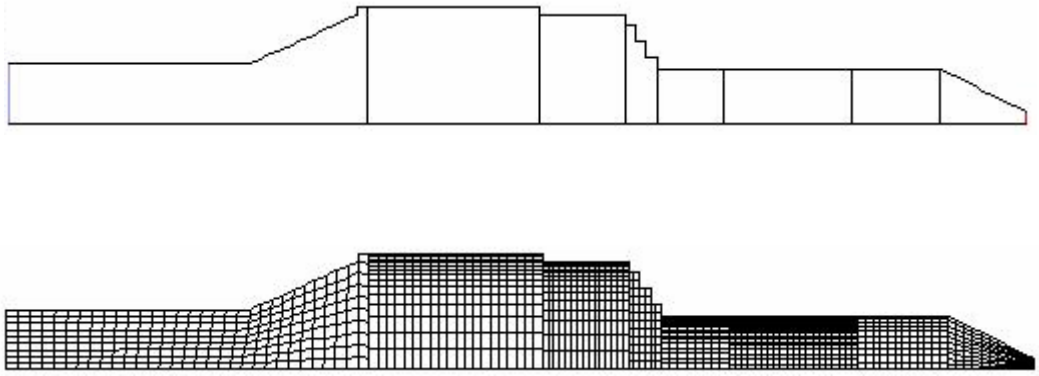

Figure 5.8. Mesh and internal geometry of Design #5 complete with porous HHX and open transitional zone to inertance tube.

The HHX is designed with the equivalent of a 50 mesh copper screens with a 2.0 inch length. This allows for flow straightening and essentially limits the flow of the cold gas by keeping the gas in the pulse-tube. The tapered transition is completely open, allowing the flow to mix and move freely into and out of the inertance tube. Figure 5.9 illustrates the temperature contours predicted by the CFD model for this design.

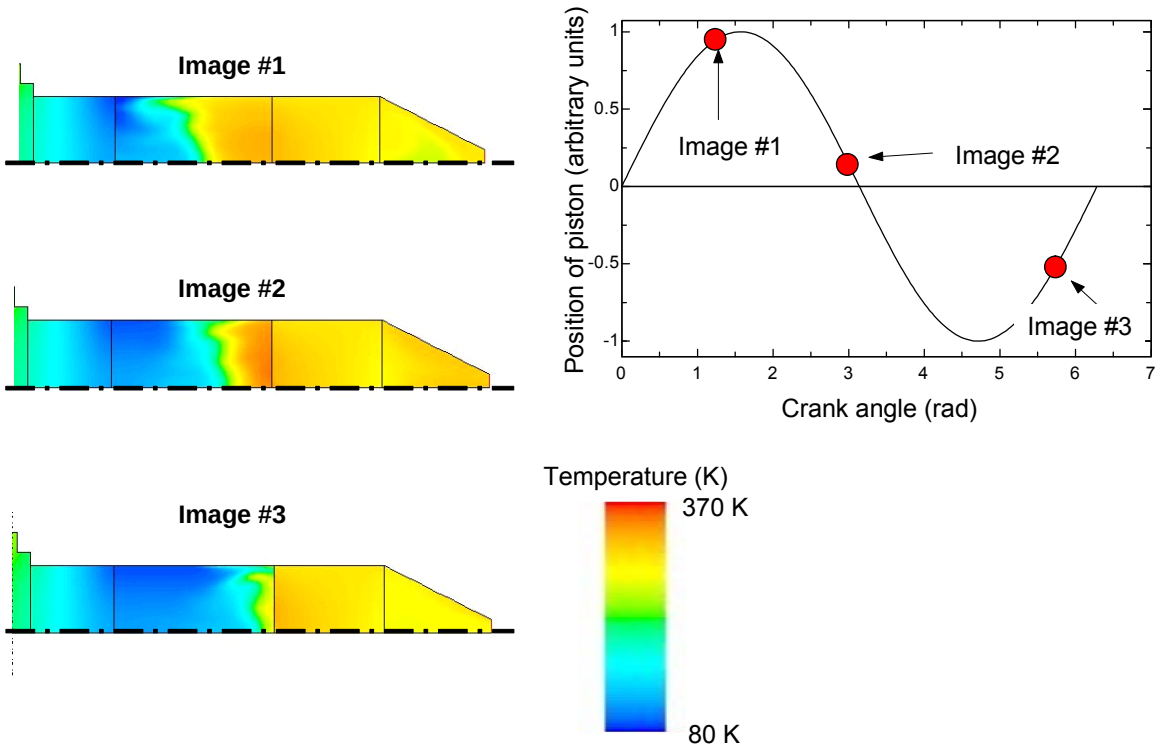

Figure 5.9. Temperature contours predicted by the CFD models for Design #5 for the 1418th cycle.

The simulation was run for 1418 cycles or 31.5 seconds of actual time. The model was run for an extended period of time because of the improved performance. Notice that the flow in the pulse-tube remains stratified in contrast to the flow associated with the other designs; the cold gas penetrates approximately 75% of the way through the pulse-tube, this is due to the longer simulation time. This design demonstrates markedly better performance than the as-specified geometry associated with the original design. The jetting of the gas that was directly responsible for the mixing of cold and hot gas, is absent from this design due to the flow straightening effect that the screens in the HHX have.

5.9 CFD Modeling Conclusions

The *Fluent* simulations show that the transitions between the sub-components in the pulse-tubes are very important to its performance and must accomplish adequate flow straightening in order to achieve an acceptable cooling capacity. The biggest design challenge is related to the drastic decrease in size from the regenerator to the pulse-tube to the inertance tube. Scaling down from the 5 inch diameter regenerator ultimately to a 0.5 inch inertance tube leads to unforeseen challenges as compared to a lower capacity pulse-tube which might require going from a 0.5 inch regenerator to a 0.25 inch inertance tube. The same problems exist in the smaller pulse-tube, but since they are on a smaller scale the flow distribution issues are not as severe as for the larger pulse-tube. When large reductions are required, the gas will tend to jet and cause unwanted mixing. The other advantage of a smaller pulse-tube is increased wall friction; the flow is more controlled in a 0.5 inch diameter pulse-tube as compared to a 2.5 inch diameter one as the walls “hold” the flow better.

Chapter 6 – Testing of the 2nd Generation High-Capacity Pulse-Tube

6.1 Introduction

The hardware modifications that were motivated by the CFD modeling described in chapter 5 are presented in this chapter. The design changes involved several of the components within the pulse-tube refrigerator; these include the inertance tube, pulse-tube, cold heat exchanger (CHX), and hot heat exchanger (HHX).

6.2 Initial Design Changes

The initial design changes were focused on addressing suspected trouble spots that were suggested by the initial pulse-tube testing and supported through subsequent component testing of the pulse-tube. For example, the amplitude of the pressure oscillation within the pulse-tube was substantially less than the amplitude measured in the compression space. This experimental result suggests that the flow resistance of one of the components between the compression space and the pulse-tube must be higher than was anticipated during the design process. In order to investigate this further, pressure drop data was obtained over a range of volumetric flow rates using a room temperature, steady flow test. The measured pressure drop as a function of the volumetric flow rate is shown in Figure 6.1. The total pressure drop through the assembly consisting of the regenerator, cold heat exchanger, pulse-tube, and hot heat exchanger is shown. Also shown is the pressure drop across the sub-assembly consisting of the cold heat exchanger (CHX), hot heat exchanger (HHX), and pulse-tube (PT) as well as the pressure drop across the hot heat exchanger alone. It is clear from this data that there is a large pressure drop across

the HHX, nearly as large as the pressure drop across the regenerator. An unacceptably large pressure drop is also observed across the cold heat exchanger (the difference between the curves labeled HHX+PT+CHX and HHX). This was unexpected and undesirable, therefore the hot and cold heat exchangers were redesigned in an effort to reduce this pressure loss and improve the flow distribution throughout the system.

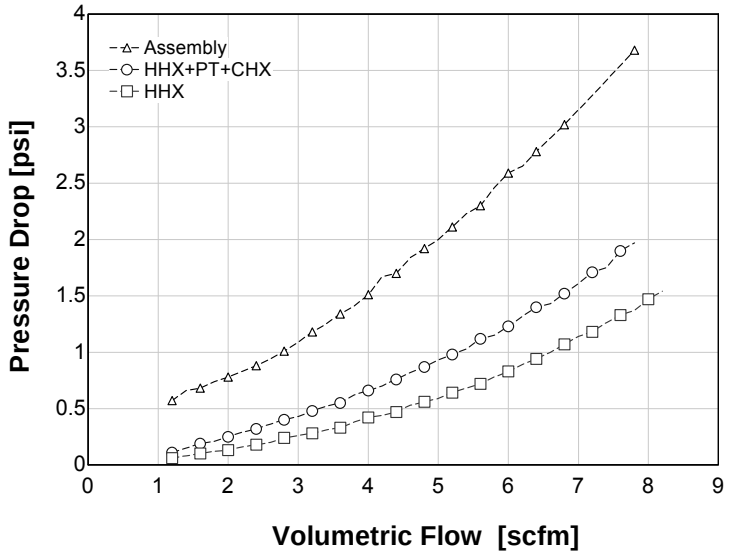

Figure 6.1. Pressure drop across the pulse-tube as a function of the volumetric flow rates. The assembly refers to the regenerator, CHX, HHX, and PT in series.

6.2.1 Hot & Cold Heat Exchanger Design Modification

The CHX was redesigned so that original, the 15 screen-filled hole pattern was eliminated and replaced by an open, screen-filled area, as shown in Figure 6.2

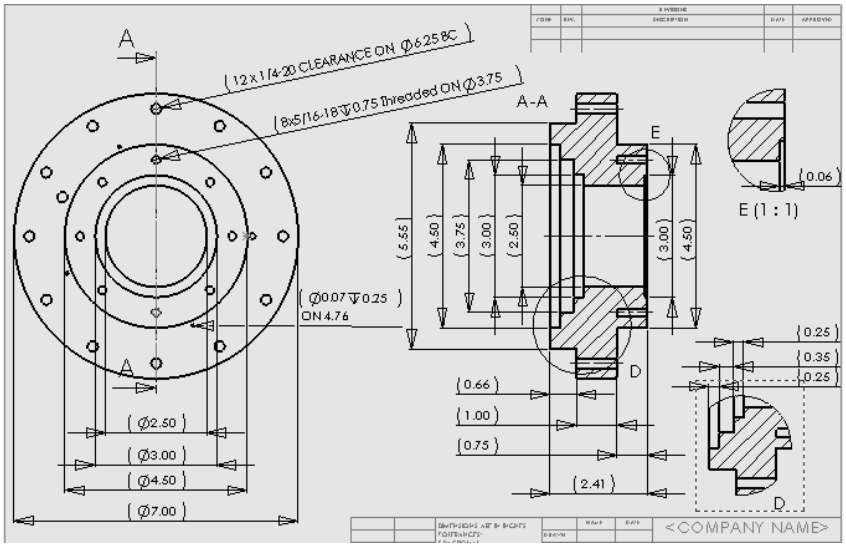

Figure 6.2. Mechanical drawing of new CHX with fifteen-hole pattern removed for better, more predictable pressure-flow behavior.

The motivation behind the elimination of the 15 holes was to remove any jetting produced by these holes within the pulse-tube. CFD modeling, described previously, clearly showed that the removal of these holes would result in a more stratified flow and therefore better pulse-tube performance. The removal of the holes will also reduce the pressure drop across the CHX which improves performance by increasing the acoustic power delivered to the pulse-tube. However, the disadvantage associated with removing the holes is that the large screens shown in Figure 6.2 do not provide an effective thermal communication to the heat source that represents the refrigeration load. The key motivation behind the 15 hole design of the CHX was to achieve a sufficient heat exchanger performance as was discussed in Chapter 3 Section 2.2.1. However, this aspect of the pulse-tube performance was deemed to be of secondary importance in relation to achieving the appropriate gross refrigeration power.

The HHX was redesigned according to the CFD modeling results presented in Chapter 5. A flow straightening cone was machined into an insert for the new HHX in order to provide a smooth transition between the HHX and inertance tube. Figure 6.3 is a detailed drawing the flow straightening HHX

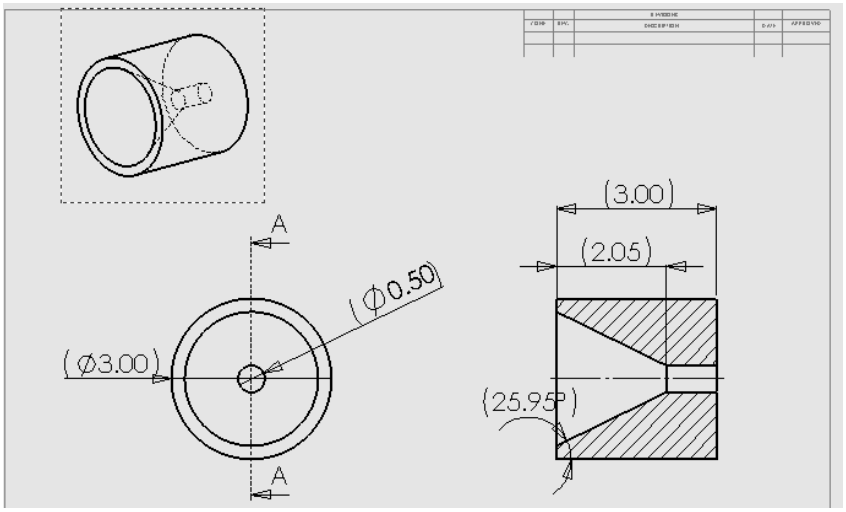

Figure 6.3. Redesign of the HHX with a flow straightening cone.

The change in the HHX design does not provide the isothermal wall condition that is prescribed by the model; however, as with the cold heat exchanger performance, this was viewed as a secondary problem compared to the significance of the flow distribution.

Figure 6.4 shows a cut-away view of the 2nd generation pulse-tube with the screens removed for clarity.

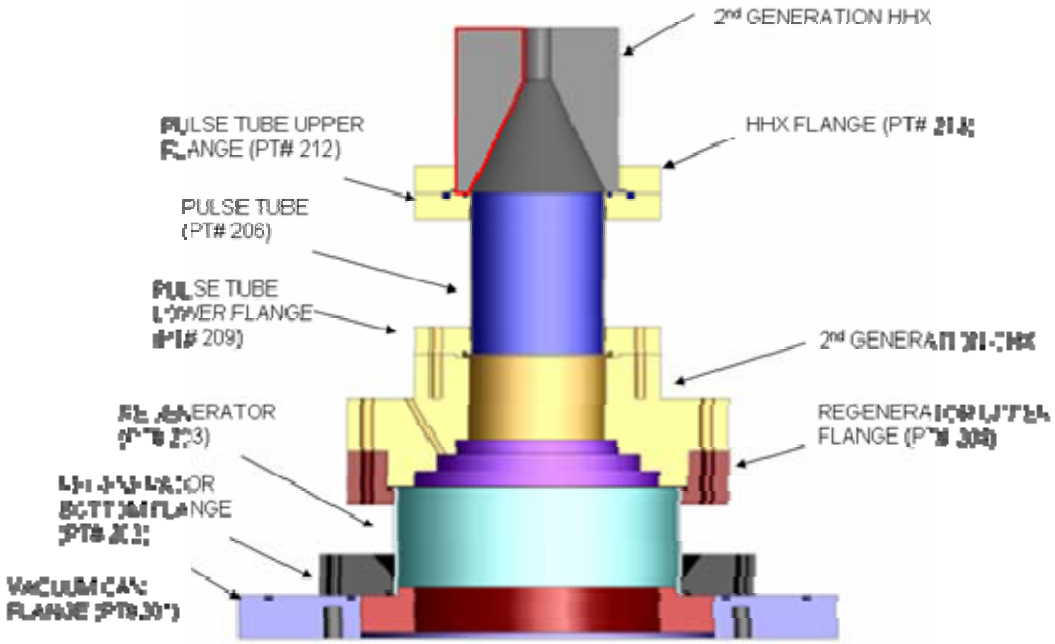

Figure 6.4. Cut-away view of the 2nd generation pulse-tube with new CHX and HHX.

Several tests were accomplished using the 2nd generation pulse-tube in various configurations.

6.2.2 Tests with no Screens in CHX and HHX

Initially, the new CHX and HHX were inserted with no screens. Five thermocouples were used to measure the performance of the apparatus; two thermocouples were placed inside the CHX and penetrated the gas flow, the others were attached externally to the regenerator, the pulse-tube, and the HHX. The rest of the test setup was unchanged from the initial test conditions that were presented in Chapter 4. Multi-layer insulation (MLI) was placed around the CHX and regenerator to minimize the radiative heat leak. This test resulted in a no-load temperature of 230 K; marginally improved from the initial test

results presented in Chapter 4 but still very far from the target. Figure 6.5 shows a cooldown curve produced by this test.

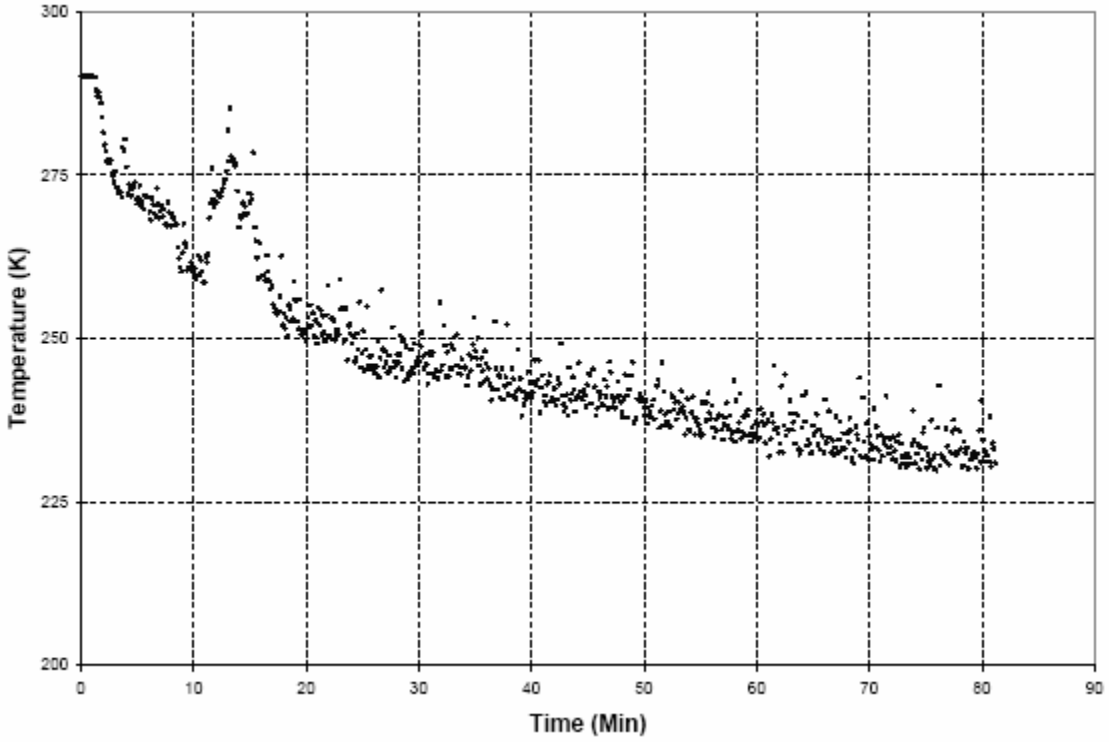

Figure 6.5. Cooldown curve from the test with no screens in the CHX or HHX.

6.2.3 Tests with 6 Screens in CHX and Open HHX

The next test added some flow straightening at the CHX in order to investigate the significance of this design change; 50-mesh flow straightening screens that are placed in the steps of the cold heat exchanger that are evident in Figures 6.2 and 6.4. Two screens were installed with epoxy in each of the steps for a total six screens. The HHX was left open and the instrumentation used for this test is the same setup as the previous test. The resulting no-load temperature was 182 K; a significant improvement in performance for an apparently minor modification to the design. This test provided some verification of

the CFD models which also predicted that flow straightening is critically important to the pulse-tube performance. Figure 6.6 shows the cooldown curve produced by this test.

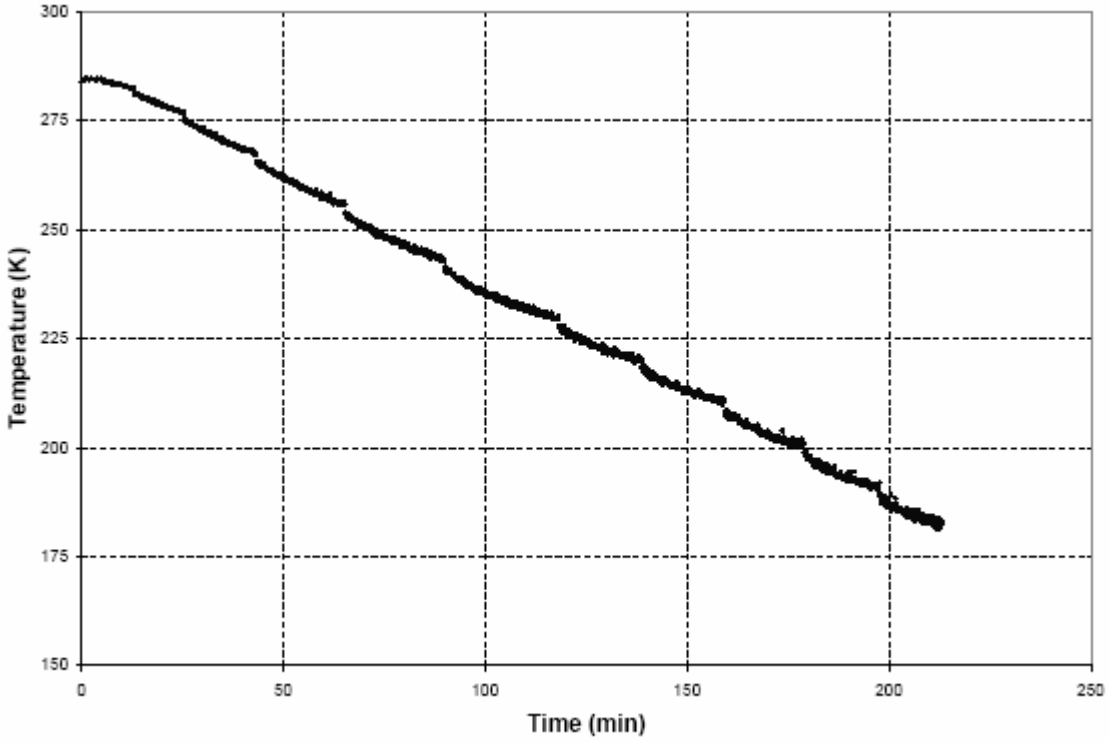

Figure 6.6. Cooldown curve for test with 6 screens in CHX and open HHX.

6.2.4 Tests with 6 Screens in CHX and 10 Screens in HHX

The HHX geometry was altered slightly so that it would accommodate 10, 50-mesh screens with 2.7 inch diameter for the transition between the HHX and the pulse-tube. The screens were packed in place and secured with epoxy. Tests was carried out at various strokes and valve positions. The instrumentation was the same as the previous test runs. The resulting no-load temperature was 112 K, which is a significant improvement over the 182 K measured with no flow straightening in the HHX. This result also provides some verification of the CFD modeling presented in Chapter 5 which

predicted that flow straightening played a critical role in both the HHX and CHX. Figure 6.7 shows the cooldown curve produced by this test

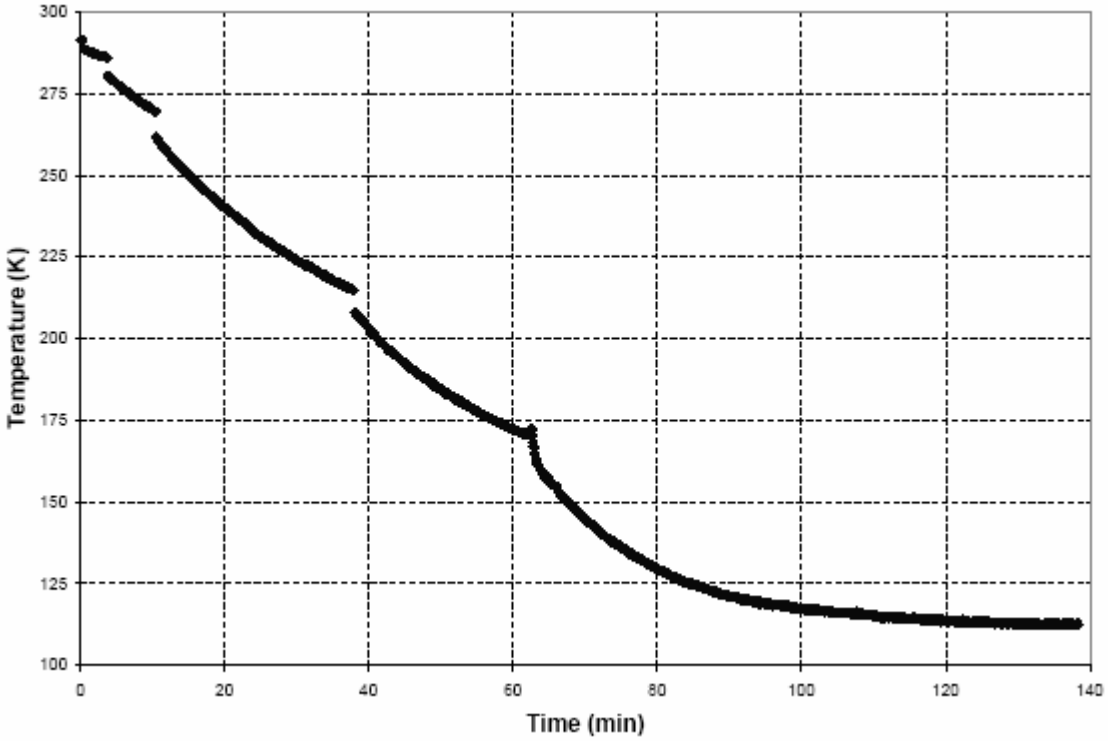

Figure 6.7. Cooldown curve for test with 6 screens in CHX and 10 screens in HHX.

6.2.5 Tests with 13 Screens in CHX and 10 Screens in HHX

The previous tests showed that flow straightening had a large impact on the pulse-tube refrigerator performance. Therefore, additional flow straighteners were place in the cold heat exchanger in order to ensure stratified flow entering the pulse-tube. The cold heat exchanger was modified in order to provide a pocket that allows 7, 2.5 inch diameter 50-mesh copper screens to be installed between the pulse-tube and the CHX. The additional screens are illustrated in Figure 6.8. The instrumentation was slightly modified; the

thermocouple placement for the test is also shown in Figure 6.8. The rest of the instrumentation remained the same from the previous test.

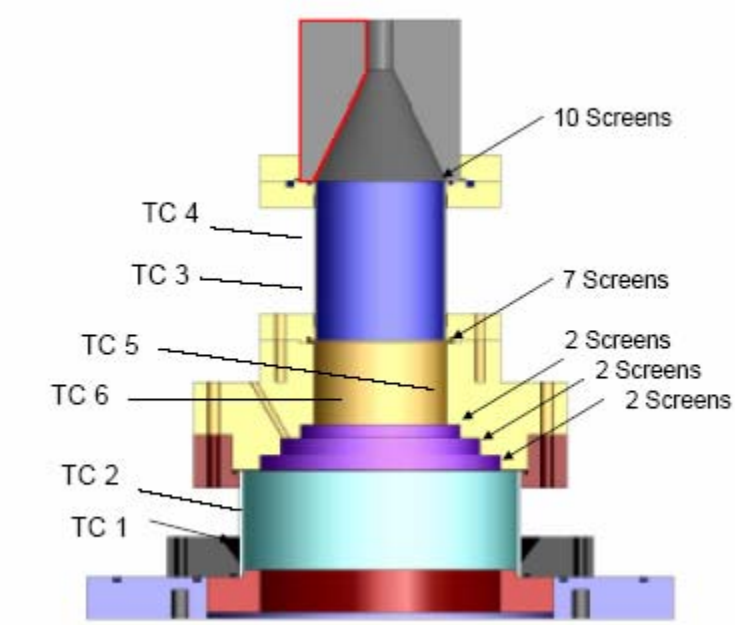

Figure 6.8. Additional screens added to the CHX and the location of the thermocouples.

The test was again carried out for various strokes and a final temperature of 140 K was achieved. Note that this is a higher temperature than could be achieved in the previous configuration. Therefore, inserting the additional screens in the CHX appears to have either created or intensified a loss mechanism resulting in reduced performance.

The flow distribution for this configuraiton was explored by running a frost test in which the pulse-tube was operated without a vacuum can or radiation shielding. The pattern of the frost formation was observed in order to identify a corresponding flow maldistribution that might be causing poor performance. Figure 6.9 shows the frost line that was developed during the test. Note the distinctly uneven distribution over the pulse-

tube with the frost advancing to the top of the pulse-tube on one side while the frost 180° away does not reach the bottom of the pulse-tube. This seems to indicate a very uneven flow distribution that may correspond to a large loss mechanism.

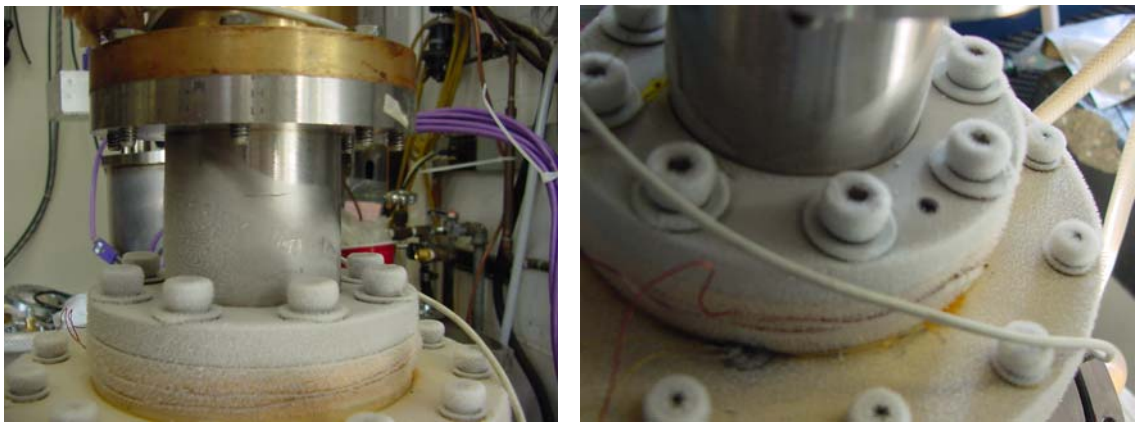

Figure 6.9. Pictures of the pulse-tube from opposites sides during frost test.

6.2.6 Tests with CHX Completely Filled with Screens and 10 Screens in HHX

Based on the frost line tests shown in Figure 6.6, it was decided that more screens should be installed in the CHX in order to improve the flow distribution. Therefore, the entire CHX block was filled with 50-mesh copper screens; the geometry of the flow straightening channel can be viewed in Figure 6.2. The test was run again for various strokes and a final temperature of 138 K was achieved. This is nominally consistent with the previous test and still much higher than the test with only 6 screens inserted in the CHX. Figure 6.10 shows the cooldown curve for this test.

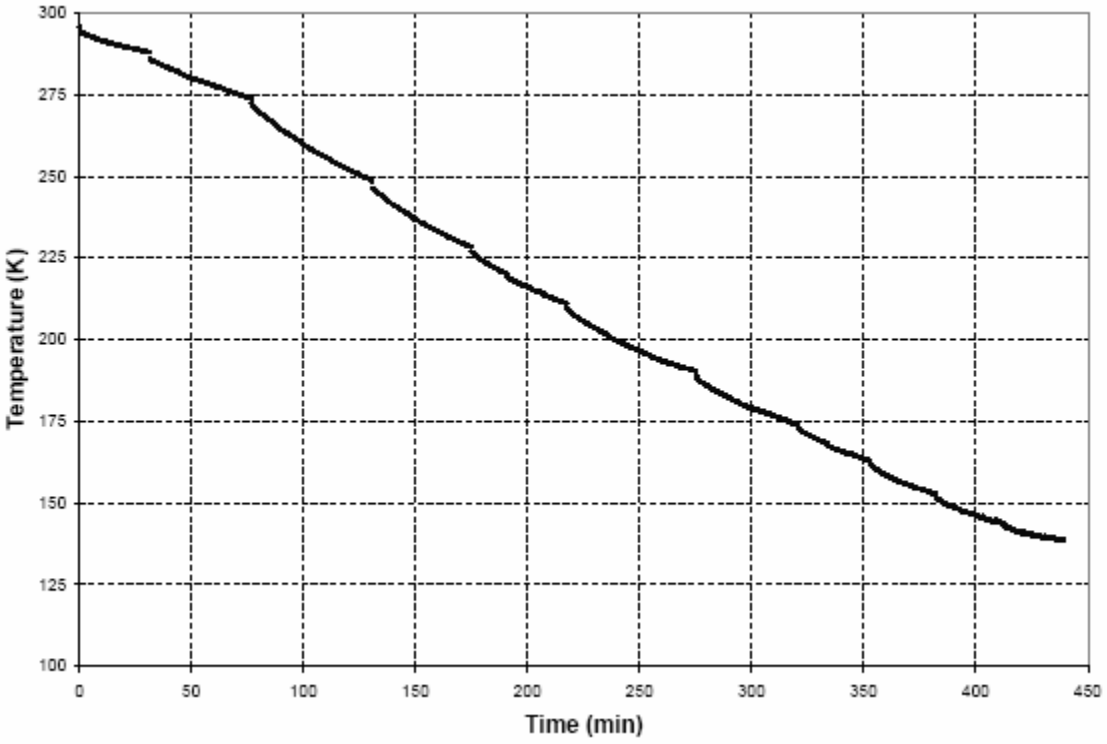

Figure 6.10. Cooldown curve for test with CHX completely filled and 10 screens in HHX.

6.3 Regenerator Bypass Flow

The original tests described in Chapter 4 clearly showed that the shortfall in performance could be attributed to either the pulse-tube or the regenerator. The results described in Section 6.2 showed that a substantial loss could be attributed to the pulse-tube. However, given the no-load temperature of 138 K that could be achieved with the CHX filled with screens, it was decided has to investigate the regenerator loss more completely.

The regenerator was designed using the program REGEN which thoroughly explores most of the possible loss mechanisms. However, REGEN is a fundamentally one-dimensional model and therefore the possibility of bypass flow is not included in the

calculation. Therefore, bypass flow was not considered during the original design of the regenerator. The sintered stack of screens used as the regenerator has a low aspect ratio (the length-to-diameter ratio is 0.4). When the rigid stack is inserted into a tube it is easy to envision the formation of a relatively large housing-to-regenerator gap due to imperfections (particularly out-of-roundness) in either the stack or the housing.

Figure 6.11 shows the conceptual flow circuit that is associated with bypass flow; two possible flow paths exist: either through the housing-to-regenerator gap or through the regenerator itself. The resistances representing these flows are in parallel as the same pressure drop is seen across either path. The bypass flow is not completely regenerated and therefore, during the hot-to-cold flow process, the bypass flow will enter the cold heat exchanger at a higher temperature than the regenerated flow. The regenerated and bypass flows are assumed to mix as they enter the cold heat exchanger in order to produce a mixed flow.

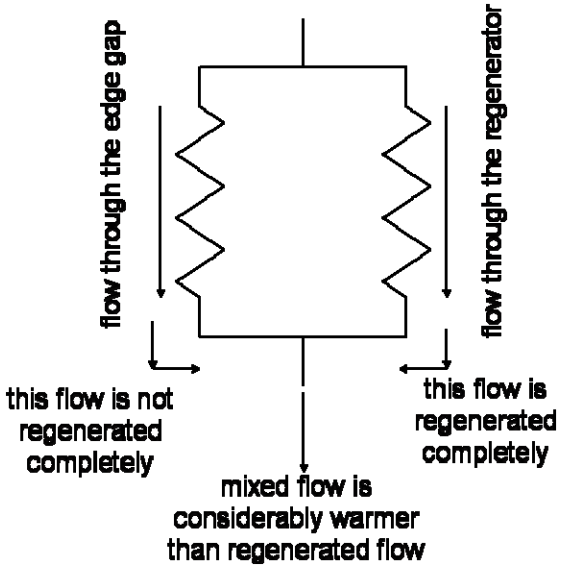

Figure 6.11. Flow resistance network illustrating the effects of regenerator bypass flow.

The possible amount of loss from this type of interaction is investigated using the simplified analysis presented here. The pressure drop across the regenerator (ΔP_r) is represented by the following equation

$$\Delta P_r = \frac{f_r \rho L_r V_r^2}{2 D_{hyd,r}} \tag{6.1}$$

where ρ is the average density, L_r is the length of the regenerator, V_r is the physical velocity of the fluid through the regenerator, and $D_{hyd,r}$ is the hydraulic diameter of the screens. The friction factor in the regenerator (f_r) is represented by Gedeon (1999):

$$f_r = \frac{129}{Re_r} + 2.91 \; Re_r^{-0.103} \tag{6.2}$$

$$Re_r = \frac{\rho V_r D_{hyd,r}}{\mu} \tag{6.3}$$

where Re_r is the Reynold's number of the regenerator flow and μ is the viscosity of helium at ambient temperature and the operating pressure of the pulse-tube which is 300 psig.

The bypass flow is assumed to be laminar (this assumption is subsequently verified) and so the pressure drop (ΔP_{by}) and friction factor (f_{by}), as stated by White (1999), are given by:

$$\Delta P_{by} = \frac{f_{by} \rho L_r V_{by}^2}{4(gap)} \tag{6.4}$$

$$f_{by} = \frac{64}{Re_{by}} \tag{6.5}$$

$$Re_{by} = \frac{2 \rho V_{by} (gap)}{\mu} \tag{6.6}$$

where *gap* is the length of the bypass annulus, V_{by} is the physical velocity in the bypass, and Re_{by} is the Reynold's number through the annulus.

The total flow rate, $\dot{m}_{mod\,el}$, is broken into two components related to the flow through the regenerator, $\dot{m}_r$, and the flow through the bypass, $\dot{m}_{by}$:

$$\dot{m}_{mod\,el} = \dot{m}_r + \dot{m}_{by} \tag{6.7}$$

The total loss of refrigeration due to the bypass flow can be bounded in the limit of no regeneration, in which case the flow leaving the cold end is at the heat rejection temperature and must be cooled to the refrigeration temperature by the cold heat exchanger prior to entering the pulse-tube. The amount of cooling required is equal to the loss of refrigeration ($\dot{Q}_{loss}$) and can be expressed as:

$$\dot{Q}_{loss} = \left(h_{hot} - h_{cold}\right)\dot{m}_{by} \tag{6.8}$$

where h_{hot} is the enthalpy of the gas at the heat rejection temperature and h_{cold} is the enthalpy of the gas at the refrigeration temperature. Figure 6.12 illustrates the loss associated with the bypass flow as a function of the regenerator-to-housing gap for various values of the total mass flow through the regenerator. Note that the nominal mass flow rate expected in the regenerator at the design conditions is 0.150 g/s; larger mass flow rates produce larger pressure drops and therefore result in larger bypass flow and associated loss. Also note that even a very small gap of 0.001 inch could result in a refrigeration loss on the order of 400 W, which is consistent with the level of performance shortfall that was experimentally observed.

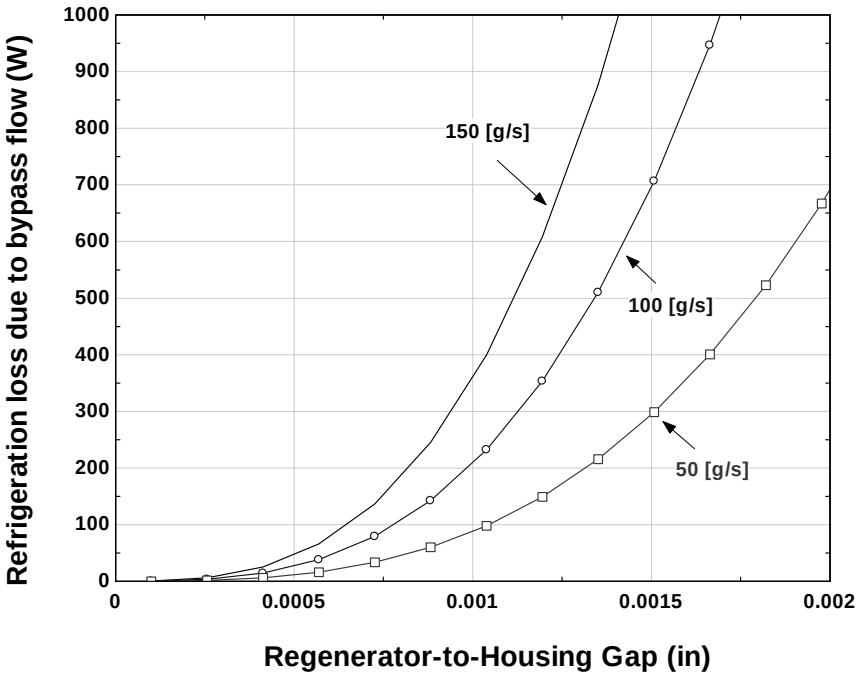

Figure 6.12. Refrigeration loss due to bypass flow as a function of the regenerator-to-housing gap for various values of the total regenerator mass flow rate.

To examine the influence of bypass flow experimentally, Teflon o-rings were placed on both sides of the regenerator and mechanically pressed into the regenerator-to-housing gap in order to force the bypass flow into the matrix at least near the ends; the idea was that if bypass flow is a substantial loss mechanism then this hardware modification should result in a measurable change in performance. On the warm end of the regenerator the o-ring was compressed using the screen holder flange that was designed to provide a pre-load on the screen stack and keep the regenerator matrix from experiencing any dynamic motion in response to the oscillating flow. The o-ring at the cold end is compressed by the cold heat exchanger. The location of the Teflon o-rings can be viewed in Figure 6.13.

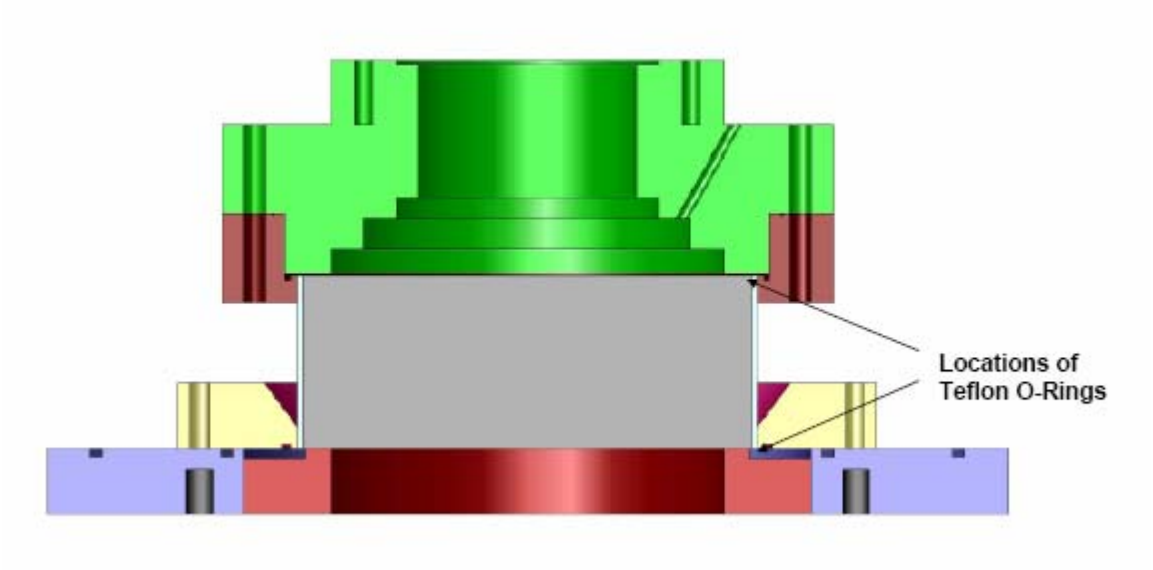

Figure 6.13. The Teflon O-rings are placed in the locations mentioned above and compressed with the bolts when tightening the screen holder and the CHX.

The instrumentation for this testing was changed from previous testing. All twelve channels of the thermocouple feed-through were utilized in order to provide more temperature information; the additional thermocouples were strategically arrayed circumferentially around the regenerator in order to identify temperature non-uniformities that might provide evidence of regenerator flow maldistribution. Figure 6.14 shows the new positions of the thermocouples.

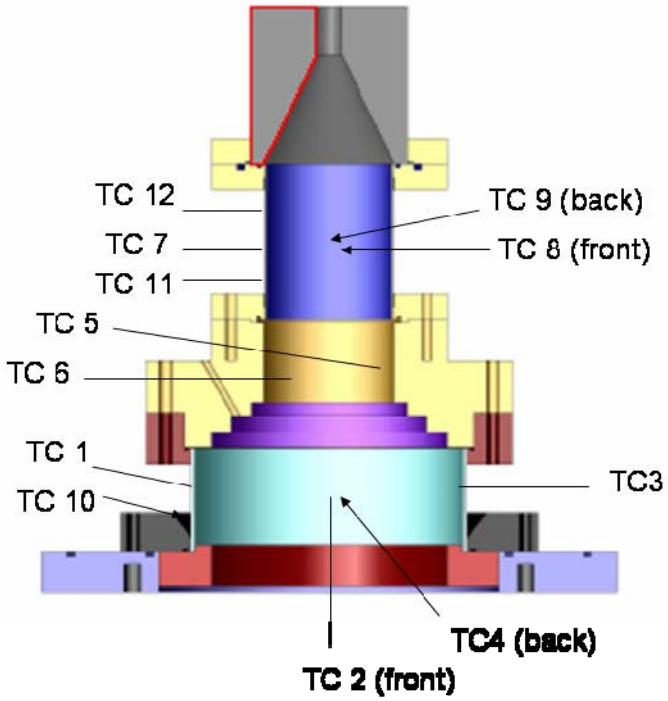

Figure 6.14. Thermocouple location for regenerator bypass tests. Thermocouples were located in order to replicate previous measurements and also to investigate the symmetry of the flow within the pulse-tube.

Five thermocouples were attached to the external surface of the regenerator: four thermocouples (TCs 1 through 4) were arrayed circumferentially at every quadrant at the axial center of the regenerator and the remaining thermocouple (TC 10) was placed inside the chamfer on the regenerator bottom flange. Two thermocouples (TCs 5 and 6) were placed inside the flow in the CHX in order to obtain an accurate measure of the gas temperature. Five thermocouples were placed on the pulse-tube; three were arrayed circumferentially 120° apart at the axial center of the pulse-tube (TCs 7, 8, and 9) and the remaining two were placed circumferentially in line with thermocouple #7 and axial locations corresponding to ¼ and ¾ of the way to the hot end (TCs 11 and 12, respectively).

The test with the modified regenerator resulted in a low end temperature of 145 K; note that the test did not show any significant improvement relative to previous testing without the Teflon o-rings and therefore fine tuning of the valve was not carried out which would have likely resulted is essentially the same no load temperature of 138 K that was described in Section 6.2.6. The test result therefore yielded essentially the same performance and indicated that either regenerator bypass loss is not significant or the Teflon o-rings did not substantially reduce this loss. Figure 6.15 shows a cooldown curve of this test.

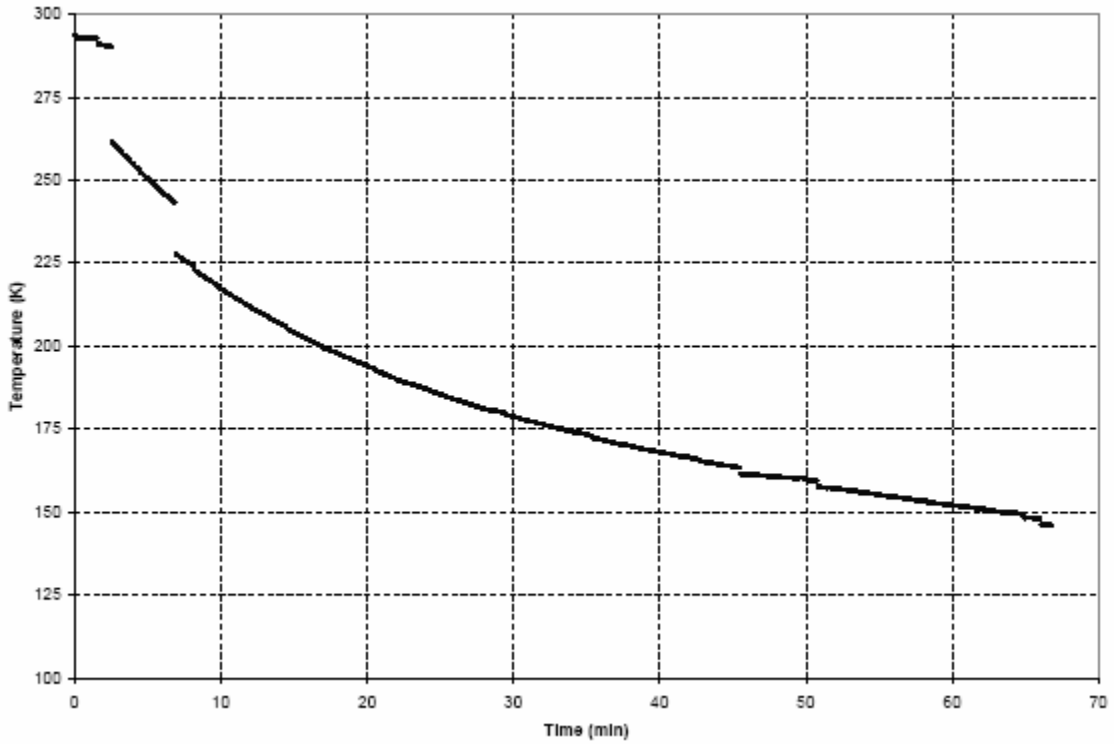

Figure 6.15. Cooldown curve showing the effects of regenerator bypass.

6.4 Second Round of Design Changes

The first round of design changes, described in Section 6.2, yielded promising results yet still did not lead to the target performance and did not provide a comprehensive understanding of the loss mechanisms. The regenerator test described in Section 6.3, while not definitive, did not provide evidence of a large loss related to regenerator bypass flow. Therefore, a 2nd round of design changes was carried out and is described in this section.

6.4.1 CHX Transition Filled with Screens, 10 Screens in HHX

During the 1st round of design changes described in Section 6.2, the test in which there were 6 screens placed in the transition region of the CHX (2 in each step) and 10 in the flow straightening adjacent to the HHX (this test was described in Section 6.2.4) resulted in the best performance with a no load temperature of 112 K . Subsequent design changes hurt the performance. These design changes were focused on placing the screens directly before the pulse-tube in the region of the CHX that has the same diameter as the pulse-tube. In the absence of screens, this region of the CHX essentially acts like an extension of the pulse-tube and therefore placing screens in this region has the effect of reducing the effective length of the pulse-tube. It was possible, therefore, that the original design of the pulse-tube which called for a 3 inch length, is not optimal and therefore the additional 1.5 inch length associated with the cold heat exchanger resulted in a substantial improvement in performance even if the flow straightening was slightly worse.

With this in mind, a test was run in which the screens in the straight section of the CHX were removed and instead, the entire transition region (the stepped region of the CHX) was filled with screens to improve the flow straightening without sacrificing the pulse-tube length. Figure 6.16 illustrates the changes for this test run.

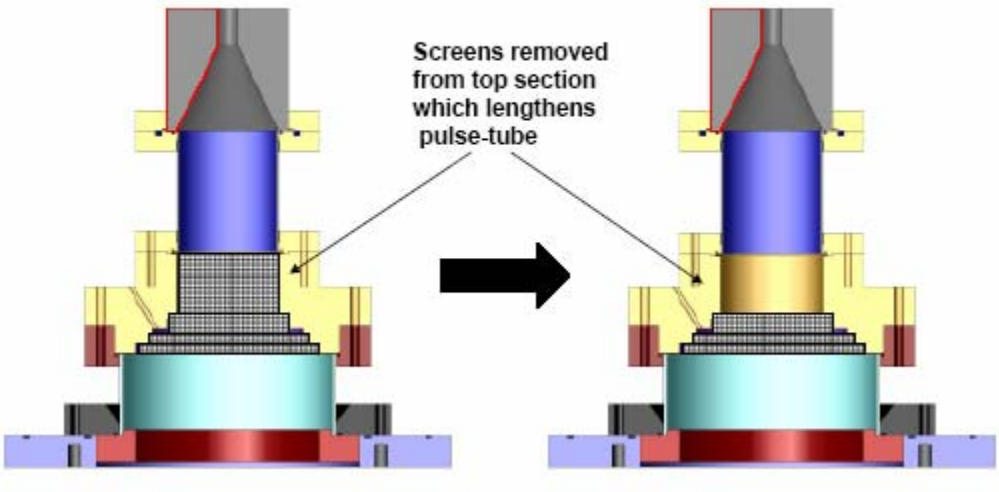

Figure 6.16. The screens were removed from the top section of the CHX to provide a longer pulse-tube and less resistance.

The no load temperature in this configuration was found to be 82 K which is a significant improvement in performance. Figure 6.17 shows a cooldown curve of this test.

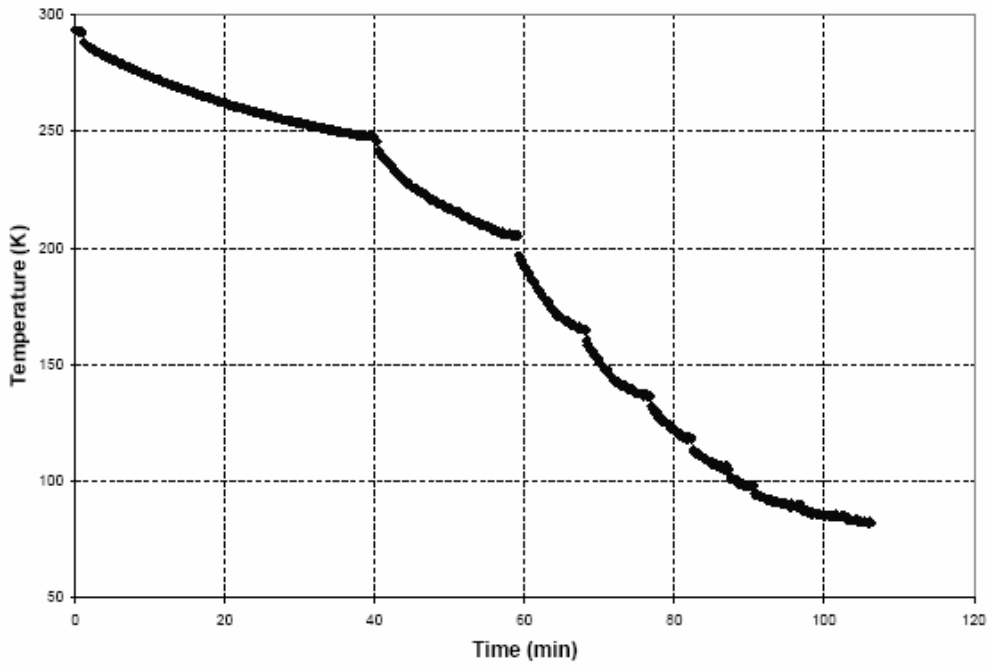

Figure 6.17. Cooldown curve for test with CHX transition filled with screens and 10 screens placed in the HHX.

6.4.2 CHX Transition Filled with Screens, 36 Fine Mesh Screens in HHX

Given the promising results described in Section 6.4.1 and the previously described improvements in performance that was observed when screens were placed in initially in the HHX, it was decided to further refine the flow straightening in the HHX. The HHX design, shown in Figure 6.18 limited the number of screens that could be inserted into the transition.

Figure 6.18. A solid model of the HHX used for this test, with the cone leading straight to the pulse-tube there was only enough rooms for a minimal amount of screens. If the HHX were machined to allow for an inch stack of screens a swirling effect similar to one in the original testing would have been present.

Therefore, a 1.0 inch stack of screens such as is recommended by the CFD modeling discussed in Chapter 5 is impossible to implement. In an attempt to add more resistance to the hot end and therefore more flow straightening, a finer mesh screen was used. The ten 50-mesh copper screens, which were placed between the HHX and pulse-tube, were replaced by a combination of 200-mesh stainless steel screens and 100-mesh copper screens that produced a total of 36 screens. The test results yielded essentially the same no-load temperature of 82 K which suggests that either the length of stack is more important than the resistance of the stack for flow straightening or that the flow straightening in the HHX was already adequate. Figure 6.19 shows a cooldown curve of this test.

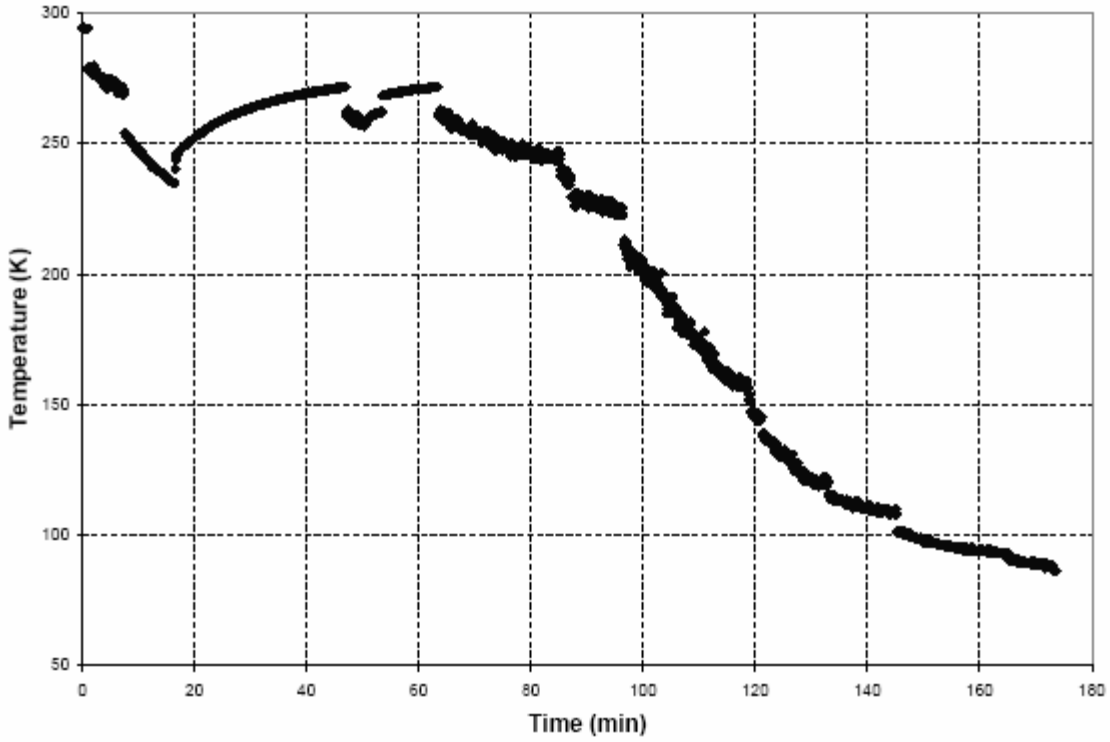

Figure 6.19. Cooldown curve for test with CHX transition filled with screens and 36 fine meshed screens placed in the HHX.

6.4.3 Water Cooled HHX with a Longer Screen Stack

Based on the limited length available for screens, discussed in Section 6.4.2, a modified HHX was designed and built which could accommodate a longer screen stack. The modified HHX was also water-cooled in order to provide the constant wall temperature boundary condition that was used in all of the modeling described in this thesis. Figure 6.20 shows an exploded assembly of the solid model for the HHX.

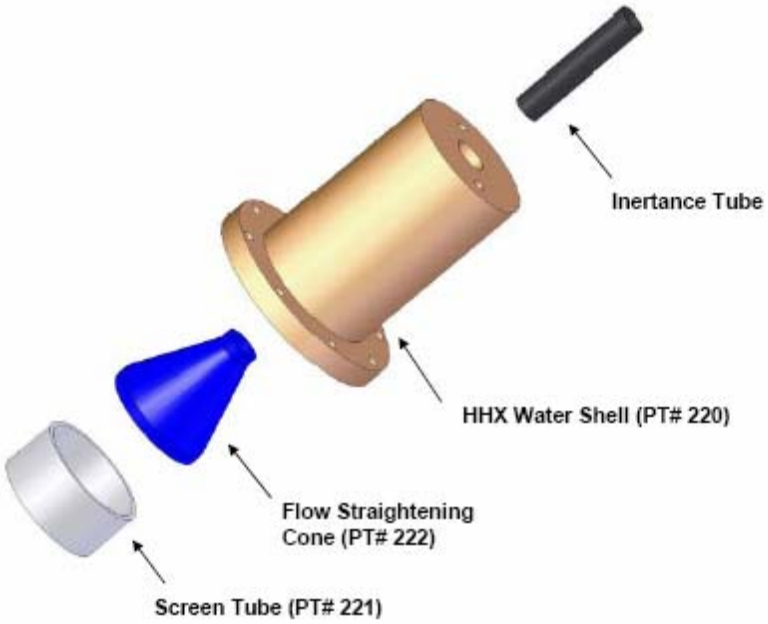

Figure 6.20. Exploded assembly of the new HHX with integrated screen bed and water cooled jacket.

The screen tube shown in Figure 6.20 is designed to hold a 1.0 inch long stack of screens. Initially, the HHX was assembled with 50-mesh copper screens which matched the CFD modeling results. The inertance tube and the screen tube are both silver soldered in order to allow for lower temperature solder to be used in a subsequent joining operation to attach the water jacket to the screen tube. The configuration is designed so that it may be disassembled and reassembled with various screen tube lengths with minimal effort. The HHX was built and assembled as specified in Appendix A, a solid model of the modified pulse-tube geometry is shown in Figure 6.21.

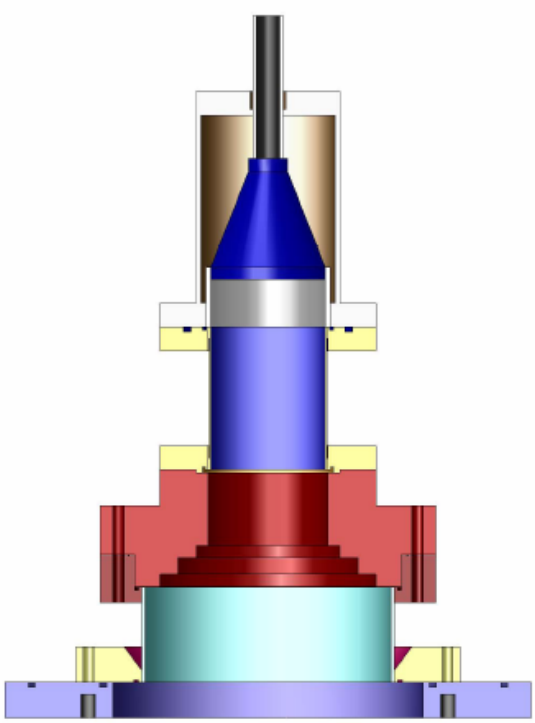

Figure 6.21. The internal geometry of the pulse-tube with the addition of the water-cooled HHX

The test results for the modified geometry showed significant improvement in the no-load temperature that could be achieved for lower stroke; however, no improvement was observed in the ultimate low temperature that could be achieved by the pulse-tube at the maximum stroke, this can be viewed in Figure 6.22.

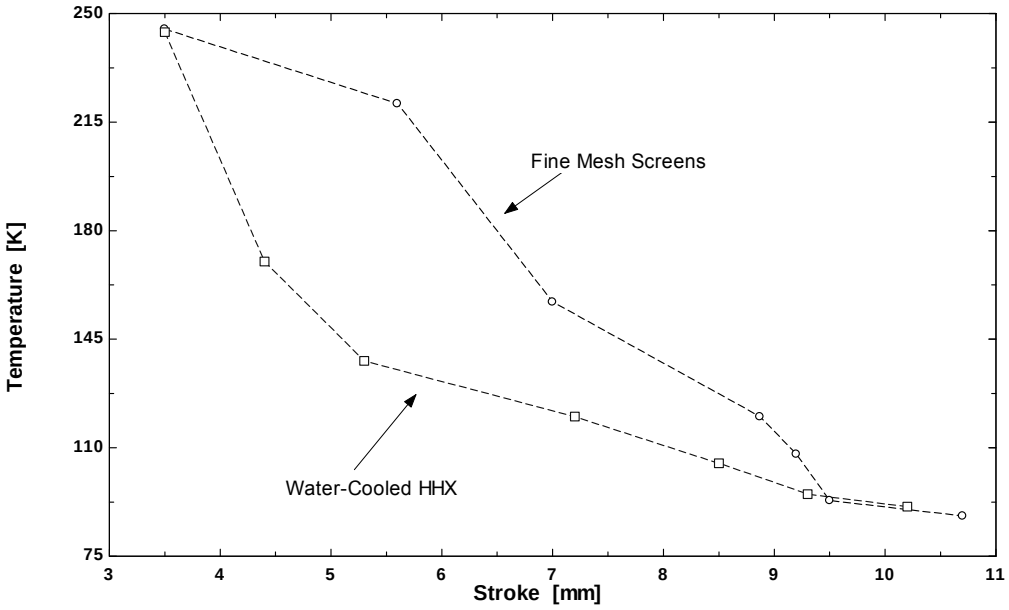

Figure 6.22. Temperature dependence on stroke comparison between the test of the water-cooled HHX against the fine meshed screen test.

Figure 6.23 shows a cooldown curve of this test.

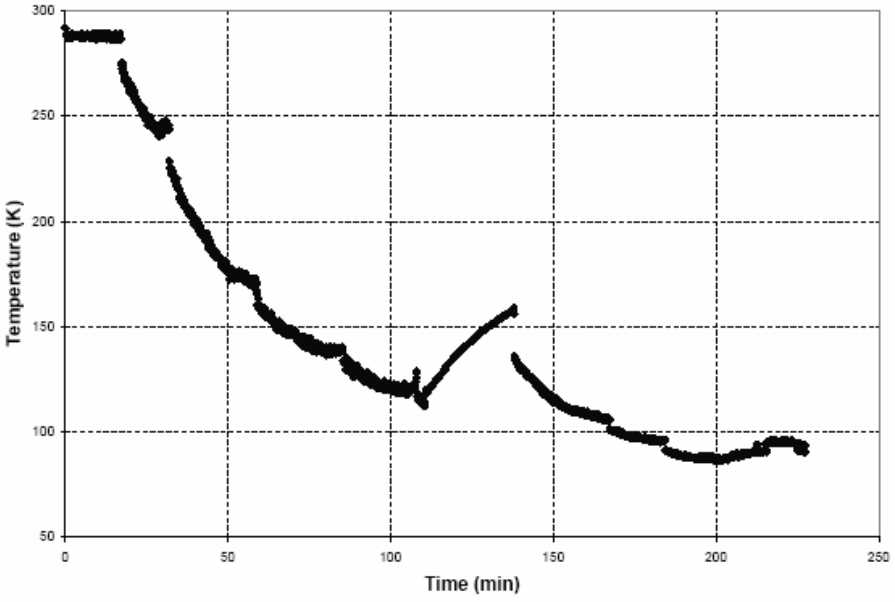

Figure 6.23. Cooldown curve for test with water-cooled HHX with longer screen stack. The raise in temperature in the middle of the cooling curve was caused by a compressor malfunction.

For this test, a nichrome heater was placed on the cold heat exchanger in order to measure a load curve. Nichrome heaters and the associated electrical leads and connections tend to overheat when they are operated in a vacuum with a large current. Therefore, extra precautions were taken so that a large amount of input power could be applied. The four heater leads were fabricated using 24 AWG copper wire; each lead represented a 0.3 W heat leak at an electrical input of 300 W. The heater was formed from a 4.5 ft length of nichrome wire which has a resistance of 33 ohms/m. The nichrome wire was silver soldered to the copper heater leads and heat sunk to the cold heat exchanger using Lakeshore VGE-7031 varnish, which is commonly referred to as GE varnish. The leads were further protected from overheating by wrapping a 100-mesh copper screen around the outside of the leads; this was done in order to provide a thermal path between any hot spots and the surrounding CHX surface.

Figure 6.13 shows the resulting load curve from this test. The conditions for this test had a stroke of 10.1 mm/piston, a mean pressure of 300 psig, a frequency of 44 Hz, and a vacuum level of 1.2×10^{-5} torr. Initially, a no-load temperature of 87 K was achieved and then the heater was activated in order to supply 20 W to the cold end. The cold head temperature rose by approximately 4 K, from 87 K to 91 K. The heater power was increased by another 20 W to nominally 37 W and the cold head temperature again rose by approximately 4 K, from 91 K to 95 K. The heater failed when the power was increased to 60 W; the failure occurred before equilibrium was reached. The load curve is very linear over the range that was investigated and one can reasonably postulate that

approximately 60 W of cooling would have been delivered at 100 K, 100 W at 108 K, and 300 W at 152 K. Figure 6.24 shows the load curve from this test.

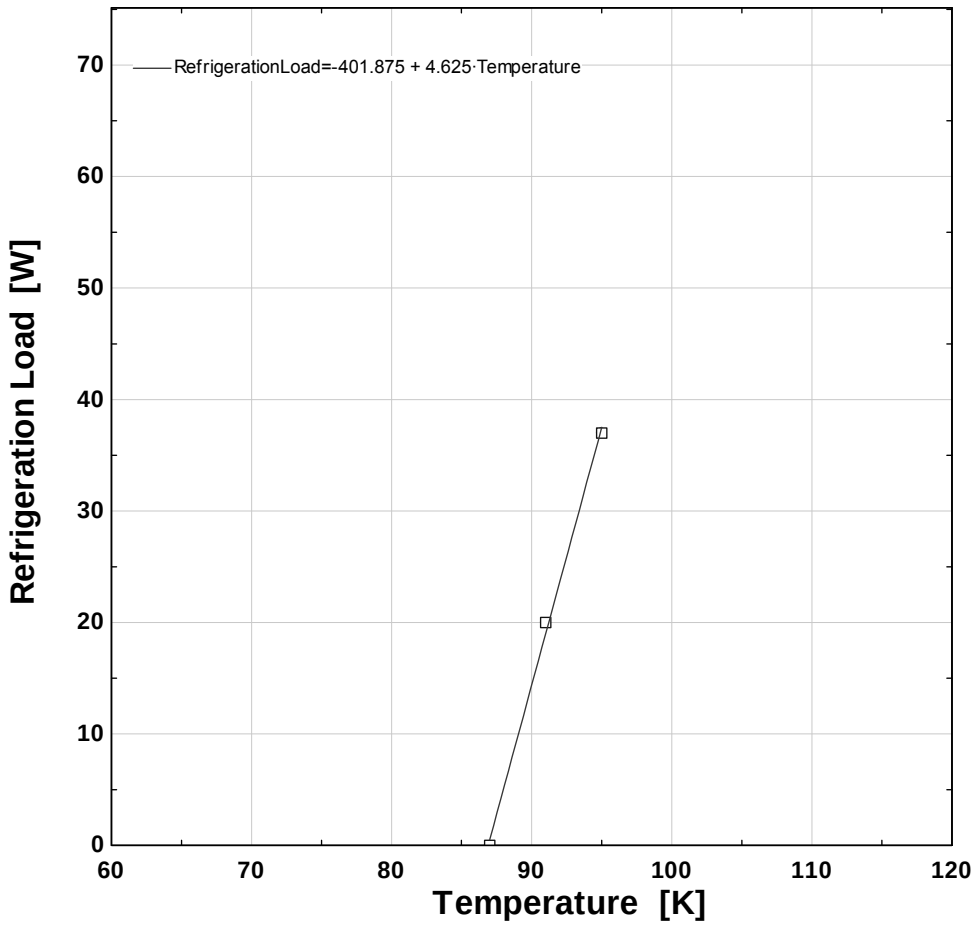

Figure 6.24. Load curve for the pulse-tube with modified HHX.

Chapter 7 – Conclusions and Recommendations

7.1 Introduction

The work described in this thesis has focused on the development of a high-capacity pulse-tube refrigerator; the design target for the device was 300 W of cooling at 65 K. The thesis describes the entire development process, including the development of a thermodynamic model of the refrigeration cycle which was used to generate a thermal-fluid design, the process of translating this thermal-fluid design to a set of mechanical design drawings, the fabrication and assembly of the resulting components, the test results and, finally, iteration on the design motivated by test results and analysis.

7.2 Conclusions

One obvious result of this project is that there is a significant difference between the behavior of low-capacity (a few watts) and high-capacity (100's of watts) pulse-tube refrigerators. Processes which are of secondary importance in a small pulse-tube (for example, conduction of the refrigeration load into the gas) become non-trivial design issues in a high-capacity pulse-tube design. Therefore, the simple design approach in which the internal geometry of a working, small-capacity pulse-tube is simply scaled up to a larger size will not produce acceptable results. This was evident in many aspects of the design and produced several unforeseen results. One very important example of this is evident in the thermodynamic design model of the pulse tube which uses a one-dimensional representation of the flow interactions inside the system. Clearly, the actual flow distribution present is not one-dimensional, there are all sorts of transitions and mixing that is impossible to account for in a one-dimensional model. Furthermore, these

effects become progressively more important as the capacity of the pulse tube increases due to the smaller aspect ratio (length-to-diameter) that tends to accompany the increasing load capacity. Flow does not have as much length to distribute radially and yet must flow farther in the radial direction. These effects were not considered adequately during the initial design of the pulse-tube. The CFD modeling that was accomplished subsequent to the design (see Chapter 5) showed clearly that the flow distribution issue was not a secondary one. The importance of flow transitions was clearly shown by the results and discussion that is presented in Chapters 5 and 6.

7.3 Recommendations

In order to make a successful pulse-tube of this size, there are many design details that should be changed. The one dimensional design model provides a convenient starting point for the development of a high-capacity pulse-tube. However, these results must be coupled with a sufficiently detailed model that is capable of investigating the effects of the flow distribution. The CFD modeling is an ideal tool for this purpose as it provides qualitative and quantitative information. The general flow patterns that are induced within the pulse-tube during operation can be examined yielding tremendous physical insight into the effect of seemingly unimportant geometric details. The initial pulse-tube design, in particular the development of efficient flow transitions, would have been much easier if CFD was used as an initial design tool. The re-design of the hardware that was required in order to improve the pulse-tube performance was difficult; much more time was required to accomplish these hardware modifications than would have been invested in an initial examination using a CFD code.

The CFD model clearly showed the influence of flow straightening at all of the component transitions; this detail was essentially neglected in the original design. Future designs should carefully consider transitions and verify the geometry using CFD models in order to ensure that the flow straightening will give the proper stratification in the pulse-tube and therefore lead to a high efficiency of transforming acoustic power to refrigeration load capacity. In particular, the flow straightening in the cold heat exchanger should be investigated further. All of the data has pointed to the fact that the regenerator is producing a higher than expected pressure drop which may be caused by a poor transition between the CHX and the regenerator. The current geometry has very shallow steps that are filled with screens; this can be seen in Figure 7.1. It is possible that this geometry will cause a large apparent regenerator resistance as the flow is channeled through the center portion of the regenerator so that its effective diameter is significantly smaller than the actual or geometric diameter. This phenomena may also impact the thermal performance of the regenerator.

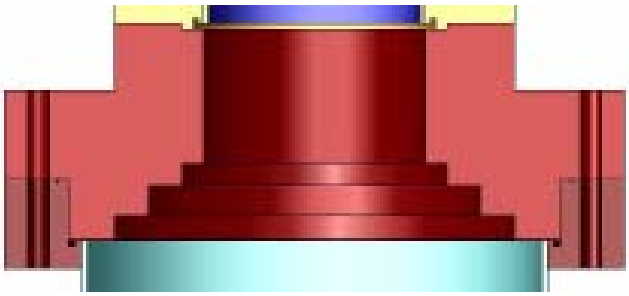

Figure 7.1. The stepped transition between the regenerator and the pulse-tube has a total height of 0.85 in.

The cold heat exchanger flow transition would likely benefit from using the design approach that was applied to the re-designed HHX which used a longer and more gradual

transitioning cone. The cone could be filled with expanded copper foam to give it better properties, both as a heat exchanger and a flow straightener.

Another area for future investigation is related to the measured pressure in the pulse-tube. The hardware changes that have been implemented to the pulse-tube refrigerator have had a consistent effect on the oscillating pressure wave that is measured at the pressure sensor located above the HHX. Figure 7.2 shows the clear difference between the very smooth and sinusoidal pressure variation measured during the first test on 5/28/04 and the more irregular pressure variation measured during the most recent test data on 3/16/05.

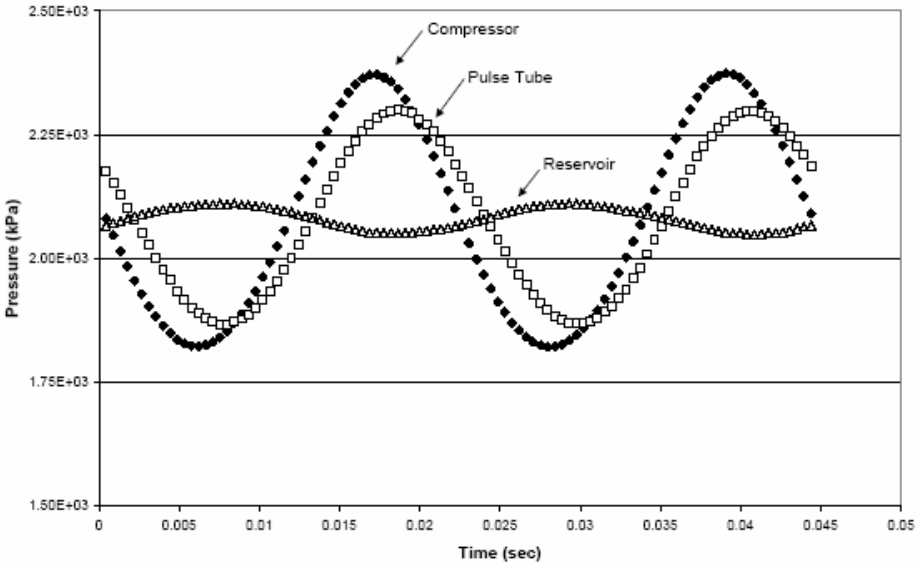

(a)

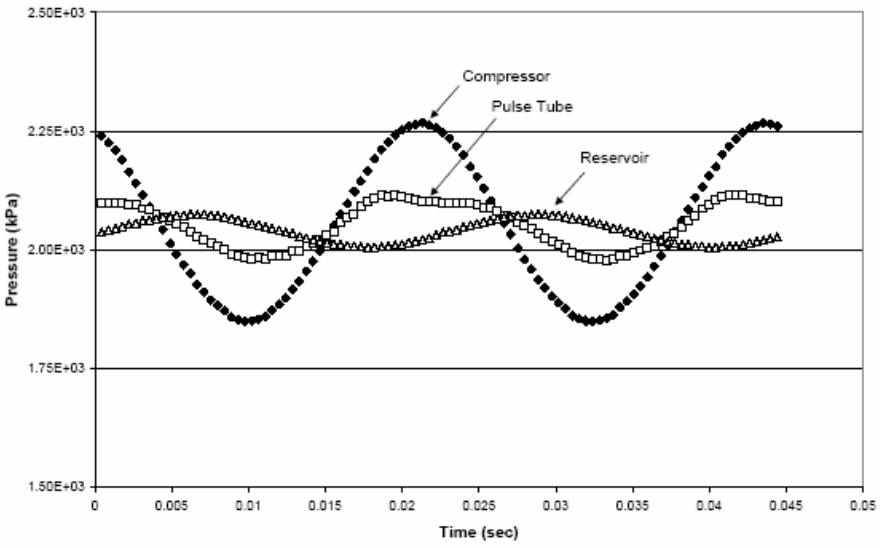

(b)

Figure 7.2. Measured pressure variation at various locations within the pulse-tube refrigerator measured (a) during the initial testing on 5/28/04, and (b) measured during testing that occurred after significant component modification on 3/16/05.

The discrepancy in the measured pressure variation may be the result of the void volume that is present in the transition between the HHX and inertance tube in the modified HHX. Figure 7.3 shows the difference in the internal geometry between the initial HHX and the final HHX.

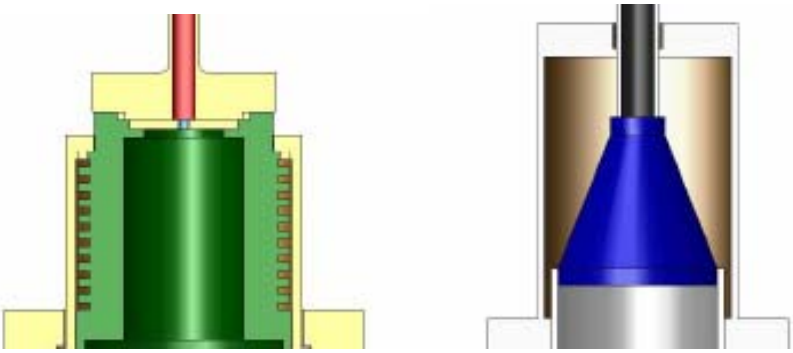

Figure 7.3. Comparison between the first (left) and final (right) HHX used in the pulse-tube testing.

The HHX used in the initial testing was entirely filled with screens; however, only the lower section of the final HHX was filled with screens while the cone shaped region remained empty. The distorted sine wave shown in Figure 7.2(b) was observed consistently for all testing accomplished using the modified HHX. The source of the distortion ought to be determined and, if possible, remedied. One potential solution might be to fill the cone with some porous media; a short-term solution might be steel wool while a better solution would be an expanded metal foam.

The design of the heater used to provide the refrigeration load should be more robust. The leads that bring the current through the vacuum space could be made significantly larger; this would result in a larger than optimal heat leak but would have reduced the high temperature that is observed at the joint between the copper and nichrome. An alternative to the nichrome heater design might be a band heater that could be placed around the large flange in the pulse tube.

References

ASME Pressure Vessel Code, Section VIII, Division I.

Beer F.P. and Johnston E.R., "Mechanics of Materials, 2nd Edition," McGraw-Hill, New York, (1992).

Diab, A. K., "Modeling and Optimization of a Hybrid Cryocooler," M. S. Thesis, UW-Madison, (2003).

Engineering Equation Solver (EES), F-Chart Software, www.fchart.com.

Fluent Inc., "Fluent User's Guide 6.1, Sec 6.19.2," Lebenon, NH (2003).

Gary, J., Daney, D., and Radebaugh, R., "Computational Model for a Regenerator," *Proc. 3rd Cryocooler Conf.*, (1985).

Gary, J, and Radebaugh, R., "An Improved Numerical Model for Calculation of Regenerator Performance (REGEN 3.1)," in *Proceedings of the Fourth Interagency Meeting on Cryocoolers.* David Taylor Research Center, 1990.

Gary J., O'Gallagher A., Radebaugh R., and Marquardt E., "REGEN3.2 User Manual," NIST, (2001).

Gedeon, D., "Sage: User's Guide, Third Edition" Gedeon Associates, Athens, OH (1999).

Incropera F.P, and DeWitt D.P., "Introduction to Heat Transfer, 4th Edition," Wiley, New York, (2002).

Juvinall R.C., and Marshek K.M., "Fundamentals of Machine Component Design, 3rd Edition," Wiley, New York, (2000).

Kays W.M, and London A.L., "Compact Heat Exchangers, 3rd Edition," Krieger, New York, (1998).

Lewis, M.A. and Radebaugh, R. "Measurement of Heat Conduction through bonded regenerator matrix material, Cryocoolers 12," Kluwer Academic/Plenum (2003) 517-522.

Miyabe, H., Takahashi, S. and Hamaguchi, K. "An approach to the design of Stirling Engine regenerator matrix using packs of wire gauzes," Proc 17th IECEC (1982) 1839-1844.

Pfotenhauer, J. M., Shi, J. L., and Nellis, G. F., "A Parametric Optimization of a Single-Stage Regenerator Using REGEN 3.2", in *Proc. of the 13th Int. Cryocoolers Conf*, (2004).

Roach P.R., and Kashani A., "Pulse tube coolers with an inertance tube: theory, modeling and practice" in *Advances on Cryogenic Engineering* **43B**, edited by P. Kittel, Plenum, New York, pp.1895-1902, (1997).

Timmerhaus K.D. and Flynn T.M., "Cryogenic Process Engineering," Plenum, New York, (1989).

White, F.M. "Fluid Mechanics, 4th Edition," McGraw-Hill, Madison, WI, (1999).

Appendix A – Mechanical Drawings

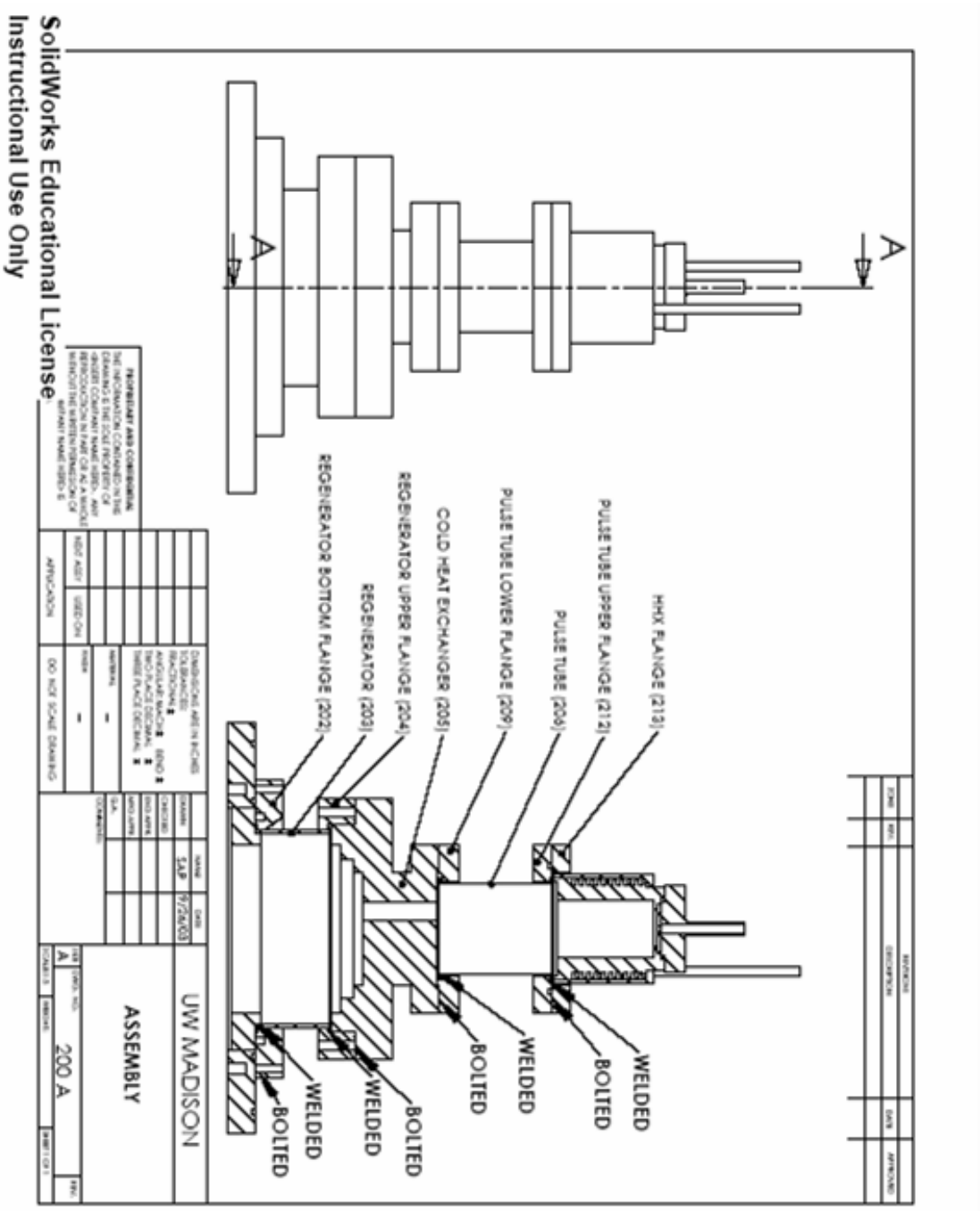

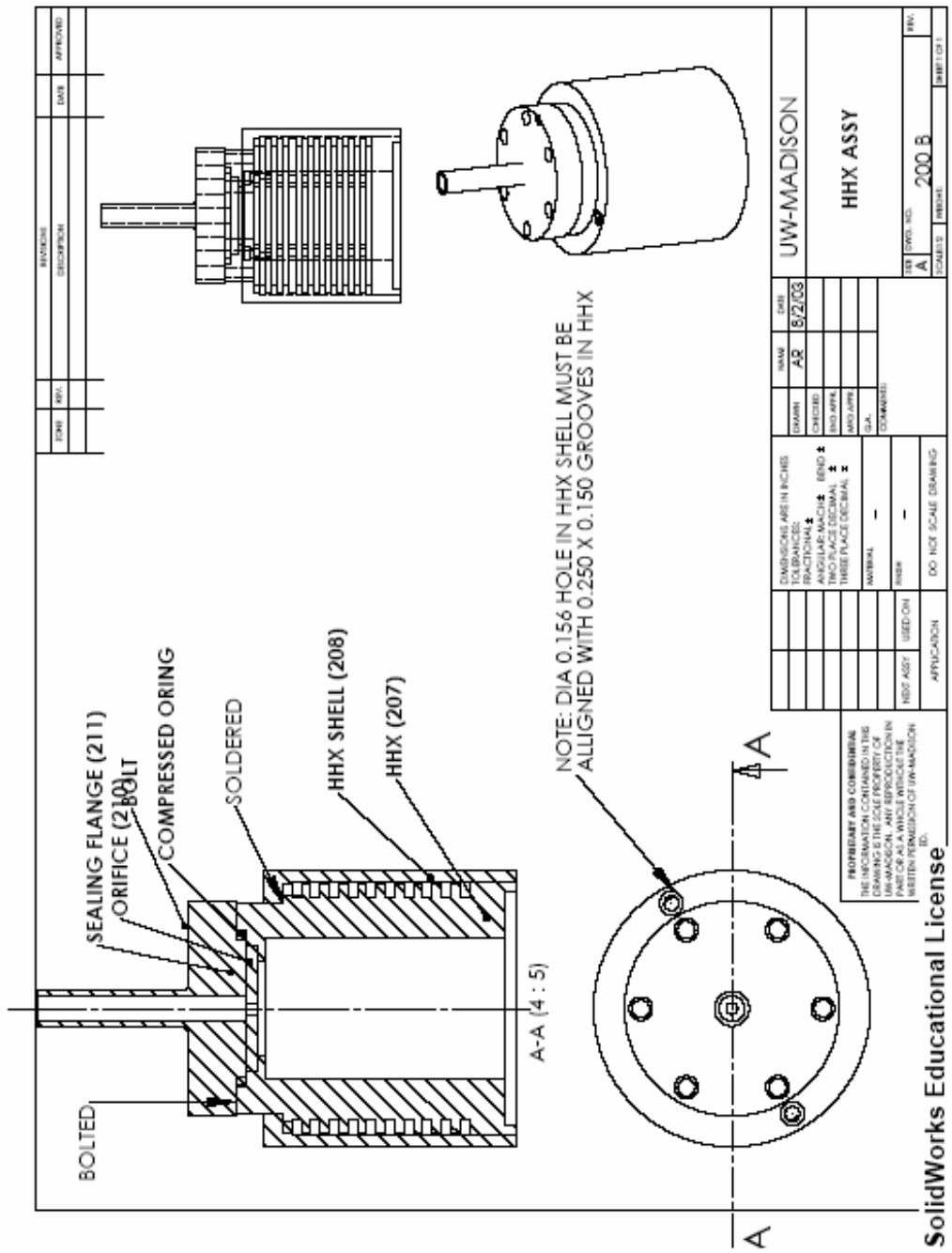

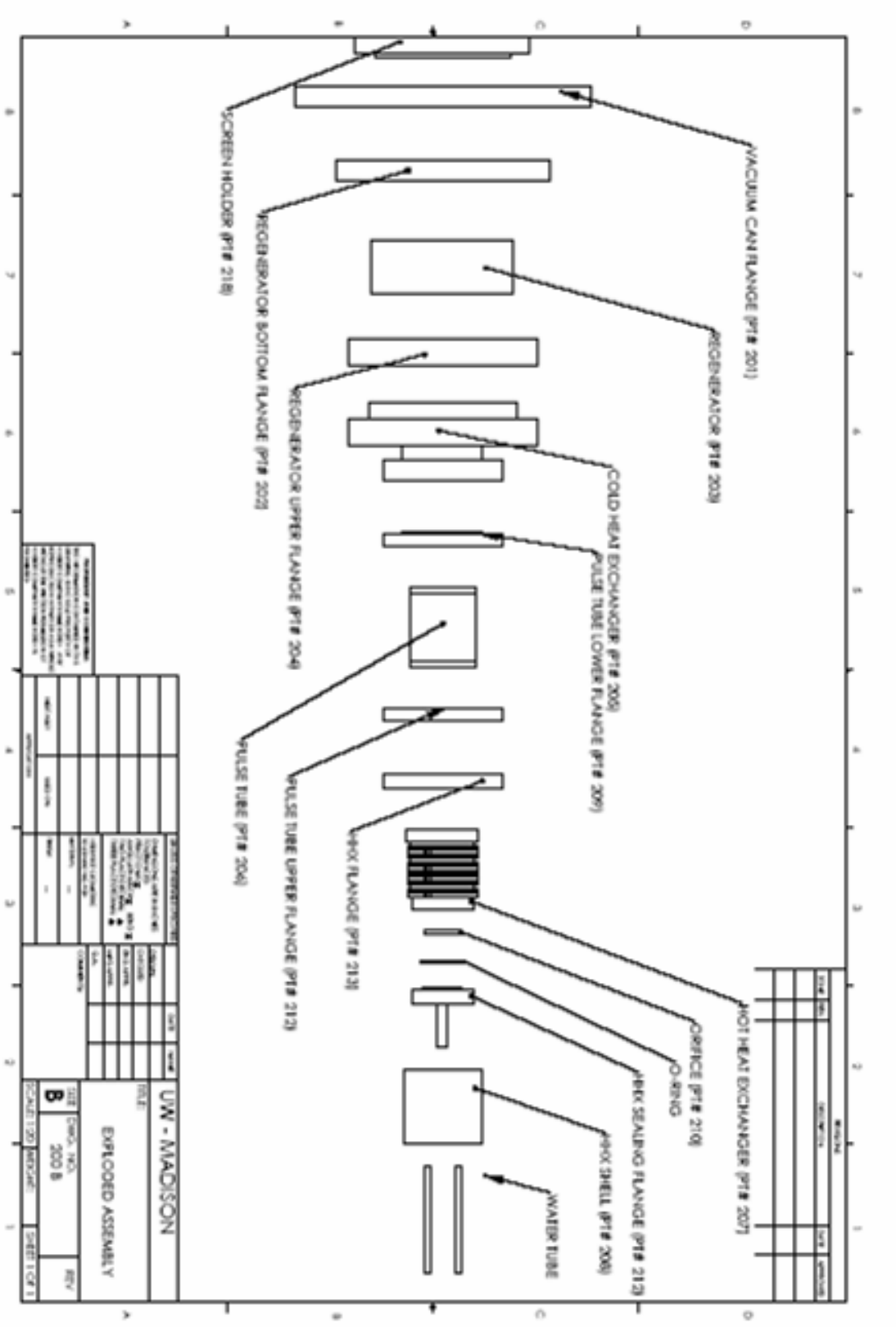
VACUUM CAN FLANGE (PT# 201)
REGENERATOR (PT# 203)
COLD HEAT EXCHANGER (PT# 205)
PULSE TUBE LOWER FLANGE (PT# 207)
HOT HEAT EXCHANGER (PT# 207)
ORIFICE (PT# 210)
O-RING
PEEK SEALING FLANGE (PT# 212)
HHX SHELL (PT# 208)
WATER TUBE
HHX FLANGE (PT# 213)
PULSE TUBE UPPER FLANGE (PT# 212)
PULSE TUBE (PT# 204)
REGENERATOR UPPER FLANGE (PT# 204)
REGENERATOR BOTTOM FLANGE (PT# 202)
SCREEN HOLDER (PT# 218)
UW - MADISON
EXPLODED ASSEMBLY
200 B
B

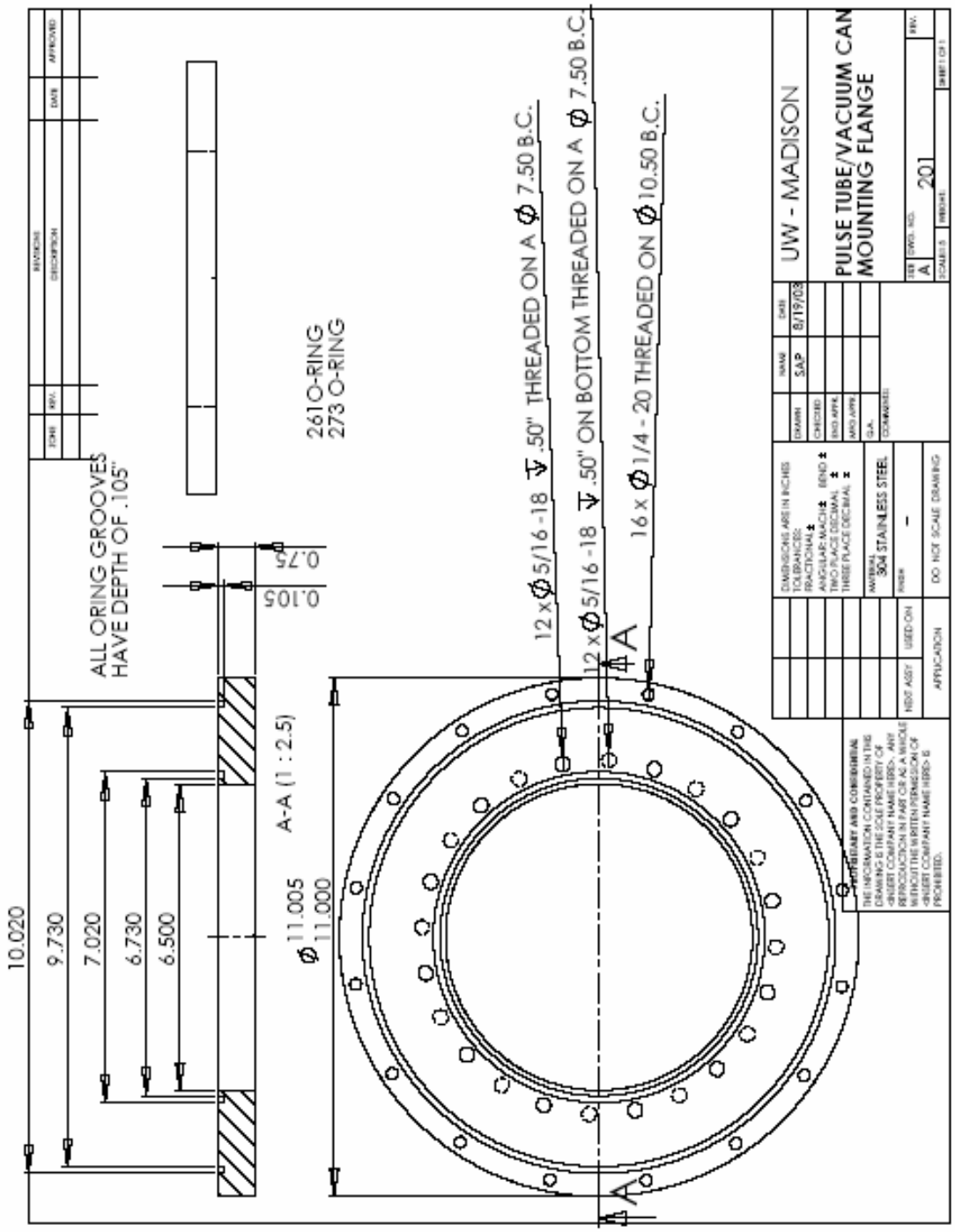
ALL ORING GROOVES
HAVE DEPTH OF .105"
261O-RING
273 O-RING
12 x Ø5/16 -18 ↧ .50" THREADED ON A Ø 7.50 B.C.
12 x Ø5/16 -18 ↧ .50" ON BOTTOM THREADED ON A Ø 7.50 B.C.
16 x Ø1/4 - 20 THREADED ON Ø10.50 B.C.
A-A (1 : 2.5)
10.020
9.730
7.020
6.730
6.500
0.105
0.75
Ø 11.005
11.000
UW - MADISON
PULSE TUBE/VACUUM CAN
MOUNTING FLANGE
304 STAINLESS STEEL
DO NOT SCALE DRAWING

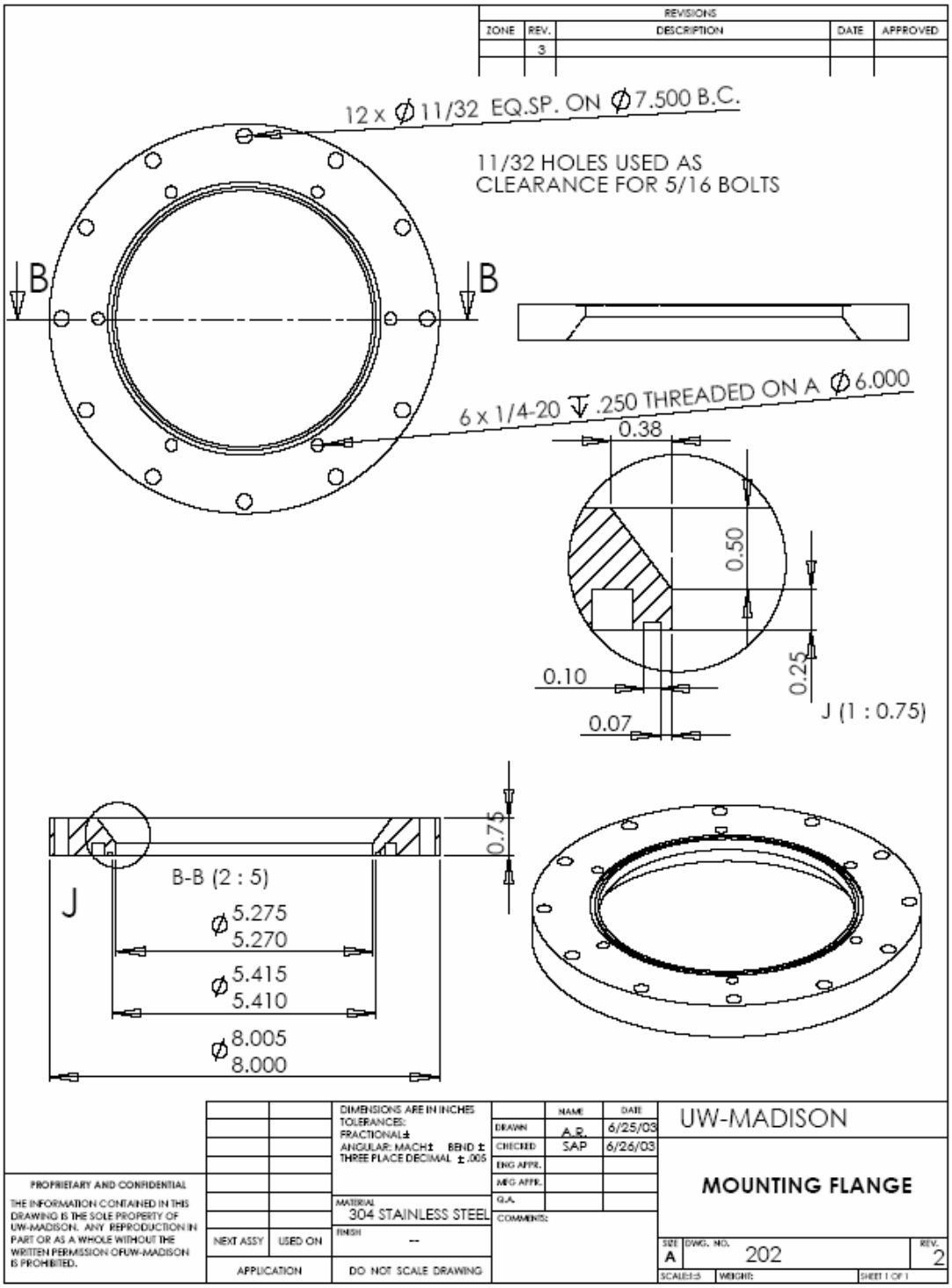
REVISIONS
ZONE REV. DESCRIPTION DATE APPROVED
3
12 x Ø11/32 EQ.SP. ON Ø7.500 B.C.
11/32 HOLES USED AS
CLEARANCE FOR 5/16 BOLTS
B
B
6 x 1/4-20 ↧ .250 THREADED ON A Ø6.000
0.38
0.50
0.10
0.07
0.25
J (1 : 0.75)
0.75
B-B (2 : 5)
J
Ø5.275
5.270
Ø5.415
5.410
Ø8.005
8.000
PROPRIETARY AND CONFIDENTIAL
THE INFORMATION CONTAINED IN THIS DRAWING IS THE SOLE PROPERTY OF UW-MADISON. ANY REPRODUCTION IN PART OR AS A WHOLE WITHOUT THE WRITTEN PERMISSION OFUW-MADISON IS PROHIBITED.
NEXT ASSY USED ON
APPLICATION
DIMENSIONS ARE IN INCHES
TOLERANCES:
FRACTIONAL±
ANGULAR: MACH± BEND ±
THREE PLACE DECIMAL ±.005
MATERIAL 304 STAINLESS STEEL
FINISH --
DO NOT SCALE DRAWING
NAME DATE
DRAWN A.R. 6/25/03
CHECKED SAP 6/26/03
ENG APPR.
MFG APPR.
Q.A.
COMMENTS:
UW-MADISON
MOUNTING FLANGE
SIZE A DWG. NO. 202 REV. 2
SCALE:5 WEIGHT: SHEET 1 OF 1

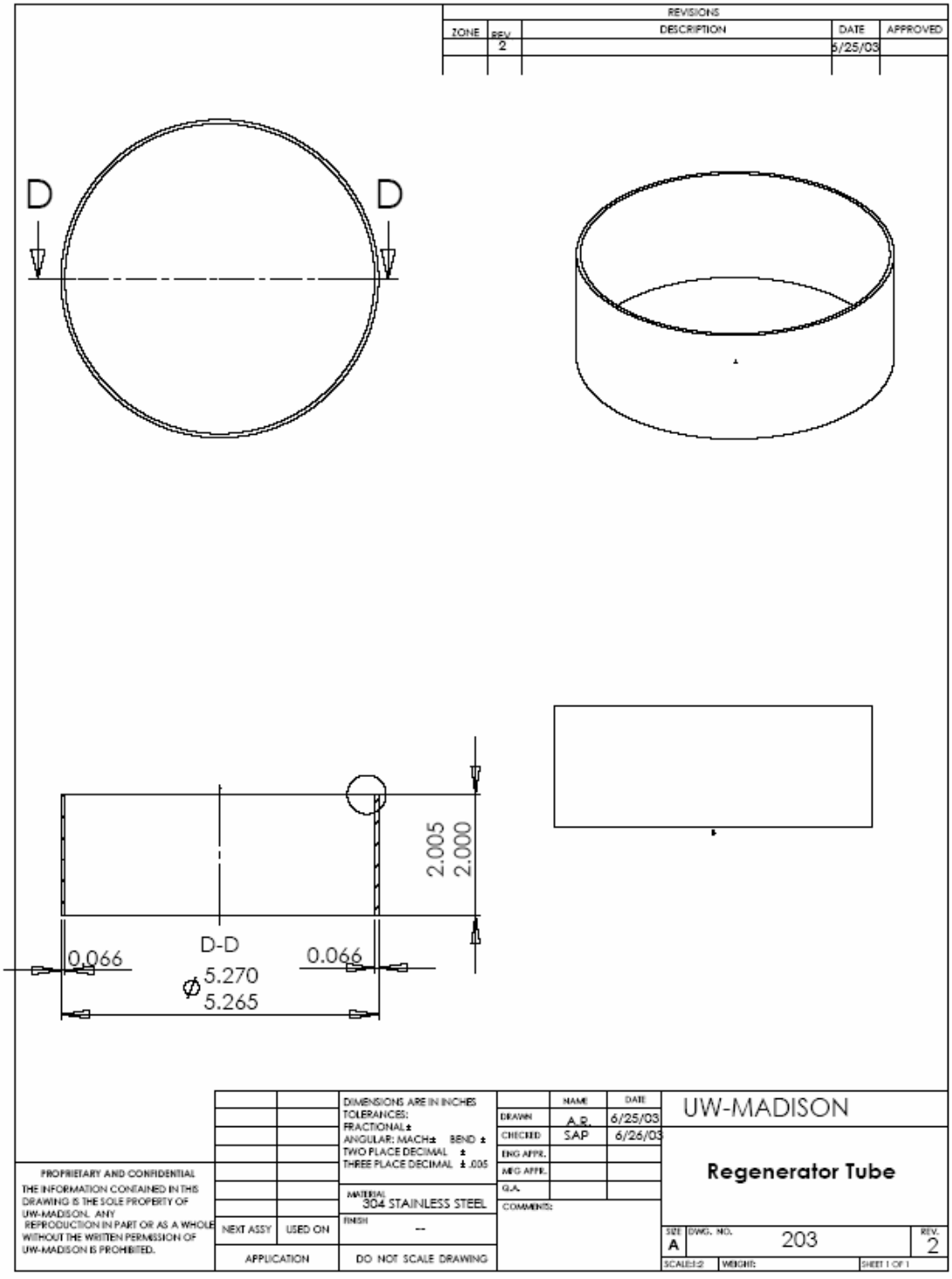
REVISIONS
ZONE
REV.
DESCRIPTION
DATE
APPROVED
2
6/25/03
D
D
2.005
2.000
0.066
D-D
0.066
Ø5.270
5.265
PROPRIETARY AND CONFIDENTIAL
THE INFORMATION CONTAINED IN THIS DRAWING IS THE SOLE PROPERTY OF UW-MADISON. ANY REPRODUCTION IN PART OR AS A WHOLE WITHOUT THE WRITTEN PERMISSION OF UW-MADISON IS PROHIBITED.
DIMENSIONS ARE IN INCHES
TOLERANCES:
FRACTIONAL ±
ANGULAR: MACH ± BEND ±
TWO PLACE DECIMAL ±
THREE PLACE DECIMAL ± .005
MATERIAL
304 STAINLESS STEEL
FINISH
--
NEXT ASSY
USED ON
APPLICATION
DO NOT SCALE DRAWING
NAME
DATE
DRAWN
A.R.
6/25/03
CHECKED
SAP
6/26/03
ENG APPR.
MFG APPR.
Q.A.
COMMENTS:
UW-MADISON
Regenerator Tube
SIZE
A
DWG. NO.
203
REV.
2
SCALE:2
WEIGHT:
SHEET 1 OF 1

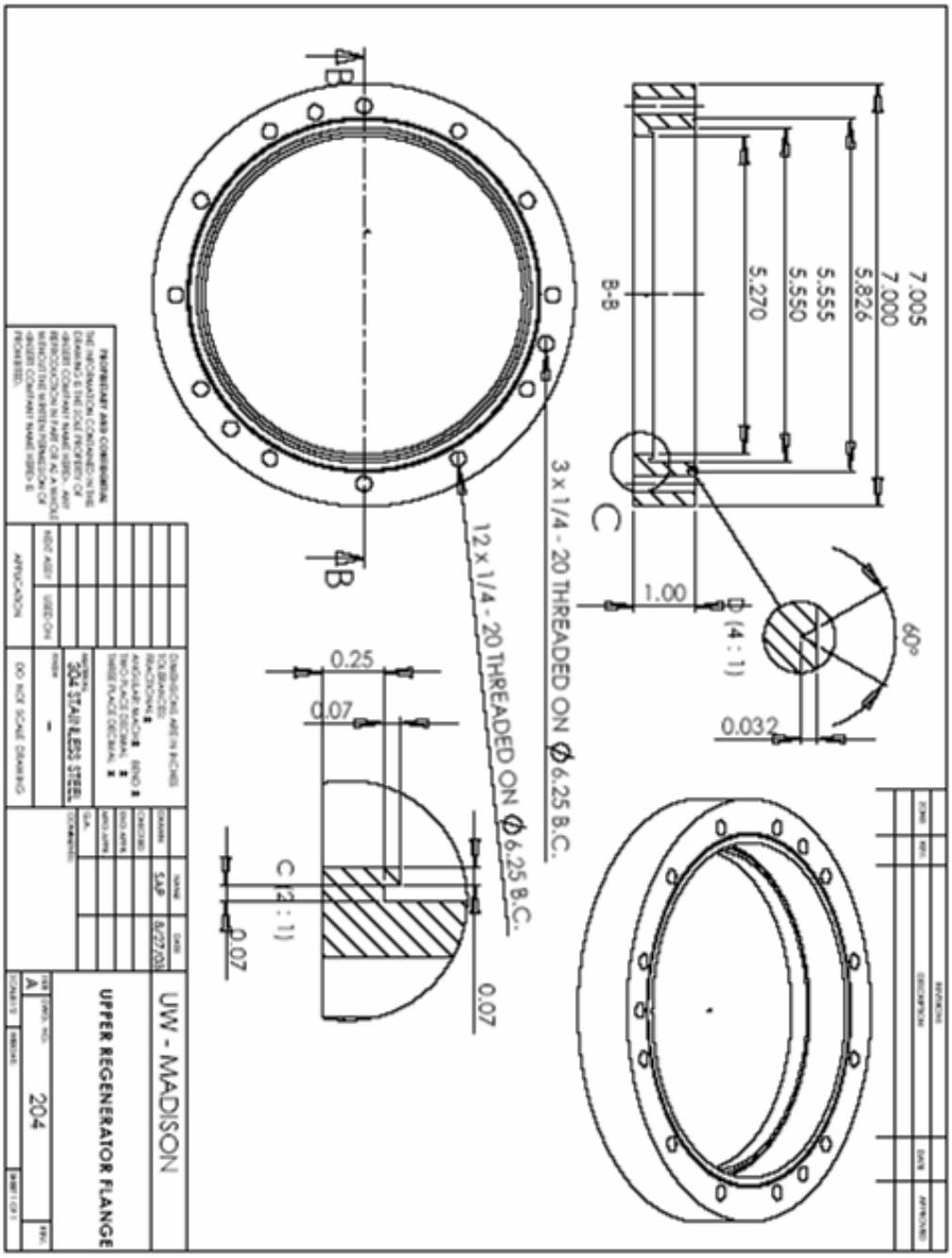
7.005
7.000
5.826
5.555
5.550
5.270
B-B
C
1.00
(4 : 1)
60°
0.032
3 x 1/4 - 20 THREADED ON Ø6.25 B.C.
12 x 1/4 - 20 THREADED ON Ø6.25 B.C.
0.25
0.07
0.07
C (2 : 1)
0.07
A
B
A
B
UW - MADISON
UPPER REGENERATOR FLANGE
204
304 STAINLESS STEEL
DO NOT SCALE DRAWING
PROPRIETARY AND CONFIDENTIAL

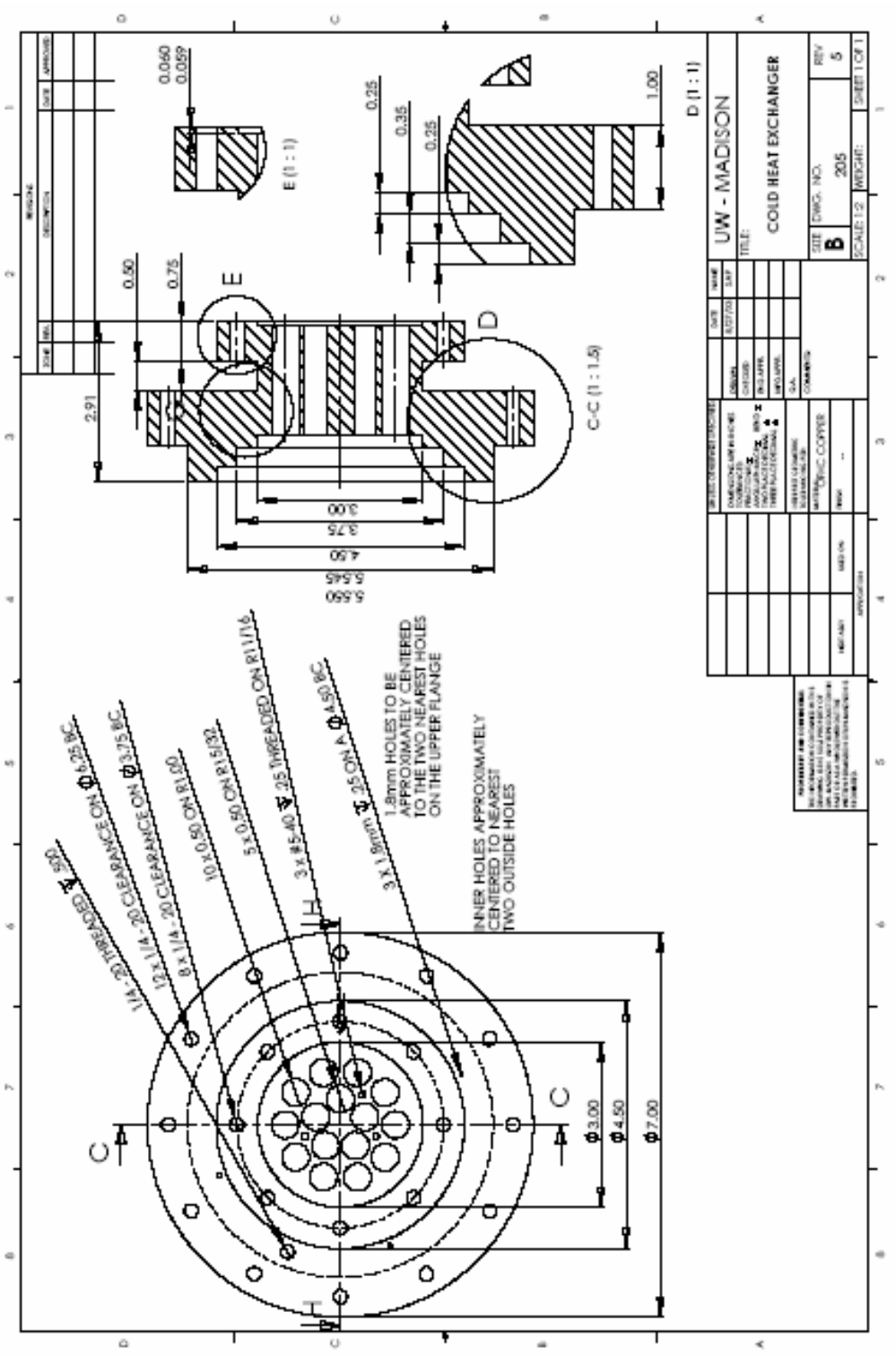
UW - MADISON
COLD HEAT EXCHANGER
C-C (1 : 1.5)
D (1 : 1)
E (1 : 1)
1.8mm HOLES TO BE APPROXIMATELY CENTERED TO THE TWO NEAREST HOLES ON THE UPPER FLANGE
INNER HOLES APPROXIMATELY CENTERED TO NEAREST TWO OUTSIDE HOLES

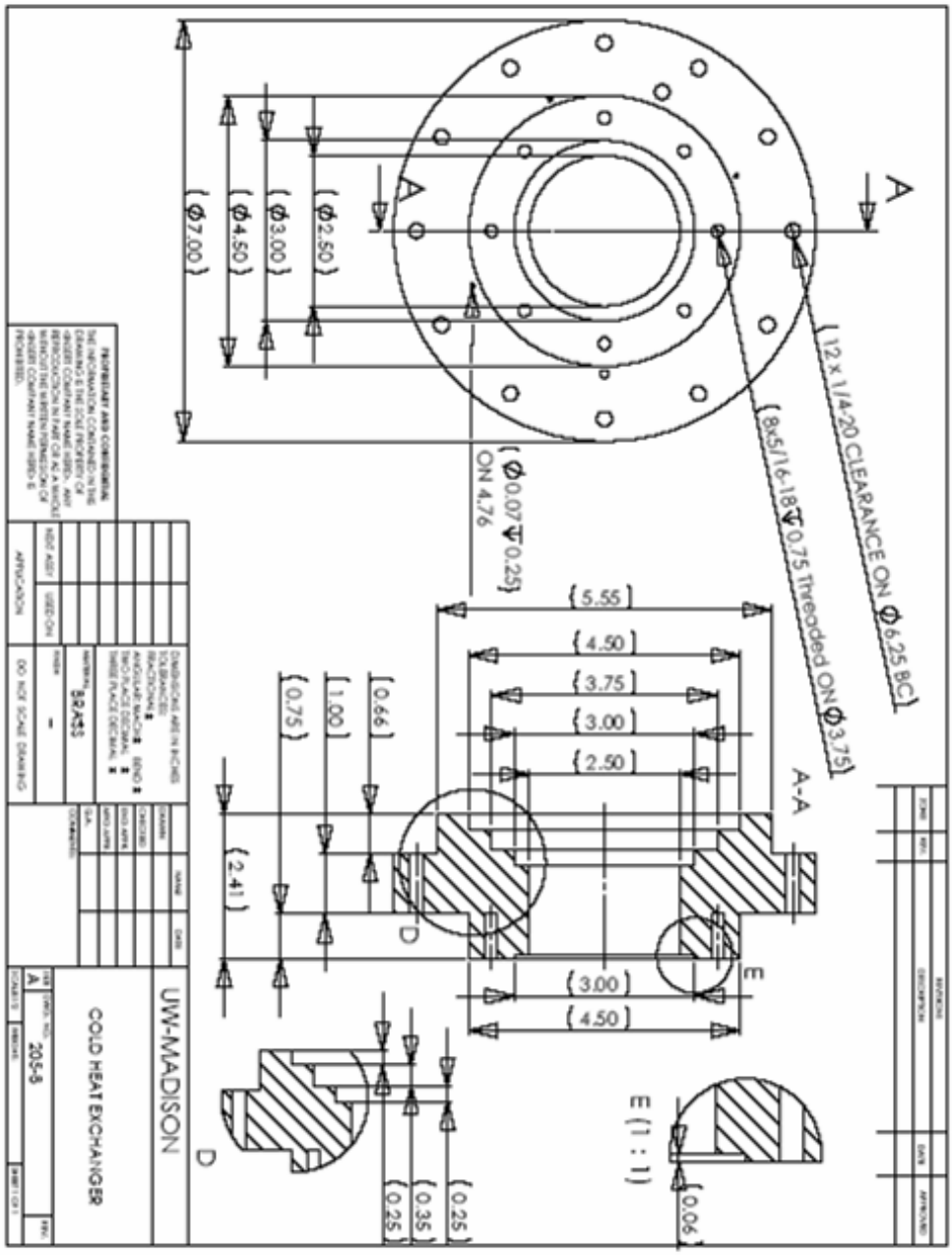
UW-MADISON
COLD HEAT EXCHANGER
205-8
A-A
E (1 : 1)
12 x 1/4-20 CLEARANCE ON Ø6.25 BC
8x5/16-18 ↧0.75 Threaded ON Ø3.75
Ø0.07 Ⓜ A 0.25
ON 4.76
Ø7.00
Ø4.50
Ø3.00
Ø2.50
5.55
4.50
3.75
3.00
2.50
0.75
1.00
0.66
2.41
3.00
4.50
0.25
0.35
0.25
0.06

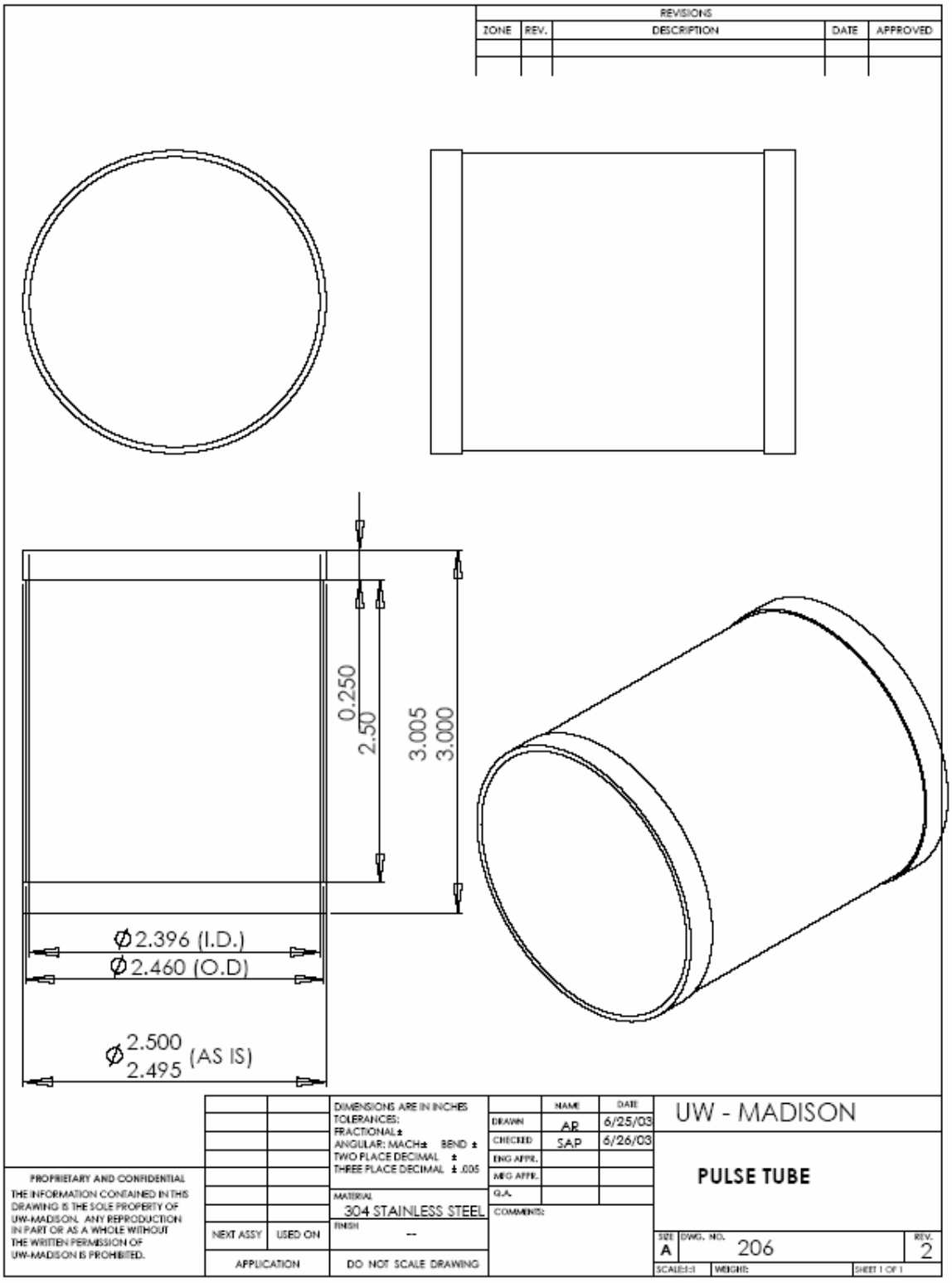
REVISIONS
ZONE
REV.
DESCRIPTION
DATE
APPROVED
0.250
2.50
3.005
3.000
Ø2.396 (I.D.)
Ø2.460 (O.D)
Ø2.500
2.495
(AS IS)
DIMENSIONS ARE IN INCHES
TOLERANCES:
FRACTIONAL ±
ANGULAR: MACH ± BEND ±
TWO PLACE DECIMAL ±
THREE PLACE DECIMAL ± .005
MATERIAL
304 STAINLESS STEEL
FINISH
--
DO NOT SCALE DRAWING
NEXT ASSY
USED ON
APPLICATION
NAME
DATE
DRAWN
AP
6/25/03
CHECKED
SAP
6/26/03
ENG APPR.
MFG APPR.
Q.A.
COMMENTS:
UW - MADISON
PULSE TUBE
SIZE
A
DWG. NO.
206
REV.
2
SCALE:1:1
WEIGHT:
SHEET 1 OF 1
PROPRIETARY AND CONFIDENTIAL
THE INFORMATION CONTAINED IN THIS DRAWING IS THE SOLE PROPERTY OF UW-MADISON. ANY REPRODUCTION IN PART OR AS A WHOLE WITHOUT THE WRITTEN PERMISSION OF UW-MADISON IS PROHIBITED.

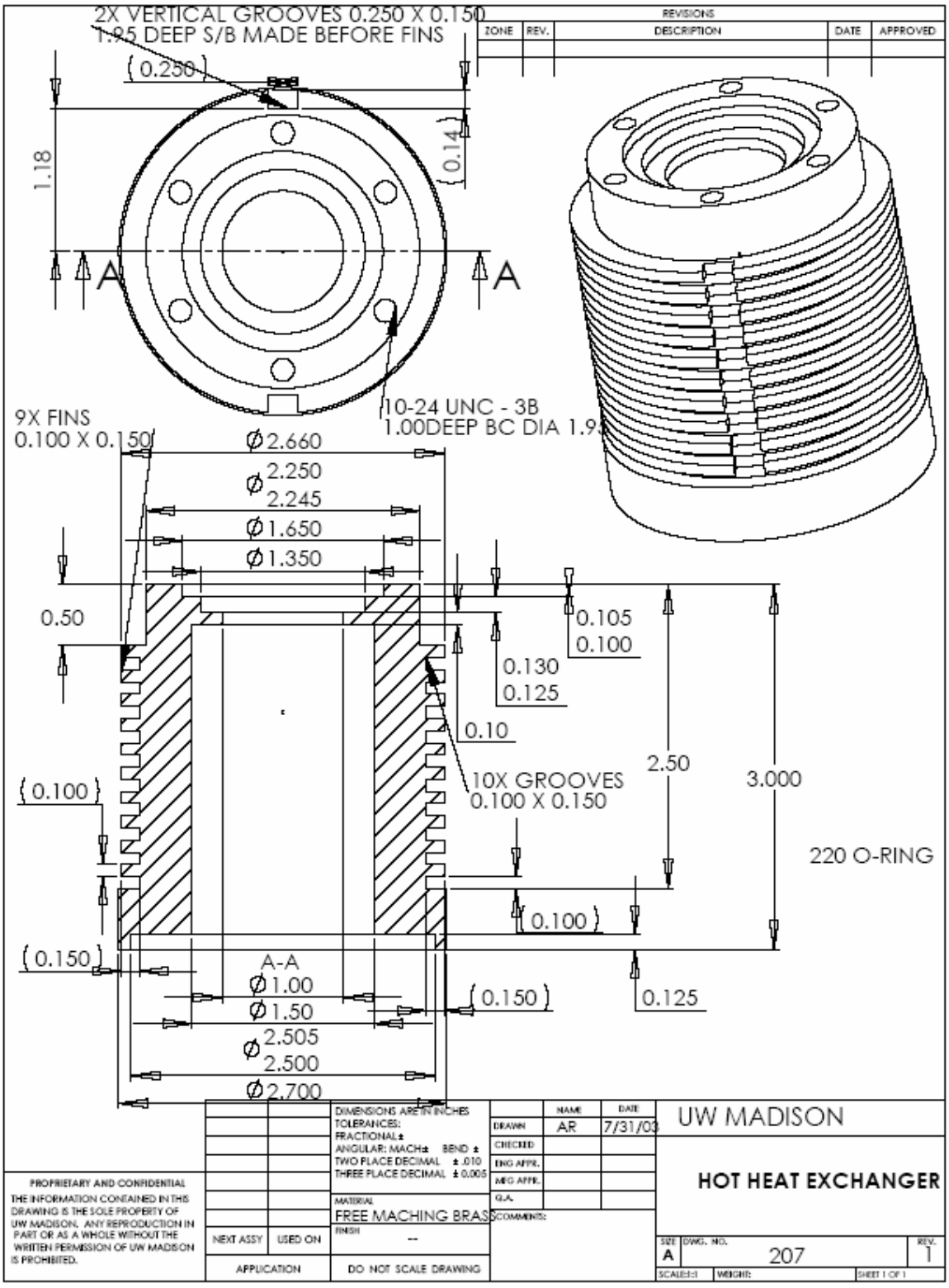
2X VERTICAL GROOVES 0.250 X 0.150
1.95 DEEP S/B MADE BEFORE FINS
REVISIONS
ZONE REV. DESCRIPTION DATE APPROVED
0.250
1.18
0.14
A
A
10-24 UNC - 3B
9X FINS
0.100 X 0.150
Ø2.660
Ø2.250
2.245
Ø1.650
Ø1.350
0.50
0.105
0.100
0.130
0.125
0.10
10X GROOVES
0.100 X 0.150
2.50
3.000
220 O-RING
0.100
0.100
0.150
A-A
Ø1.00
Ø1.50
2.505
2.500
Ø2.700
0.150
0.125
DIMENSIONS ARE IN INCHES
TOLERANCES:
FRACTIONAL ±
ANGULAR: MACH ± BEND ±
TWO PLACE DECIMAL ± .010
THREE PLACE DECIMAL ± 0.005
MATERIAL
FREE MACHING BRASS
FINISH
--
NAME DATE
DRAWN AR 7/31/03
CHECKED
ENG APPR.
MFG APPR.
Q.A.
COMMENTS:
UW MADISON
HOT HEAT EXCHANGER
SIZE A
DWG. NO. 207
REV. 1
SCALE:1:1
WEIGHT:
SHEET 1 OF 1
NEXT ASSY USED ON
APPLICATION
DO NOT SCALE DRAWING
PROPRIETARY AND CONFIDENTIAL
THE INFORMATION CONTAINED IN THIS DRAWING IS THE SOLE PROPERTY OF UW MADISON. ANY REPRODUCTION IN PART OR AS A WHOLE WITHOUT THE WRITTEN PERMISSION OF UW MADISON IS PROHIBITED.

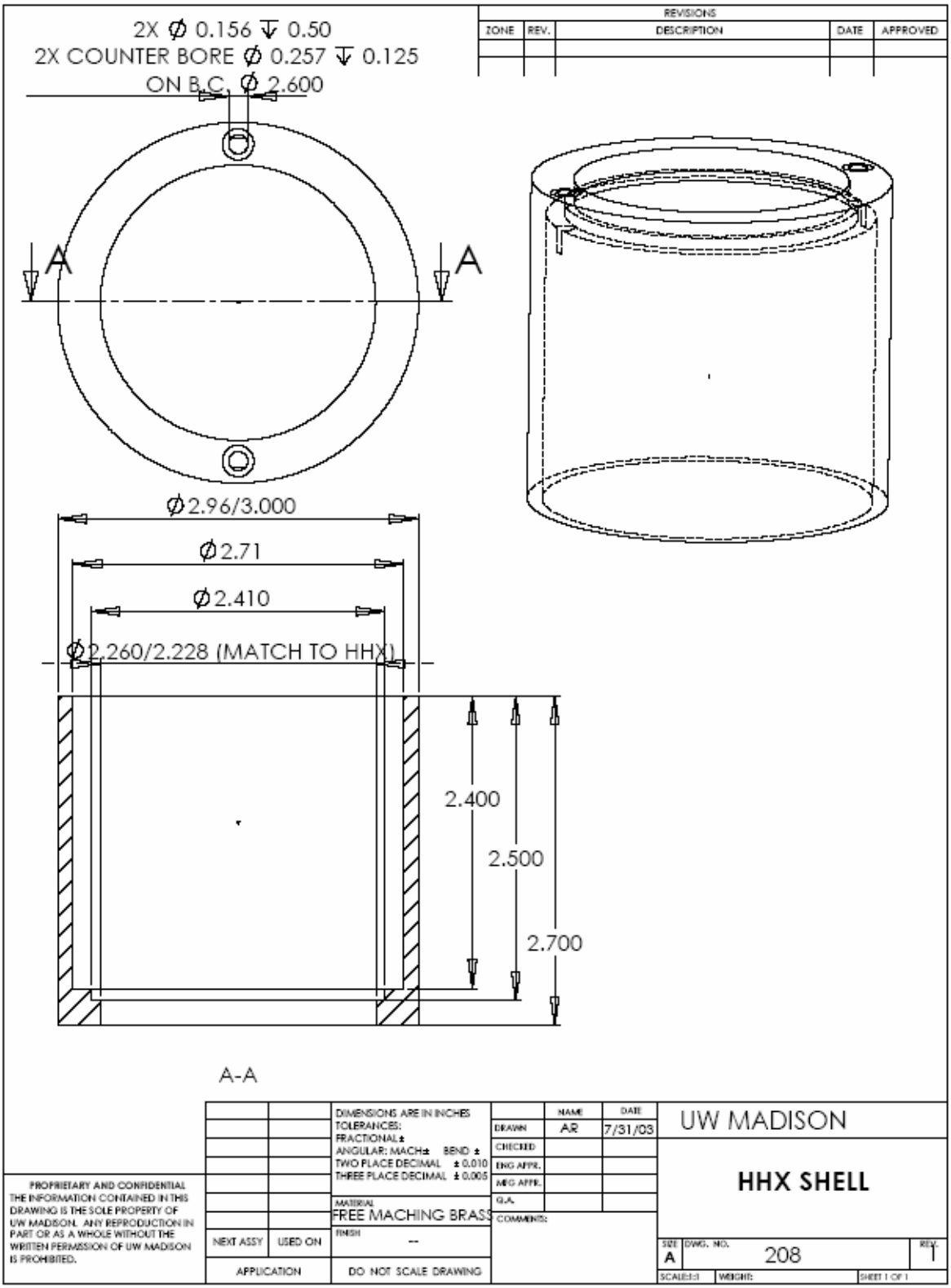
2X ⌀ 0.156 ↧ 0.50
2X COUNTER BORE ⌀ 0.257 ↧ 0.125
ON B.C. ⌀ 2.600
A
A
⌀2.96/3.000
⌀2.71
⌀2.410
⌀2.260/2.228 (MATCH TO HHX)
2.400
2.500
2.700
A-A
REVISIONS
ZONE
REV.
DESCRIPTION
DATE
APPROVED
DIMENSIONS ARE IN INCHES
TOLERANCES:
FRACTIONAL ±
ANGULAR: MACH ± BEND ±
TWO PLACE DECIMAL ± 0.010
THREE PLACE DECIMAL ± 0.005
MATERIAL
FREE MACHING BRASS
FINISH
--
NEXT ASSY
USED ON
APPLICATION
DO NOT SCALE DRAWING
NAME
DATE
DRAWN
AR
7/31/03
CHECKED
ENG APPR.
MFG APPR.
Q.A.
COMMENTS:
PROPRIETARY AND CONFIDENTIAL
THE INFORMATION CONTAINED IN THIS DRAWING IS THE SOLE PROPERTY OF UW MADISON. ANY REPRODUCTION IN PART OR AS A WHOLE WITHOUT THE WRITTEN PERMISSION OF UW MADISON IS PROHIBITED.
UW MADISON
HHX SHELL
SIZE
A
DWG. NO.
208
REV.
1
SCALE:1:1
WEIGHT:
SHEET 1 OF 1

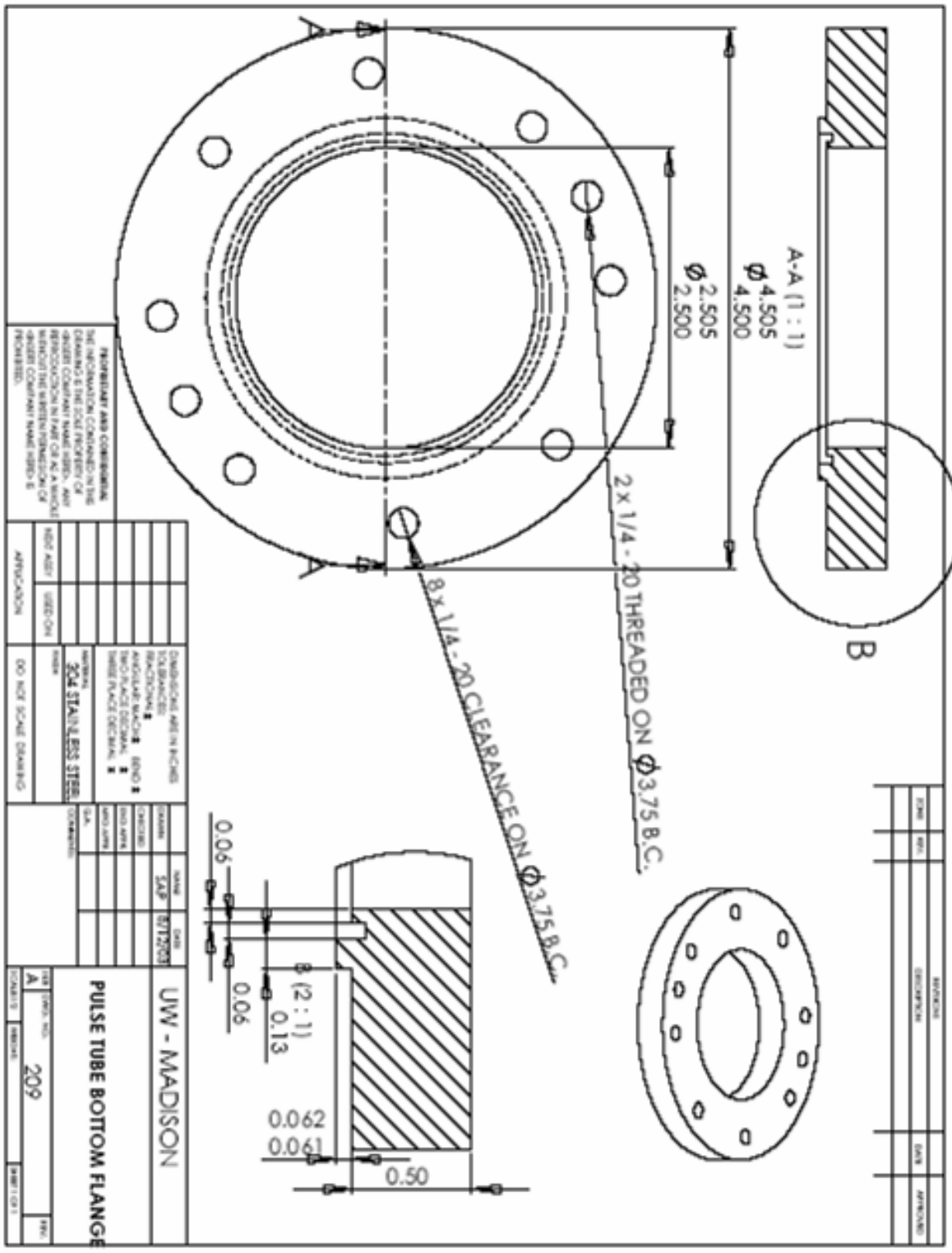
A-A (1 : 1)
Ø4.505
4.500
Ø2.505
2.500
2 x 1/4 - 20 THREADED ON Ø3.75 B.C.
8 x 1/4 - 20 CLEARANCE ON Ø3.75 B.C.
B (2 : 1)
0.06
0.06
0.13
0.062
0.061
0.50
B
A
A
304 STAINLESS STEEL
DO NOT SCALE DRAWING
SAP
8/17/05
UW - MADISON
PULSE TUBE BOTTOM FLANGE
209
A

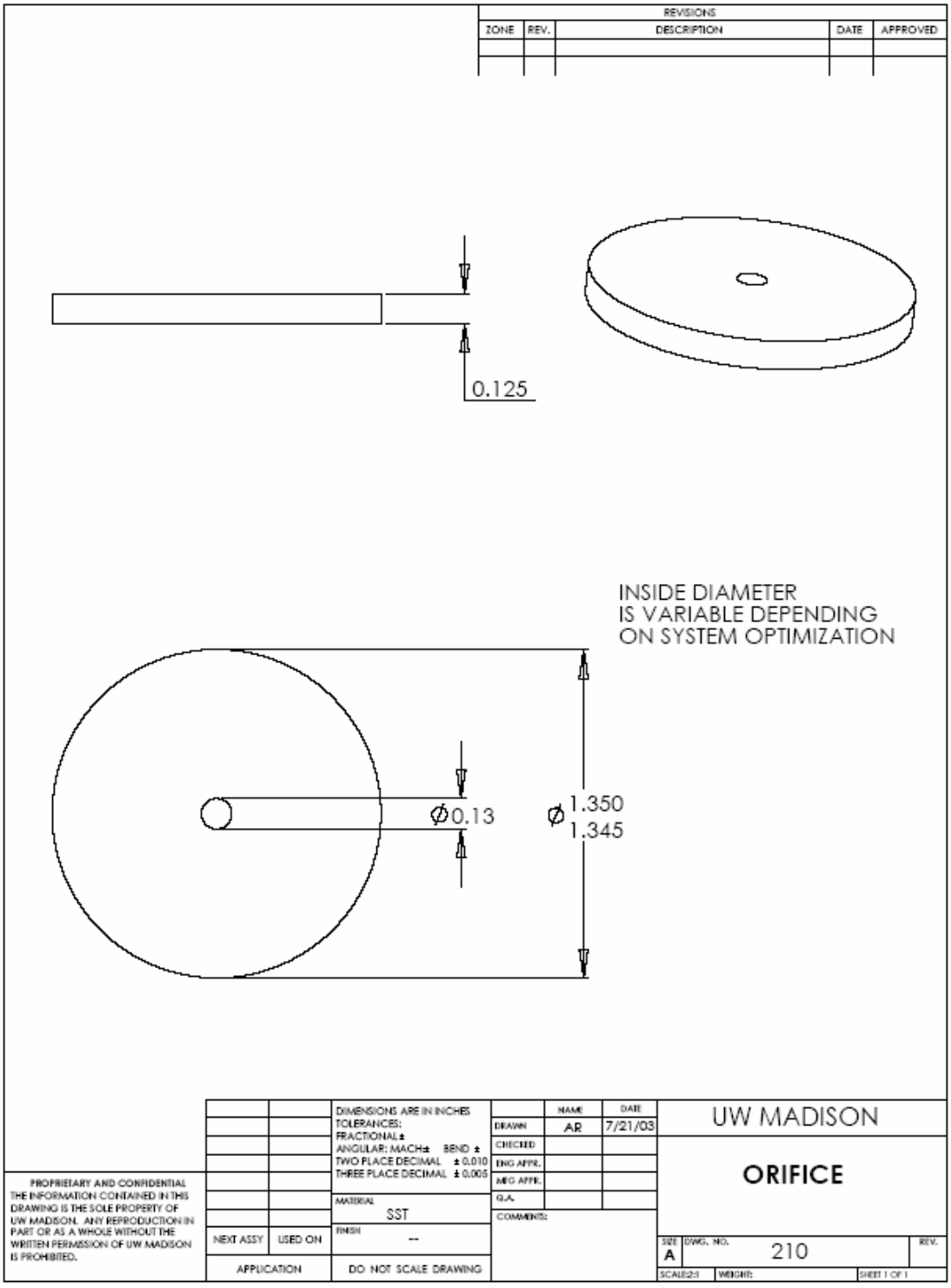
REVISIONS
ZONE
REV.
DESCRIPTION
DATE
APPROVED
0.125
INSIDE DIAMETER
IS VARIABLE DEPENDING
ON SYSTEM OPTIMIZATION
Ø0.13
Ø1.350
1.345
DIMENSIONS ARE IN INCHES
TOLERANCES:
FRACTIONAL ±
ANGULAR: MACH ± BEND ±
TWO PLACE DECIMAL ± 0.010
THREE PLACE DECIMAL ± 0.005
MATERIAL
SST
FINISH
--
NEXT ASSY
USED ON
APPLICATION
DO NOT SCALE DRAWING
NAME
DATE
DRAWN
AR
7/21/03
CHECKED
ENG APPR.
MFG APPR.
Q.A.
COMMENTS:
UW MADISON
ORIFICE
SIZE
A
DWG. NO.
210
REV.
SCALE:2:1
WEIGHT:
SHEET 1 OF 1
PROPRIETARY AND CONFIDENTIAL
THE INFORMATION CONTAINED IN THIS DRAWING IS THE SOLE PROPERTY OF UW MADISON. ANY REPRODUCTION IN PART OR AS A WHOLE WITHOUT THE WRITTEN PERMISSION OF UW MADISON IS PROHIBITED.

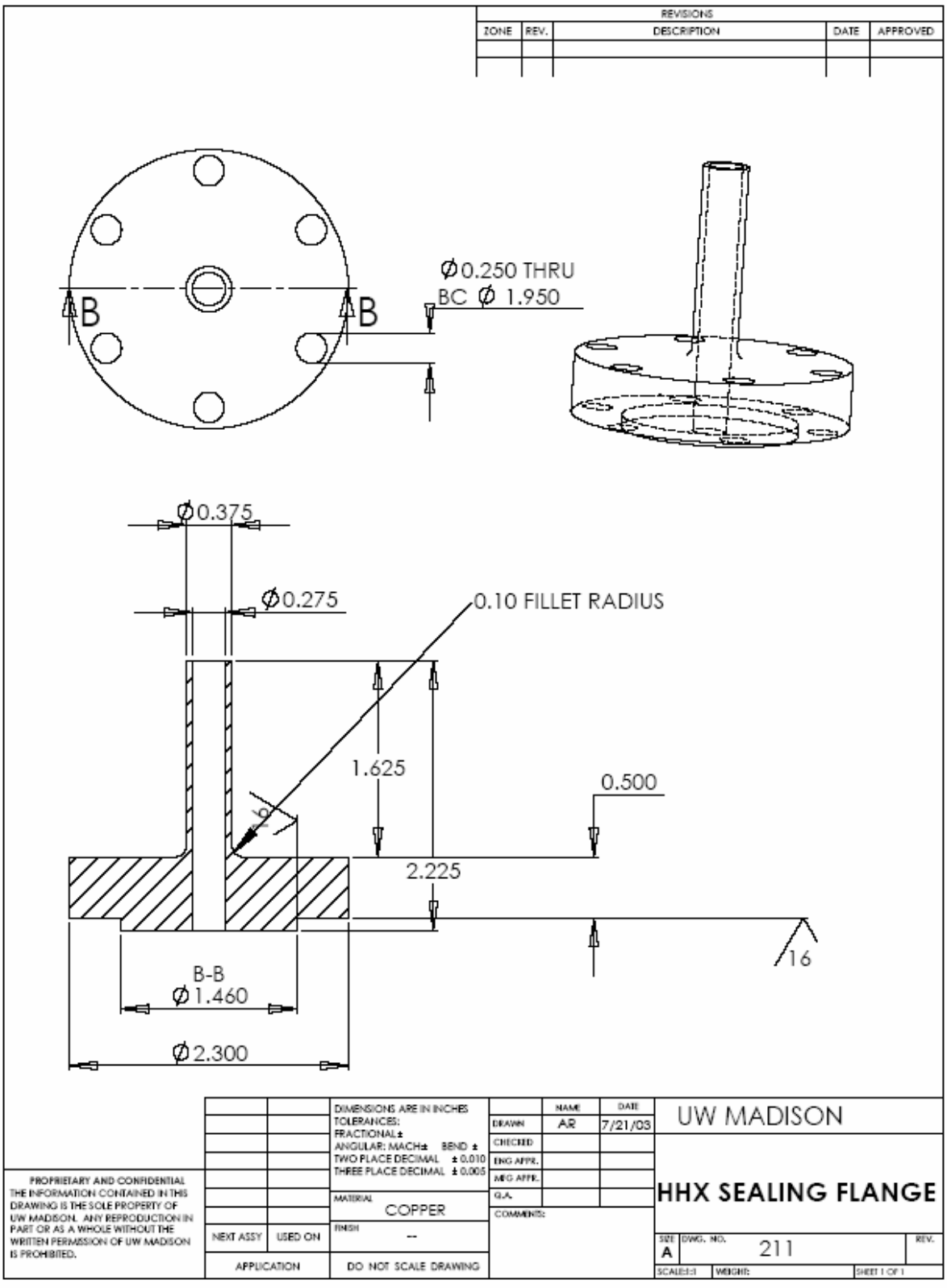
REVISIONS
ZONE
REV.
DESCRIPTION
DATE
APPROVED
B
B
Ø0.250 THRU
BC Ø 1.950
Ø0.375
Ø0.275
0.10 FILLET RADIUS
1.625
0.500
2.225
16
B-B
Ø1.460
Ø2.300
PROPRIETARY AND CONFIDENTIAL
THE INFORMATION CONTAINED IN THIS DRAWING IS THE SOLE PROPERTY OF UW MADISON. ANY REPRODUCTION IN PART OR AS A WHOLE WITHOUT THE WRITTEN PERMISSION OF UW MADISON IS PROHIBITED.
NEXT ASSY
USED ON
APPLICATION
DIMENSIONS ARE IN INCHES
TOLERANCES:
FRACTIONAL ±
ANGULAR: MACH ± BEND ±
TWO PLACE DECIMAL ± 0.010
THREE PLACE DECIMAL ± 0.005
MATERIAL
COPPER
FINISH
--
DO NOT SCALE DRAWING
NAME
DATE
DRAWN
AR
7/21/03
CHECKED
ENG APPR.
MFG APPR.
Q.A.
COMMENTS:
UW MADISON
HHX SEALING FLANGE
SIZE
A
DWG. NO.
211
REV.
SCALE:1
WEIGHT:
SHEET 1 OF 1

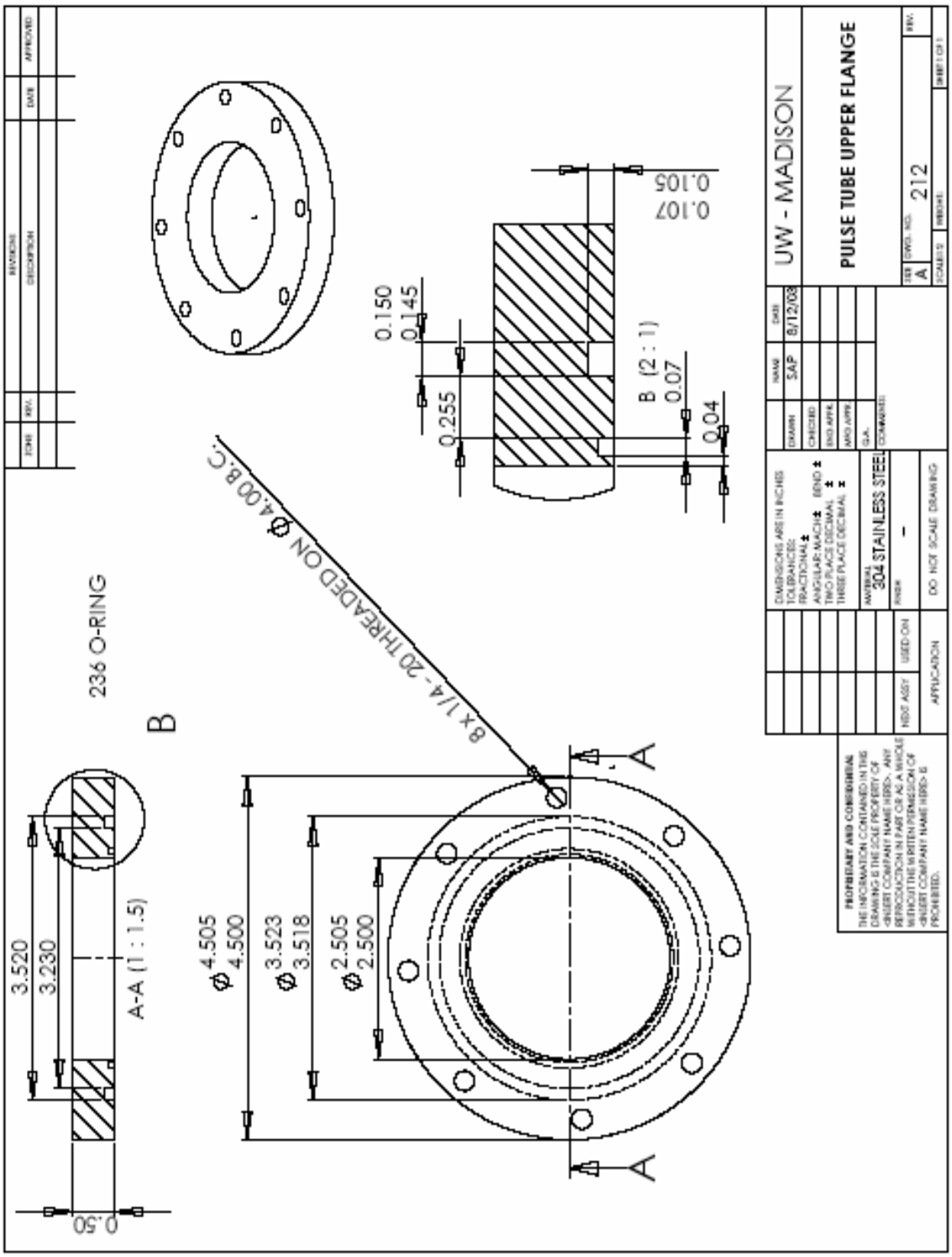
UW - MADISON
PULSE TUBE UPPER FLANGE
212
A
8/12/03
SAP
304 STAINLESS STEEL
236 O-RING
8X 1/4 - 20 THREADED ON Ø4.00 B.C.
A-A (1 : 1.5)
B (2 : 1)
3.520
3.230
0.50
Ø4.505
4.500
Ø3.523
3.518
Ø2.505
2.500
0.150
0.145
0.255
0.107
0.105
0.07
0.04

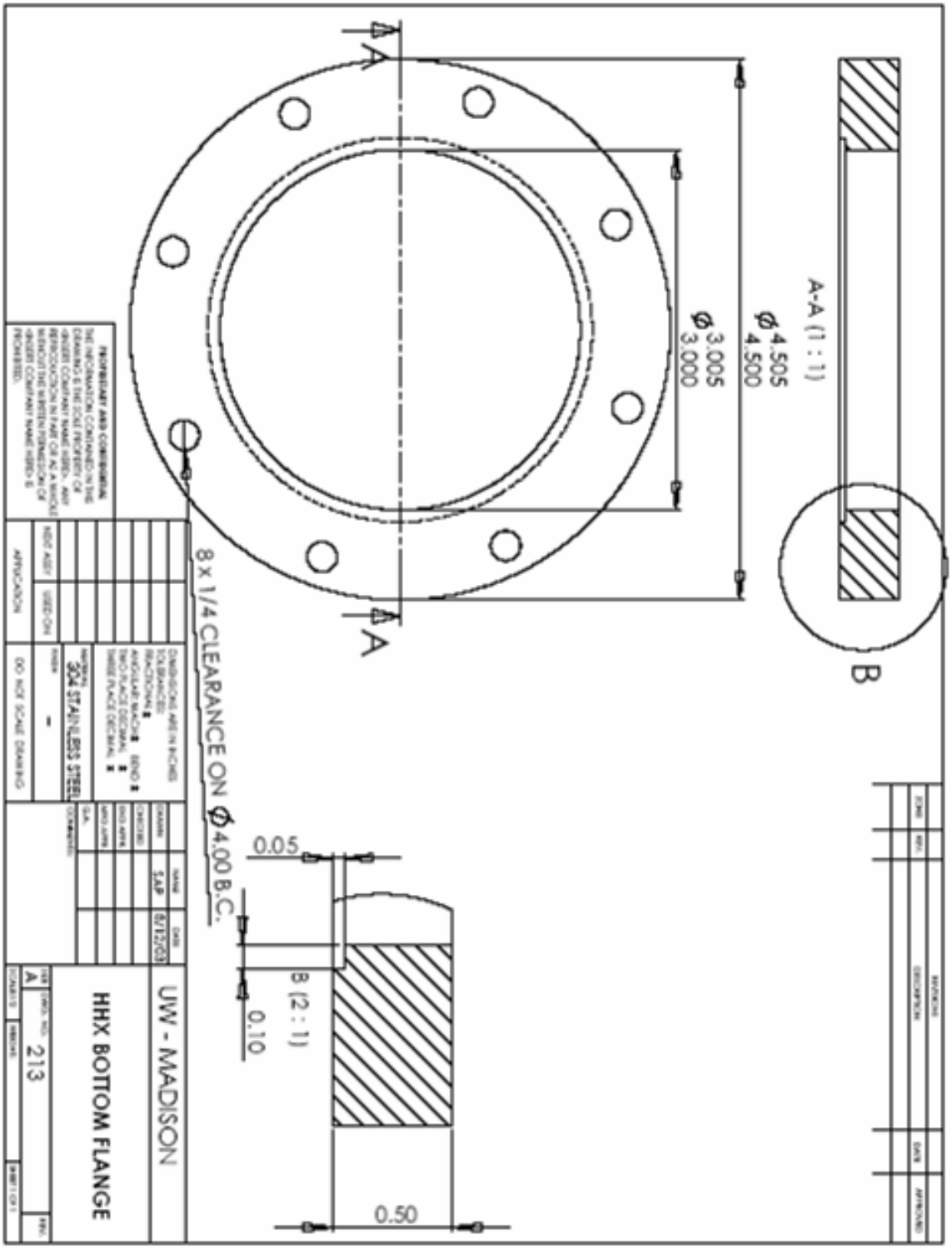
A
A
A-A (1 : 1)
B
Ø4.505
4.500
Ø3.005
3.000
8 X 1/4 CLEARANCE ON Ø4.00 B.C.
0.05
0.10
0.50
B (2 : 1)
HHX BOTTOM FLANGE
UW - MADISON
213
304 STAINLESS STEEL
DO NOT SCALE DRAWING

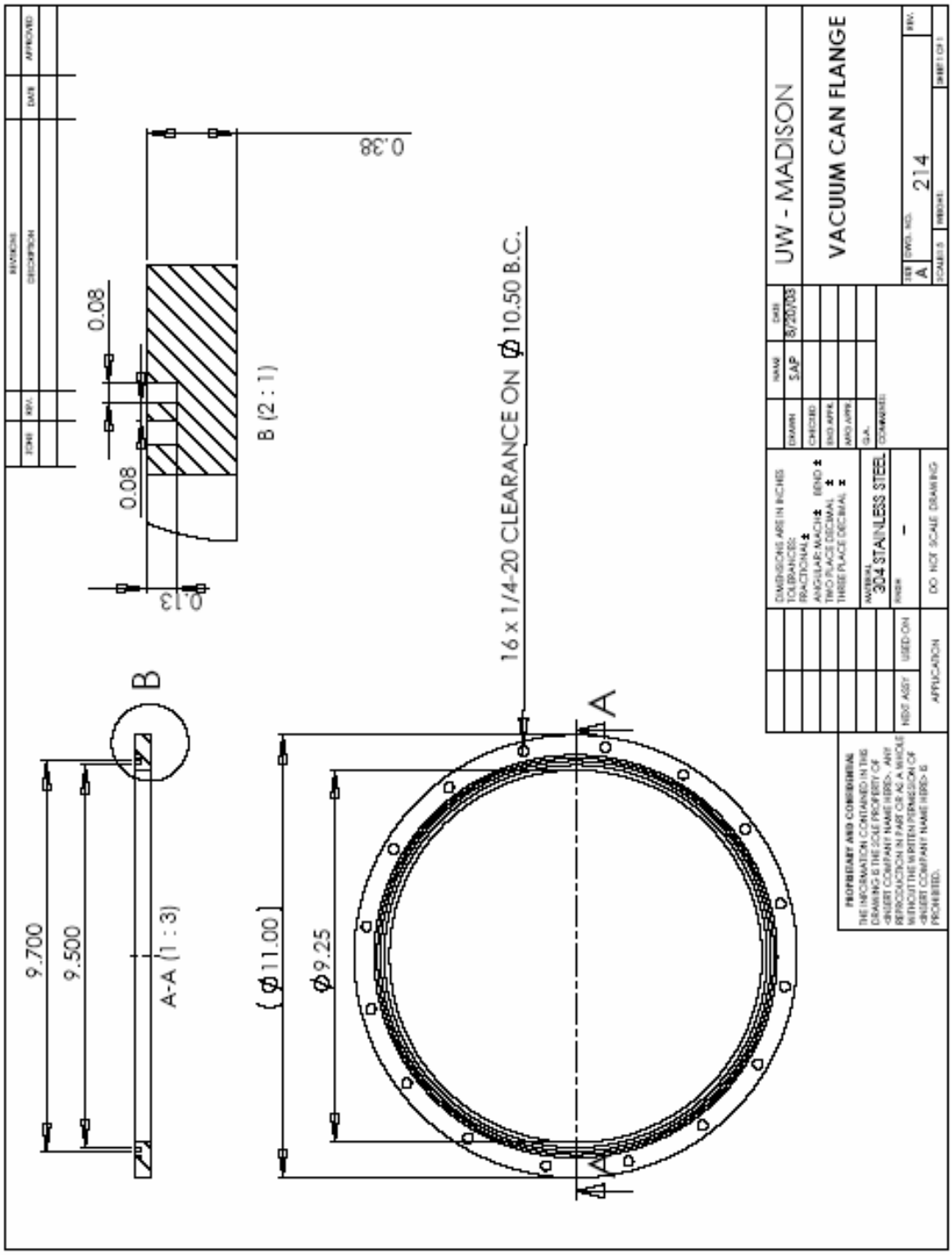
UW - MADISON
VACUUM CAN FLANGE
214
16 x 1/4-20 CLEARANCE ON ⌀10.50 B.C.
⌀9.25
(⌀11.00)
9.700
9.500
A-A (1 : 3)
B (2 : 1)
0.08
0.08
0.38
304 STAINLESS STEEL
DO NOT SCALE DRAWING

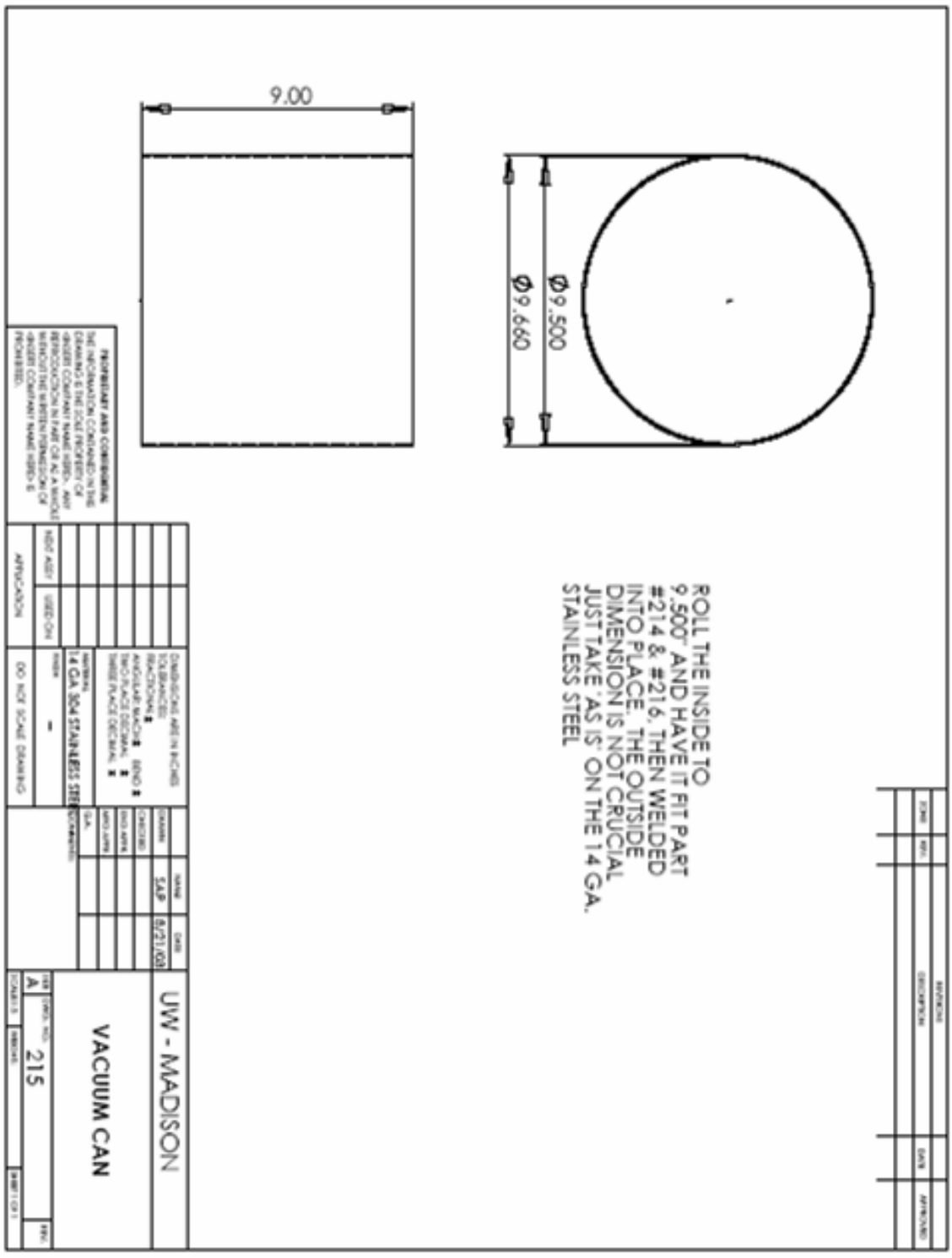
9.00
Ø9.500
Ø9.660
ROLL THE INSIDE TO
9.500" AND HAVE IT FIT PART
#214 & #216. THEN WELDED
INTO PLACE. THE OUTSIDE
DIMENSION IS NOT CRUCIAL
JUST TAKE 'AS IS' ON THE 14 GA.
STAINLESS STEEL
UW - MADISON
VACUUM CAN
215
A
14 GA 304 STAINLESS STEEL
DO NOT SCALE DRAWING

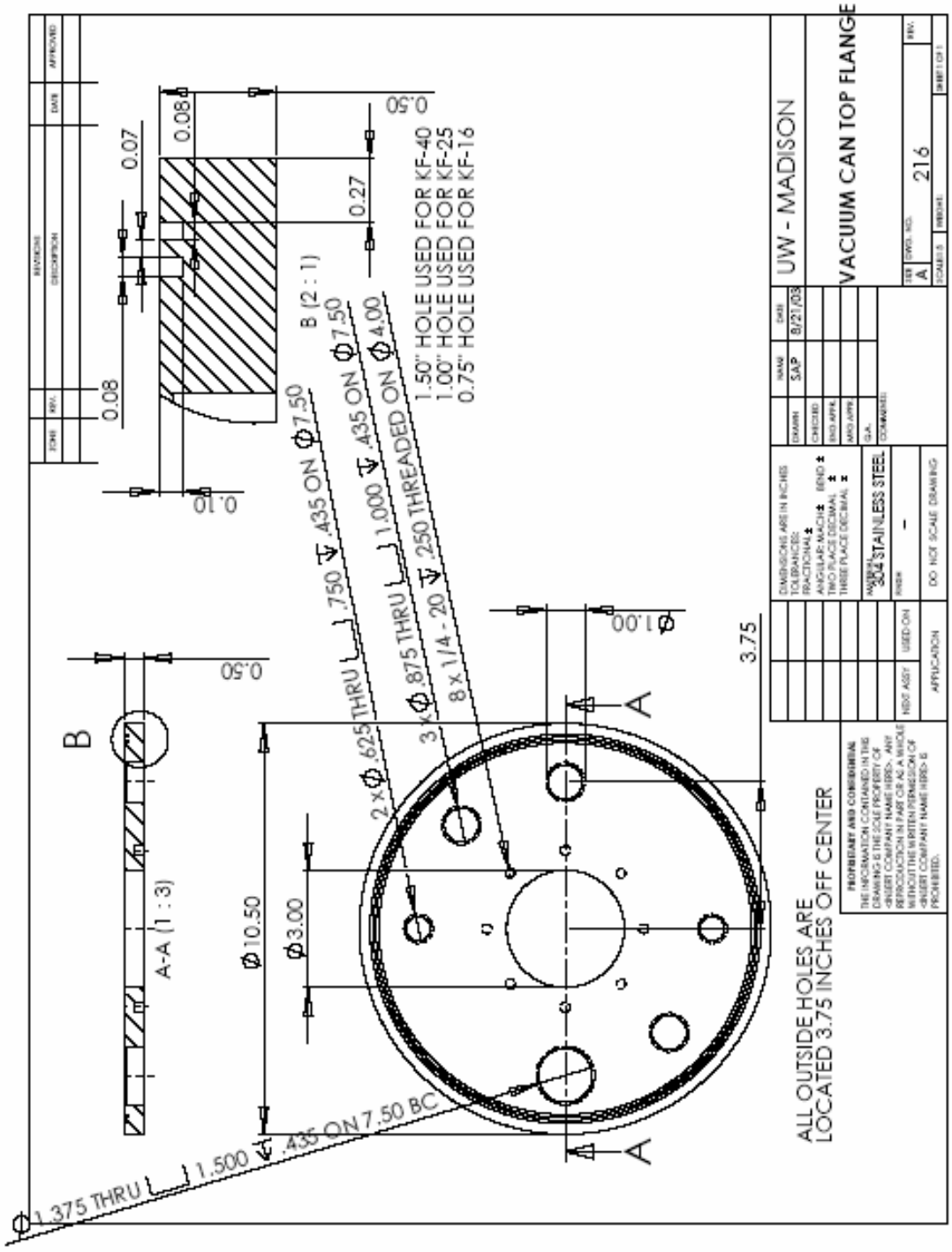
VACUUM CAN TOP FLANGE
UW - MADISON
216
304 STAINLESS STEEL
8/21/03
SAP
ALL OUTSIDE HOLES ARE
LOCATED 3.75 INCHES OFF CENTER
1.50" HOLE USED FOR KF-40
1.00" HOLE USED FOR KF-25
0.75" HOLE USED FOR KF-16
8 X 1/4 - 20 ∓ .250 THREADED ON Ø4.00
3 X Ø.875 THRU ⌴ 1.000 ∓ .435 ON Ø7.50
2 X Ø.625 THRU ⌴ .750 ∓ .435 ON Ø7.50
Ø1.375 THRU ⌴ 1.500 ∓ .435 ON 7.50 BC
Ø10.50
Ø3.00
3.75
1.00
0.50
0.10
0.08
0.07
0.27
A-A (1 : 3)
B (2 : 1)

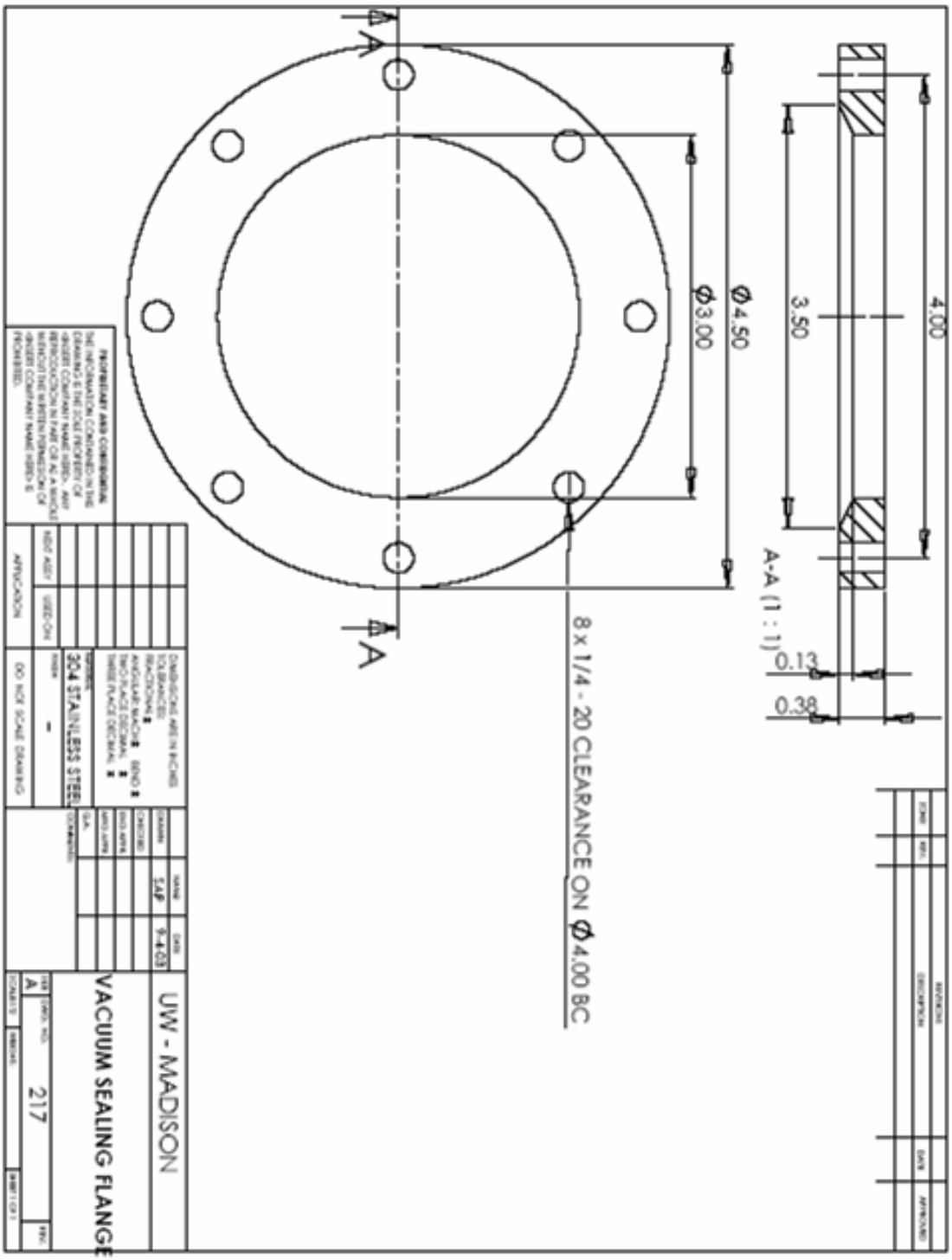
4.00
3.50
A-A (1 : 1)
0.13
0.38
Ø4.50
Ø3.00
A
A
8 X 1/4 - 20 CLEARANCE ON Ø4.00 BC
UW - MADISON
VACUUM SEALING FLANGE
217
304 STAINLESS STEEL
SAP
9-4-03
DO NOT SCALE DRAWING

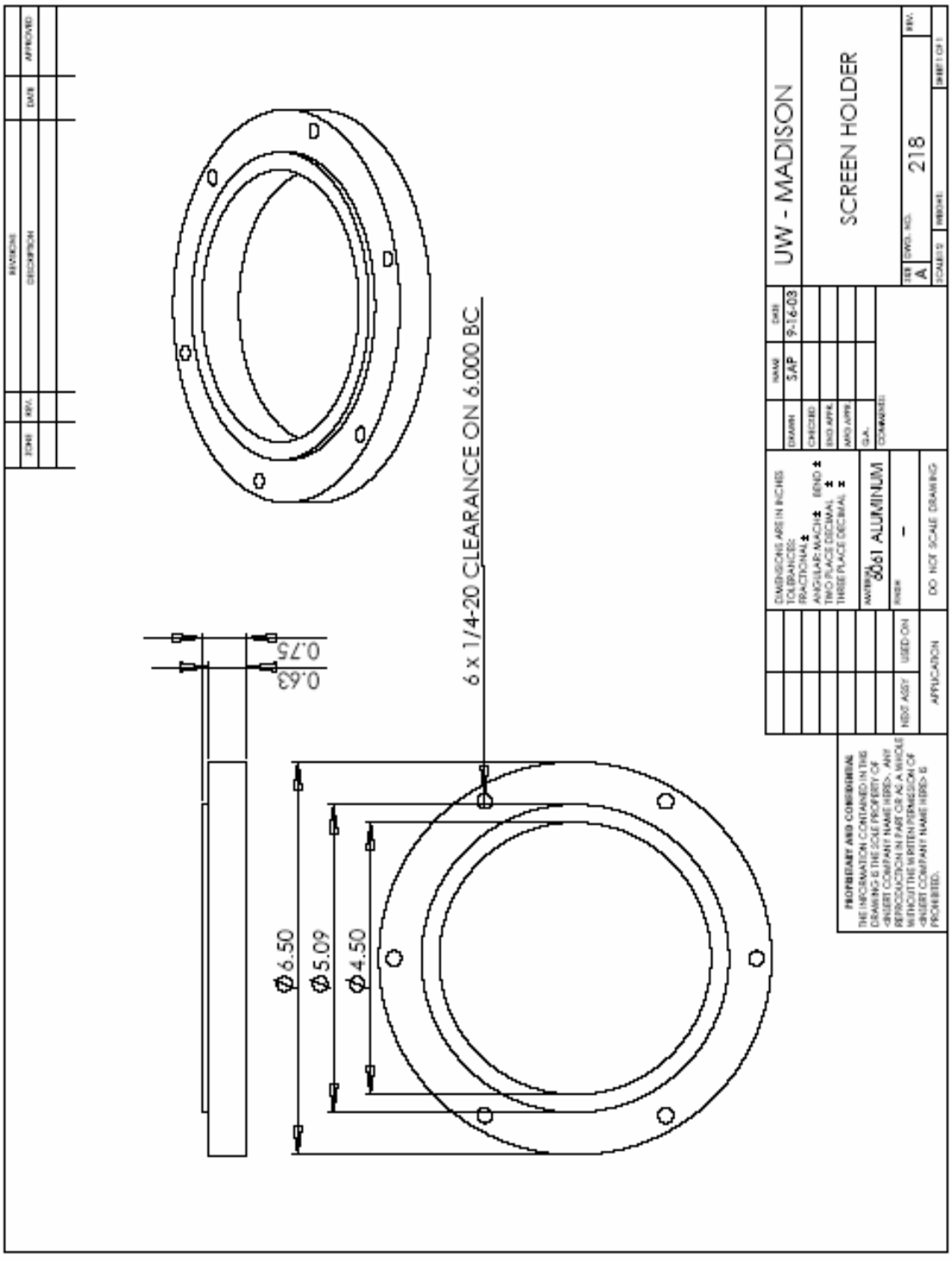
6 x 1/4-20 CLEARANCE ON 6.000 BC
0.63
0.75
Ø6.50
Ø5.09
Ø4.50
UW - MADISON
SCREEN HOLDER
218
A
9-16-03
S.AP
6061 ALUMINUM
DO NOT SCALE DRAWING

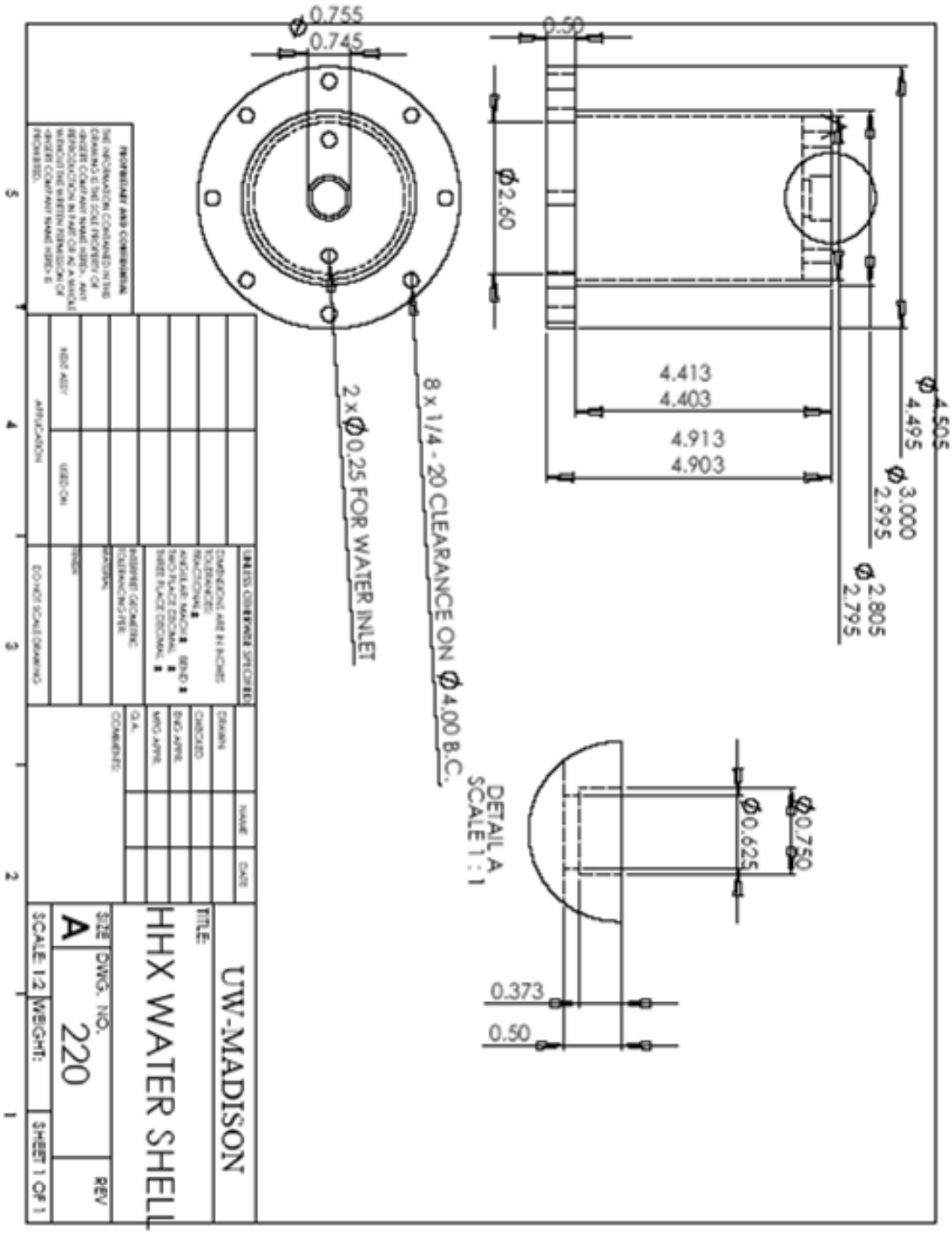
Ø0.755
0.745
0.50
Ø2.60
4.413
4.403
4.913
4.903
Ø4.505
4.495
Ø3.000
2.995
Ø2.805
2.795
2 x Ø0.25 FOR WATER INLET
8 x 1/4 - 20 CLEARANCE ON Ø4.00 B.C.
DETAIL A
SCALE 1 : 1
Ø0.750
Ø0.625
0.373
0.50
UW-MADISON
HHX WATER SHELL
SIZE A
DWG. NO. 220
REV
SCALE: 1:2
WEIGHT:
SHEET 1 OF 1

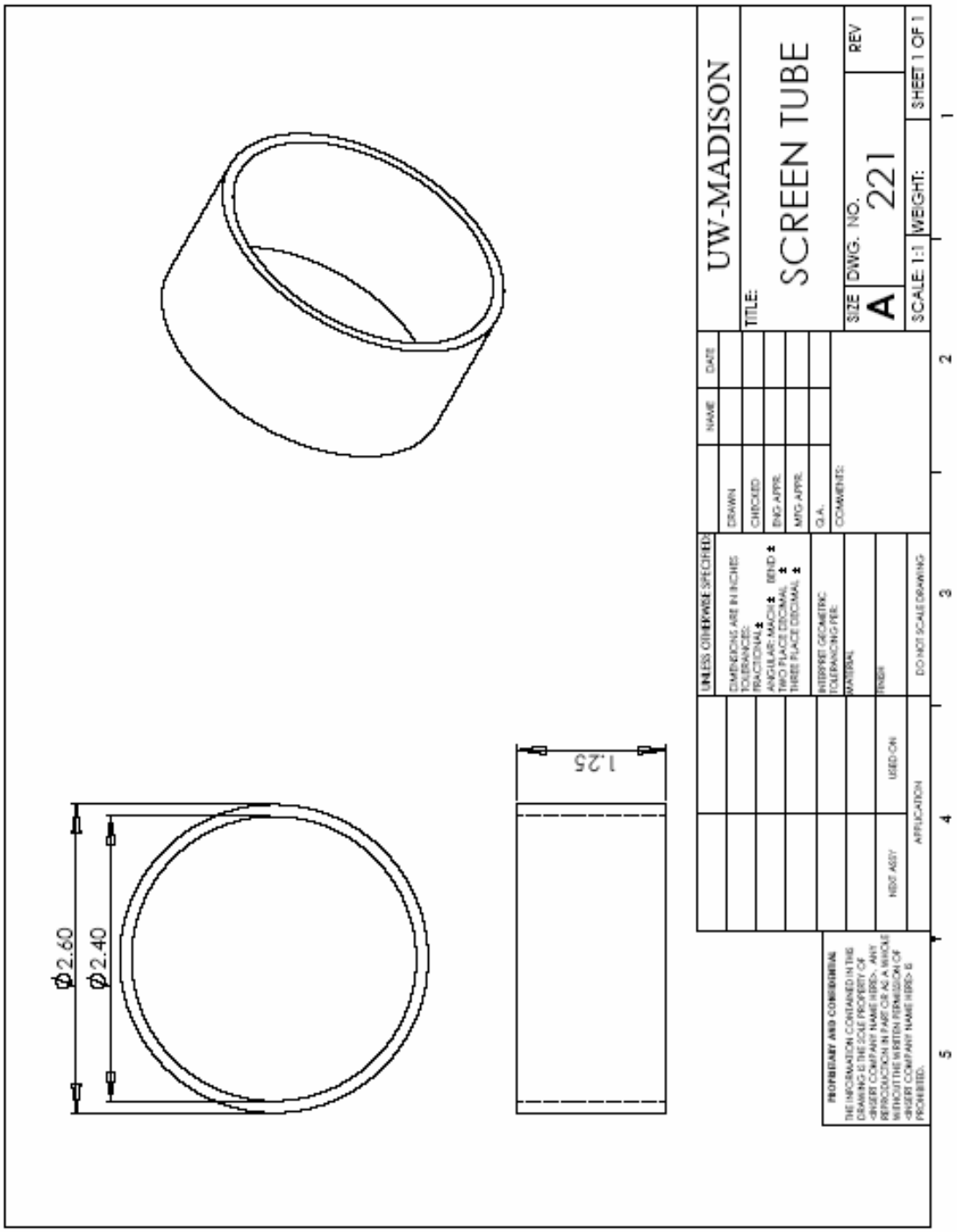
Ø2.60
Ø2.40
1.25
UW-MADISON
SCREEN TUBE
SIZE A
DWG. NO. 221
REV
SCALE: 1:1
WEIGHT:
SHEET 1 OF 1
UNLESS OTHERWISE SPECIFIED:
DRAWN
CHECKED
ENG APPR.
MFG APPR.
Q.A.
COMMENTS:
NAME
DATE
PROPRIETARY AND CONFIDENTIAL
NEXT ASSY
USED ON
APPLICATION
DO NOT SCALE DRAWING

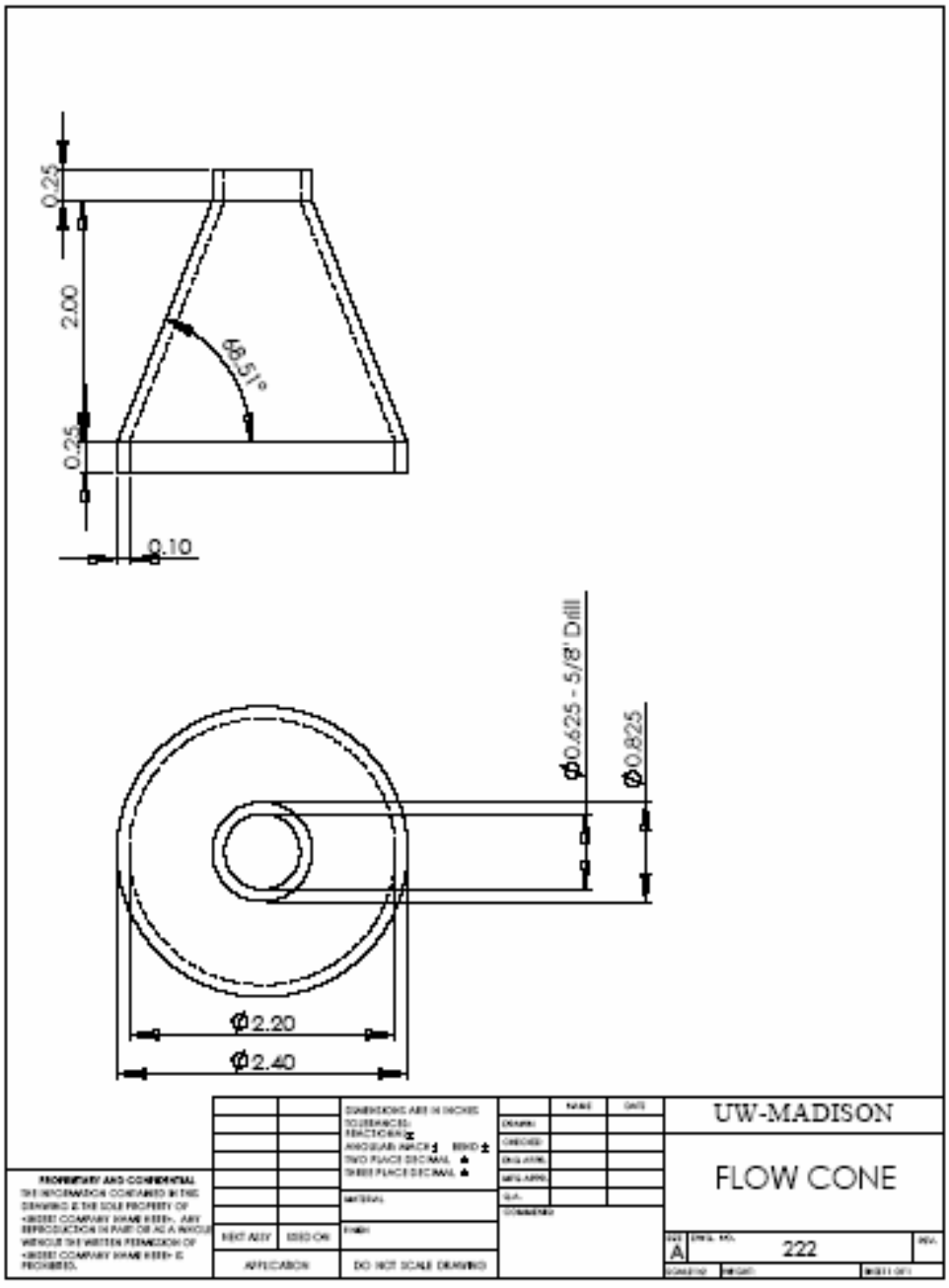
0.25
2.00
48.51°
0.25
0.10
Φ0.625 - 5/8" Drill
Φ0.825
Φ2.20
Φ2.40
UW-MADISON
FLOW CONE
222
A

Appendix B – Thermodynamic Model

Single-Stage Pulse-Tube Model

Input Parameters						
Heat rejection temperature	T_rej	300	K			
Load temperature	T_exp	60	K			PUT Variables in MATLAB
System charge pressure	P_charge	2309107.143	Pa	335	psia	
Gas type	gas	He				GET Variables from MATLAB
Gas constant	Rg	2077	J/kg-K			
Constant pressure specific heat capacity	cP	5188				
Ratio of heat capacities	gamma	1.667630987				
Compressor						
Compressor piston diameter	Dp_c	0.13462	m	5.3	inch	
Number of compressor pistons	Np_c	2				
Full Compressor Stroke	S_c	0.02794	m	1.1	inch	
Compressor swept volume	V_swept	0.000795363	m^3	795.3631	cc	=Np_c*S_c*PI()*Dp_c^2/4
Fractional stroke	f_c	0.95				
Compressor frequency	freq_c	45	Hz			
Compressor dead volume	V_c_dead	0.00213	m^3	2130	cc	
Period of compressor stroke	tau	0.022222222	sec	22.22222	microsec	=1/freq_c
Compressor efficiency	eta_c	0.65				
Pulse-Tube						
Pulse-tube inner diameter	D_pt	0.05969	m	2.35	inch	
Pulse-tube wall thickness	t_pt	0.0008128	m	0.032	inch	
Pulse-tube length	L_pt	0.0762	m	3	inch	
Pulse-tube volume	V_pt	0.00021323	m^3	213.2299	cc	=L_pt*PI()*D_pt^2/4
Pulse-tube metal	metal_pt	SS304				
Phase Shifter						
Dimensionless inertance resistance	Rps	0.25				
Dimensionless inertance fluid inductance	Lps	0.06				
Inertance resistance	rst_in	4.35E+06	Pa-s/kg			=Rps*tau*Rg*T_rej/V_swept
Inertance fluid inductance	Ind_in	2.32E+04	1/m			=Lps*tau^2*Rg*T_rej/V_swept
Reservoir volume	V_Rsv	0.0025		2.5	liter	
Regenerator						
Regenerator length	L_r	0.0508	m	2	inch	
Regenerator inner diameter	D_r	0.1304544	m	5.136	inch	
Regenerator wall thickness	tw_r	0.0015748	m	0.062	inch	
Regenerator tube material	metal_r_t	SS304				
Hydraulic diamter	dh_r	0.00005544	m	55.44	micrometer	
Regenerator porosity	sigma_r	0.6858				
Regenerator dead volume	V_r	0.00046566	m^3	465.6596	cc	=sigma_r*PI()*D_r^2*L_r/4
Mass average temperature of regenerator dead volume	T_r	149.1203843	K			=(T_rej-T_exp)/LN(T_rej/T_exp)
Equivalent amplitude of mass flow at cold end of regen.	m_dot_r_cold_amp	0.114460431	kg/s			=(Mdoteavg*PI()/2)*P_charge*V_swept/(tau*Rg*T_rej)
Equivalent amplitude of mass flow at hot end of regen.	m_dot_r_hot_amp	0.123496668	kg/s			=(Mdotcavg*PI()/2)*P_charge*V_swept/(tau*Rg*T_rej)
Phase between hot and cold mass flows (>0 if cold peaks before hot)	massphase	-0.955044167	rad	-54.72	degree	=Massphase
regenerator frontal area	area_r	0.012728565	m^2			=PI()*(D_r-2*tw_r)^2/4
pressure ratio used for Regen	PRatio_r	1.219185126				=PRpt
average pressure in the regenerator	Pr_avg	2312217.886	Pa			=Pcavg*P_charge
Phase between mass flow and pressure at cold end of pulse tube (>0 if mdot peaks before P)	Pphase	-0.427256601	rad	-24.48	degree	=Pphase
Average pressure drop across the regenerator	DELPAV	3.57E+04	Pa	35.7	kPa	
Average mass flow rate through the regenerator	m_dot_r_avg	0.075744097	kg/s			=(Mdoteavg+Mdotcavg)*P_charge*V_swept/(tau*Rg*T_rej*2)
Equivalent regenerator resistance	rst_r	471323.8574	Pa/(kg/s)			
PV Work from regen at cold end of regenerator	PVWK1	6.73E+02	W			
PV Work from regen at warm end of regenerator	PVWK0T	-4.06E+03	W			
Loss related to pressurization of void volume	PRLOSS	3.60E+01	W			
Loss related to regenerator ineffectiveness	RGLOSS	1.95E+02	W			
Conduction through matrix material	HTFLUX	5.90E+00	W			
Regen's estimate of net cooling power	NTCADJ	4.37E+02	W			

Numerical Parameters					
number of time steps per cycle	n	**250**			
tolerance on cyclic steady state	tol	**0.001**			
Performance Summary					
Maximum possible refrigeration power	qdotemax	612.4031078	W		=Qdote*P_charge*V_swept/tau
Ratio of Pulse tube to expansion space volume	PTvol\expvol	5.083546297			=lambdapt/lambdaemax
Compressor PV Input Power	wdotcPV	3828.168898	W	3.828169 kwatt	=Wdotc*P_charge*V_swept/tau
Compressor Electrical input power	wdotc_e	5889.490612	W	5.889491 kwatt	=wdotcPV/eta_c
Net refrigeration	qdot_load	***319.2326454***	W		=qdotemax-PRLOSS-RGLOSS-HTFLUX-qdot_r_tube-qdot_pt_tube-qdot_shuttle
Coefficient of Performance	COP	0.083390429			
Other Loss Calculation					
Regenerator Tube conductivity	k_r_tube	12.31243445	W/m-K		=get_km(metal_r_t,T_exp,T_rej)
Regenerator tube cross-sectional area	A_r_tube	0.000637616	m^2		=PI()*(D_r^2-(D_r-2*tw_r)^2)/4
Regenerator tube heat leak	qdot_r_tube	37.0894949	W		=k_r_tube*A_r_tube*(T_rej-T_exp)/L_r
Pulse-tube conductivity	k_pt_tube	12.31243445	W/m-K		=get_km(metal_pt,T_exp,T_rej)
Pulse-tube cross-sectional area	A_pt_tube	0.000150342	m^2		=PI()*(D_pt^2-(D_pt-2*t_pt)^2)/4
Pulse-tube heat leak	qdot_pt_tube	5.830165961	W		=k_pt_tube*A_pt_tube*(T_rej-T_exp)/L_pt
Mean change in gas position over a cycle	Dxgas_pt	0.018733964	m	0.737558 inch	=(lambdaemax+lambdahmax)*V_swept/(PI()*(D_pt-2*t_pt)^2/4)/2
Mean change in gas temperature over a cycle	DTgas_pt	14.86337924	K		=(T_rej+T_exp)*(PRpt^((gamma-1)/gamma)-1)/2
Approximate wall temperature change over shuttle region	DTwall_pt	59.00461219	K		=(T_rej-T_exp)*Dxgas_pt/L_pt
Average gas viscosity in pulse-tube	mu_g_pt	1.39528E-05	Pa*sec		=get_mu(gas,T_exp,T_rej)
Average Reynolds number for developing flow in pulse tube	Re_pt	44550.02895			=(P_charge/(Rg*(T_exp+T_rej)/2))*Dxgas_pt*2*D_pt/(tau*mu_g_pt)
Prandtl number in pulse-tube	Pr_pt	**0.7**			
Nusselt number in pulse tube	Nu_pt	124.4542471			=0.664*Re_pt^0.5*Pr_pt^0.333
Thermal conductivity of gas in pulse-tube	k_g_pt	0.107026259	W/m-K		=get_kg(gas,T_exp,T_rej)
Heat transfer coefficient in pulse tube	h_pt	711.0012692	W/m^2-K		=k_g_pt*Nu_pt/Dxgas_pt
Shuttle heat transfer loss	qdot_shuttle	13.78180149	W		=h_pt*(Dxgas_pt*PI()*D_pt/2)*((DTwall_pt-DTgas_pt)/2)/2

```
function[dPptdphi,dPcdphi,dMdotpsdphi,dPRsvdphi,lambdac,dlambdacdphi,Mdotc,Mdote]=dXdphi_ ↙
PTss(Ppt,Pc,Mdotps,PRsv,phi,Rps,Lps,lambdaRsv,gamma,thetae,lambdar,Rr,thetar,lambdacd,f,l ↙
ambdapt)

Mdote=(Pc-Ppt)/Rr;
lambdac=lambdacd+(1+f*sin(phi))/2;
dlambdacdphi=f*cos(phi)/2;
dPcdphi=-(Mdote+2*pi*Pc.*dlambdacdphi)./(2*pi*(lambdar/thetar+lambdac));
Mdotc=-2*pi*(Pc.*dlambdacdphi+lambdac.*dPcdphi);
dPRsvdphi=Mdotps/(2*pi*lambdaRsv);
Mdotpsn=(Ppt-PRsv)/Rps;
dMdotpsdphi=(Ppt-PRsv-Rps*Mdotps)/(2*pi*Lps);
dPptdphi=(thetae*Mdote-Mdotps)*gamma/(2*pi*lambdapt);
```

```
function[Wdotc,Qdotc,Qdote,Qdoth,phi,Ppt,Pc,Mdotps,PRsv,lambdac,Mdotc,Mdote,lambdae,lambdah,Msys,errMsys]=PTss(Rps,Lps,lambdaRsv,gamma,thetae,lambdar,Rr,thetar,lambdacd,f,lambdapt,n,tol)


wt=1;

Ppt=zeros(n,1);
Pc=zeros(n,1);
Mdotps=zeros(n,1);
PRsv=zeros(n,1);
lambdac=zeros(n,1);
Mdotc=zeros(n,1);
Mdote=zeros(n,1);

Ppt(1,1)=1;
Pc(1,1)=1;
Mdotps(1,1)=0;
PRsv(1,1)=1;
phi(1,1)=0;
done=0;

for i=0:n
   phi(i+1,1)=i*2*pi/n;
end
Dphi=2*pi/n;

while(done==0)
    for i=1:n
      [dPptdphi1,dPcdphi1,dMdotpsdphi1,dPRsvdphi1,lambdac,dlambdacdphi,Mdotc,Mdote]=dXdphi_PTss(Ppt(i),Pc(i),Mdotps(i),PRsv(i),phi(i),Rps,Lps,lambdaRsv,gamma,thetae,lambdar,Rr,thetar,lambdacd,f,lambdapt);
      [dPptdphi2,dPcdphi2,dMdotpsdphi2,dPRsvdphi2,lambdac,dlambdacdphi,Mdotc,Mdote]=dXdphi_PTss(Ppt(i)+dPptdphi1*Dphi/2,Pc(i)+dPcdphi1*Dphi/2,Mdotps(i)+dMdotpsdphi1*Dphi/2,PRsv(i)+dPRsvdphi1*Dphi/2,phi(i)+Dphi/2,Rps,Lps,lambdaRsv,gamma,thetae,lambdar,Rr,thetar,lambdacd,f,lambdapt);
      [dPptdphi3,dPcdphi3,dMdotpsdphi3,dPRsvdphi3,lambdac,dlambdacdphi,Mdotc,Mdote]=dXdphi_PTss(Ppt(i)+dPptdphi2*Dphi/2,Pc(i)+dPcdphi2*Dphi/2,Mdotps(i)+dMdotpsdphi2*Dphi/2,PRsv(i)+dPRsvdphi2*Dphi/2,phi(i)+Dphi/2,Rps,Lps,lambdaRsv,gamma,thetae,lambdar,Rr,thetar,lambdacd,f,lambdapt);
      [dPptdphi4,dPcdphi4,dMdotpsdphi4,dPRsvdphi4,lambdac,dlambdacdphi,Mdotc,Mdote]=dXdphi_PTss(Ppt(i)+dPptdphi3*Dphi,Pc(i)+dPcdphi3*Dphi,Mdotps(i)+dMdotpsdphi3*Dphi,PRsv(i)+dPRsvdphi3*Dphi,phi(i)+Dphi,Rps,Lps,lambdaRsv,gamma,thetae,lambdar,Rr,thetar,lambdacd,f,lambdapt);

      Ppt(i+1,1)=Ppt(i,1)+(dPptdphi1+2*dPptdphi2+2*dPptdphi3+dPptdphi4)*Dphi/6;
      Pc(i+1,1)=Pc(i,1)+(dPcdphi1+2*dPcdphi2+2*dPcdphi3+dPcdphi4)*Dphi/6;
      Mdotps(i+1,1)=Mdotps(i,1)+(dMdotpsdphi1+2*dMdotpsdphi2+2*dMdotpsdphi3+dMdotpsdphi4)*Dphi/6;
      PRsv(i+1,1)=PRsv(i,1)+(dPRsvdphi1+2*dPRsvdphi2+2*dPRsvdphi3+dPRsvdphi4)*Dphi/6;
   end
   errPt=Ppt(n+1,1)-Ppt(0+1,1);
   errPc=Pc(n+1,1)-Pc(0+1,1);
   errMdotps=Mdotps(n+1,1)-Mdotps(0+1,1);
   errPRsv=PRsv(n+1,1)-PRsv(0+1,1);
   Ppt(n+1,1)
    err=max([abs(Ppt(n+1,1)-Ppt(0+1,1)),abs(Pc(n+1,1)-Pc(0+1,1)),abs(Mdotps(n+1,1)-Mdotps
```

```
(0+1,1)),abs(PRsv(n+1,1)-PRsv(0+1,1))]);
    err
   if(err<tol)
      done=1;
   else
      Ppt(0+1,1)=wt*Ppt(n+1,1)+(1-wt)*Ppt(0+1,1);
      Pc(0+1,1)=wt*Pc(n+1,1)+(1-wt)*Pc(0+1,1);
      Mdotps(0+1,1)=wt*Mdotps(n+1,1)+(1-wt)*Mdotps(0+1,1);
      PRsv(0+1,1)=wt*PRsv(n+1,1)+(1-wt)*PRsv(0+1,1);
  end
end

[dPptdphi,dPcdphi,dMdotpsdphi,dPRsvdphi,lambdac,dlambdacdphi,Mdotc,Mdote]=dXdphi_PTss(Ppt ↙
,Pc,Mdotps,PRsv,phi,Rps,Lps,lambdaRsv,gamma,thetae,lambdar,Rr,thetar,lambdacd,f,lambdapt);
Wdotc=-trapz(lambdac,Pc);
Qdotc=Wdotc;
lambdae=thetae*cumtrapz(phi,Mdote)./(2*pi*Ppt);
lambdah=-cumtrapz(phi,Mdotps)./(2*pi*Ppt);
Qdote=trapz(lambdae,Ppt);
Qdoth=-trapz(lambdah,Ppt);

Msys=lambdaRsv*PRsv+lambdar*Pc/thetar+lambdae.*Ppt/thetae+lambdah.*Ppt+lambdac.*Pc;
errMsys=(max(Msys)-min(Msys));
```